

University of Alberta

**Synergism in Erosion-Corrosion Caused by Interaction of  
Electrochemical and Mechanical Factors**

by

**HAI XIA GUO** ©

A thesis submitted to the Faculty of Graduate Studies and Research  
in partial fulfillment of the requirements for the degree of

Doctor of Philosophy  
in  
Chemical Engineering

**DEPARTMENT OF CHEMICAL AND MATERIALS ENGINEERING**

Edmonton, Alberta, Canada

Fall 2006



Library and  
Archives Canada

Bibliothèque et  
Archives Canada

Published Heritage  
Branch

Direction du  
Patrimoine de l'édition

395 Wellington Street  
Ottawa ON K1A 0N4  
Canada

395, rue Wellington  
Ottawa ON K1A 0N4  
Canada

*Your file* *Votre référence*  
*ISBN: 978-0-494-23038-1*  
*Our file* *Notre référence*  
*ISBN: 978-0-494-23038-1*

#### NOTICE:

The author has granted a non-exclusive license allowing Library and Archives Canada to reproduce, publish, archive, preserve, conserve, communicate to the public by telecommunication or on the Internet, loan, distribute and sell theses worldwide, for commercial or non-commercial purposes, in microform, paper, electronic and/or any other formats.

The author retains copyright ownership and moral rights in this thesis. Neither the thesis nor substantial extracts from it may be printed or otherwise reproduced without the author's permission.

#### AVIS:

L'auteur a accordé une licence non exclusive permettant à la Bibliothèque et Archives Canada de reproduire, publier, archiver, sauvegarder, conserver, transmettre au public par télécommunication ou par l'Internet, prêter, distribuer et vendre des thèses partout dans le monde, à des fins commerciales ou autres, sur support microforme, papier, électronique et/ou autres formats.

L'auteur conserve la propriété du droit d'auteur et des droits moraux qui protègent cette thèse. Ni la thèse ni des extraits substantiels de celle-ci ne doivent être imprimés ou autrement reproduits sans son autorisation.

---

In compliance with the Canadian Privacy Act some supporting forms may have been removed from this thesis.

Conformément à la loi canadienne sur la protection de la vie privée, quelques formulaires secondaires ont été enlevés de cette thèse.

While these forms may be included in the document page count, their removal does not represent any loss of content from the thesis.

Bien que ces formulaires aient inclus dans la pagination, il n'y aura aucun contenu manquant.

  
**Canada**

## ABSTRACT

---

A serious synergistic effect arises from the coexistence of two basic material loss processes during erosion-corrosion, electrochemical dissolution due to corrosion and mechanical degradation due to erosion. This synergy contributes strongly to the total material loss. Consequently, it is critical to understand the interaction mechanisms between erosion and corrosion so as to develop means to address the loss of material. This thesis describes both the influence of erosion on corrosion and the influence of corrosion on erosion that contribute to the synergy between erosion and corrosion of carbon steel A1045.

The dependence of erosion-enhanced corrosion on the corrosion system was studied using both a non-passive and a passive corrosion system. In the non-passive system, erosion showed no significant acceleration effect on corrosion when corrosion was controlled by active dissolution. In the passive corrosion system, erosion caused an increase in the corrosion rate through impairment of the passive film. The effects of erosion were characterized using the parameters for an equivalent electrical circuit. The parameters for the passive film growth kinetics, including the diffusivities and densities of defects within the passive film, were determined using Mott-Schottky analysis. These parameters were correlated with the resistance of electrode to erosion-enhanced corrosion. In addition, electrochemical tests revealed that erosion promoted initiation of pitting corrosion by breaking down the passive

film, but impeded propagation of metastable pits by impairing the occluded environment for pitting corrosion development.

A chemo-mechanical effect was employed to understand the influence of corrosion on erosion. The surface hardness of the electrode decreased when an anodic current was impressed, which led to a higher erosion rate. Nanoindentation tests confirmed that hardness was reduced, and demonstrated that the degradation in mechanical properties declined with increasing depth from surface. The chemo-mechanical effect was manifested as a linear relationship between the rate of corrosion-enhanced erosion and the logarithm of anodic current density.

Under high flow rate conditions in corrosive solution free of particles, the mass loss rates obtained from traditional weight loss measurements were found higher than those calculated using Faraday's law. Analysis of the data showed that the additional material loss arose from corrosion-induced erosion.

## ACKNOWLEDGEMENTS

---

I would like to take this opportunity to express my gratitude to all the people who provided great help for my Ph.D study.

Firstly, I would like to express my sincere gratitude and appreciation to my supervisor, Professor Jingli Luo, whose guidance and encouragement really gave me much help throughout the whole course of this study. From her, I learned how to find, analyze and solve the problems during research. More importantly, her enthusiasm and attitude to her job set an excellent example for me. I believe that all I learned from her will help me through my whole life.

My deep appreciation also goes to Professor Hani Henein and Professor Thomas Etsell for their stimulating and greatly helpful suggestion during the progress of this research. Every time meeting with them, I learned from them, not only knowledge, but also their attitude toward research.

I greatly thank Dr. Baotong Lu for his valuable help for my research. His encouragement has helped me overcome the hardship during this work. Every time I talked with him, I always learned more than I expected.

I sincerely thank Ms. Chongguo Wang for her recommendation for my graduation study. I would also like to extend my appreciation to Mr. Bin Peng, Ms. Xiaochun Li, Mr. Adeyinka Adeleke, Mr. Shouyan Wang, Mr. Shaoxin Huang, Ms. Junfang Lu and Ms. Jinxia Li for their help, friendship and contribution towards a wonderful research environment.

I acknowledge NSERC (Natural Science and Engineering Research Council of Canada) for the financial support for this research.

Finally, my special thanks must be given to my parents and my husband, Baoliang Shi, for their endless love, selfless support and invaluable encouragement. Without them, all of this would have only been a dream.

# TABLE OF CONTENTS

<b>Chapter 1 Introduction .....</b>	<b>1</b>
<b>References .....</b>	<b>2</b>
<b>Chapter 2 Literature Review .....</b>	<b>3</b>
<b>2.1 Weight losses in erosion-corrosion processes .....</b>	<b>4</b>
2.1.1 Pure corrosion processes .....	6
2.1.1.1 General corrosion processes.....	6
2.1.1.2 Corrosion systems and forms .....	7
2.1.1.3 Corrosion in flowing environments .....	9
2.1.2 Pure erosion processes .....	10
2.1.2.1 Micro-cutting model.....	11
2.1.2.2 Deformation wear model.....	12
2.1.2.3 Fatigue model.....	12
2.1.2.4 Localization model.....	13
2.1.3 Synergistic effect.....	15
<b>2.2 Factors affecting erosion-corrosion .....</b>	<b>16</b>
2.2.1 Hydrodynamic parameters .....	16
2.2.2 Metallurgical features.....	18
2.2.2.1 Effect of mechanical properties.....	18
2.2.2.2 Effects of microstructure and composition .....	20
2.2.3 Properties of slurry .....	22
2.2.3.1 Particle property .....	22
2.2.3.2 Particle concentration.....	24
2.2.3.3 Impingement angle.....	25
<b>2.3 Mechanisms of synergistic effect between erosion and corrosion .....</b>	<b>27</b>
2.3.1 Effect of erosion on corrosion.....	27
2.3.1.1 Promoting mass transfer.....	27
2.3.1.2 Stripping off the protective film.....	28

2.3.1.3 Localizing corrosion.....	28
2.3.1.4 Roughening of the surface .....	29
2.3.1.5 Strain effect .....	30
2.3.2 Effect of corrosion on erosion.....	31
2.3.2.1 Preferential dissolution of the matrix phase.....	31
2.3.2.2 Roughening of the surface .....	31
2.3.2.3 Removal of work hardened surface.....	32
2.3.2.4 Localized attack .....	33
<b>2.4 Chemo-mechanical effect.....</b>	<b>33</b>
<b>2.5 Approach and apparatus for erosion-corrosion study .....</b>	<b>37</b>
2.5.1 Erosion-corrosion map .....	37
2.5.2 Experimental apparatus for erosion-corrosion tests.....	40
2.5.3 Experimental techniques for erosion-corrosion study.....	43
2.5.3.1 Weight loss method.....	43
2.5.3.2 Electrochemical techniques.....	44
2.5.3.3 Surface analysis methods .....	50
<b>2.6 Nanoindentation technique .....</b>	<b>51</b>
<b>2.7 Summary of present status of erosion-corrosion studies.....</b>	<b>53</b>
<b>2.8 Topic selection and technical approach .....</b>	<b>54</b>
<b>References .....</b>	<b>58</b>
<b>Chapter 3 Experimental Apparatus and Procedures .....</b>	<b>66</b>
<b>3.1 Materials and Solutions .....</b>	<b>66</b>
<b>3.2 Experimental apparatus and setups .....</b>	<b>70</b>
3.2.1 Rotating cylinder electrode system .....	70
3.2.2 Tensile tests .....	72
3.2.3 Micro-hardness tests.....	72
3.2.4 Nanoindentation tests .....	75
<b>3.3 Separating the material losses from different processes .....</b>	<b>77</b>
<b>3.4 Experimental procedures .....</b>	<b>78</b>
3.4.1 Weight loss tests.....	78

3.4.2 Micro-hardness tests.....	78
3.4.3 Tensile test.....	79
3.4.4 Electrochemical experiments .....	79
3.4.4.1 Corrosion potential.....	79
3.4.4.2 Potentiostatic measurements .....	80
3.4.4.3 Galvanostatic measurements.....	80
3.4.4.4 Potentiodynamic polarization.....	80
3.4.4.5 Polarization resistance.....	80
3.4.4.6 Electrochemical impedance spectrum.....	81
3.4.4.7 Mott-Schottky measurements.....	81
3.4.4.8 Electrode scratch test.....	81
3.4.5 Nanoindentation tests .....	82
<b>3.5 Experimental calibrations .....</b>	<b>83</b>
3.5.1 Sand degradation.....	83
3.5.2 Calibrations for nanoindentation test .....	83
<b>References .....</b>	<b>86</b>
<b>Chapter 4 Effect of Erosion on Corrosion .....</b>	<b>87</b>
<b>4.1 In a non-passive corrosion system .....</b>	<b>87</b>
4.1.1 Experimental results.....	89
4.1.1.1 $E_c$ decay.....	89
4.1.1.2 Potentiodynamic polarization.....	89
4.1.1.3 Potentiostatic polarization.....	90
4.1.1.4 Polarization resistance.....	92
4.1.2 Discussion .....	93
4.1.2.1 Effect of erosion on mass transfer.....	94
4.1.2.2 Effect of erosion on surface film.....	95
4.1.2.3 Effect of deformation on electrode reaction.....	97
4.1.3 Summary .....	99
<b>4.2 In a passive corrosion system.....</b>	<b>100</b>
4.2.1 Effect of erosion on passivation of carbon steel .....	101

4.2.1.1 Experimental results.....	101
4.2.1.1.1 $E_c$ measurement.....	101
4.2.1.1.2 Potentiostatic curve measurements.....	102
4.2.1.1.3 Polarization curve measurements.....	104
4.2.1.1.4 Scratch tests.....	104
4.2.1.1.5 Electrochemical impedance measurements.....	106
4.2.1.2 Discussion.....	115
4.2.1.2.1 Effect of erosion on corrosion and passive film.....	115
4.2.1.2.2 System dependence of erosion-enhanced corrosion.....	117
4.2.1.3 Summary.....	118
4.2.2 Study on erosion-enhanced corrosion by Mott-Schottky analysis.....	119
4.2.2.1 Results and discussion.....	120
4.2.2.1.1 Passive behavior in the three solutions.....	120
4.2.2.1.2 Resistance to erosion-enhanced corrosion.....	122
4.2.2.1.3 Mott-Schottky analysis.....	131
4.2.2.1.4 Correlation between defect flux, film growth and erosion-enhanced corrosion.....	136
4.2.2.2 Summary.....	140
4.2.3 Effect of sand impingement on pitting corrosion.....	141
4.2.3.1 Experimental results and discussion.....	141
4.2.3.1.1 Pitting induction time measurements.....	141
4.2.3.1.2 Pitting potential measurements.....	142
4.2.3.1.3 Potentiostatic measurements.....	148
4.2.3.1.4 Surface morphology.....	150
4.2.3.1.4 Synergy between erosion and chloride.....	150
4.2.3.2 Summary.....	152
<b>References.....</b>	<b>152</b>
<b>Chapter 5 Effect of Corrosion on Erosion.....</b>	<b>156</b>
<b>5.1 Effect of anodic current on erosion in sand slurry.....</b>	<b>157</b>
5.1.1 Total weight losses and corrosion-enhanced erosion.....	157

5.1.2 Possible effect from solution.....	157
5.1.3 Chemo-mechanical model for corrosion-enhanced erosion.....	160
5.1.3.1 Dependence of erosion rate on mechanical property .....	161
5.1.3.2 Relation of mechanical property to corrosion.....	163
5.1.3.3 Dependence of synergistic effect on corrosion .....	166
5.1.4 Summary .....	169
<b>5.2 Corrosion-enhanced erosion in flowing solution.....</b>	<b>170</b>
5.2.1 An interesting experimental phenomenon.....	170
5.2.2 Phenomenon analysis .....	171
5.2.3 Factors affecting the corrosion-induced erosion .....	176
5.2.3.1 Effect of velocity.....	176
5.2.3.2 Effect of anodic current density .....	179
5.2.3.3 Effect of hardness.....	179
5.2.3.4 Effect of solution pH.....	181
5.2.4 Discussion .....	182
5.2.5 Summary .....	187
<b>5.3 Investigation of chemo-mechanical effect by nanoindentation techniques</b>	<b>188</b>
.....	
5.3.1 Introduction .....	188
5.3.2 Nanoindentation tests in air and in liquid.....	189
5.3.3 Effect of anodic dissolution on surface hardness .....	195
5.3.3.1 Surface hardness degradation.....	195
5.3.3.2 Hysteresis effect of hardness degradation.....	202
5.3.3.3 Decline of hardness degradation with depth .....	203
5.3.4 Effect of cathodic reaction on surface hardness.....	206
5.3.5 Summary .....	208
<b>5.4 Other effect of corrosion on erosion .....</b>	<b>209</b>
<b>5.5. The corrosion-enhanced erosion in passive system.....</b>	<b>213</b>
<b>References .....</b>	<b>217</b>

<b>Chapter 6 Summary and Future Work .....</b>	<b>220</b>
<b>6.1 Main conclusions .....</b>	<b>220</b>
<b>6.2 Contribution to knowledge.....</b>	<b>221</b>
<b>6.3 Contribution to literature.....</b>	<b>224</b>
<b>6.4 Suggestions for future work.....</b>	<b>224</b>
<b>Appendix: Erosion-Corrosion of TiC Reinforced Alloys.....</b>	<b>226</b>
<b>A.1 Introduction .....</b>	<b>226</b>
<b>A.2 Results and Discussion .....</b>	<b>227</b>
A.2.1 The synergistic effect between erosion and corrosion .....	227
A.2.1.1 The pure erosion rate.....	227
A.2.1.2 The pure corrosion behavior .....	229
A.2.1.3 The synergistic effect .....	230
A.2.2 Interaction mechanism for erosion and corrosion .....	233
A.2.2.1 Effect of erosion on corrosion.....	233
A.2.2.2 The chemo-mechanical effect .....	235
A.2.2.3 The microscope observation and corrosion-enhanced erosion .....	237
A.2.3 Effect of $cl^-$ on synergy .....	248
<b>A.3 Summary.....</b>	<b>251</b>
<b>References .....</b>	<b>252</b>

## LIST OF TABLES

Table 3-1. Chemical components of AISI 1045 (wt %)	66
Table 3-2. Chemical components of pure iron (wt %)	66
Table 3-3. Main properties of the silica sand	67
Table 4-1. Equivalent circuit parameters as a function of velocity	111
Table 4-2. Equivalent circuit parameters as a function of sand concentration	111
Table 4-3. Defect diffusivities and other parameters for the passive films formed in the borate solutions	135

## LIST OF FIGURES

Figure 2-1. Interaction of flow, erosion and corrosion. ....	4
Figure 2-2. Various weight losses during erosion-corrosion processes. ....	6
Figure 2-3. Material removal process during erosion [20]. ....	14
Figure 2-4. Dependence of erosion rate on the hardness of target material [18]. ....	19
Figure 2-5. Dependence of erosion rate on particle size for impact by quartz particles [78]. ....	23
Figure 2-6. Dependence of material loss on slurry concentration for a mild steel in a silica sand/water slurry [40]. ....	24
Figure 2-7. Dependence of erosion rate on impingement angle [82]. ....	26
Figure 2-8. Creep curves of copper with anodic current on and off [121]. ....	36
Figure 2-9. Steady creep rates of brass vs. anodic current density [124]: (a) 3.5% NaCl solution, (b) 0.45 M CH <sub>3</sub> COOH + 0.05 M CH <sub>3</sub> COONa solution	37
Figure 2-10. Erosion-corrosion map [140]: (a) mechanism map, (b) wastage map. .	39
Figure 2-11. Equivalent circuit of Randle model [4]. ....	46
Figure 2-12. Data display of electrochemical impedance spectroscopy for a corroding electrode simulated by Randle model [4]: (a) Nyquist plot, (b) Bode plot. .....	48
Figure 2-13. Typical indentation load-displacement curve defining key parameters.	53
Figure 2-14. Content of the thesis work. ....	57
Figure 3-1. Microstructure of samples. ....	68
Figure 3-2. Micrograph of the sand used in the present work. ....	69
Figure 3-3. Size distribution of the sand used in the present work. ....	69
Figure 3-4. Configuration of the sample and schematic of the setup for erosion corrosion tests. ....	71
Figure 3-5. Configuration of the sample and schematic of the setup for tensile tests.	73
Figure 3-6. Configuration of the samples and schematic of the setup for micro- hardness tests. ....	74

Figure 3-7. Schematic of the equipment used for in situ nanoindentation tests. ....	76
Figure 3-8. Load function for nanoindentation tests with peak load of 1000 $\mu\text{N}$ . ....	82
Figure 3-9. Pure erosion rate of carbon steel A1045 with sand degradation. ....	84
Figure 3-10. Hardness (a) and reduced modulus (b) of fused quartz. ....	85
Figure 4-1. Polarization curve for carbon steel A1045 rotating at 9000 rpm in 0.1 M $\text{Na}_2\text{SO}_4$ solution. ....	88
Figure 4-2. Synergistic effect between erosion and corrosion for carbon steel A1045 in a slurry of 35% sand/0.1 M $\text{Na}_2\text{SO}_4$ solution at 9000 rpm. ....	89
Figure 4-3. Corrosion potential decay of A1045 steel in 0.1M $\text{Na}_2\text{SO}_4$ solution. ....	90
Figure 4-4. Polarization behavior of carbon steel A1045 in 0, 20 and 35% slurries: (a) rotating at 6000 rpm and (b) 9000 rpm. ....	91
Figure 4-5. Current response of carbon steel A1045 arising from initiation of rotating and sand impingement at an applied potential of -400 mV. ....	92
Figure 4-6. Polarization resistances of carbon steel A1045 in slurries as a function of velocity and sand concentration. ....	93
Figure 4-7. Effect of rotating velocity on polarization behavior of carbon steel A1045 in a slurry containing 35% sand. ....	94
Figure 4-8. Effect of scratching on carbon steel A1045 under constant potential: (a) Current density at -400 mV, (b) Micrograph of the sample after scratching. ....	96
Figure 4-9. Current response for carbon steel A1045 in scratch test at 20 mV vs. $E_c$ with air bubbled at sample surface. ....	97
Figure 4-10. Polarization curve of carbon steel A1045 in borate buffer solution. ....	100
Figure 4-11. Corrosion potential decay of carbon steel A1045 in the borate solution. ....	102
Figure 4-12. Potentiostatic curves for carbon steel A1045 at an applied potential of 200 mV in borate solution: (a) as a function of velocity; (b) as a function of sand concentration at 9000 rpm. ....	103

Figure 4-13. Potentiodynamic polarization curves of carbon steel A1045 in borate solution: (a) in flowing solution at different velocities; (b) in slurries with different sand concentrations at 9000 rpm .....	105
Figure 4-14. Current density curves for carbon steel A1045 in borate solution during scratch test at an applied potential of 200 mV. ....	106
Figure 4-15. Nyquist plots (a) and Bode plots (b & c) for carbon steel A1045 in borate solution at different velocities. ....	108
Figure 4-16. Nyquist plots (a) and Bode plots (b & c) for carbon steel A1045 in slurries with different sand concentrations at 6000 rpm. ....	110
Figure 4-17. Equivalent circuit for the carbon steel/borate solution system.....	110
Figure 4-18. Electrochemical parameters fitted with the equivalent circuit as a function of velocity: (a) $R_r$ & $1/C$ ; (b) $a_1$ & $a_2$ .....	113
Figure 4-19. Electrochemical parameters fitted with the equivalent circuit as a function of sand concentration: (a) $R_r$ & $1/C$ ; (b) $a_1$ & $a_2$ .....	114
Figure 4-20. Potentiodynamic polarization curves for carbon steel A1045 in borate solutions: (a) in still solution, (b) rotating at 9000 rpm.....	121
Figure 4-21. Potentiostatic curves for carbon steel A1045 rotating at 9000 rpm in the 0.3 M solution at a potential of 200 mV (a) and 800 mV (b).....	122
Figure 4-22. Current densities of carbon steel A1045 as a function of sand concentration at a potential of 200 mV (a) and 800 mV (b). ....	124
Figure 4-23. Schematic transient current peak arising from sand impingement: .....	125
Figure 4-24. Pure erosion rate as a function of sand concentration at a rotation velocity of 9000 rpm. ....	126
Figure 4-25. Current densities of carbon steel A1045 as a function of pure erosion rate in borate solutions at 200 mV (a) and 800 mV (b).....	127
Figure 4-26. Current density curves for carbon steel A1045 in borate solutions in scratch test at an applied potential of 200 mV and 800 mV.....	130
Figure 4-27. Mott-Schottky plots for carbon steel A1045 in the 0.03 M, 0.1 M and 0.3 M solution. The electrode was pre-passivated for 1 h at 200 mV (a), 400mV (b) and 800 mV (c). ....	132

Figure 4-28. Donor densities of carbon steel A1045 as a function of film form potential in the 0.3 M, 0.1 M and 0.03 M borate solution.....	133
Figure 4-29. Dependence of donor density on borate solution concentration. The electrode was pre-passivated at 800 mV for 1h in the solutions. ....	137
Figure 4-30. Donor densities determined for carbon steel A1045 in flowing solution and still solution. ....	139
Figure 4-31. Potentiostatic current curves for carbon steel A1045 at an applied potential of 200 mV and a rotation velocity of 9000 rpm. ....	142
Figure 4-32. Potentiodynamic polarization curves for carbon steel A1045 in 15% slurry containing different $\text{Cl}^-$ concentrations at rotation velocity of 6000 rpm.....	143
Figure 4-33. Pitting potentials of carbon steel A1045 as a function of $\text{Cl}^-$ concentration at rotation velocity of 6000 rpm. ....	143
Figure 4-34. Cyclic polarization curves for carbon steel A1045 in slurry containing 0.05 M $\text{Cl}^-$ at a rotation velocity of 6000 rpm. ....	144
Figure 4-35. Pitting potentials of carbon steel A1045 as a function of slurry concentration at rotation velocity of 6000 rpm. ....	145
Figure 4-36. Areas of hysteresis loops in Figure 4-35 as a function of slurry concentration. ....	145
Figure 4-37. Slope of potential polarization curve as a function of sand concentration in slurries containing 0.05 M $\text{Cl}^-$ . ....	148
Figure 4-38. Current response of carbon steel A1045 to chloride ions and sand impingement at potential of 200 mV and rotation velocity of 6000 rpm. ....	149
Figure 4-39. Current densities of carbon steel A1045 as a function of slurry concentration and chloride ions at 200 mV and rotation velocity of 6000 rpm.....	149
Figure 4-40. Morphology of carbon steel A1045 after anodic polarization as the $\text{Cl}^-$ concentration was 0.02 M and rotation velocity was 6000 rpm: (a) in solution (b) in 15% slurry.....	151

Figure 5-1. Weight loss of carbon steel A1045 as a function of anodic current density in 0.1 M Na <sub>2</sub> SO <sub>4</sub> solution: (a) in 25% slurry; (b) in 35% slurry. ....	158
Figure 5-2. Weight loss of carbon steel A1045 as a function of anodic current.....	159
Figure 5-3. Pure erosion rates of carbon steel A1045 in tap water, new and used Na <sub>2</sub> SO <sub>4</sub> solution with 35% sand. ....	160
Figure 5-4. Vicker's hardness of carbon steel A1045 as a function of heat treated temperatures. ....	161
Figure 5-5. Dependence of pure erosion rate of carbon steel A1045 on Vicker's hardness in 25% slurry. ....	162
Figure 5-6. Hardness degradation of carbon steel A1045 caused by applied anodic current: (a) in tap water, (b) in 1 M NaHCO <sub>3</sub> solution, (c) in 0.001 M Na <sub>2</sub> SO <sub>4</sub> solution, and (d) in 0.1 M Na <sub>2</sub> SO <sub>4</sub> solution. ....	165
Figure 5-7. Normalized corrosion-enhanced erosion as a function of anodic current density in slurries containing 25% sand (a) and 35% sand (b). ....	167
Figure 5-8. Normalized corrosion-enhanced erosion for as-received and annealed carbon steel A1045 in 35% slurry. ....	168
Figure 5-9. Ratio of $W_m/W_f$ for carbon steel A1045 at an applied current density of 2 mA/cm <sup>2</sup> .....	172
Figure 5-10. Polarization behavior of carbon steel A1045 in 0.1 M Na <sub>2</sub> SO <sub>4</sub> solution at different rotating velocities. ....	174
Figure 5-11. Dependence of corrosion-induced erosion on rotating velocity with an applied current density of 2 mA/cm <sup>2</sup> : (a) $W_m/W_f$ vs. velocity, (b) $W_{c-e}$ vs. velocity.....	177
Figure 5-12. Dependence of corrosion-induced erosion on rotating velocity with an applied current density of 1.5 mA/cm <sup>2</sup> : (a) $W_m/W_f$ vs. velocity; (b) $W_{c-e}$ vs. velocity.....	178
Figure 5-13. Dependence of corrosion-induced erosion on current density in 0.1 M Na <sub>2</sub> SO <sub>4</sub> solution.....	179

Figure 5-14. Corrosion-induced erosion as a function of velocity for as-received and annealed carbon steel A1045 samples in 0.1 M Na <sub>2</sub> SO <sub>4</sub> solution: (a) $W_m / W_f$ vs. velocity; (b) $W_{c-e}$ vs. velocity.....	180
Figure 5-15. Corrosion-induced erosion of carbon steel A1045 as a function of rotating velocity in solution with different pH.....	181
Figure 5-16. Corrosion-induced erosion as a function of current density in 35% slurry and in solution at velocity of 9000 rpm.....	183
Figure 5-17. Dependence of corrosion-induced erosion on hardness degradation where $W_{c-e}$ was measured in flowing solution at 9000 rpm. ....	184
Figure 5-18. Effect of current density on the wastage ratio $W_i / W_f$ for carbon steel A1045 in 0.1 M Na <sub>2</sub> SO <sub>4</sub> solution. ....	186
Figure 5-19. Schematic for corrosion-induced erosion: (a) under cathodic protection, (b) in still solution, (c) in flowing solution. ....	186
Figure 5-20. Typical nanoindentation image on pure iron sample. ....	189
Figure 5-21. Mechanical properties of iron measured in air at the maximum load of 200-2000 $\mu$ N: (a) Load-depth curves, (b) Hardness vs. contact depth; (c) Modulus vs. contact depth.....	192
Figure 5-22. Depth dependence of hardness for pure iron, plotted according to Equation (5-17).....	192
Figure 5-23. Effect of loading/unloading rate on nanoindentation hardness of pure iron.....	193
Figure 5-24. Comparison of nanoindentation test results in air and in deionized water. ....	194
Figure 5-25. Potentiodynamic polarization curve for pure iron in 0.01 M Na <sub>2</sub> SO <sub>4</sub> solution. ....	195
Figure 5-26. Effect of anodic current on load-depth curves of iron: (a) $P_{max}=500 \mu$ N; (b) $P_{max}=1200 \mu$ N; (c) $P_{max}=1800 \mu$ N.....	197
Figure 5-27. Effect of anodic current on the surface hardness of iron.....	198
Figure 5-28. Effect of anodic current on the elastic modulus of iron. ....	198

Figure 5-29. Comparison of the load-depth curves for iron measured by in situ and ex situ tests at $P_{\max} = 500 \mu\text{N}$ . .....	200
Figure 5-30. Comparison of the surface hardness of iron measured in air and in solution by in situ and ex situ tests. ....	201
Figure 5-31. Hardness degradation as a function of time after electrochemical dissolution. ....	203
Figure 5-32. Hardness ratio and difference as a function of contact depth for pure iron in 0.01 M $\text{Na}_2\text{SO}_4$ solution. ....	204
Figure 5-33. Modulus ratio and difference as a function of contact depth for pure iron in 0.01 M $\text{Na}_2\text{SO}_4$ solution with an applied current of $1\text{mA}/\text{cm}^2$ . ....	205
Figure 5-34. Effect of cathodic current on the surface hardness of iron. ....	207
Figure 5-35. Effect of hydrogen charging on the surface hardness of iron. ....	208
Figure 5-36. Comparison of the experimental corrosion-enhanced erosion data and the calculated values with chemo-mechanical model under different conditions. ....	209
Figure 5-37. Pure erosion rates of the corroded and uncorroded carbon steel samples (x-axis represents the corrosion time). ....	210
Figure 5-38. Friction coefficients of iron in air, in solution and after corrosion. ....	212
Figure 5-39. The weight loss distribution of carbon steel A1045 in borate solution at velocity of 9000 rpm under 600 mV. ....	214
Figure 5-40. The percentage of corrosion enhanced erosion as a function of passive potential in borate solution at velocity of 9000 rpm. ....	214
Figure 5-41. The total weight loss (a) and normalized corrosion-enhanced erosion (b) as a function of passive potential in borate solution at a rotating velocity of 9000 rpm. ....	215
Figure 5-42. Comparison of the normalized corrosion enhanced-erosion data for passive system and non-passive system. ....	216

## LIST OF SYMBOLS

Symbols	Meanings
$a$	Exponent for calculating impedance of CPE
$a_1$	Exponent for calculating impedance of CPE <sub>1</sub>
$a_2$	Exponent for calculating impedance of CPE <sub>2</sub>
$A$	Projected contact area
$A_0$	$\kappa' BHv$
$A_c$	Surface area of capacitor
$A_e$	Intensity of particle impingement
$b$	Experimental constant for impedance of CPE
$\bar{b}$	Burgers vector
$b_0$	Experimental constant for donor density
$b_a$	Tafel slope for anodic polarization
$b_c$	Tafel slope for cathodic polarization
$B$	Experimental constant for chemo-mechanical effect
$c_1$ through $c_5$	Coefficients for calculating the indenter shape
$C$	Electrode capacitance
$C_{cl^-}$	Concentration of chloride ions
$C_b$	Bulk concentration of the species involved in reaction
$C_s$	Concentration of the reactive species at the metal surface
$C_{sand}$	Sand concentration
$d$	Pipe diameter
$d_c$	Thickness of capacitor
$d_i$	Difference between the outer and inner radii
$D$	Diffusion coefficient
$D_0$	Diffusivity of the defects in the passive film
$e$	Electron charge

$e_0$	2.718
$E$	Potential
$E_0$	Amplitudes of potential
$E_b$	Pitting potential
$E_{fb}$	Flat band potential
$E_i$	Young's modulus of the indenter
$E_r$	Reduced modulus
$E_s$	Young's modulus of the specimen
$\Delta E$	Overpotential
$f(\alpha)$	A functional relationship for the dependence of erosion rate on impact angle
$F$	Faraday constant
$h_c$	Indentation contact depth
$h_{max}$	Maximum depth
$h^*$	A length that characterizes the depth dependence of hardness
$(h^*)'$	Character length with applied current
$H$	Hardness
$H'$	Hardness measured with anodic current applied
$H_0$	Hardness of the bulk material
$H_0'$	True material hardness with applied current
$H_v$	Vickers hardness without anodic current present at the electrode surface
$H_v^*$	Vickers hardness with anodic current present at the electrode surface
$\Delta H_v$	Change in hardness due to anodic dissolution at the surface
$i$	Current density
$i_0$	Peak current value
$i_a$	Anodic current density

$i_{a,\sigma}$	Anodic dissolution current density with the presence of stress
$i_c$	Cathodic current density
$i_{corr}$	Corrosion current density
$i_{lim}$	Limited current density
$i_p$	Passive current density
$i_{th}$	Threshold anodic current density to induce the chemo-mechanical effect
$I$	Current
$I_0$	Amplitudes of current
$j$	$\sqrt{-1}$
$J$	Flux of the donors
$J_0$	Steady state flux of donors
$J^c$	Donor flux due to concentration gradient
$J^p$	Donor flux due to potential gradient
$k$	Boltzmann constant
$k_e$	Elastic stress factor
$k_p$	Plastic stress factor
$k_\sigma$	A stress factor that characterizes the influence of stress on anodic dissolution rate
$K$	Mass transfer coefficient
$K_0$	$=F\varepsilon_i/(RT)$
$K_1$	Apparent mass transfer coefficient in the bulk solution
$K_2$	Apparent mass transfer coefficient in the film
$K_3$	Coefficient for electrochemical reaction at the metal surface
$l$	Average diagonal length of the indenter impression
$L$	Thickness of the film
$m$	Exponent for corrosion-induced erosion
$m_1$ and $m_2$	Constants dependent on the erosion-corrosion system

$M$	Molar weight of the metal
$M_p$	Weight of the particles per unit volume of solution
$n$	The number of the mole of electrons
$N$	Charge carrier density
$N_D$	Donor density
$N_v$	Avogadro's number
$P$	Applied indenting load
$P_{max}$	The maximum load
$r_i$	Inner cylinder radii
$R$	Gas constant
$Re$	Reynolds number
$R_{sol}$	Solution resistance
$R_r$	Charge transfer resistance for the corrosion reaction
$S$	Stiffness
$Sc$	Schmidt number
$Sh$	Sherwood number
$t$	Time
$T$	Absolute temperature
$U_f$	Film formation potential
$v$	Experimental constant for pure erosion rate
$V$	Flow velocity
$w_1$ and $w_2$	Experimental constant for donor density
$W_c$	Corrosion rate with presence of erosion
$W_{c0}$	Pure corrosion rate without presence of erosion
$W_{c-e}$	Corrosion-enhanced erosion
$W_e$	Erosion rate with presence of corrosion
$W_{e0}$	Pure erosion rate without presence of corrosion
$W_{e-c}$	Erosion-enhanced corrosion
$W_f$	Corrosion rate calculated with the Faraday's law
$W_m$	Corrosion rate measured with weight loss method

$W_s$	Wastage produced by synergistic effect
$W_t$	Total weight loss of the material
$Z$	Electrode impedance
$Z_{CPE}$	Impedance of CPE
$Z'(w)$	Real component of electrode impedance
$Z''(w)$	Imaginary component of electrode impedance
$\alpha, \beta,$ and $\gamma$	Constants depending the flow conditions and geometries of the test devices
$\alpha_0$ and $\beta_0$	Experimental parameters for pitting potential
$\beta'$	Depression angle
$\epsilon$	Dielectric constant
$\epsilon_0$	Permittivity of vacuum
$\epsilon_L$	Mean electric field strength within the passive film
$\eta$	A constant for Taylor relation
$\theta$	Phase angle between potential and current
$\kappa$	Experimental constant for pure erosion rate
$\kappa'$	Experimental constant for corrosion-induced erosion
$\mu$	Viscosity of slurry
$\mu_0$	Shear modulus
$\nu_s$	Poisson's ratio of the specimen
$\nu_i$	Poisson's ratio of the indenter.
$\rho$	Density of slurry
$\tau$	Current decay constant,
$\nu$	Kinetic viscosity of the solution
$\phi$	Angle between indenter surface and sample surface
$\varphi$	Coefficient related to the geometry of the indenter
$\omega$	Angular velocity
$\Omega$	Molar volume per cation

## LIST OF ABBRIVATIONS

<b>Abbreviations</b>	<b>Meanings</b>
AFM	Atomic Force Microscopy
AISI	American Iron and Steel Institute
ANSI	American National Standards Institute
ASTM	American Society For Testing And Materials
CE	Counter Electrode
CP	Cathodic Protection
CPE	Constant Phase Elements
EIS	Electrochemical Impedance Spectroscopy
EDX	Energy Dispersive X-Ray Spectroscopy
GNDs	Geometrically Necessary Dislocations
MMCs	Metal Matrix Composites
$E_c$	Corrosion potential
PDM	Point Defect Model
PTFE	Polytetrafluoroethylene
RCE	Rotating Cylinder Electrode
RE	Reference Electrode
SCE	Saturated Calomel Electrode
SEM	Scanning Electron Microscopy
SIMS	Secondary Ion Mass Spectrometry
TEM	Transmission Electron Microscopy
XRD	X-Ray Diffraction Analysis
XPS	X-Ray Photoelectron Spectroscopy
WE	Working Electrode

# Chapter 1

# Introduction

When metallic materials are exposed to a flowing corrosive environment, the electrochemical reaction occurring on the metal surface will cause corrosion, and the mechanical impact of flowing fluid and solid particles will cause erosion. Both of these processes can result in severe material losses. The premature failure of materials caused by the combination of these two processes is termed as erosion-corrosion. In practice, erosion-corrosion causes immense losses in industries, especially in those involving transportation of materials, such as offshore oil and gas, mineral processing and mining. For example, the annual losses due to the sum effect of both erosion and corrosion phenomena in the United States exceeded \$300 billion in 1990 and continue to grow [1]. This figure represented approximately 7% of the Gross National Product. In Northern Alberta, erosion-corrosion is also a serious problem for the oil sands industry which requires handling and processing of substantial silica-based solids. In the tailings pipe system of Syncrude Canada Ltd. the aggressive nature of 50 wt% sand slurry results in a significant materials loss. To overcome this problem, Syncrude expends \$40 million on replacement and maintenance of tailings pipes.

During erosion-corrosion processes, two basic material loss processes are involved: electrochemical dissolution due to corrosion and mechanical degradation due to erosion. However, the total material loss rate resulting from erosion-corrosion is generally much higher than that due to the linear sum of the two individual processes [2-5]. The additional material loss arises from an interaction/synergistic effect between these two processes. The erosion and corrosion processes interactively accelerate each other, resulting in more severe material loss and premature material failure. The losses due to this synergy can be as high as 80% of the total material loss [6].

In order to develop effective solutions to reduce the risk of early component failure due to erosion-corrosion and to extend component life, it is critical to understand the interaction between erosion and corrosion and to reveal the mechanism that results in the synergy. In addition, understanding the involved synergistic effect between mechanical factors and electrochemical factors will provide valuable information for related studies of phenomena, such as stress corrosion cracking and corrosion fatigue [7, 8].

For these reasons, the objective of this research is to clarify the interaction between erosion and corrosion occurring in slurry flow processes, and to provide information useful for industrial applications and for advancing research in erosion-corrosion and related areas. The effect of erosion on corrosion and the effect of corrosion on erosion will be experimentally investigated separately for different corrosion systems.

## References

- [1] J.W. Cox, Wear and corrosion resistant hard coatings for non-cutting tool applications, in Handbook of Hard Coatings, R.F. Bunshah, Editor, William Andrew Publishing, 2001, p.411.
- [2] I.M. Hutchings, The Erosion of Materials by Liquid Flow, Cambridge, UK, MTI Publication No. 25, Material Technology Institute of the Chemical Process Industries, 1986.
- [3] M.M. Stack, International Materials Reviews 50 (1) (2005) 1.
- [4] A. Neville and X. Hu, British Corrosion Journal 37 (1) (2002) 43.
- [5] G.T. Burstein and K. Sasaki, Electrochimica Acta 46 (2001) 3675.
- [6] Z. Yue, P. Zhou, and J. Shi, in Wear of Materials, ASME, New York, 1987, p.763.
- [7] A. Jones, Metallurgy Transaction A 16 (1985) 1133.
- [8] T. Magnin, A. Chambreuil, and B. Bayle, Acta Materials 44 (4) (1996) 1457.

## Chapter 2

## Literature Review

Due to its potential to cause severe damage, erosion-corrosion has been placed within the top five corrosion related concerns. This area has attracted a lot of research interest from industries and academia since the 1960's.

In erosion-corrosion processes, flowing of the media, impingement of solid particles and electrochemical reactions coexist. Their interaction results in differences in material failure mechanisms. **Figure 2-1** illustrates the interaction among media flow, erosion and corrosion. The areas of interaction between corrosion and flow, flow and erosion, and corrosion and erosion are respectively referred to flow-induced-corrosion (or flow-accelerated-corrosion), slurry erosion and corrosive wear [1]. Erosion-corrosion is defined as the material loss or failure processes due to the conjoint action of erosion by flowing of media containing solid particles and corrosion dissolution of material. Erosion-corrosion can also be induced in other systems, such as those containing high velocity and high temperature gaseous flows, or those involving friction due to relative motion of components. For the latter case, as corrosion occurs simultaneously, material failure is said to result from corrosive wear. Erosion-corrosion at high temperatures has been reviewed in Reference [2].

Study on erosion-corrosion, an interdisciplinary field, needs to employ knowledge from fluid mechanics, multi-flow in most cases, transport processes, materials science and engineering, and electrochemical engineering. Thus the complexity is not surprising. In this chapter, the various weight losses in erosion-corrosion will be analyzed first. The pure corrosion, pure erosion processes and the main factors affecting erosion-corrosion will then be described. The mechanisms for synergism between erosion and corrosion and the chemo-mechanical effect will be reviewed and discussed. Additionally, some investigative approaches and the

technologies applied for study of erosion-corrosion will be presented. Finally, the objectives and scope of this research will be given.

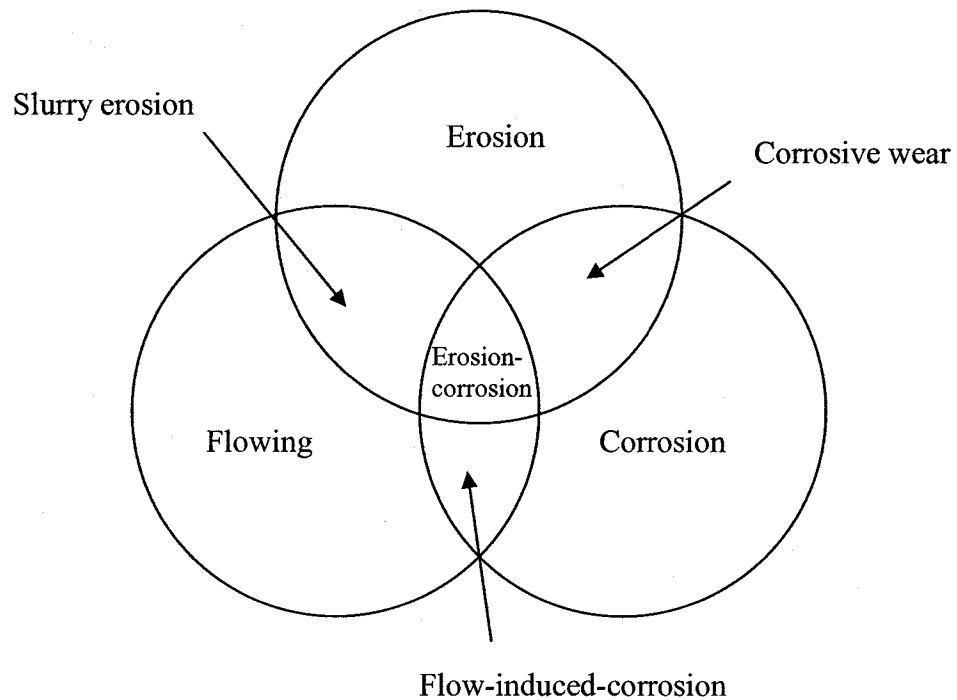


**Figure 2-1. Interaction of flow, erosion and corrosion.**

## 2.1 Weight losses in erosion-corrosion processes

According to the mechanism of material loss, the wastage of material in erosion-corrosion processes is considered to be the sum of the contributions due to mechanical erosion and electrochemical corrosion:

$$W_t = W_c + W_e \quad (2-1)$$

where 
$$W_c = W_{c0} + W_{e-c} \quad (2-2)$$

and 
$$W_e = W_{e0} + W_{c-e} \quad (2-3)$$

$W_t$  — the total weight loss of the material;

$W_c$  — the corrosion rate with presence of erosion;

$W_e$  — the erosion rate with presence of corrosion;

$W_{c0}$  — the pure corrosion rate without presence of erosion;

$W_{e0}$  — the pure erosion rate without presence of corrosion;

$W_{e-c}$  — the corrosion rate promoted by erosion, i.e. erosion-enhanced corrosion;

and

$W_{c-e}$  — the erosion rate enhanced by corrosion, i.e. corrosion-enhanced erosion.

**Figure 2-2** illustrates the relationship of the various weight losses during erosion-corrosion processes. The sum of the material losses caused by the erosion-enhanced corrosion and corrosion-enhanced erosion is often regarded as the wastage produced by the synergistic effect  $W_s$  [3].

$$W_s = W_{e-c} + W_{c-e} \quad (2-4)$$

In most cases  $W_s$  is greater than zero, because the mechanical erosion and electrochemical corrosion processes interact and concurrently accelerate each other.

In erosion processes, the material losses are in the form of small debris due to cutting, plastic deformation or contact fatigue caused by the cavitation of flowing fluid or the impact of solid particles. Therefore, erosion has the nature of a mechanical degradation process. In contrast, in corrosion processes the metallic atoms lose electrons, leave the metal surface and enter into the environment in the form of ions or compounds, which has the nature of an electrochemical process.

Before investigating the interaction of erosion and corrosion, it is necessary to understand the individual processes.

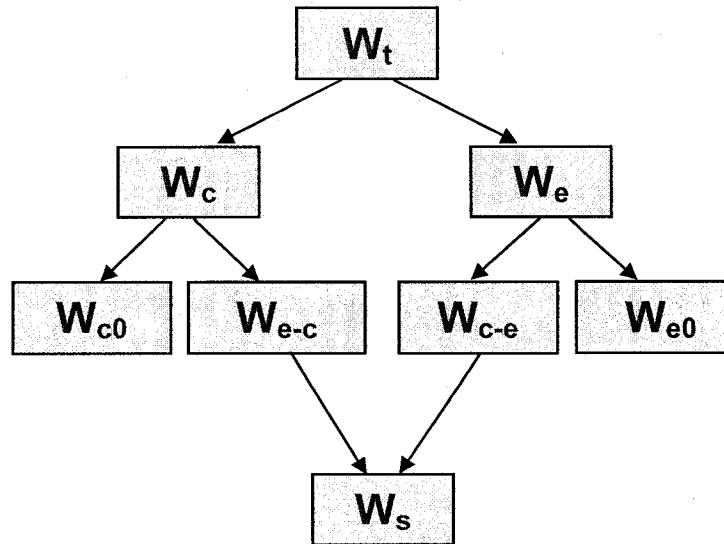


**Figure 2-2. Various weight losses during erosion-corrosion processes.**

### 2.1.1 Pure corrosion processes

As metallic materials are exposed to aqueous media, soil, or even humid air environments, corrosion takes place on the metal surface. It is the destructive result of the chemical reaction between a metal alloy and its environment. In nature, most metal atoms are present in chemical compounds, which are the thermodynamically stable state. Energy is required to extract a metal from its minerals. These extracted metals, however, are subject to corrosion under the thermodynamic driving force. Therefore, corrosion has been called extractive metallurgy in reverse [4].

#### 2.1.1.1 General corrosion processes

Most corrosion processes in aqueous environments involve the transfer of electronic charge, and thus the nature of the corrosion process is electrochemical. The basic three consecutive steps in the electrochemical reaction of a metallic electrode are: (1) the transport of reactant to the electrode surface; (2) the surface electrochemical reaction; (3) the transport of product away from the electrode surface.

Each step is complex. When the corroding metal surface is directly exposed to the environment, without a barrier of film or corrosion product, the process of mass transfer in solution is the only step for the transport of reactant and product. If the metal electrode is covered by a film or deposited corrosion product, the mass transfer process will be more complicated, since transfer within the film is also involved [5, 6].

The surface electrochemical reaction also has complexities. It has been found that, even for a very simple electrode reaction, the whole reaction is not completed in one step. Rather, several steps are involved, generally including atom adsorption, discharging the first electron, forming complex ions with other species, and further discharging into the final product. Extensive investigation has been conducted into the reactions of iron in acidic environments, which has been regarded as the most basic reaction for corrosion processes for steels. Two reaction mechanisms are generally accepted: the non-catalytic approach for iron with low reactivity, and the catalytic approach for iron with high reactivity. The detailed reaction steps have been reviewed by Cao [7].

#### **2.1.1.2 Corrosion systems and forms**

According to whether or not a protective passive film forms on a metal surface, corrosion systems can be usually categorized into passive systems and non-passive systems. In a passive system, the metals exhibit excellent corrosion resistance because of the protection of the passive film. The passive film, which could be an adsorption film or three-dimensional oxide film, can reduce the rates of corrosion reactions at the metal-passive film interface, or limit the mobility of ions and atoms, thereby leading to lower corrosion rates. Therefore, the corrosion behaviour of the passive system significantly depends on the film formation kinetics, and the structure and properties of the passive film. Considerable study on passive systems has concentrated on this area.

In a non-passive system, however, the metal atoms dissolve into the environment freely, without formation of any significant barriers. Although it is

possible that some corrosion product deposits on the electrode surface, their protective capability is negligible when compared with the passive film. Thus the controlling steps in the whole corrosion process are charge transfer at the metal surface and/or mass transfer resistance in the fluid environment. When charge transfer is the rate-determining step for corrosion, the system is also referred to as an active dissolution corrosion system. Usually, in active systems the metals corrode with relatively high rates.

Based on the distribution of the anodic and cathodic sites on the electrode surface and the resulting morphology, the corrosion process can also be classified as uniform corrosion, galvanic corrosion, crevice corrosion, pitting corrosion, intergranular corrosion, etc. The first one is general corrosion, where the anodic and cathode sites are not fixed at certain electrode surface locations. At any location, the electrode surface anodic reaction and the cathodic reaction take place alternatively. As a result, the whole electrode surface corrodes uniformly. The other corrosion forms, in contrast, represent different types of localized corrosion, where certain areas act as anodes in the corrosion cell and thus have higher corrosion rates than other areas. Although localized corrosion generally would not consume as much material as uniform corrosion, penetration or failure caused by localized corrosion are often more rapid, and thus it is more insidious and difficult to control.

For non-passive systems, uniform corrosion is the main form of corrosion, while for passive systems, localized corrosion, especially pitting corrosion, dominates the corrosion failure process. Because there are high dissolution rates in a small area, pitting corrosion can result in perforation and severe damage of metallic materials. Usually, the development of pitting corrosion occurs in two stages: initiation and propagation. The adsorption/penetration of aggressive anions, mechanical damage or local acidification are generally believed to be the reasons for the initiation of pitting corrosion [8, 9]. After initiation, metastable pits are formed. The surface film at these meta-stable pits can be repaired through a repassivation process or develop into stable corrosion pits through the propagation process, an auto-catalytic process. At the propagation stage, the localized current density within the pit is very high. The

dissolving metal ions hydrolyze, resulting in an acidified environment. The acidic environment within the pit, in turn, will increase the metal dissolution rate further, thereby causing a rapid perforation rate [7]. Hence, for passive systems, pitting corrosion is a very important and dangerous type of corrosion.

### 2.1.1.3 Corrosion in flowing environments

When a metal electrode is exposed to flowing aqueous environments, the corrosion rate is usually accelerated. As mentioned above, the corrosion process involves mass transfer and surface reactions. Thus, the effect of velocity can be understood from examination of these two steps. The most direct influence on corrosion is the acceleration of mass transfer by enhanced convection due to the flowing environment. As the system is subjected to high flow velocity, the formation and adsorption of the films (passive films, layers of corrosion products) will be affected by the mechanical effect. In extreme cases, the metallic substrate itself may suffer mechanically induced deterioration [10].

Since the flow velocity in most cases is in a moderate range, the major influence of flowing media is the acceleration of mass transfer. The term 'flow-accelerated corrosion' describes this effect. When the corrosion rate is controlled by mass transfer processes, the corrosion rate, i.e. the limiting current density  $i_{lim}$ , can be correlated directly to the mass transfer coefficient,  $K$ , [4]:

$$i_{lim} = nKFC_b \quad (2-5)$$

where  $n$  is the number of moles of electrons involved in the corrosion reaction,  $F$  is the Faraday constant and  $C_b$  is the bulk concentration of the reaction species. At the same time, the mass transfer coefficient can be correlated to different flow parameters such as velocity, Reynolds number, and wall shear stress, as described in the following empirical expression [11]:

$$Sh = \alpha Re^\beta Sc^\gamma \quad (2-6)$$

where  $\alpha$ ,  $\beta$  and  $\gamma$  are constants depending on the flow conditions and geometries of the test devices.  $Sh$  ( $= Kd/D$ ) is Sherwood number,  $Re$  ( $= dV\rho/\mu$ ) is Reynolds number and  $Sc$  ( $= \mu/\rho D$ ) is Schmidt number;  $d$  is the pipe diameter,  $D$  the diffusion coefficient,  $V$  the flow velocity,  $\rho$  and  $\mu$  the density and viscosity of the slurry. Poulson [11] summarized the empirical expressions for mass transfer coefficients of various specimens. The relationship between the corrosion rate and hydrodynamic parameter, velocity or Reynolds number, can be expressed as [11]

$$i_{\text{lim}} = \alpha \cdot n \cdot F \cdot \left(\frac{D}{d}\right) \cdot (Re)^\beta \cdot (Sc)^\gamma \cdot C_b \quad (2-7)$$

However, the correlation between the mass transfer coefficients and corrosion rate is only valid for reactions having mass transfer as the rate-determining step. In practise, however, most corrosion systems exhibit mixed control. Otherwise the corrosion rate would be independent of the material. In mixed controlled corrosion processes the resistance to corrosion generally comes from three factors: mass transfer in the bulk solution (apparent mass transfer coefficient  $K_1$ ), mass transfer in the film (apparent mass transfer coefficient  $K_2$ ), and electrochemical reaction at the metal surface (apparent coefficient for electrochemical reaction  $K_3$ ). The resistance arising from the electrochemical reaction is not ignorable, and is comparable with that from mass transfer. Under such conditions, the overall corrosion rate can be described as follows [12]:

$$i = nF \frac{C_b - C_s}{\frac{1}{K_1} + \frac{1}{K_2} + \frac{1}{K_3}} \quad (2-8)$$

where  $i$  is the current density and  $C_s$  is the concentration of the reactive species at the metal surface.

### 2.1.2 Pure erosion processes

Extensive research has been conducted into erosion processes and several comprehensive reviews have been published. Consequently, a detailed literature review for erosion models is not included here. Engel [13] reviewed studies up to

1978, and Sarkar [14] extended the review to 1980. An exhaustive review by Meng and Ludema [15] covered studies to 1995, and Lycakowski and Bouillard [16] reviewed data up to 2002, concentrating on erosion occurring in fluidized-bed combustors.

In models for erosion, the impingement involves a single hard particle and a planar target. Depending on the model, the target material is assumed to be removed in a purely ductile mode, purely brittle mode, or a combination of ductile and brittle modes.

In all of the current models of erosion mechanisms, the essence of small solid particle erosion is that the surface material is removed by a micro-mechanical deformation /fracture process. For ductile materials, the impacting particles cause severe and localized plastic strain that eventually exceeds the strain limit, resulting in failure of the deformed material. For brittle materials, the forces of the erodent particles cause cracking and chipping off of micro-size pieces.

#### **2.1.2.1 Micro-cutting model**

The micro-cutting model proposed by Finnie [17, 18] was the first used to study erosion of ductile metals. The main assumption in this model is that a particle approaching the eroding surface at a certain impingement angle will remove material in much the same way as a machine tool would. The particle is assumed to be much harder than the target material and does not break up. The surface material is assumed to deform plastically during the cutting process, and the volume of material removed can be calculated from the trajectory of the particle.

Finnie's model is good for ductile specimens at small angles of attack (up to  $45^\circ$ ). Above  $45^\circ$ , however, it underpredicts the erosion rate. At  $90^\circ$ , it predicts no erosion rate at all, which is not correct. This problem was not solved by further work on this model [19]. Also, the model predicts no erosion at  $0^\circ$ . In spite of its shortcomings, the micro-cutting model mechanism was used extensively by investigators in this field from 1958 to about 1975. Based on scanning electron

microscope examination of erosion surfaces, Levy [20], and Shewmon and Sundararajan [21] concluded that the cutting tool analogy does not describe the primary mechanism by which the ductile structural metals erode.

#### **2.1.2.2 Deformation wear model**

A deformation model developed by Bitter [22, 23] assumes a combination of the ductile and brittle modes. Bitter divided erosion into 'deformation wear' and 'cutting wear'. The former was caused by repeated deformation during collisions, eventually resulting in detachment of materials; the latter was caused by the cutting action of free moving particles. The two effects occur simultaneously and can be linearly superimposed. Thus, Bitter's work extends Finnie's model and improves it by bringing in a concept of threshold erosion rate. Physically, a particle can't erode the material surface if its impinging velocity is lower than the threshold velocity. In Bitter's brittle erosion model, the erosion rate is postulated to be equal to the energy dissipation of an elastic sphere deforming the planar target material surface elastically and plastically, divided by an energy needed to remove material.

For the ductile erosion part, this model is similar to the cutting model, and thus it is not surprising that Bitter's model produces wear curves similar to Finnie's for soft materials, but predicts non-zero wear at  $90^\circ$ . For hard brittle materials, the model predicts wear curves that reach the maximum at  $90^\circ$ . The deformation model involves more material properties than the cutting model, and also involves the material properties of the particles.

#### **2.1.2.3 Fatigue model**

Hutchings [24] developed a fatigue model for erosion at normal incidence through analysing the failure criterion during erosion processes. In accordance with this model, the erosion process involves an accumulation of plastic deformation in the surface layers of the target material, and the maximum plastic strain within a fragment of material must be attained before the detachment of material in the form of platelets. This maximum strain was named the critical strain, a measure of the

ductility of the material. Thus, the erosion at normal incidence was treated as a problem of low cycle fatigue, and the Coffin-Manson power law relationship was applied to predict the erosion rate.

This model predicted successfully the dependence of erosion rate on the impact velocity. However, as mentioned by the author, the major simplification embodied in this theory is its neglect of strain hardening. It assumed that the metal has a constant dynamic hardness and, therefore, that the strain increment introduced by every impact is the same. This will not be true, since the hardness of the material will increase because of the work hardening effect. Also, determining the critical strain and the relation of material properties to fatigue life is difficult, which makes it hard to apply this theory to predict the erosion rate. In addition, although the theory uses a criterion of critical plastic strain to determine whether or not an element of metal can be removed, it does not take into account the precise mechanism by which the removal takes place.

#### **2.1.2.4 Localization model**

Sundararajan and Shewmon [25] developed the localization model, in which the erosion loss was predicted by considering the balance of the energy needed for material removal and that of particle impingement. Similar to Hutchings' fatigue model, it employed a critical strain criterion to explain solid particle erosion at normal impact by assuming that the formation of a localized lip of material along the rim of the crater and its removal during subsequent impacts were mainly responsible for the material loss. The formation of the localized lip occurred once a critical strain was exceeded in the deforming volume beneath the impacting particle. Further effort made this model applicable for all impact angles and any shape of eroding particle [26].

Based on extensive investigation using micrographs of eroded ductile metals, Levy [20] proposed an extrusion-forging mechanism (platelet mechanism) to describe the material loss processes in erosion, which was qualitatively similar to the localization model. **Figure 2-3** shows schematically the material removal process.

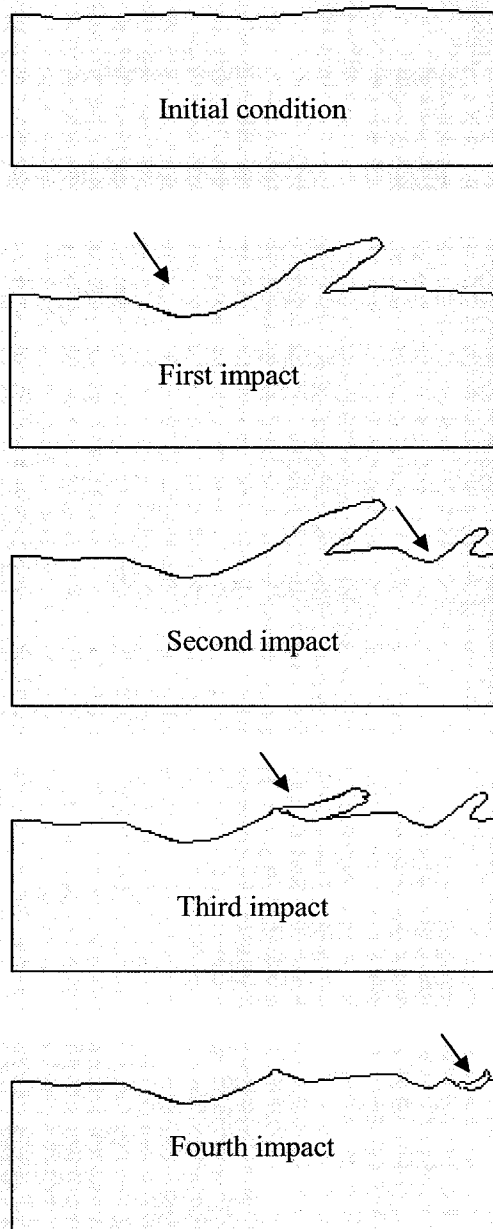


**Figure 2-3. Material removal process during erosion [20].**

Large amount of lips or platelets are initially extruded from shallow craters made by particle impacts. These platelets are bent and even cracked, and thus vulnerable to being knocked off the surface by subsequent particle impacts.

Endo and Nagae [27] compared the erosion rate obtained by experimental erosion tests and that expected from different models. They found that the

localization model showed better agreement with the experimental erosion rates, but for some steels this model overestimated the erosion rate.

These models can provide good predictions for the erosion behaviour of material under certain conditions. However, none of them has been recognized as a general model which can be used to predict the effect of all the parameters on erosion behaviour.

### 2.1.3 Synergistic effect

As indicated by Equations (2-1) through (2-4), the total material loss with the presence of both erosion and corrosion is usually higher than the sum of their individual effects, showing the existence of a synergistic effect. Such a synergistic effect leads to a dramatic increase in damage rate, and reports in this area have been extensive since the 1950's. Li et al. [28] found that the synergistic effect was 40-50% of the total weight loss of aluminium in acidic slurry and 0.5 M NaCl slurry, although the pure corrosion rates were only 0.03 mg/cm<sup>2</sup>·h and 0.67 mg/cm<sup>2</sup>·h, respectively. Matsumura et al. [29] showed that the total weight loss of pure iron in NaOH slurry was 20% higher than that without corrosion, even though the pure corrosion rate was too small to be measured. Yue et al. [30] found that when chrome white iron was eroded in low pH slurry, the contribution of synergism could be as high as 86.3%. Neville et al. [31-34] conducted slurry-erosion tests with various metallic materials, including Co-based alloys, Ti-based alloys, and stainless steels, and the results showed clearly the existence of a significant synergistic effect between erosion and corrosion. Besides the acceleration of total weight loss, Burstein and Sasaki [35, 36] detected the electrochemical transient current and corrosion pits generated by solid impingement using a coupled acoustic emission sensor.

To quantitatively describe the severity of synergism, Wood and Hutton [37] proposed a magnification factor, which was defined as the ratio of the total weight loss to the sum of the pure erosion rate and pure corrosion rate. It was found the

magnification factor for austenitic stainless steel was in the range of 1.2 to 3 in 2 wt% slurry [1, 38].

Clearly, the synergistic effect plays a very important role in the erosion-corrosion material degradation process. Suppressing this interaction will reduce the rate of material deterioration and thus prolong its service life. However, to realize this target it is first necessary to understand the interaction mechanism of these two processes.

## **2.2 Factors affecting erosion-corrosion**

Since erosion-corrosion arises from the combination and interaction of erosion and corrosion, it will be affected by all the numerous factors which influence corrosion and erosion. The main factors will be discussed here, and these are classified into three categories, hydrodynamics of the slurry, metallurgical properties of the target material, and properties of the slurry.

### **2.2.1 Hydrodynamic parameters**

The effect of hydrodynamic parameters on erosion-corrosion can be understood from its effect on corrosion and erosion.

For corrosion processes, the influence of flow velocity in single phase flow systems was described in Section 2.1.3 by the correlation between mass transfer and Reynolds number, while in liquid/solid two-phase flow systems the effect of sand impingement also needs to be considered. Zhou et al. [39] studied the relationship between the corrosion current density and the velocity (Reynolds number) using a rotating cylinder electrode system, and found that it maintained a relationship similar to that in Equation (2-6), but the exponent value was larger in slurry than in solution.

The effect of flow velocity on the mechanical degradation of material by solid particles has been shown. According to Meng and Luderma's summary [15], the

impact velocity of particles is one of the most important parameters that determine the erosion rate, while the particles' velocity is related to the slurry velocity directly.

It has been found that a power law relationship exists for the dependence of the total erosion-corrosion rate on the flow velocity, and the value of the exponents typically has values between 1 and 4 [40-42]. For example, Postlethwaite et al. [43] established a general expression for the erosion-corrosion rate of the form

$$W_t = m_1 M_p f(\alpha) V^{m_2} \quad (2-9)$$

where  $M_p$  is the weight of the particles per unit volume of solution,  $f(\alpha)$  a functional relationship for the dependence of erosion rate on impact angle,  $m_1$  and  $m_2$  constants that are assumed to be dependent on the erosion-corrosion system. The value of  $m_2$  is generally between 2 and 3.

The flow velocity is not necessarily the best parameter for characterizing the influence of media. As pointed out by Nesic et al. [44, 45], for attached flow it is acceptable to use Reynold's number or shear stress to correlate the flow with erosion-corrosion. But when separated flow conditions are involved at geometrical irregularities such as weld beads or fittings, there is no simple relation between the bulk flow parameters or the local near-wall hydrodynamic and mass transfer conditions. In addition, the flow-geometry-dependence of the correlation results in difficulty in transferring the results between different systems [46]. Similar velocities and Reynolds numbers in the two systems do not guarantee hydrodynamic and mass transfer similarity. The use of wall shear stress was believed to be able to overcome this problem. However, wall shear stress alone cannot describe the effect of particle impingement on the corrosion processes [47].

## **2.2.2 Metallurgical features**

### **2.2.2.1 Effect of mechanical properties**

The dependence of erosion-corrosion on material mechanical properties arises mainly from their effect on erosion. Nevertheless, discrepancies exist in this topic. Many mechanical properties of materials, such as hardness, toughness, strength, ductility, strain hardening etc., have been found to be related to erosion rate in many cases, and some of these parameters were chosen as parameters in erosion models. None of them, however, has been found to possess a general relationship to erosion rate.

Among these mechanical properties, hardness is an important and interesting parameter. Many attempts have been made to define a direct correlation, but its relation to erosion rate now is considered controversial. It is traditionally believed that the erosion rates of metallic materials decrease with an increase in hardness [48-50]. In Finnie's model [18], Hutchings's model [24], Sheldon and Kanhere's model [51], and Oka et al.'s equation [52], the erosion rate is inversely proportional to the power of the hardness of the target material. Oka et al. [52] mentioned specifically that the hardness was not the initial hardness but rather the surface hardness during the course of erosion, which can be obtained by estimating the degrees of work hardening and softening by heat generation. Also, Hutchings [40] summarized the results on experimental erosion tests using a wide range of materials and pointed out that the mechanical erosion rates depended heavily on the relative hardness (the difference between the hardness of target material and particles). However, a body of evidence for the reverse conclusion, that hardness is not a factor in establishing the erosion resistance, is also available [20]. Levy and Hickey [53] reported that the erosion resistance of diffused and sprayed-on protective coatings did not directly relate to their hardness. Neville et al. [32, 54] found that the resistance of high alloy stainless steels and cobalt alloys to total material loss did not follow the trend of increasing resistance as the hardness increased.

Although discrepancies exist about the effect of material hardness, a good correlation generally has been recognized for pure metals and alloys with similar compositions. For example, Finnie [18] showed that a reasonable relationship existed between material hardness and erosion resistance for annealed metals, as shown in Figure 2-4.

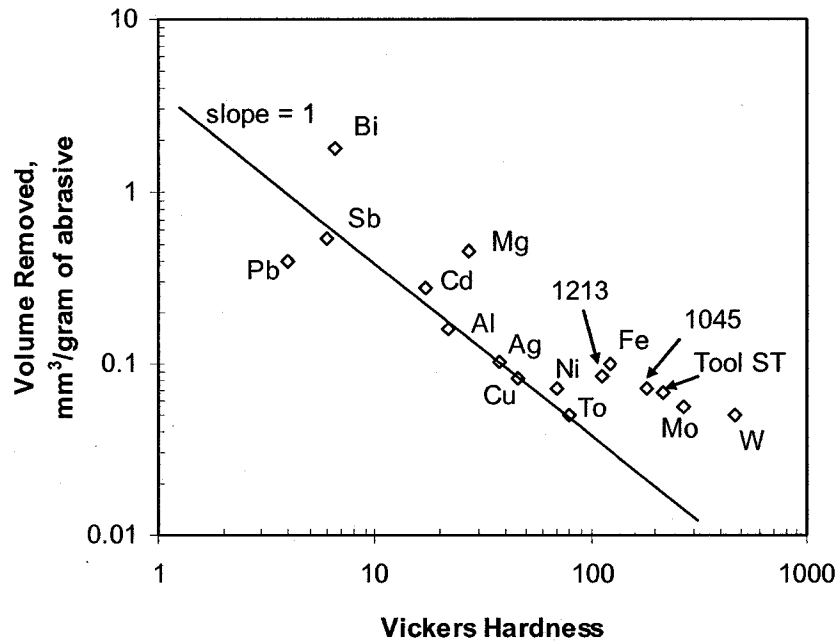


Figure 2-4. Dependence of erosion rate on the hardness of target material [18].

However, when corrosion is also present, the relationship between the rate of total weight loss and hardness becomes more complex. Since during erosion-corrosion the two basic material degradation processes interact with each other, there arises a question whether the dependence of erosion on hardness would influence the corrosion process. Wang and Stack [55] isolated the corrosion contribution to the total weight loss and found that only the erosion resistance of mild and stainless steels increased with increasing hardness.

Additionally, the correlation between erosion resistance and hardness of base metal also depends on the erosion mechanism. Heitz [12] pointed out that, if the

mechanical damage was restricted to the surface layer, especially in corrosion product scale or passive film which normally existed in a single-phase flow system, the adherence, cohesion and hardness of the surface layer would determine the mechanical stability. In this case, the hardness of base metal is not related to the erosion-corrosion processes. Instead, chemical changes in these layers may be the cause of breakdown of the surface layers, with the subsequent onset of erosion-corrosion. In the liquid/solid flow, however, the interaction of the solid particles and the base metal dominates, and erosion resistance can be improved by increasing the hardness of base metal.

Theoretical analysis and experimental evidence indicate that hardness and strength of the surface layer will decrease when anodic dissolution current density of metal increases [56]. Thus, with a correlation between the erosion resistance of metals and the hardness or strength, a corrosion-enhanced erosion process is expected to arise from this chemo-mechanical effect. Such an effect, which will be discussed in section 2.4, has been applied in the chemo-mechanical polish process to machine hard materials [57].

#### **2.2.2.2 Effects of microstructure and composition**

As important factors related to the mechanical properties and corrosion behavior of material, the microstructure and composition are critical in establishing the erosion-corrosion resistance.

##### **Steels**

Experimental evidence indicates that the phase composition and grain size can significantly influence the erosion-corrosion resistance [58-61]. Steels with low-bainitic structure possess relatively high erosion-corrosion resistance [58]. Peterson et al. [59] compared the erosion resistance of steels with different microstructures, and concluded that, at most angles of impingement, the microstructures can be ranked in order of increasing erosion rate as follows: spheroidite, pearlite, tempered martensite and martensite. Lindsley and Marder [60] investigated the erosion resistance and

morphology of spheroidized Fe-C alloys with various carbon contents and microstructures, and found that the erosion resistance increased when the mean free path between both the grain boundaries and the carbides decreased. A Hall-Petch-type relationship was found between the mean free path of microstructure and both erosion resistance and hardness. Bregliozzi et al. [61] also found the grain size of the steels had an important impact on the nature of the damage produced on the sample surface, and the resistance to erosion-corrosion increased with decreasing grain size.

The erosion resistance of carbon steel, generally increases with increasing carbon content [40, 62, 63]. For other alloy steels, experimental data indicate that the addition of alloy elements Cr, Mo, Mn, Ni would improve erosion-corrosion resistance [64-67]. For example, the erosion-corrosion resistance of steels increases with increasing chromium concentration. As a result, high chrome cast steel is more resistant to erosion-corrosion than plain cast iron, and stainless steels are more resistant than carbon steels and low alloy steels [33, 55]. This better resistance to erosion-corrosion is attributed to improvement in corrosion resistance and mechanical properties arising from higher Cr concentration [68].

### **Metal Matrix Composites**

Metal matrix composites (MMCs) comprising a ductile metal matrix and hard particles phases are candidate materials for protection against erosion-corrosion. They can be used as bulk material or hard coating. In recent years considerable interest has been paid to extend their use in engineering applications. The matrix materials usually include Ni, Co, Al and their alloys. Austenitic stainless steel was also used [69]. The hard particles commonly used include hard carbide or oxide particles, such as WC, B<sub>4</sub>C, TiC, SiC, Al<sub>2</sub>O<sub>3</sub>, TiO<sub>2</sub>, and SiO<sub>2</sub>.

The erosion-corrosion resistance of MMCs is closely related to the volume fraction and size of the hard particle phase. However, experimental results for the effect of the fraction of hard phase on the erosion-corrosion resistance were contradictory: one group of investigators reported that resistance increased with hard particle content [60, 70] while others found the reverse effect [71, 72]. Through

microscopic examination of the eroded surface, Pugsley et al. [73] ascribed the discrepancy to a change in the material removal mechanism. Stack [74] used a schematic diagram to show the transition of the erosion mechanism from ductile to brittle behavior as a result of increasing ceramic material in the matrix. The conclusions for the effect of hard particle size are more consistent. Decrease in particle size improved erosive wear resistance of the composite [75]. This relationship accounts for the growing interest in nanocrystalline particle composites.

The erosion-corrosion resistance of MMCs also depends heavily on the corrosion resistance of the matrix, since the matrix material tends to dissolve preferably. The hard particles will be readily removed by erosion if they lose support by the matrix. Wentzel et al.'s investigation [76] showed that the inherent corrosion resistance of pure nickel matrix did not increase the erosion-corrosion resistance of the MMCs in slurry flow, but both the nickel-chromium-cobalt grades and the nickel-chromium grades improved the erosion-corrosion behavior. This result indicated that the erosion-corrosion resistance of MMCs can be further improved by optimizing the matrix composition.

### **2.2.3 Properties of slurry**

There is a tremendous amount of literature and practical experience on material loss under mechanical load, but most of the data are from tribology and wear studies. There are only a few reports in the literature giving consideration to corrosion effects. For this reason only the effects of particle properties, solids concentration, and impingement angle are described here.

#### **2.2.3.1 Particle property**

The properties of the solid particle have a profound effect on the erosion-corrosion rate, but mainly the erosion rate is more sensitive to the particle properties. Studies on the effect of particle properties on corrosion are limited. Stack et al. [77] investigated the effect of erodent particle size on the polarisation behaviour of

chromium steel in 1 M NaOH deaerated solution, but the results did not show any apparent difference with size for 50, 100 and 150  $\mu\text{m}$  alumina particles.

In contrast to the corrosion process, the erosion rate strongly depends on the hardness, size and shape of the particles. As discussed above, the hardness difference between particles and target material surface is important for erosion processes. It was found that particles 1.2 to 1.5 times harder than the worn surface caused very much higher wear rates than softer particles [40]. The size of the particles also affected the erosion-corrosion rate. **Figure 2-5** [78] shows the dependence of erosion rate on particle size for impact by quartz particles. Interestingly, the erosion rate of steel tended to increase up to a critical value, and above this size remained constant. The fragmentation of particles above a critical size was thought to be responsible for this phenomenon. As pointed out by Stack [74], the volume loss per particle impact may help to explain the observed effects. The shape of the particles also influences the erosion rate strongly, although it has proved to be difficult to quantify this parameter. Generally it is believed that the more sharp and angular the particles are the greater the erosion rate will be.

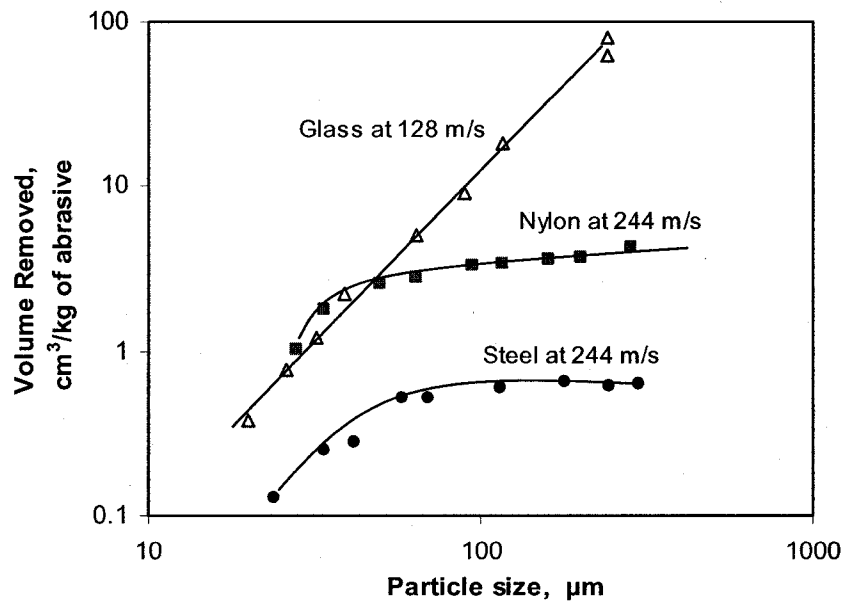


**Figure 2-5.** Dependence of erosion rate on particle size for impact by quartz particles [78].

The standard test for the abrasivity of the particles is ANSI/ASTM G75-82, in which a standard white cast iron specimen is slid against a neoprene surface in a trough containing a slurry with 50% solids content in distilled water. The weight loss of the specimen is measured after two hours, and is used to establish a value of 'abrasivity index' or 'Miller Number' as the degree of abrasivity. The more abrasive the particles, the higher the Miller number.

### 2.2.3.2 Particle concentration

As Hutchings [40] pointed out, if each particle acts independently in the slurry it would be expected that the erosion rate should depend linearly on the particle concentration. This behaviour is observed at low particle concentrations. However, at higher particle concentrations, the wear rate rises progressively more slowly as the concentration increases, due to interference among particles. **Figure 2-6** shows the dependence of material loss of a mild steel on silica sand slurry concentration. The departure from linearity occurs at a volume concentration about 12%. When a power-law relation is used to fit the data, the exponent is less than unity.

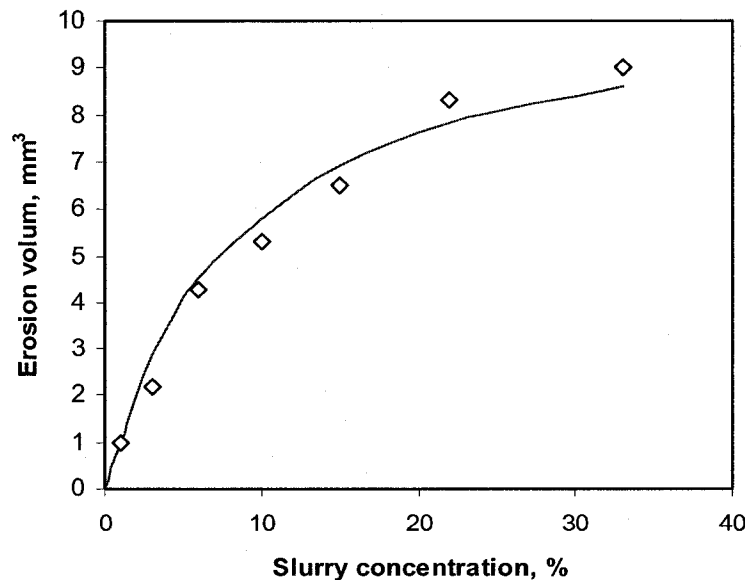


**Figure 2-6. Dependence of material loss on slurry concentration for a mild steel in a silica sand/water slurry [40].**

However, when a corrosion process occurs simultaneously with erosion, the situation is more complicated. Since the total weight loss of the material in erosion-corrosion processes consists of three parts: pure erosion, pure corrosion and synergism between these, the relationship between the total weight loss and sand concentration will be a function of the dependence of each part on sand concentration. Neville et al. [79] investigated the effect of sand load on the mass loss using a impinging jet and 3.5% NaCl/sand slurry with concentration no higher than 1000 mg/L. They found that the current densities of UNS S32654 and UNS S31603 increased linearly with the solid loading, but there was a critical point at which the current started to oscillate at a much greater rate for both alloys. The total weight loss of these two stainless steels did not follow the same trend: the former showed a linear relationship while the later exhibited a power function. However, for cast iron [80] and Co-based alloy [34], the total weight loss under the same conditions showed an exponential relationship to sand load, with the exponent having a value less than unity.

Thus, the corrosion process and the interaction mechanism of erosion and corrosion in different systems may each affect the dependence of the total mass loss on solid concentration. To understand this process better, a model describing the relationship of the corrosion reaction kinetics and solid impingement was required for slurry erosion-corrosion processes. Based on this need, Lu and Luo [81] derived a theoretical model to predict the electrochemical passive current response of a passivated electrode in slurry erosion processes. The model's predictions proved a good fit for the experimental passive current data as a function of particle concentration.

### 2.2.3.3 Impingement angle

The dependence of impingement angle has also been a subject that attracted extensive interest. **Figure 2-7** [82] shows the typical relation between erosion rate and impingement angle, in which Al was used as a representative ductile material and  $\text{Al}_2\text{O}_3$  as a representative brittle material. For ductile materials, maximum erosion

occurs at low angles, usually between 15° to 30°. Most metals and alloys exhibit such behavior, and it is believed that failure is mainly due to extensive plastic deformation of surface material. Brittle materials, on the other hand, behave quite differently from ductile materials. For brittle materials maximum erosion rates occur at normal incidence. Most ceramics and glasses exhibit this behavior. The failure is mainly related to crack propagation and chipping. What should be noted is that the erosion rate at 0° should not be zero, as discussed in section 2.1.1.1.

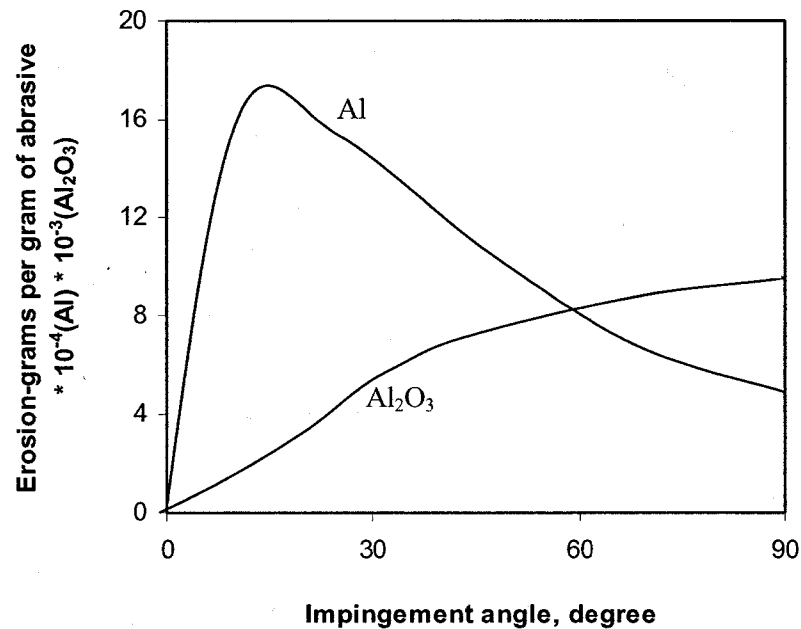


**Figure 2-7. Dependence of erosion rate on impingement angle [82].**

The effect of impingement angle has also been investigated with respect to both erosion and corrosion processes. Burstein and Sasaki [83] found that the rupture or removal of the oxide film on the surface by the abrasive particles caused sharp current rises. The current rise was greater and the rise time was longer at oblique angles compared with those at normal incidence. Weight loss measurements demonstrated that the synergistic effect between erosion and corrosion was enhanced by a more oblique angle of impact, which was attributed to an increase in the degree of denudation of the metal surface by individual particle impingements at more oblique

angles. Stack et al. [84, 85] estimated impact angle effects based on models from the solid particle erosion literature. In accordance with these results, erosion-corrosion maps were constructed showing the change in mechanisms and wastage rates as a function of impact angle and other experimental parameters.

## **2.3 Mechanisms of synergistic effect between erosion and corrosion**

The combined action of mechanical and chemical processes often results in mutual reinforcement, which makes the erosion-corrosion processes more complicated [86]. Although much effort has been directed toward investigating the interactions, the synergy mechanism is still not thoroughly understood due to its complexity. Recent research results from investigations of the mechanisms for the erosion-enhanced corrosion and the corrosion-enhanced erosion are reviewed separately here.

### **2.3.1 Effect of erosion on corrosion**

#### **2.3.1.1 Promoting mass transfer**

The analysis of the effect of hydrodynamic parameters on erosion-corrosion processes shows that any effect on promoting mass transfer will accelerate the corrosion rate in those systems for which the corrosion reaction is controlled by mass transfer. The presence of solid particles in the flowing solution leads to the disturbance of the fluid field in the system, which may enhance the transport process of both reactants and corrosion products, and thereby promote the corrosion process [12, 87]. In order to analyze erosion enhancement of the mass transfer rate, Zhou et al. [39] compared the corrosion rates in solution (single phase flow) and in slurry (300 g/L; 100  $\mu\text{m}$  alumina) for an electrochemical reaction controlled by mass transfer. It was found that the ratio of the dissolution current in slurry, i.e., the mass transfer rate, to that in solution was always higher than unity. This result suggested that erosion enhanced corrosion by accelerating the mass transfer rate in the slurry.

### **2.3.1.2 Stripping off the protective film**

In many corrosion systems a protective film is likely to form on the metal surface. The film plays an important role in the erosion-corrosion mechanism of materials. When the film is protective, it has the ability to inhibit erosion-corrosion damage through suppressing corrosion. In slurry erosion-corrosion processes, however, cavitation bubble collapse or impingement of a solid particle can damage or remove the corrosion product or the film, leading to the exposure of fresh metal surface to the corrosive environment which then will suffer further severe damage. This mechanism can be applied to all the passive systems and those systems in which the corrosion product is protective of the base metal. Numerous experimental results regarding this mechanism have been reported for passive metals, such as stainless steels [88-91], Ti alloys [31, 92], and Co alloys [34]. It was observed that impingement of solid particles can alter the corrosion behavior of the material significantly and even could eliminate the passive zone if the concentration or velocity of the slurry was high enough. Zhou et al. [39] also found that the ratio of the dissolution current in the slurry to that in solution was higher at -0.67 V than at -0.8 V, because the impact of particles removed the corrosion deposits that formed at -0.67 V but not at -0.8 V.

### **2.3.1.3 Localizing corrosion**

Another possible explanation for erosion-enhanced corrosion in slurry arises from localizing corrosion. When a metal is subject to erosive particle impact, each erosive event causes rupture or removal of the oxide film from the surface. Pitting corrosion will thereby be enhanced, either at the bare metal surface or at a localised occlusion generated by erosion. It seems that this effect is very similar to stripping off the protective film, but the emphasis lies on the detrimental effect of particle impact on the generation of corrosion pits. Burstein and Sasaki [35, 36] applied the electrochemical noise technique in 0.6 M NaCl solution/silica sand slurry, and found that the metastable pits formed on stainless steel can ensue immediately after a short duration of erosive particle impingement below the pitting potential. The occurrence

frequency of metastable pits after particle impingement is larger than that under non-erosive conditions. Thus they concluded that the erosion process increased the susceptibility of stainless steel to pitting corrosion. Chen et al. [93] also investigated the damage mechanism of a pipeline steel in tailing water containing 10% silica sand and found that the cracking of the outer layer of corrosion scale caused by particle impact led to the formation of occluded cells resulting in pitting corrosion.

However, contradictory results also have been reported. For example, experiments using a rotating electrode fully immersed in aerated 200 ppm NaCl solution showed that erosion slightly inhibited the pitting corrosion on AISI 304L [94]. More work needs to be done to clarify the interaction of the impact of solid particles and the generation and growth of corrosion pits.

#### **2.3.1.4 Roughening of the surface**

The effect of roughening of a surface from erosion arises from the dependence of corrosion rate on electrode surface roughness. Generally, the higher the surface roughness, the greater the corrosion rate [95, 96], and hence it is expected that erosion can facilitate the corrosion reaction by increasing electrode roughness with impact action. Kim et al. [97] studied the relationship between surface roughness and the erosion-corrosion properties of TiN coated films (on titanium based alloy and stainless steel), and found the erosion-corrosion and corrosion resistance of textured surface with lower surface roughness was better. Sasaki and Burstein [98] investigated the generation of surface roughness during slurry erosion-corrosion and its effect on pitting potential. They found that surface roughness was a critical parameter in determining the pitting potential of stainless steel 304L. The pitting potential decreased with an increase in roughness, and there was a linear relationship between the pitting potential and the reciprocal of grit number to which the electrode surface was polished. However, the pitting potential of the surface measured during the erosion process by the slurry was much lower than that measured after erosion. This observation implied that although surface roughness can affect pitting corrosion to some extent it was not the major factor by which erosion lowered the pitting

potential. Instead, it was inferred that some other effects due to the erosion process itself gave rise to the greater pitting susceptibility.

### **2.3.1.5 Strain effect**

In flowing slurry with high velocity, the solid particles with high kinetic energy impact the material surface and cause elastic and plastic deformation at the surface layer. This process, arising from the impingement, can be considered to be similar to cold work, which can introduce deformation substructures, such as dislocation networks, twins, deformation bands, cell structures and emerging slip steps at the surfaces [99]. However, the effect of deformation on corrosion behavior is still the subject of much debate.

Some researchers took the view point that deformation/cold work can affect corrosion resistance by increasing the number of active anodic sites on the surface [100]. Several experimental results supported this point of view and showed that the corrosion rate increased with prior strain [101-103]. Li et al. [95, 101] attributed the increase in corrosion to decrease of electron work function, the minimum energy required to remove electrons from inside a metal to its surface with zero kinetic energy. Theoretical analysis of the strain effect on anodic dissolution processes [56, 104, 105] led to a quantitative correlation between corrosion parameters and strain energy. However, some investigations carried out in the past indicated that the role of cold working on the localized corrosion resistance of stainless steels was unclear [106, 107]. Lu and Luo [108] showed that neither elastic nor plastic deformation in the pseudo-static deformation processes can significantly change the corrosion rate of an electrode for an anodic dissolution system.

The effect of strain on corrosion appears to have strong system dependence. The mechanical properties of the material, such as work hardening compatibility, and the corrosion behaviour of the system may influence the response of corrosion to deformation. Mayuzumi et al. [109] found the effect of cold work on corrosion was different for stainless steel 304 and 310 Nb. In addition, other factors may also have an effect. Li et al. [110] investigated the effect of strain rate on the current density of

stainless steel in 10% H<sub>2</sub>SO<sub>4</sub> solution and found that the current density apparently increased with strain. But it was very possible that this increase in current was caused by disruption of the passive film by the tensile stress, and not by the strain itself, since the stainless steel showed passive behavior in 10% H<sub>2</sub>SO<sub>4</sub> solution.

### **2.3.2 Effect of corrosion on erosion**

#### **2.3.2.1 Preferential dissolution of the matrix phase**

A mechanism including preferential dissolution of the matrix phase was proposed for the corrosion-enhanced erosion of hard particulate reinforced metals, such as MMCs [111-113]. For these materials, the mechanical properties profoundly depend on the strong combination of the matrix phase and the hard phase. Hence, the interface between alloy and hard particle plays an important role in the process of material removal in erosion-corrosion. On the other hand, it has been pointed out that the interface of metallic matrix and dispersed solid is the most active region for corrosion, and thus the interfacial regions are found to be worn out more actively than the regions away from the interface [113, 114]. The preferential dissolution of the matrix around the hard particles weakens the binding of particles with the metallic matrix, leading to easy removal of the hard particles from the surface of the microstructure. As a result, there is degradation of the mechanical properties of the material and concomitant acceleration of the material loss rate caused by erosion. Based on this point, Bester [112] even concluded that the addition of ceramic reinforcement particles to matrix alloys has a detrimental effect on their slurry erosion resistance. This analysis, however, only applies to the accelerated erosion by corrosion for materials strengthened with hard precipitates, but does not explain the effect in materials comprising mainly a single phase structure.

#### **2.3.2.2 Roughening of the surface**

The dissolution of the metallic material in a corrosion process is generally not uniform. Instead, some areas are more active and thus have higher dissolution rates.

As a result, the roughness of the surface will increase as corrosion proceeds. Postlethwaite [115] compared the surface of pipeline in a 20 vol% aqueous slurry of silica sand with and without inhibitor and found that the erosion-corrosion rates and surface roughness of the pipeline steel both decreased by means of reducing corrosion rate with an inhibitor. Thus, he showed that corrosion can increase the erosion rate by roughening of the metal surface. This statement is acceptable with the condition that the erosion process is very sensitive to the impingement angle of solid particles [20, 40]. It is of interest to compare the dimensions of the roughness arising from the corrosion process with the diameter of the solid particles. In many cases, the latter is much larger than the former, under which condition the roughness resulting from localized corrosion will not have a significant effect on the erosion process.

### **2.3.2.3 Removal of work hardened surface**

Matsumura et al. [29] agreed that an increase in surface roughness would play a role in corrosion-enhanced erosion, but they suggested that the impingement of the particle destroys the passive film and promotes dissolution of the work-hardened layer, which, in turn, degrades the erosion resistance of material. Undoubtedly, under solid particles' repeated impacts, a thin layer underneath the surface will get work-hardened. However, whether this mechanism works for a system during slurry erosion-corrosion processes depends on two aspects. The first is the cold work hardenability of the target material. It has been known that some materials, such as stainless steels, have strong work hardenability, while other materials experience no significant work-hardening effect. In these cases, this mechanism should be more significant for the former. The second factor is the ratio of corrosion intensity to erosion intensity. The erosion and corrosion processes take place simultaneously and will reach a dynamic equilibrium state over time. The enhancement of erosion by corrosion will be maximized as the rates of dissolution and work-hardening, which is determined by the erosion intensity, become comparable.

#### **2.3.2.4 Localized attack**

Li et al. [28] studied the behaviour of commercially pure aluminium in various aqueous slurries. They pointed out that roughening of the surface is not the main reason for an increase in erosion rate, since an acidic solution caused much less corrosion and hence less roughening than did on  $\text{Na}_2\text{SO}_3$  solution, yet it caused a much greater effect on the subsequent erosion rate. They also measured the micro-hardness of aluminium surfaces eroded by different solutions and did not find a relationship between the hardness and the corrosion rate. They concluded that elimination of the work-hardened layer was not the main cause for the acceleration of erosion by corrosion in their systems. Based on observations of the surface morphology of eroded samples in various slurry conditions, they proposed a new mechanism in which corrosion affects erosion mainly through the detachment of flakes formed at the surface. The impact of erodent particles causes plastic flow and the formation of flakes, and corrosion is localized at the root of the flakes where the cyclic strains caused by successive particle impacts are large. This localized corrosion leads to the development of sharp cracks, especially at the roots of the flakes. Subsequent particle impacts cause the cracks to propagate quickly, thereby accelerating the detachment of the flakes and leading to an enhanced erosion rate.

#### **2.4 Chemo-mechanical effect**

When a chemical reaction occurs on the metallic material's surface, and at the same time a mechanical load is applied to the material, these two processes have been found to interact with each other since mid-20th century. This phenomenon is defined as the chemical-mechanical effect, which includes two aspects: one is the effect of mechanical behavior on the chemical process, and the other is the effect of chemical dissolution on the mechanical properties/behaviour of the material. For the first aspect, besides the strain effect on the corrosion rate that has been discussed in Section 2.3.1.5, it has also been found that some materials show higher dissolution

rates under load. Here we focus on the effect of chemical/electrochemical dissolution on the mechanical properties of materials.

In the 1930's and 1940's, Rehbinder and his collaborators [116-118] reported a new physico-chemical phenomenon in the deformation and mechanical treatment of solids: the addition of small amounts of surface-active substances to a metal surface is capable of considerably lowering the mechanical and electrical properties of the metal. The results were published in *Nature* [118]. It was reported that the contact of such liquids with polycrystalline specimens of lead, tin and copper accelerated plastic flow under a given stress. This phenomenon was termed as the 'Rehbinder effect' in later literature. Further investigations found that different surface-active media can increase, decrease or have no effect on the mechanical properties [119]. The form and the degree of the Rehbinder effect manifested depend on the intensity of interatomic or intermolecular actions between the solid and the medium. The Rehbinder effect is essentially one type of chemo-mechanical effect. Although the experiments and theory have been met with scepticism [120], it has been applied in many research areas, such as the chemo-mechanical polish process developed for grinding hard materials [57].

More directly, based on thermodynamics Gutman [56] developed a theoretical analysis of the interaction between the deformation of metallic material and chemical/electrochemical dissolution. According to this theory, during anodic dissolution a two-dimensional dissolution nucleus is continuously formed with a mono-atomic depth. Because this mono-atomic layer step on the surface can serve as the source of new dislocations, an additional dislocation flux forms during the anodic dissolution process. The presence of dislocations increases the disorder and the entropy of the crystal and lowers the free energy, which enhances the mobility of the dislocations. As a result, the resistance to plastic deformation decreases. On a macroscopic scale, the yield strength of the surface material decreases and the surface material becomes soft. Moreover, softening caused by the weakening of inter-atomic bondings as a result of dissolution of the surface layer leads to micro-stress relaxation and a decrease in the chemical potential of dislocations in this layer. The chemical

potential gradient between the surface layer and the bulk material is also likely to result in an additional dislocation flux, and the dislocations will move to the surface layer. In addition to the theoretical analysis, Gutman [56] also reported experimental evidence for the enhanced plasticity induced by electrochemical dissolution.

With the intention to further assess the effect of metal dissolution on creep behaviour (popular experiments for evaluating the Rehbinder effect), Revie and Uhlig [121-123] studied the creep rates of copper and iron wires with anodic dissolution. **Figure 2-8** shows the typical creep curves with the effect of an anodic dissolution rate of  $0.9 \text{ mA/cm}^2$  in a deaerated acetate buffer solution. The creep rate was approximately doubled by anodic dissolution, and returned to the original rate when the imposed current was cut off. Based on the observed lag in creep response, they attributed the effect of anodic dissolution to the generation of a sublayer with supersaturated vacancies. These experimental results have been confirmed by other researchers [105, 124], and a linear relationship between the creep rate and the logarithm of anodic current density was reported, as shown in **Figure 2-9** [124]. In addition, the yield strength, tensile strength and fatigue life were found to decrease with anodic dissolution [105, 125]. Further, Jones et al. [126-128] investigated the room-temperature diffusion in Cu/Ag thin-film couples promoted by anodic dissolution, and provided more direct experimental evidence for the vacancy mechanism.

The chemo-mechanical effect has been applied to explain several experimental phenomena, although it remains controversial. In corrosion fatigue and stress corrosion cracking study, Jones [128, 129] proposed a localized surface plasticity effect, Magnin et al. [130, 131] developed a corrosion-enhanced plasticity model, and Galvele [132] proposed a surface-mobility mechanism. All these three mechanisms involve the generation of vacancies during electrochemical dissolution. Moreover, Pickering and Wagner [133, 134], and Seo and Sato [135] employed the concept of 'excess divacancies with high diffusivity' in illustrating the selective dissolution of binary alloys and their passivation processes.

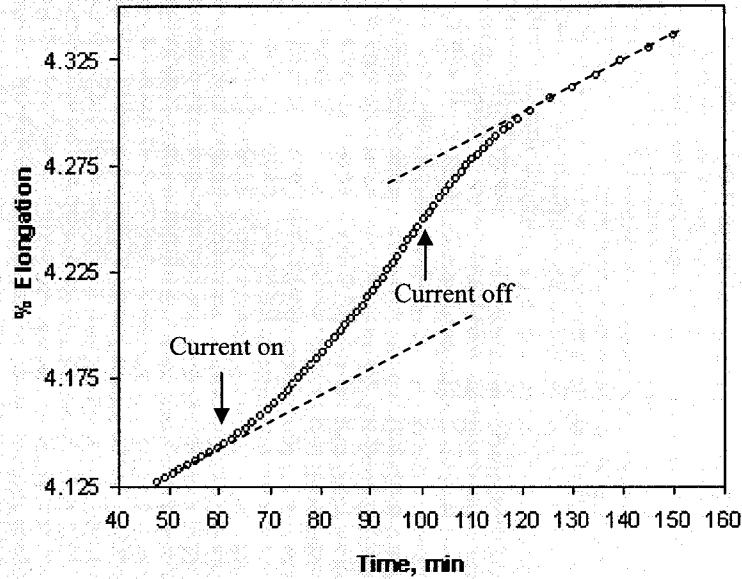


**Figure 2-8. Creep curves of copper with anodic current on and off [121].**

Similar to corrosion fatigue, corrosion creep, and stress corrosion cracking, erosion-corrosion is also a process involving the interaction of chemical processes and mechanical properties of materials. However, the application of chemo-mechanical effects in this area is still limited [104]. Recently, Lu and Luo [136] proposed a chemical-mechanical model for corrosion-enhanced erosion, which provides the relationship between corrosion current and accelerated erosion rate. According to this model, the surface hardness of metallic electrodes will decrease as anodic current is applied, and the relative hardness degradation  $\Delta H_v/H_v$  can be correlated approximately to the anodic current density present at the electrode surface  $i_a$  as follows

$$\frac{\Delta H_v}{H_v} = -B \log \left[ \frac{i_a}{i_{th}} \right] \quad (2-10)$$

where  $\Delta H_v = H_v^* - H_v$  is the change in hardness due to anodic dissolution at the surface,  $H_v$  and  $H_v^*$  the hardness without and with anodic current present at the electrode surface respectively,  $B$  ( $>0$ ) an experimental constant and  $i_{th}$  the threshold

anodic current density required to induce the chemo-mechanical effect, i.e. when  $i_a \leq i_{th}$ ,  $\Delta H_v = 0$ . On the other hand, the correlation between the hardness and mechanical erosion rate of carbon steel can be formulated approximately using empirical expressions, from which the relationship between the corrosion parameter and corrosion-enhanced erosion can be developed. Some experimental results have been qualitatively consistent with the result predicted by this model. However, the predicted corrosion-enhanced erosion rate is much lower than the experimental values [136].

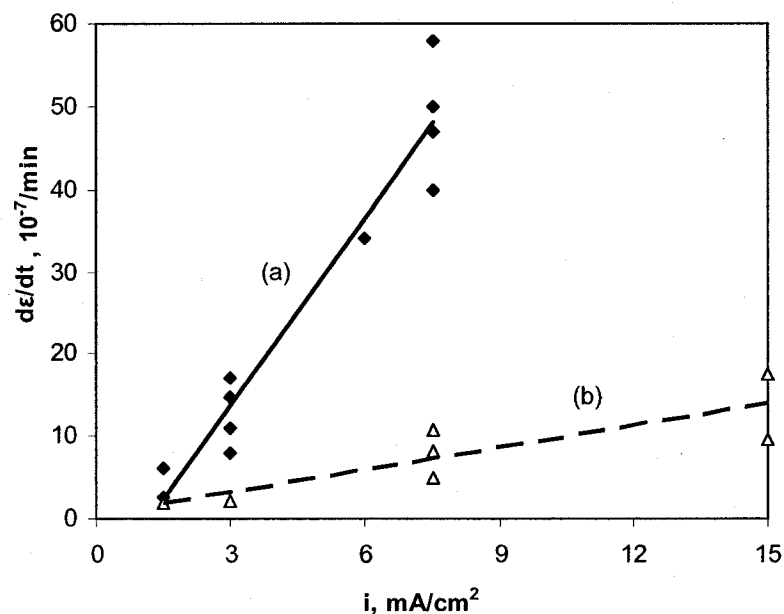


Figure 2-9. Steady creep rates of brass vs. anodic current density [124]: (a) 3.5% NaCl solution, (b) 0.45 M CH<sub>3</sub>COOH + 0.05 M CH<sub>3</sub>COONa solution

## 2.5 Approach and apparatus for erosion-corrosion study

### 2.5.1 Erosion-corrosion map

In the early 1990s, Lim and Ashby [137, 138] developed a wear map which can be used to illustrate the regimes in which different material damage mechanisms predominate as a function of the main wear parameters. This map was an important

advancement in methods for tribology study. In light of the concept of the wear-map, Stack et al.[139] developed an erosion-corrosion map, with the intention of clarifying which weight loss mechanism is dominant under various conditions and thereby establishing the relationships between the erosion-corrosion rate and prevailing parameters, such as flow velocity, oxygen concentration, sand concentration, pH of slurry, applied potential, etc. The methodology of constructing the erosion-corrosion map in aqueous slurry has been discussed in several papers [77, 140-142]. The essential methodology is to determine the five weight losses, i.e.,  $W_t$ ,  $W_{c0}$ ,  $W_{e0}$ ,  $W_{c-e}$ , and  $W_{e-c}$ , from experiments that discriminate between them [143-145], or to employ equations derived from an erosion and corrosion models [140, 142, 146]. Then, the regime boundaries are defined in terms of the ratio of erosion rate and corrosion rate. The regimes are classified as follows:

erosion dominated	$W_c / W_e < 0.1$
erosion-corrosion	$0.1 \leq W_c / W_e < 1$
corrosion-erosion	$1 \leq W_c / W_e < 10$
corrosion dominated	$W_c / W_e \geq 10$

Based on these classifications, the relevant parameters can be calculated for the boundaries, and the two-parameter erosion-corrosion mechanism maps could be constructed. **Figure 2-10 (a)** shows by example the erosion-corrosion mechanism map of pure Fe in acidic media (pH 5) containing alumina particles, based on particle velocity and applied potential [140]. From this map, the main weight loss source under different conditions can be determined. In addition, the wastage regimes, which are based on subjective tolerance levels, were defined in terms of mm per year as follows:

$W_t < 0.1$	Low
$1 < W_t \leq 0.1$	Medium
$W_t > 1$	High

Then the wastage map of erosion-corrosion as a function of different parameters can be built. **Figure 2-10 (b)** shows the wastage map corresponding to the parameters for **Figure 2-10 (a)**. The total weight loss levels under different conditions can be obtained from this kind of map.

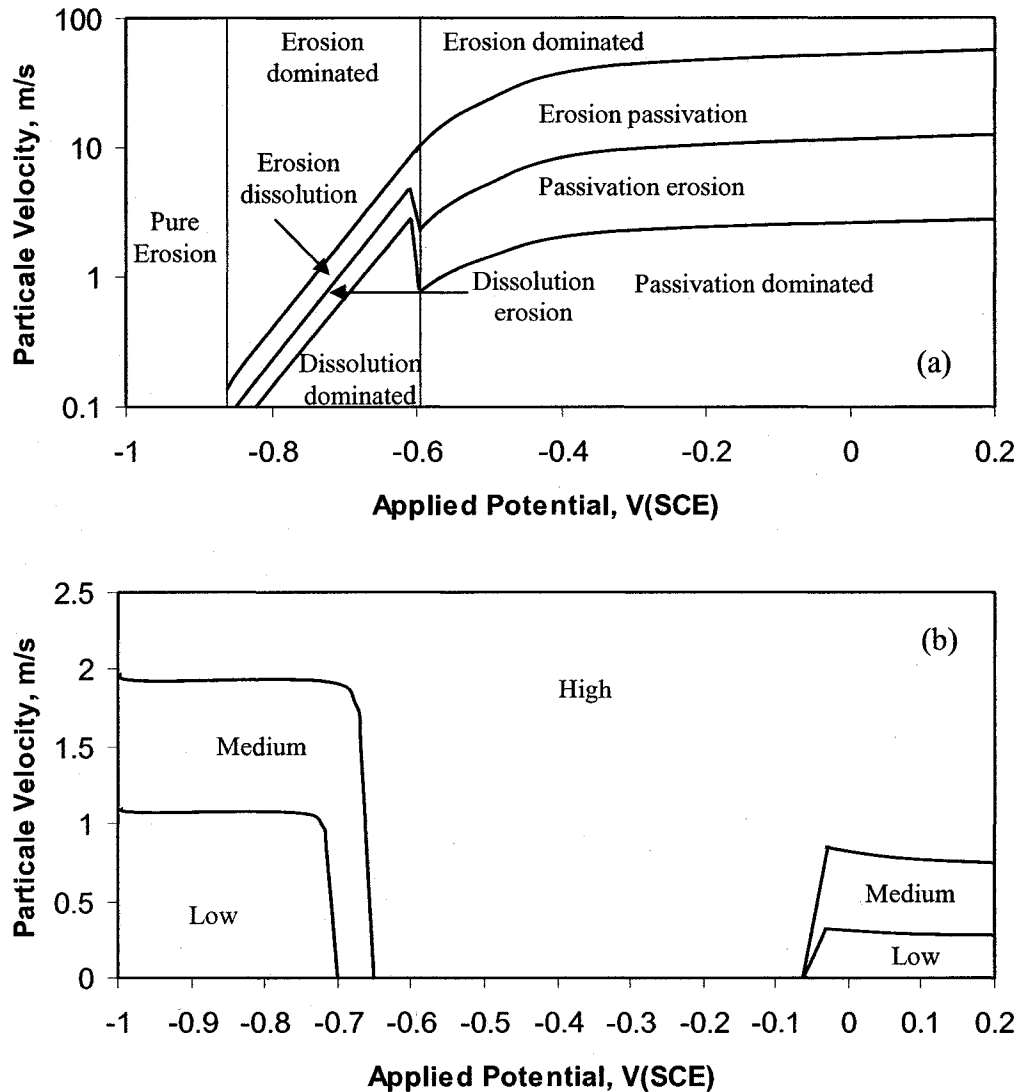


**Figure 2-10. Erosion-corrosion map [140]: (a) mechanism map, (b) wastage map.**

An erosion-corrosion map is useful for estimating material loss in erosion-corrosion processes for specific service conditions. However, as each map is defined using only two parameters, its applicability is limited, because a full description of erosion-corrosion requires use of a large number of variables. The difficulty in combining these variables into dimensionless groups was addressed by Stack et al. [141] in 1999, based on the modeling work described above. They combined eleven variables into eight dimensionless groups. The results indicated that the technique provided important advantages in dealing with the large number of variables associated with a single erosion-corrosion interaction, although there were limitations arising from the assumptions made in the approach.

However, the practicality of the approach is limited, as it is still too complicated for practical engineering applications. Additional work must be carried out in this area, particularly in the aqueous erosion-corrosion field, to develop maps that are "user-friendly" tools. Stack et al. [46] also have constructed materials performance maps for describing resistance to erosion in aqueous slurries. When the effects of metallurgical features are also reflected in the erosion-corrosion map, their methods will provide a more powerful tool for materials selection for structures encountering erosion-corrosion in service.

### **2.5.2 Experimental apparatus for erosion-corrosion tests**

The apparatus for studying slurry erosion-corrosion is very similar to that for examining the effects of flow on corrosion. The main difference is mainly that for the latter there are no solid particles in flowing aqueous solution, while for the former solid particles, such as silica sand, alumina sand, corundum sand etc., are entrained, leading to a multi-flow hydrodynamic pattern. Poulson [11] summarized the existing laboratory techniques for studying the effect of flow velocity on electrochemical corrosion processes, and pointed out that the methods adopted for simulating fluid flow effects on corrosion should satisfy following basic requirements:

- The hydrodynamic laminar, transitional, and turbulent regimes and flow characteristics is well defined.
- Mass transport correlations are readily available, or at least are easily determined.
- The corroding surface is equi-potential so that the material corrodes by the same mechanism at all points.

However, for slurry erosion-corrosion studies, in most cases if not all the cases, the velocity of the slurry is in a turbulent regime, as the solid particles need to be carried by the drag force from the flowing liquid.

Three types of apparatus are mainly employed in erosion-corrosion study: flow-through pipe loop, rotating cylinder electrode system (RCE), and impinging jet system.

The flow-through pipe loop, with similar dimension size as the full-scale system, is the most direct method of simulating erosion-corrosion in slurry because of the similarity in geometry and flow pattern to the practical condition. Heitz [12] suggested that nondisturbed or disturbed pipe flows are the most suitable, since the particle distribution through the cross section is more uniform. However, the cost of setting up and running this system is relatively high.

The RCE system usually consists of a concentric outer cylindrical container and an inner rotating cylindrical electrode. The RCE system has the advantages that it is less expensive, more easily constructed, and convenient to use than the pipe loop system, and the particle impingement angle in the RCE system is close to those in straight pipelines. For these reasons, the RCE system is often used in the laboratories to investigate erosion-corrosion behavior of materials. When the RCE system is used to investigate erosion-corrosion behavior of materials in slurries, however, one problem arises from keeping sand uniformly suspended in the slurry, because it is difficult to control sand concentration distributions in the fluid. Sometimes axial flow has been adopted to suspend solid particles in the slurry [62], but under these conditions the influence of axial flow on the hydrodynamic conditions of the fluid must be taken into account [147]. Zhou et al. [39, 148] modified the RCE cell by

adding four or six buffers to increase turbulence and so obtain a more uniform two-phase flow field. Unfortunately, the hydrodynamic parameters of the fluid are then more difficult to estimate for this modified RCE system.

An impingement jet system comprises a submerged jet impinging a slurry onto a flat specimen at a controlled angle. Its main advantage is that the velocity and angle of fluid impingement are both well defined so that it is widely used to study the effect of impact angle of fluid on erosion-corrosion processes [32, 83, 149]. The main disadvantage of the impingement jet method is the non-uniform hydrodynamic and electrochemical conditions on the specimen surface, which results in a non-uniform distribution of local thickness loss in the wear scar [148]. Moreover, the size of the wear scar produced by the jet impingement and the thickness distribution within the wear scar depend heavily on the impingement angle. In this case, the actual erosion-corrosion rate of materials depends on the local hydrodynamic and electrochemical conditions and it cannot be assessed accurately using the total weight loss method [11].

A problem that arises is the difficulty of comparing test data obtained using different types of apparatus. Efforts have been made to correlate the test results in order to bring the extensive data together, to develop correlations between them, and more importantly to relate the results to practical geometries. Chen et al. [147] compared the corrosion data of 90:10 Cu-Ni alloy in flowing 1 M NaCl from the flow-through pipe, annular flow pipe and RCE systems. They found that on the basis of the mass transport coefficients, the corrosion rates determined using one system could be transferred to another, but the mass transport coefficients are flow-geometry-dependent. Poulson [11] correlated the data from different types of apparatus based on mass transfer coefficients in single phase flow. It remains unclear whether the corrosion rate measured from the RCE system can be transferred to the flow-through pipe system when erosion-corrosion takes place in multiphase flow (slurry).

As pointed out by Hutchings [40], an important factor to be considered in any simulation test is the effect of particle degradation. The erosion-corrosion rate is

independent of time for tests when fresh slurry is continuously supplied to the system. However, if the slurry is re-circulated, then particle degradation will lead to a progressive decrease in the erosivity of the slurry, resulting in data that may be very misleading. In some cases, it is not practical to continuously supply fresh slurry, in which case the effects of particle degradation must be accommodated during analysis of the data.

### **2.5.3 Experimental techniques for erosion-corrosion study**

#### **2.5.3.1 Weight loss method**

Weight loss method is the most commonly used technique in erosion-corrosion study and corrosion study, because it can provide the most direct and important information about the material loss. Usually, the weights of the test specimen are measured before and after tests, and thus the overall weight loss rate of material can be calculated from the weight difference. To remove the corrosion product or other impurity deposited onto or adsorbed on the surface, the specimen must be cleaned after tests. Standards for the cleaning solution and procedure have been developed for various metallic materials by ASTM. As the synergistic effect of erosion and corrosion is studied, it is important to differentiate the material losses due to different processes, as expressed by Equation (2-1). The total material loss and the pure erosion rate are usually measured using the weight loss method. The corrosion components can be obtained using the weight loss method or electrochemical measurements.

The weight loss method also is often employed to investigate the effect of any specific test parameter on the erosion-corrosion processes. However, one problem with this approach is that it can't determine non-uniform material loss. For example, in pitting corrosion or in jet impingement tests, some specific sites on the specimen surface have much higher material loss rates than others. Even when the total material loss is not high, the material may still be liable to failure. In such a case, the overall

weight loss rate alone is not suitable to characterize the material loss, and localized effects must also be considered.

### **2.5.3.2 Electrochemical techniques**

Landolt et al. [150] pointed out that electrochemical methods present two unique advantages for the study of tribological systems in corrosive environments. One is that electrochemical methods allow control of the reaction occurring on the metal surface so that the effect of corrosive environment on erosion-corrosion can be investigated by simply changing the potential/current. Secondly, electrochemical methods can be employed to monitor the in situ and real time current/potential response of metal during erosion-corrosion processes. For this reason, several commonly used electrochemical methods in corrosion study and their applications in erosion-corrosion area are summarized below.

#### **Potentiostatic/galvanostatic tests**

Potentiostatic and galvanostatic tests are traditional methods to control the corrosion status on a metal surface. It is well known that certain relationships exist between potential and reaction rate for specific systems. Thus, by connecting the sample to a potentiostat/galvanostat, the potential/current of the metal can be controlled. At the same time, the current/potential can be recorded, and thus the changes occurring on the metal surface are monitored. Hence, potentiostatic/galvanostatic tests can be used to determine the effect of erosion on a corrosion system. Neville et al. [151, 152] used the potentiostatic method to determine current density as a function of erosion time, media temperature, solid loading, etc.

#### **Polarization tests**

Polarization tests are a basic and quick method to get information for a corrosion system. The operation of this experimental technique is not complicated, and valuable information, such as the corrosion potential and corrosion current, can be obtained from the polarization curve. Hence, the measurement of polarization is

usually the first step for investigation on corrosion related behaviour. From the dependence of current on potential, the critical factor for controlling the corrosion reaction can be determined. As the electrochemical dissolution of a metal is controlled by charge transfer on the electrode surface and the polarization potential is far away from the equilibrium potential, the Tafel relationship will hold:

$$\Delta E = -b_a \log i_{corr} + b_a \log i_a \quad \text{for anodic process} \quad (2-11 \text{ a})$$

and 
$$\Delta E = -b_c \log i_c + b_c \log i_{corr} \quad \text{for cathodic process} \quad (2-11 \text{ b})$$

where  $\Delta E$  is the overpotential,  $i_{corr}$  the corrosion current density,  $i_c$  the cathodic current density, and  $b_a$  and  $b_c$  the Tafel slope for anodic polarization and cathodic polarization, respectively.

Polarization curves are also used to determine the pitting potential in pitting corrosion. The potential above which the current increases quickly is referred to as the critical pitting potential. A cyclic polarization technique is often used to evaluate pitting corrosion susceptibility. During this test, the potential scan is reversed to the negative direction after a given anodic current density has been reached. Then a hysteresis loop can be observed in the plot and the pitting corrosion susceptibility can be evaluated from the area of the hysteresis loop.

In erosion-corrosion studies, polarization tests are often used to investigate the influence of solid erosion on corrosion behaviour of a material. By comparing the polarization curves measured in different erosion environments, the accelerating action of erosion on passive metallic material can be observed directly. Importantly, the erosion-enhanced corrosion rate in Equation 2-2 also can be determined by the difference of the corrosion rates measured in solution with and without the presence of solid particles.

### **Electrochemical Impedance Spectroscopy**

Electrochemical impedance spectroscopy (EIS) was first used by Randels and Somerton in 1952, and now has been established as a powerful tool for describing electrochemical interfaces. In this technique, small amplitude alternating potential

signal of widely varying frequency is applied to the electrode, and the fundamental parameters related to the electrochemical kinetics can be determined by analyzing from the response at the electrode.

In EIS analysis, an equivalent circuit is usually used to characterize the corroding system, which is based on the equivalent response to the same electrical disturbance. A good equivalent circuit not only gives a response consistent with electrical signals in the actual system, but also consists of electrical elements that have physical significance. The simplest equivalent circuit is the Randle model, shown in **Figure 2-11** [4]. It is composed of a parallel combination of a resistance,  $R_r$ , and a capacitance,  $C$ , in series with another resistance,  $R_{sol}$ . Here  $R_{sol}$  represents the solution resistance,  $C$  the capacitance of the double layer formed at the electrode surface, and  $R_r$  the charge transfer resistance for the corrosion reaction. This equivalent circuit is suitable for modeling a simple corroding system where the reaction is at steady state and diffusion or adsorption is not important. In most cases, however, the actual corrosion system is more complicated. Therefore, the aim of impedance measurements is to find which equivalent circuit fits best, and how its elements reflect the electrode reaction parameters. Also, it is necessary to note that there is no unique equivalent circuit for a specific corrosion system. The fits can be improved by adding more adjustable elements to the circuit. Therefore, good agreement between the experimental data and the impedance fit from an equivalent model circuit does not necessarily mean that the model is correct. Some elements in the circuit models may not possess appropriate physical meanings in terms of the electrochemical reactions.

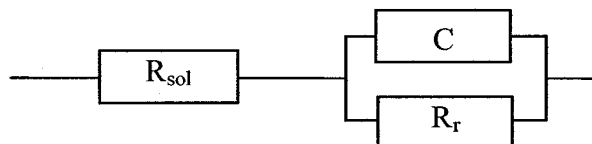


**Figure 2-11. Equivalent circuit of Randle model [4].**

Electrochemical impedance can be measured at various polarization potentials. At each polarization potential, an ac signal with small amplitude (no more than 10 mV) is applied on the electrode. The reason for using ac signals with small amplitudes is that perturbations of the electrochemical system will not extend out of the linear regime. The current response is also a sine wave with the same frequency as that of the potential perturbation, but with a phase shift. For a given frequency, the electrode impedance,  $Z(\omega)$ , can be expressed by the following equations [7]:

$$E = E_0 \cdot e^{j\omega t} \quad (2-12)$$

$$I = I_0 \cdot e^{j\omega t + \theta} \quad (2-13)$$

$$Z(\omega) = \frac{E}{I} = |Z(\omega)| \cdot e^{-j\theta} \quad (2-14)$$

where  $j = \sqrt{-1}$ ,  $E$  and  $I$  are the electrode potential and current,  $E_0$  and  $I_0$  are the amplitudes of potential and current respectively,  $\omega = 2\pi f$  is the angular velocity and  $\theta$  is the phase angle between potential and current. Various processes at the surface absorb electrical energy at discrete frequencies, causing a time lag and a measurable phase angle between the time-dependent excitation and the response signals. The impedance is expressed in terms of a real component,  $Z'(\omega)$ , and an imaginary component,  $Z''(\omega)$ ,

$$Z(\omega) = Z'(\omega) - jZ''(\omega) \quad (2-15)$$

Two methods are commonly used to display the impedance data according to the mathematical forms by Equation (2-14) and (2-15). The first one is a Nyquist plot, presented as  $Z''(\omega)$  vs.  $Z'(\omega)$ , and the second one is a Bode plot, presented as  $\log|Z|$  and  $\theta$  vs.  $\log f$ . The plots shown in **Figure 2-12** are for the equivalent circuit shown in **Figure 2-11** [4]. The Nyquist plot shows a semicircle, with increasing frequency in a counterclockwise direction. At high frequency, the imaginary component disappears, leaving only the solution resistance. At low frequency, the imaginary component disappears again, leaving a sum of solution resistance and charge transfer resistance.

The Bode plot gives analogous results. At intermediate frequencies, the capacitance plots linear with a slope of -1 and maximum phase angle,  $\theta$ .

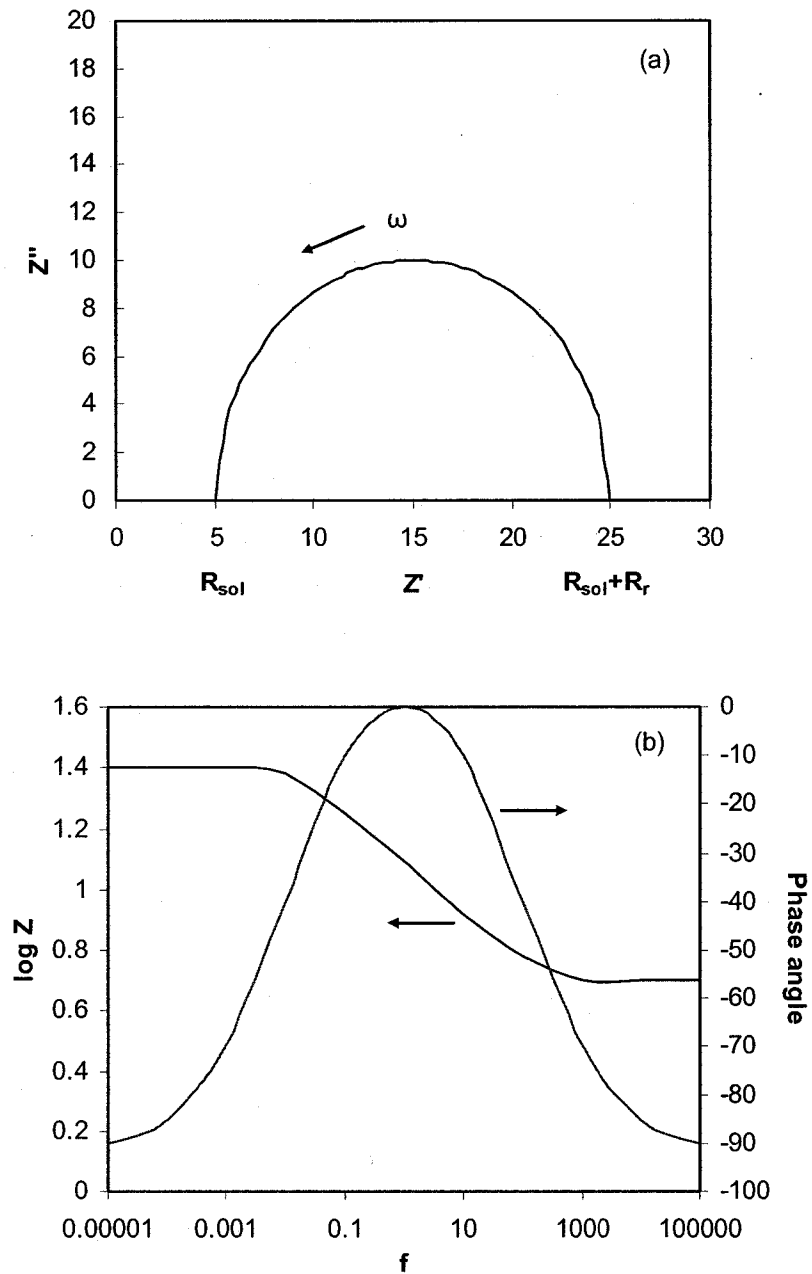


**Figure 2-12. Data display of electrochemical impedance spectroscopy for a corroding electrode simulated by Randle model [4]: (a) Nyquist plot, (b) Bode plot.**

EIS is a very useful technique for determining the fundamental parameters relating to the electrode reactions. It has been widely used in the study of metal corrosion, but has limited application in the erosion-corrosion study. Yong et al. [153] measured the EIS of a duplex stainless steel in flowing 3.5% NaCl solution containing sand, and found that the EIS takes the shape of a capacitive loop in the high frequency region and a straight line in the low frequency region when the flow velocity is below the critical value. Wang et al. [154] assessed the efficiency of corrosion inhibitors in reducing material damage occurring as a consequence of erosion and corrosion processes by the EIS technique, and they analyzed the data with the equivalent circuit shown in **Figure 2-12**.

### **Mott-Schottky Analysis**

Mott-Schottky analysis is used to study the electronic property of materials. Based on the semiconductor nature of passive films and the correspondence between electronic property and corrosion resistance, Mott-Schottky has become a popular method to study passive films. The outer layer of passive films contains the space charge layer and sustains a potential drop across the film [155]. The charge distribution at the semiconductor/electrolyte interface is usually determined using the Mott-Schottky relationship by measuring the electrode capacitance,  $C$ , as a function of electrode potential,  $E$ , [155]:

$$\frac{1}{C^2} = \frac{2}{\epsilon\epsilon_0 eN} \left( E - E_{fb} - \frac{kT}{e} \right) \quad \text{for n-type semiconductor} \quad (2-15 \text{ a})$$

$$\frac{1}{C^2} = \frac{2}{\epsilon\epsilon_0 eN} \left( E_{fb} - E - \frac{kT}{e} \right) \quad \text{for p-type semiconductor} \quad (2-15 \text{ b})$$

where  $\epsilon$  is the dielectric constant of the passive film,  $\epsilon_0$  the permittivity of vacuum ( $8.854 \times 10^{-12}$  F/m),  $e$  the electron charge,  $N$  the charge carrier density,  $E_{fb}$  the flat band potential,  $k$  the Boltzmann constant and  $T$  the absolute temperature. A plot of  $1/C^2$  vs.  $E$  for a n-type semiconductor has a straight-line section with a positive slope, while a

p-type semiconductor has a negative slope.  $N$  can be determined from the slope, and  $E_{fb}$  from extrapolation of the linear portion to the intercept with the axis ( $I/C^2 = 0$ ).

Charge carrier density is important as a parameter affecting both the growth kinetics and stability of passive films. Meanwhile, the erosion-enhanced corrosion is strongly related to the passivation process for a passive system. Hence Mott-Schottky analysis can provide very useful information for erosion-corrosion studies of passive corrosion systems. However, prior to this work, this analysis method had not been employed for studies of erosion-corrosion.

### **2.5.3.3 Surface analysis methods**

Modern physical surface analysis techniques, including composition and morphology analysis methods, have played important roles in erosion-corrosion studies. The commonly used analysis methods include, but are not limited to, X-ray diffraction analysis (XRD), scanning electron microscopy (SEM), energy dispersive X-ray spectroscopy (EDX), transmission electron microscopy (TEM), atomic force microscopy (AFM), X-ray photoelectron spectroscopy (XPS), secondary ion mass spectrometry (SIMS), etc. Improved understanding of the roles of some elements or phases can be achieved by analyzing the chemical composition of the sample after erosion-corrosion tests, and the morphology of the eroded sample can provide clues to the erosion mechanism. Levy [20] developed the platelet mechanism of erosion based on large amounts of physical observations of eroded sample surfaces, mostly using SEM at high magnifications. The hard particle-removing mechanism proposed for the synergistic effect between erosion and corrosion on MMCs is also attributed to the observation on the failed samples [111-113]. Salaita and Tate [156] attempted to apply several surface analysis techniques for studies of the erosion-corrosion of stainless steel, and they achieved the element distribution on the corroded sample surface.

## 2.6 Nanoindentation technique

As discussed in Section 2.4, study on the chemo-mechanical effect involves characterization of mechanical behaviour at very small scales. The nanoindentation technique is a recently developed technique for mechanical property testing on a micro- or nanometre scale.

Nanoindentation systems measure mechanical properties in much the same way as conventional mechanical testing systems. In nanoindentation, a sharp diamond indenter is driven into and withdrawn from the specimen. At the same time the load is applied and the displacements of the indenter are measured. Properties are derived from the measurements of the load and displacement. The advantages of nanoindentation are obvious as compared with the conventional method. First, since the deformation scale is much smaller, nanoindentation is more suitable for studying microstructure materials, such as thin films. Second, the mechanical properties can be determined directly from the indentation load and displacement measurements, without the need to image the hardness impression. Finally, more mechanical properties, not only hardness, can be evaluated using nanoindentation tests.

Mechanical properties such as hardness and elastic modulus can be evaluated by analyzing the load-depth data. The analysis method developed by Oliver and Pharr [157, 158] has been widely used. The hardness,  $H$ , is defined by [159]

$$H = \frac{P_{max}}{A} \quad (2-16)$$

where  $P_{max}$  is the maximum load and  $A$  is the projected contact area of the indenter at  $P_{max}$ . The reduced modulus,  $E_r$ , of the target material can be determined using [157]

$$E_r = \frac{\sqrt{\pi}}{2\sqrt{A}} S \quad (2-17)$$

where  $S$  is the stiffness at the peak load. The reduced modulus accounts for the fact that the measured elastic displacement includes contributions from both the specimen and the indenter, and is defined as in the equation [158]

$$\frac{1}{E_r} = \frac{(1-\nu_s^2)}{E_s} + \frac{(1-\nu_i^2)}{E_i} \quad (2-18)$$

where  $E_s$  and  $\nu_s$  are Young's modulus and Poisson's ratio for the specimen;  $E_i$  and  $\nu_i$  are the same parameters for the indenter.

**Figure 2-13** shows the schematic load-depth curve obtained from nano-indentation tests. By fitting the unloading curve with a power law relationship,  $S$  can be calculated. The contact area,  $A$ , if the indenter shape is ideal, can be estimated from the indentation contact depth  $h_c$  according to the geometrical relationship. In practical applications, however, this relationship is achieved by a calibration procedure in which a series of indentations are conducted on fused quartz. The final area function for the present tip can be determined using the following equation [158]

$$A(h_c) = 2.598h_c^2 + c_1h_c + c_2h_c^{1/2} + c_3h_c^{1/4} + c_4h_c^{1/8} + c_5h_c^{1/16} \quad (2-19)$$

where the coefficients  $c_1$  through  $c_5$  are constants to correct the indenter shape. The contact depth can't be obtained directly during measurements, and thus the following equation is used to calculate  $h_c$  from the maximum depth  $h_{max}$  [158],

$$h_c = h_{max} - \varphi \frac{P_{max}}{S} \quad (2-20)$$

where  $\varphi$  is a coefficient related to the geometry of the indenter.

Due to its capacity to determine the mechanical properties of materials from very small scale deformations, nanoindentation has become one of the most widely used techniques for measuring the mechanical properties of thin films [160]. Further, owing to its advantages in characterization of mechanical properties on a nanometre scale, some processes involving mechanical property changes on a small scale can be investigated using the nanoindentation technique. A good example is the work done by Seo and Chiba [161, 162]. Usually, nanoindentation tests are performed in air, but they can also be conducted in solution. Taking this advantage, Seo and Chiba investigated the mechanical properties of passive films formed on metallic material in solution at different potentials during the film forming process, which they termed

nano-mechano-electrochemistry. With this technique, they compared the mechanical properties of passive film formed on different crystalline planes and for the first time investigated the effect of film forming potential on film mechanical properties.

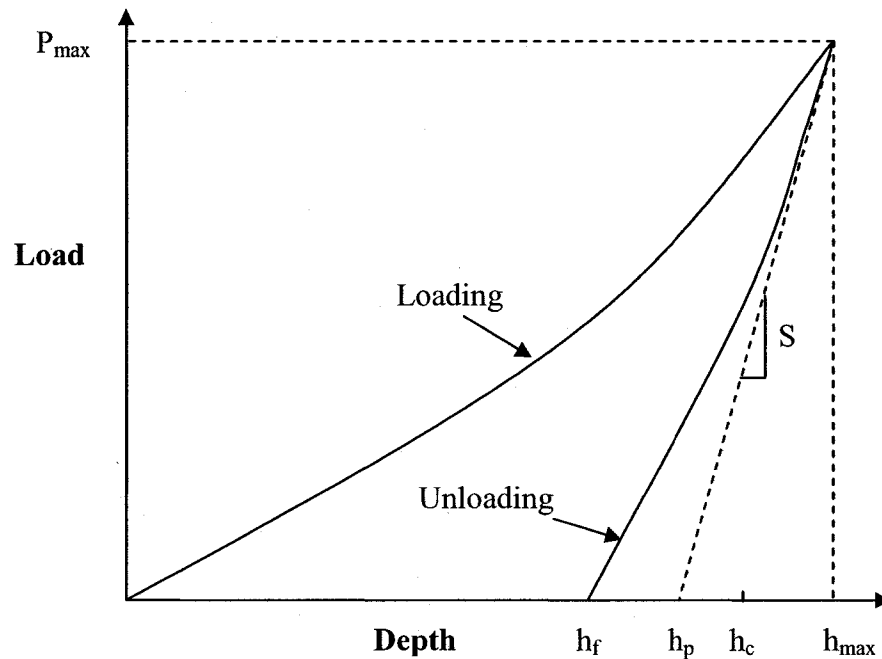


**Figure 2-13. Typical indentation load-displacement curve defining key parameters.**

In addition, nano-scratch tests can be carried out with the same setup for nanoindentation. While the indenter scratches on the specimen surface, the normal force is controlled and the lateral force is measured. Then, the friction coefficient, an important parameter for tribology, can be determined from the ratio of these two forces [163].

## **2.7 Summary of present status of erosion-corrosion studies**

The above review on the status of research into erosion-corrosion behavior of metals includes the various material loss processes, factors controlling erosion-

corrosion rate, mechanism of the synergistic effect between erosion and corrosion, chemo-mechanical effect and experimental techniques. Considerable progress has been achieved in determining the controlling factors that influence the erosion-corrosion processes, and attempts also have been made to develop qualitative models to describe these processes and make predictions suitable for practical application. However, further extensive and intensive work is necessary to obtain a better understanding for the phenomenon of erosion-corrosion.

- (1) The numerous parameters that affect erosion-corrosion rate complicate the estimation of material losses under practical industrial service conditions. Preliminary attempts have been made to combine sets of parameters into dimensionless groups. More 'user-friendly' analytical methods are required, and advances in the knowledge of flow mechanics in multi-phase flows are of special importance for this work.
- (2) Three principal types of experimental apparatus, flow-through pipe loop, rotating cylinder system and impingement jet system, have been employed in slurry erosion-corrosion studies. The strong dependence of the test results on the type of experimental apparatus, even when using the same type of apparatus but with different sizes, leads to difficulty in comparing and analyzing the results.
- (3) The synergistic effects between erosion and corrosion are not well understood. Different mechanisms have been suggested to model different systems. Most mechanisms proposed for the interaction of erosion and corrosion are qualitative. Quantitative correlation among erosion-enhanced corrosion, corrosion-enhanced erosion, process parameters and material parameters is lacking.

## **2.8 Topic selection and technical approach**

Considering the potentially significant synergistic effect in material loss during erosion-corrosion, the present work focuses on the third question mentioned above:

the interaction effect between erosion and corrosion processes. In carrying out the research work, the following aspects have been considered:

- (1) The effect of erosion on corrosion and corrosion on erosion, i.e., corrosion-enhanced erosion and erosion-enhanced corrosion, are investigated separately. In a considerable amount of the previous research, only a synergistic component resulting from the interaction of erosion and corrosion was proposed and the influence of erosion and corrosion on each other was considered to be a single effect, which made it difficult to understand the action mechanism behind each component.
- (2) The interaction between erosion and corrosion is studied not only from the experimental phenomenon, but also from the nature of processes, i.e., the interaction between electrochemical reaction and material mechanical behavior. Therefore, some experiments, which do not appear like 'erosion-corrosion' tests, are designed for this intention.
- (3) Depending on the combination of the metal and its environment, the corrosion behaviour of a system can be categorized into non-passive systems and passive systems. Since the corrosion behaviour that metals exhibit in these two systems is completely different, the system dependence of synergy is investigated.

The objective of the present work is to clarify the interaction between erosion and corrosion in a flowing environments, providing useful information for industrial applications and advancement of research. To fulfill the objectives, carbon steel is chosen as the main experimental material due to its wide applications in industries. Two main research systems are selected: one is a non-passive system containing carbon steel/ $\text{Na}_2\text{SO}_4$  solution and the other is a passive system consisting of carbon steel and boric buffer solution. The content of the work is shown in **Figure 2-14**. Firstly, the influence of erosion on corrosion is investigated in the non-passive system and the passive system. In the non-passive system, the effects from erosion including mass transfer, deformation and corrosion product removal are analyzed experimentally. In the passive system, the effect of erosion on corrosion is

investigated from its influence on the equivalent electrical circuit of the system, and the erosion-enhanced corrosion is analyzed by examining the parameters for growth kinetics of passive films. Secondly, most work about the influence of corrosion on erosion is performed in the active system, since it can essentially reflect the influence of electrochemical dissolution on erosion. In this part, corrosion-enhanced erosion is first studied in slurries, and the chemo-mechanical effect is investigated using an in situ nanoindentation technique. In addition, an experimental phenomenon in flowing corrosive solution free of solid particles is interpreted by corrosion-enhanced erosion. The erosion-corrosion behavior of several MMCs is investigated as well and the results are attached in the appendix.

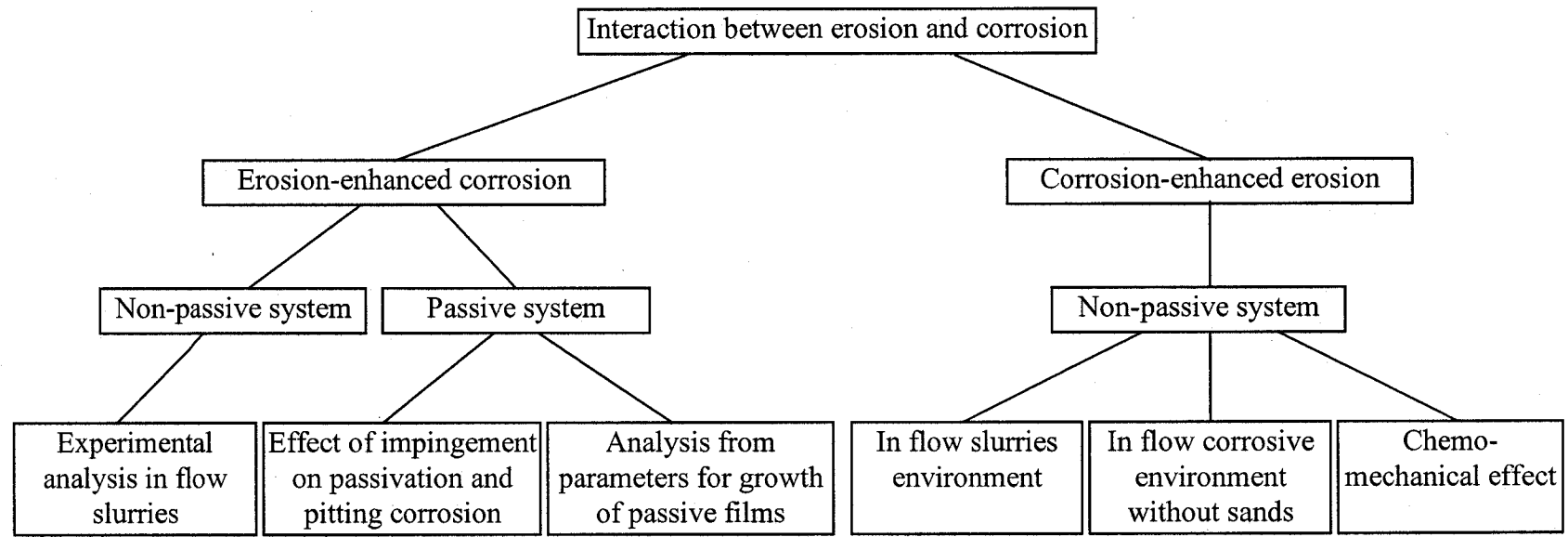


Figure 2-14. Components of the thesis.

## References

- [1] R.J.K. Wood, J.A. Wharton, A.J. Speyer, and T. K.S., *Tribology International* 35 (2002) 631.
- [2] M.M. Stack, F.H. Stott, and G.C. Wood, *Wear* 162 (1993) 706.
- [3] ASTM Standard Designation G119-93: Standard Guide for Determining Synergism between Wear and Corrosion, 1993, p.139.
- [4] D.A. Jones, *Principles and Prevention of Corrosion*, Upper Saddle River, USA, Prentice Hall, 1996.
- [5] N. Sato, ed., *Passivity and its breakdown on iron and iron base alloys*, NACE, ed. R.W. Staehle H. Okada, Houston, 1976, p.1.
- [6] D.D. Macdonald and M. Urquidi-Macdonald, *Journal of the Electrochemical Society* 137 (1990) 2395.
- [7] C.N. Cao, *Principles of Electrochemical Corrosion*, Beijing, China, Chemical Industry Press, 2004.
- [8] H.H. Uhlig, *Journal of the Electrochemical Society* 97 (1950) 215C.
- [9] J.R. Galvele, *Journal of the Electrochemical Society* 123 (1976) 464.
- [10] J. Weber, *British Corrosion Journal* 27 (3) (1992) 193.
- [11] B. Poulson, *Corrosion Science* 23 (4) (1983) 391.
- [12] E. Heitz, *Corrosion* 47 (2) (1991) 135.
- [13] P.A. Engel, *Impact wear of materials*, Amsterdam, Elsevier, 1978.
- [14] A.D. Sarkar, *Friction wear*, New York, Academic Press, 1980.
- [15] H.C. Meng and K.C. Ludema, *Wear* 181-183 (1995) 443.
- [16] R.W. Lyczkowski and J.X. Bouillard, *Progress in Energy and Combustion Science* 28 (2002) 543.
- [17] I. Finnie, in *Proceeding of the Third National Congress on Applied Mechanics*, New York, American society of Mechanical Engineers, 1958, p.527.
- [18] I. Finnie, *Wear* 19 (1972) 81.
- [19] I. Finnie and D.H. McFadden, *Wear* 48 (1978) 181.
- [20] A.V. Levy, in *ASM International, Materials Park, OH, USA*, 1995,

- [21] P. Shewmon and G. Sundararajan, Annual Review of Materials Science 13 (1983) 303.
- [22] J.G.A. Bitter, Wear 6 (1963) 5.
- [23] J.G.A. Bitter, Wear 6 (1963) 169.
- [24] I.M. Hutchings, Wear 70 (1981) 269.
- [25] G. Sundararajan and P.G. Shewmon, Wear 84 (1983) 237.
- [26] G. Sundararajan, Wear 149 (1991) 111.
- [27] S. Endo and M. Nagae, ISIJ International 36 (1) (1996) 87.
- [28] Y. Li, G.T. Burstein, and I.M. Hutchings, Wear 186 (2) (1995) 515.
- [29] M. Matsumura, Y. Oka, H. Hiura, and M. Yano, ISIJ Int. 31 (2) (1991) 168.
- [30] Z. Yue, P. Zhou, and J. Shi, in Wear of Materials, ASME, New York, 1987, p.763.
- [31] A. Neville and B.A.B. McDougall, Wear 8836 (2001) 1.
- [32] A. Neville and X. Hu, Wear 250-251 (2001) 1284.
- [33] A. Neville, T. Hodgkiess, and J.T. Dallas, Wear 186-187 (1995) 497.
- [34] A. Neville, M. Reyes, T. Hodgkiess, and A. Gledhill, Wear 238 (2000) 138.
- [35] G.T. Burstein and K. Sasaki, Corrosion Science 42 (2000) 841.
- [36] G.T. Burstein and K. Sasaki, Electrochimica Acta 46 (2001) 3675.
- [37] R.J.K. Wood and S.P. Hutton, Wear 140 (1990) 387.
- [38] A. Fan, J. Long, and Z. Tao, Wear 193 (1996) 73.
- [39] S. Zhou, M.M. Stack, and R.C. Newman, Corrosion Science 38 (1996) 1071.
- [40] I.M. Hutchings, The Erosion of Materials by Liquid Flow, Cambridge, UK, MTI Publication No. 25, Material Technology Institute of the Chemical Process Industries, 1986.
- [41] A.V. Levy and P. Yau, Wear 98 (1-3) (1984) 163.
- [42] A.V. levy, N. Jee, and P. Yau, Wear 117 (2) (1987) 115.
- [43] J. Postlethwaite, M.H. Dobbin, and K. Bergevin, Materials Science Forum 8 (1986) 13.
- [44] S. Nesic and J. Postlethwaite, The Canadian Journal of Chemical Engineering 69 (1991) 698.

- [45] S. Nestic and J. Postlethwaite, *The Canadian Journal of Chemical Engineering* 69 (1991) 704.
- [46] M.M. Stack and N. Pungwiwat, *Wear* 215 (1998) 67.
- [47] J. Postlethwaite, B.J. Brady, M.W. Hawrylak, and E.B. and Tinker, *Corrosion* 34 (7) (1978) 245.
- [48] S. Aso, S. Goto, Y. Komatsu, W. Liu, and M. Liu, *Wear* 233-235 (1999) 160.
- [49] N.J.G. Chacon and F.H. Stott, *Corrosion Science* 35 (5-8) (1993) 1045.
- [50] R. Dasgupta, B.K. Prasad, A.K. Jha, O.P. Modli, S. Das, and A.H. Yegneswaran, *Wear* 213 (1997) 41.
- [51] G.L. Sheldon and A. Kanhere, *Wear* 21 (1972) 195.
- [52] Y.I. Oka, M. Matsumura, and T. Kawabata, *Wear* 162-164 (1993) 688.
- [53] A. Levy and G. Hickey, *Wear* 108 (1986) 61.
- [54] U. Malayoglu and A. Neville, *Wear* 259 (1-6) (2005) 219.
- [55] H.W. Wang and M.M. Stack, *Journal of Materials Science* 38 (2000) 5263.
- [56] E.M. Gutman, *Mechanochemistry of Materials*, Great Abington, Cambridge, UK, Cambridge International Science Publishing, 1998.
- [57] B.J. Larsen and H. Liang, *Wear* 233-235 (1999) 647.
- [58] B.Q. Wang, G.Q. Geng, and A.V. Levy, *Wear* 151 (1991) 351.
- [59] L.G. Peterson, G.A. Sargent, and H. Conrad, *Wear of Materials (ASME 1985)* 661.
- [60] B.A. Lindsley and A.R. Marder, *Metallurgical and Materials Transactions A* 29 (1998) 1071.
- [61] G. Bregliozzi, A. Di Schino, H. Haefke, and J.M. Kenny, *Journal of Materials Science Letters* 22 (13) (2003) 981.
- [62] B.W. Madsen, *Wear of Materials (1985)* 345.
- [63] G.M.C. Lee, *Wear* 141 (1) (1990) 185.
- [64] J.D. Majumdar and I. Manna, *Materials Science and Engineering A* 267 (1999) 50.
- [65] D.J. Mills and R.D. Knutsen, *Wear* 215 (1998) 83.

- [66] A. Toro, A. Sinatora, D.K. Tanaka, and A.P. Tschiptschin, *Wear* 251 (2001) 1257.
- [67] H.M. Jing, X.Q. Wu, Y.G. Zheng, Z.M. Yao, and W. Ke, *Acta Metallurgica Sinica* 38 (10) (2002) 1067.
- [68] W.A. Metwally and M.K. Samy, *Steel Research* 65 (10) (1994) 455.
- [69] Y. Gao, F. Zhang, J. Xing, W. Tang, and C. Bao, *Journal of Xi'an Jiaotong University* 35(7) (2001) 727.
- [70] S.Y. Yu, H. Ishi, and T.H. Chuang, *Metallurgy and Materials Transaction A* 27 (1996) 2655.
- [71] P.P. Trazaskoma, *Corrosion* 46 (1996) 402.
- [72] B.F. Levin, J.N. DuPont, and A.R. Marder, *Wear* 238 (2) (2000) 160.
- [73] V.A. Pugsley and C. Allen, *Wear*, 233-235 (1999) 93.
- [74] M.M. Stack, *International Materials Reviews* 50 (1) (2005) 1.
- [75] K. Ghosh, T. Troczynski, and A.C.D. Chaklader, *Journal of Thermal Spray Technology* 7 (1) (1998) 78.
- [76] E.J. Wentzel and C. Allen, *Wear* 181 (1995) 63.
- [77] M.M. Stack, J.S. James, and Q. Lu, *Wear* 256 (2004) 557.
- [78] Y. Oka and M. Matsumura, *Wear of Materials* (1983) 360.
- [79] X. Hu and A. Neville, *Wear* 256 (2004) 537.
- [80] A. Neville, T. Hodgkiess, and H. Xu, *Wear* 233-235 (1999) 523.
- [81] B.T. Lu and J.L. Luo, in *The 16th International Corrosion Congress, Beijing, China, 2005, Sept 19-24, Paper No. 12.*
- [82] I. Finnie, J. Wolak, and K. Y, *Journal of Materials* 2 (3) (1967) 682.
- [83] G.T. Burstein and K. Sasaki, *Wear* 240 (2000) 80.
- [84] B.D. Jana and M.M. Stack, *Wear* 259 (1-6) (2005) 243.
- [85] M.M. Stack, Y. Purandare, and P. Hovsepian, *Surface and Coatings Technology* 188 (2004) 556.
- [86] B. Poulson, *Wear* 235 (1999) 497.
- [87] Y.G. Zheng, Z.M. Yao, X.Y. Wei, and W. Kei, *Wear* 186 (2) (1995) 555.
- [88] B.W. Madsen, *Wear* 123 (1988) 127.

- [89] X.Z. Zhao, N. Cui, J.L. Luo, and S. Chiovelli, *British Corrosion Journal* 37 (1) (2002) 63.
- [90] T.A. Adlrm and R.P. Walters, *Wear* 162-164(2) (1993) 713.
- [91] D. Li, X. Mao, and R. Zhu, *Corrosion* 49(11) (1993) 877.
- [92] M.D. Bermudez, F.J. Carrion, G. Martinez-Nicolas, and R. Lopez, *Wear* 258 (1-4) (2005) 693.
- [93] C.W. Chen, B.T. Lu, and J.L. Luo, in *Conference of Metallurgist of CIM*, Vancouver, Canada, 2003, p.43.
- [94] C. Duret-Thural, J.P. Audouard, and L. Renard, in *Innovation stainless steel*, Florence, Italy, 1993, p.p. 3.207.
- [95] W. Li and D.Y. Li, *Acta Materialia* 54 (2) (2006) 445.
- [96] N.P. Hunt, S.J. Cunningham, C.G. Golden, and M. Sheriff, *Angle Orthodontist* 69 (5) (1999) 433.
- [97] H.D. Kim, I. Kim, D.Y. Sung, M.G. Lee, S. Dost, and H.W. King, *Designing, processing and properties of advanced engineering materials*, Pts 1 and 2 *Materials Science Forum*: 449-4 (2004) 781.
- [98] K. Sasaki and G.T. Burstein, *Corrosion Science* 38 (12) (1996) 2111.
- [99] U.K. Mudali, P. Shankar, S. Ningshen, R.K. Dayal, H.S. Khatak, and B. Raj, *Corrosion Science* 44 (2002) 2183.
- [100] K. Elayaperumal, P.K. De, and J. Balachandra, *Corrosion* 28 (7) (1972) 269.
- [101] S. Yin and D.Y. Li, *Materials Science and Engineering A* 394 (2005) 266.
- [102] H. Huang and W.J.D. Shaw, *Corrosion* 48 (11) (1992) 931.
- [103] H.H. Huang, *Biomaterials* 23 (2002) 59.
- [104] J.H. Xie, A.T. Alpas, and D.O. Northwood, *Journal of Materials Science* 38 (2003) 4849.
- [105] H. Yangliang, *Materials and Corrosion* 55 (2) (2004) 102.
- [106] R. Stefec and F. Franz, *Corrosion Science* 18 (2) (1978) 161.
- [107] G. Salvago, G. Fumagalli, and D. Sinigaglia, *Corrosion Science* 23 (5) (1983) 515.

- [108] B.T. Lu and J.L. Luo, in *The 2nd Environment-Induced Cracking in Materials*, (EICM-2), Banff, Alberta, Canada, 2004,
- [109] M. Mayuzumi, J. Ohta, and T. Arai, *Corrosion* 54 (4) (1998) 271.
- [110] J. Li, Y.G. Zheng, J.Q. Wang, Z.M. Yao, Z. Wang, F. and W. Ke, *Wear* 186-187 (1995) 562.
- [111] M. Reyes and A. Neville, *Journal of Materials Engineering and Performance* 10 (6) (2001) 723.
- [112] J.A. Bester and A. Ball, *Wear* 162-164 (1993) 57.
- [113] S. Das, D.P. Mondal, R. Dasgupta, and B.K. Prasad, *Wear* 236 (1-2) (1999) 295.
- [114] Y.L. Saraswathi, S. Das, and D.P. Mondal, *Metallurgical and Materials Transactions A* 36 (8) (2005) 2259.
- [115] J. Postlethwaite, *Corrosion* 37 (1) (1981) 1.
- [116] P. Rehbinder and J.B. Aron, *Comptes Rendus de L Academie Des Sciences de L URSS* 28 (1940) 802.
- [117] A.A. Trapeznikov and P. Rehbinder, *Comptes Rendus De L Academie Des Sciences De L Urss* 18 (1938) 185.
- [118] P. Rehbinder, *Nature* 159 (4052) (1947) 866.
- [119] V.I. Savenko and E.D. Shchukin, *Wear* 194 (1-2) (1996) 86.
- [120] E.N.D.C. Andrade, R.F.Y. Randall, and M.J. Makin, *Process Physical Society* B 63 (1950) 990.
- [121] R.W. Revie and H.H. Uhlig, *Acta Metallurgy* 22 (1974) 619.
- [122] R.W. Revie and H.H. Uhlig, *Corrosion Science* 12 (1972) 669.
- [123] H.H. Uhlig, *Journal of the Electrochemical Society* 123 (11) (1976) 16991701.
- [124] B. Gu, W.Y. Chu, L.J. Qiao, and C.M. Hsiao, *Corrosion Science* 36 (8) (1994) 1437.
- [125] D. Duquette and H.H. Uhlig, *ASM Transactions Quarterly* 61 (1968) 449.
- [126] D.A. Jones and A.F. Jankowski, *Scripta Metallurgica et Materialia* 29 (1993) 701.

- [127] D.A. Jones, A.F. Jankowski, and G.A. Davidson, *Metallurgical and Materials Transactions* 28A (1997) 843.
- [128] D.A. Jones, *Corrosion* 52 (5) (1996) 356.
- [129] A. Jones, *Metallurgy Transaction A* 16 (1985) 1133.
- [130] T. Magnin, A. Chambreuil, and B. Bayle, *Acta Materials* 44 (4) (1996) 1457.
- [131] T. Magnin, *ISIJ International* 35 (3) (1995) 223.
- [132] J.R. Galvele, *Corrosion Science* 35 (1993) 419.
- [133] H. Pickering, *Journal of the Electrochemical Society* 117 (1970) 8.
- [134] H. Pickering and C. Wagner, *Journal of the Electrochemical Society* 114 (1967) 698.
- [135] M. Seo and N. Sato, *Langmuir* 3 (6) (1987) 917.
- [136] B.T. Lu and J.L. Luo, *Journal of Physical Chemistry B* 110 (9) (2006) 4217.
- [137] M.F. Ashby and S.C. Lim, *Scripta Metallurgica et Materialia* 24 (5) (1990) 805.
- [138] S.C. Lim and M.F. Ashby, *Acta Materialia* 35 (1995) 1.
- [139] M.M. Stack and F.H. Stott, *Corrosion Science* 35(5-8) (1993) 1027.
- [140] M.M. Stack, N. Corlett, and S. Zhou, *Wear* 203-204 (1997) 474.
- [141] M.M. Stack, N. Corlett, and S. Turgoose, *Wear* 233-235 (1999) 535.
- [142] M.M. Stack, N. Corlett, and S. Zhou, *Wear* 225(1) (190-198) (1999)
- [143] M.M. Stack, S. Zhou, and R.C. Newman, *Wear* 186-187 (1995) 523.
- [144] M.M. Stack and B.D. Jana, *Wear* 256 (2004) 986.
- [145] M.M. Stack and N. Pungwiwat, *Wear* 256 (5) (2004) 565.
- [146] M.M. Stack, N. Corlett, and S. Turgoose, *Wear* 255 (2003) 225.
- [147] T.Y. Chen, A. Moccari, and D.D. Macdonna, *Materials technology institute of the chemical process industries, Inc, MTI Publication, No. T-3* (1992)
- [148] S. Zhou, M.M. Stack, and R.C. Newman, *Corrosion* 52 (1996) 934.
- [149] G. Schmitt, C. Werner, and M.J. Schoning, *Corrosion* (2002) Paper No. 2280.
- [150] D. Landolt, S. Mischler, and M. Stemp, *Electrochimica Acta* 46 (2001) 3913.
- [151] A. Neville and T. Hodgkiess, *Wear* 233-235 (1999) 596.
- [152] A. Neville and X. Hu, *British Corrosion Journal* 37 (1) (2002) 43.

- [153] X.Y. Yong, Y.Z. Lin, J.J. Liu, and S.J. Liu, *Acta Metallurgica Sinica* 37 (7) (2001) 745.
- [154] C. Wang, A. Neville, S. Ramachandran, and V. Jovancicevic, *Wear* 258 (1-4) (2005) 649.
- [155] K. Azumi, T. Ohtsuka, and N. Sata, *Journal of the Electrochemical Society* 134 (1987) 1352.
- [156] G.N. Salaita and P.H. Tate, *Corrosion* 52 (7) (1996) 493.
- [157] W.C. Oliver and G.M. Pharr, *Journal of Materials Research* 7 (6) (1992) 1564.
- [158] W.C. Oliver and G.M. Pharr, *Journal of Materials Research* 19 (1) (2004) 3.
- [159] W.D. Callister, *Materials science and engineering: an introduction*, 1994.
- [160] W.D. Nix, *Materials Science and Engineering A* 234 (1997) 37.
- [161] M. Chiba and M. Seo, *Corrosion Science* 44 (10) (2002) 2379.
- [162] M. Seo and M. Chiba, *Electrochimica Acta* 47 (1-2) (2001) 319.
- [163] M. Chiba and M. Seo, *Electrochimica Acta* 50 (2004) 967.

## Chapter 3 Experimental Apparatus and Procedures

Most measurements in the present work were repeated at least twice to confirm the reproducibility and the validity of the results. All the tests were carried out at 22 °C, and no specific temperature control was applied.

### 3.1 Materials and Solutions

Carbon steel AISI 1045 (A1045) was used for most of the electrochemical tests and erosion corrosion tests. The nominal composition (wt%) is listed in **Table 3-1**. The material for nanoindentation tests was chosen to be a commercial pure iron. Since this part of work was designed to investigate the influence of electrochemical dissolution on mechanical properties, a pure metal was preferred, avoiding disturbance from phase composition and alloy elements. The chemical composition of the pure iron is listed in **Table 3-2**.

**Table 3-1. Chemical components of AISI 1045 (wt %).**

	C	Mn	S	P	Fe
AISI 1045	0.43-0.50	0.60-0.90	0.05 max	0.04 max	Balance

**Table 3-2. Chemical components of pure iron (wt %).**

	C	Mn	P	Si	Cr	Al	B	Fe
Iron	0.003	0.12	0.006	0.01	0.01	0.32	0.009	Balance

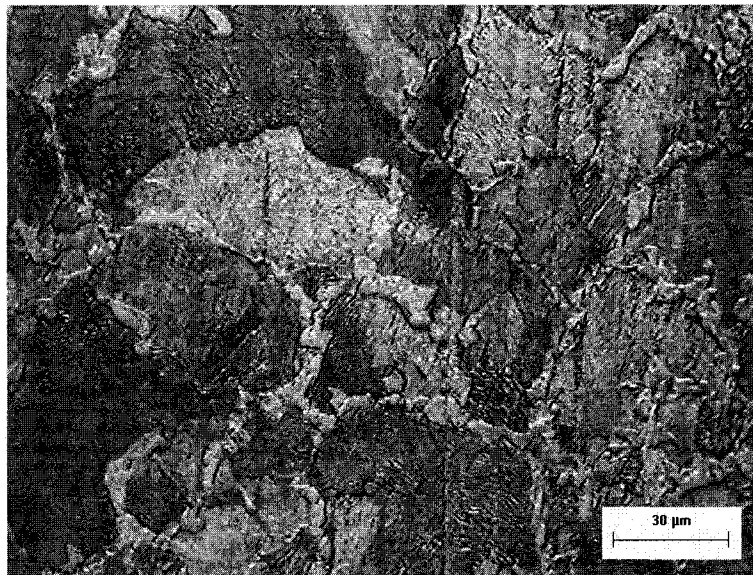
**Figures 3-1 (a) and (b)** are metallographic photos for carbon steel A1045 and pure iron, respectively. For A1045, the average grain size was around 30  $\mu\text{m}$ , and the structure was a network of ferrite around pearlite. The bright grains were the hypoeutectoid precipitated ferrite phase while the darker grains were the pearlite. For pure iron, the average grain size was above 50  $\mu\text{m}$ , and very little precipitated phases can be found in the microstructure.

For the erosion corrosion tests and most of the electrochemical tests, the work surfaces of the samples were ground with silicon carbide abrasive papers down to 600-grit. For the scratch tests and nanoindentation tests, the specimens were mechanically ground with SiC abrasive paper to 1200-grit and then polished with diamond paste of 6  $\mu\text{m}$  and alumina particles of 0.05  $\mu\text{m}$ . After polishing, the specimens were cleaned sequentially with acetone, alcohol and deionized water, and then dried by air.

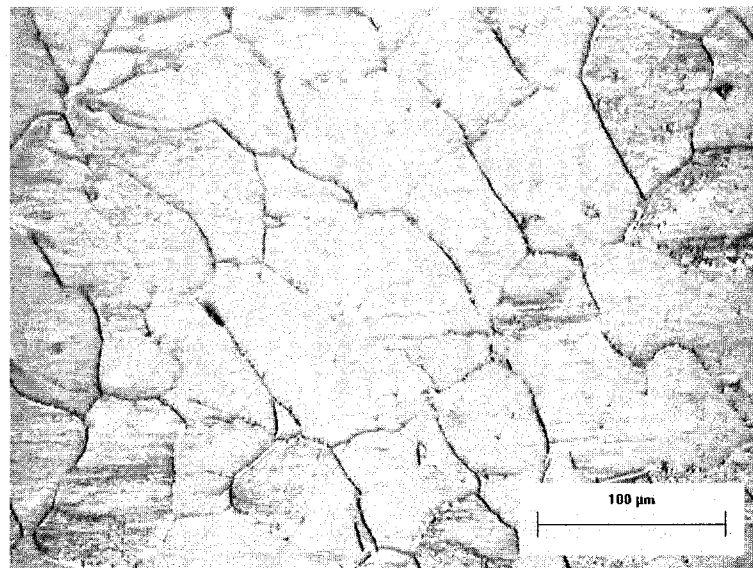
The sand used in this work was unground silica sand with size of 200-300  $\mu\text{m}$ , commercially available from the U. S. Silica Company, Ottawa. The main chemical and physical properties of the sand are listed in **Table 3-3**. The SEM picture and the size distribution of the sand are presented in **Figure 3-2** and **Figure 3-3**, respectively. The sizes of the sand particles were quite uniform. Slurry concentrations are given in weight percent.

**Table 3-3. Main properties of the silica sand**

Chemical	Mineral	Size (mesh)	Diameter ( $\mu\text{m}$ )	Grain Shape	Spe. gravity ( $\text{g}/\text{cm}^3$ )	Hardness (Mohs)
99.70% $\text{SiO}_2$	Quartz	50-70	200-300	Round	2.65	7



(a) Carbon steel A1045



(b) Pure iron

**Figure 3-1. Microstructure of samples.**

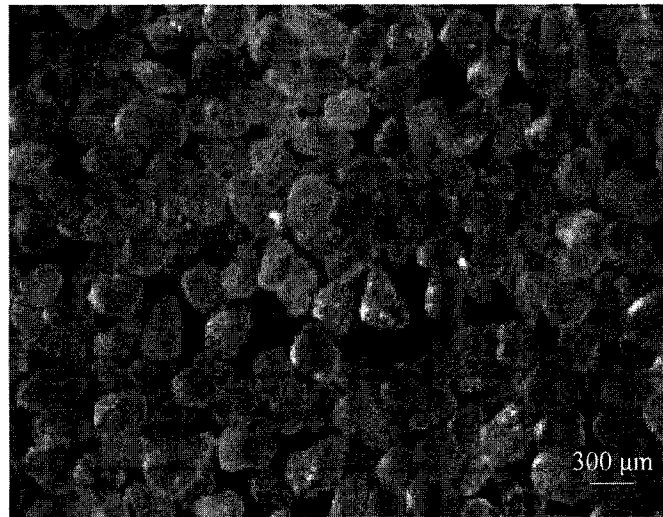


**Figure 3-2. Micrograph of the sand used in the present work.**

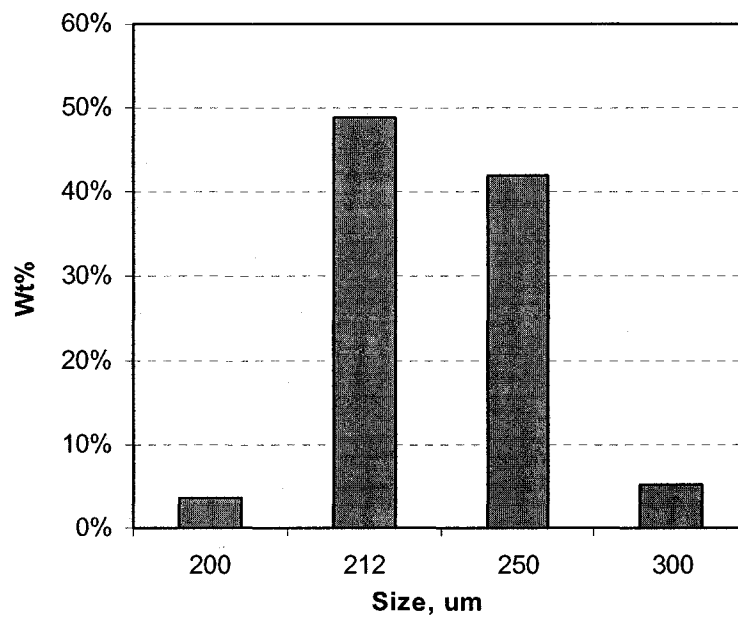


**Figure 3-3. Size distribution of the sand used in the present work.**

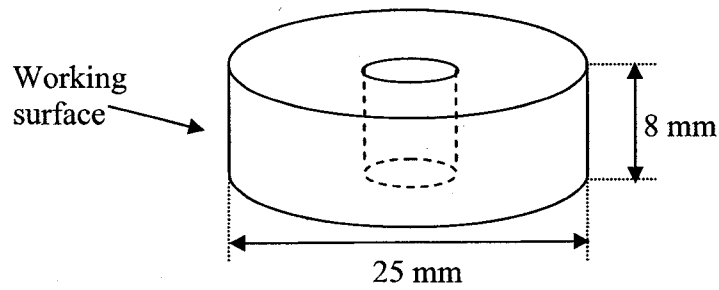
The solutions employed were a 0.1 M  $\text{Na}_2\text{SO}_4$  solution with pH 6.8 for the non-passive corrosion system, and a 0.3 M  $\text{H}_3\text{BO}_3$  + 0.075 M  $\text{Na}_2\text{B}_4\text{O}_7 \cdot 10\text{H}_2\text{O}$  solution with pH 8.4 for the passive corrosion system. In the nanoindentation tests, the concentration of sodium sulphate solution was decreased to 0.01 M in order to reduce the corrosion rate. In the experiments involving pitting corrosion, selected amounts of sodium chloride were added to the borate solution to prepare solutions containing designed concentrations of chloride ions. In some tests, the pH values of the solutions were adjusted using 0.1 M  $\text{H}_2\text{SO}_4$  or NaOH solutions. All the solutions were made using chemicals of analytical reagent grade and deionized water.

## 3.2 Experimental apparatus and setups

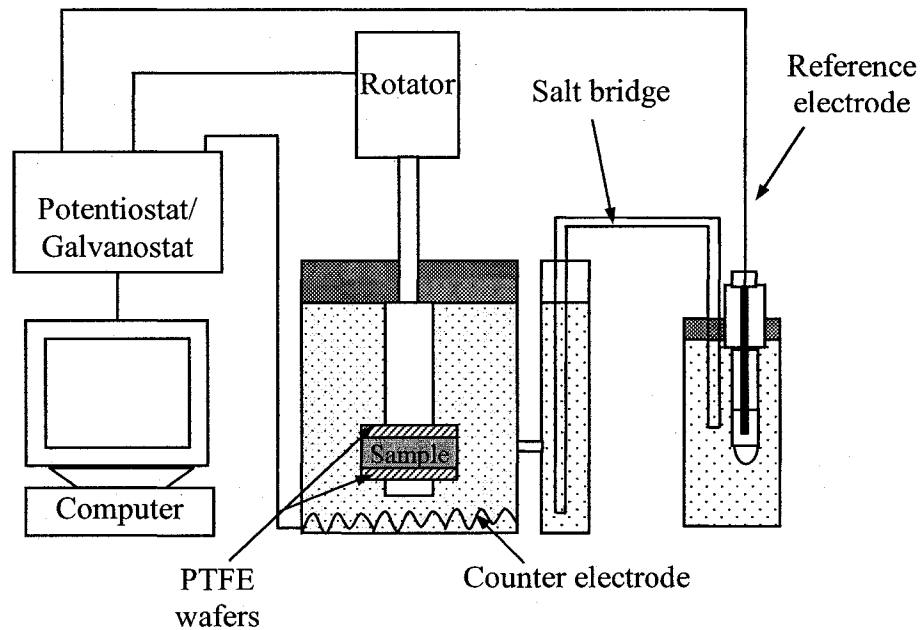
### 3.2.1 Rotating cylinder electrode system

The specimens for erosion corrosion tests were in the shape of a ring with 25 mm in outer diameter and 8 mm in height. **Figure 3-4 (a)** shows the configuration of the samples.

The setup of the RCE system chosen for the erosion corrosion tests is shown in **Figure 3-4 (b)**. The sample was driven by an AFMSRX rotator (Pine instrument Company, PA, USA) and the rotating velocity was adjustable in the range 0-10,000 rpm. The cylindrical specimen holder was made of Teflon and mounted on a stainless steel shaft. The specimens were mounted in the shaft. Washers of PTFE and rubber were used to prevent crevice corrosion. A platinum wire, as the counter electrode, was placed in the bottom of the cell. The reference electrode was a saturated calomel electrode (SCE) connected by a salt bridge placed in the side-cylinder. A rinsed porous ceramic tip was fixed between the major and side cylinders to prevent possible mingling action of the electrolytes.



(a) Configuration of erosion corrosion samples



(b) Setup for erosion corrosion tests

**Figure 3-4. Configuration of the sample and schematic of the setup for erosion corrosion tests.**

The electronic contact between the surface of the shaft and the interval hole of the sample was important for electrochemical measurement. Before carrying out tests, the electronic contact was checked using a multimeter to insure good contact.

The rotating speed was calibrated using a tachometer. According to the dimensions of the specimen and the rotating speed, the apparent velocities

corresponding to rotating speeds of 3000, 6000 and 9000 rpm were calculated to be 4, 8, and 12 m/s respectively.

### 3.2.2 Tensile tests

Tensile tests were performed to investigate the strain effect arising from impingement of solid particles on the material surface. **Figure 3-5** schematically illustrates the configuration of the sample and setup for the tensile test. A 'dog bone' shaped sample was used and the dimension size was as shown in the figure. An INSTRON machine operated using Instron Series IX software was employed to apply load to the sample and to control the deformation rate. The Gamry electrochemical system was used to simultaneously monitor the current response of the sample.

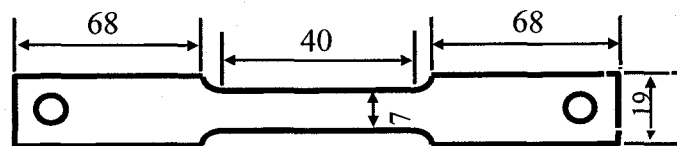
### 3.2.3 Micro-hardness tests

The hardness of the sample surface with and without applied anodic current was measured. The configuration of samples and the setup are shown in **Figure 3-6**. Plate samples were set into epoxy leaving  $1 \text{ cm}^2$  exposed as the working surface. The same conventional three-electrode cell was used as for the erosion corrosion electrochemical tests. The current applied to the sample surface was controlled using a potentiostat. The Vickers micro-hardness of steel samples was measured with a Shimadzu micro-hardness tester under the action of an indenting load.

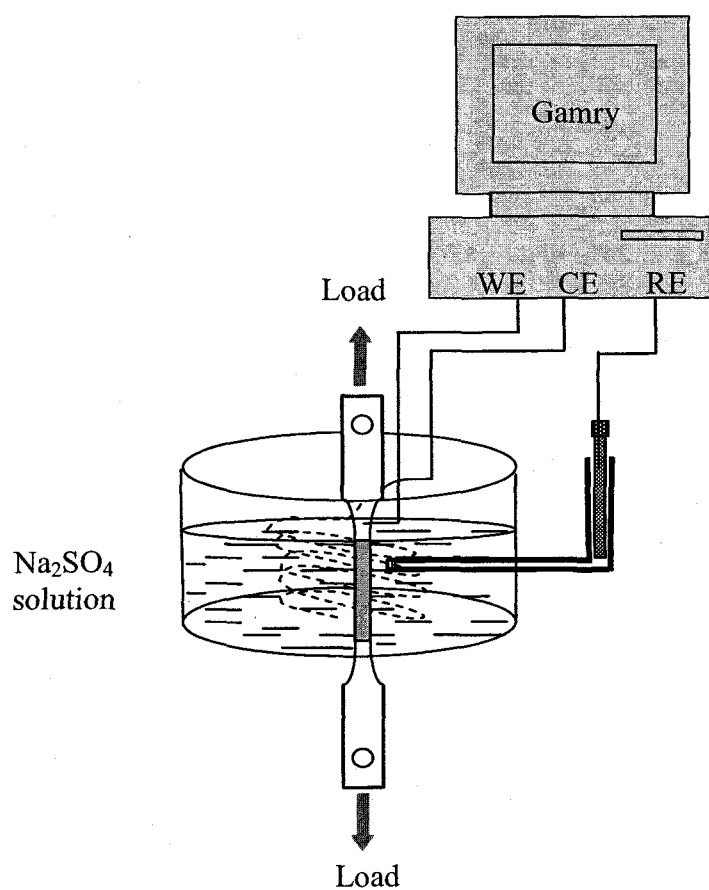
This setup allowed determination of the real time response of material to the electrochemical dissolution, so that the hardness of the sample surface layer could be determined as a function of applied current. The disadvantage of this setup was that the load was relatively high for the thin target surface layer, but low for this type of measurement, with the consequence that the test data had a relatively high level of scatter.

In addition, electrode scratch tests were carried out to simulate the impingement effect of sand particles. A similar setup to **Figure 3-6** was used, but without the hardness tester. With a constant potential applied to the samples, the electrode surface

was scratched with a pointed-tip PTFE rod, and the current response was recorded using the potentiostat.

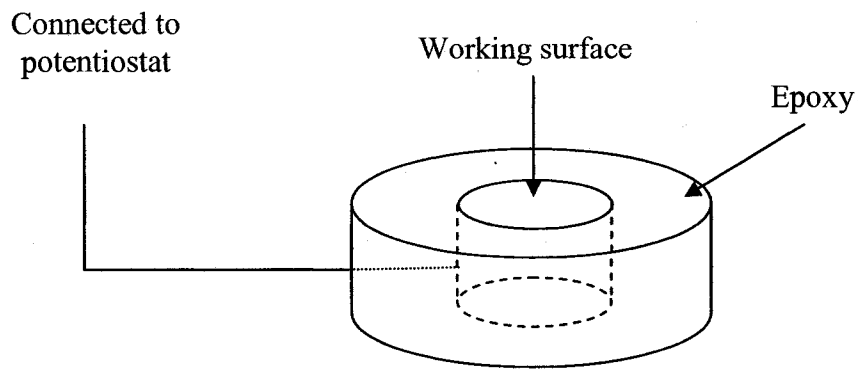


(a) Configuration of samples (dimensions in mm)

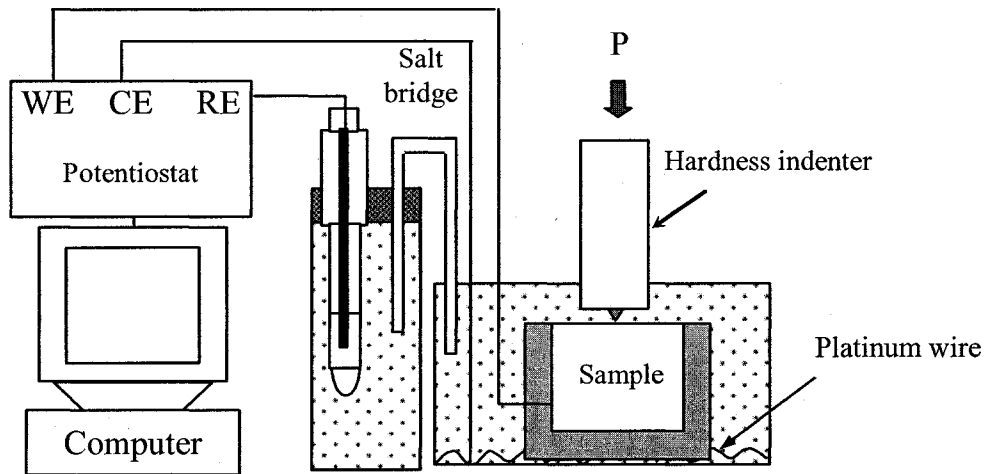


(b) Setup for tensile tests

Figure 3-5. Configuration of the sample and schematic of the setup for tensile tests.



(a) Configuration of samples



(b) Setup for scratch tests and in situ micro-hardness tests

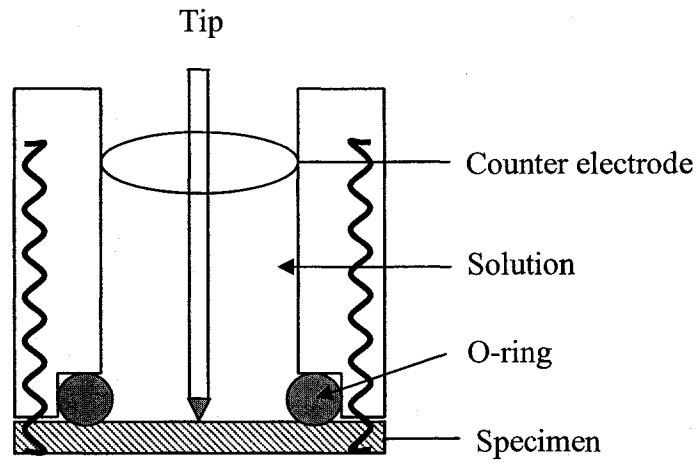
Figure 3-6. Configuration of the samples and schematic of the setup for micro-hardness tests.

### 3.2.4 Nanoindentation tests

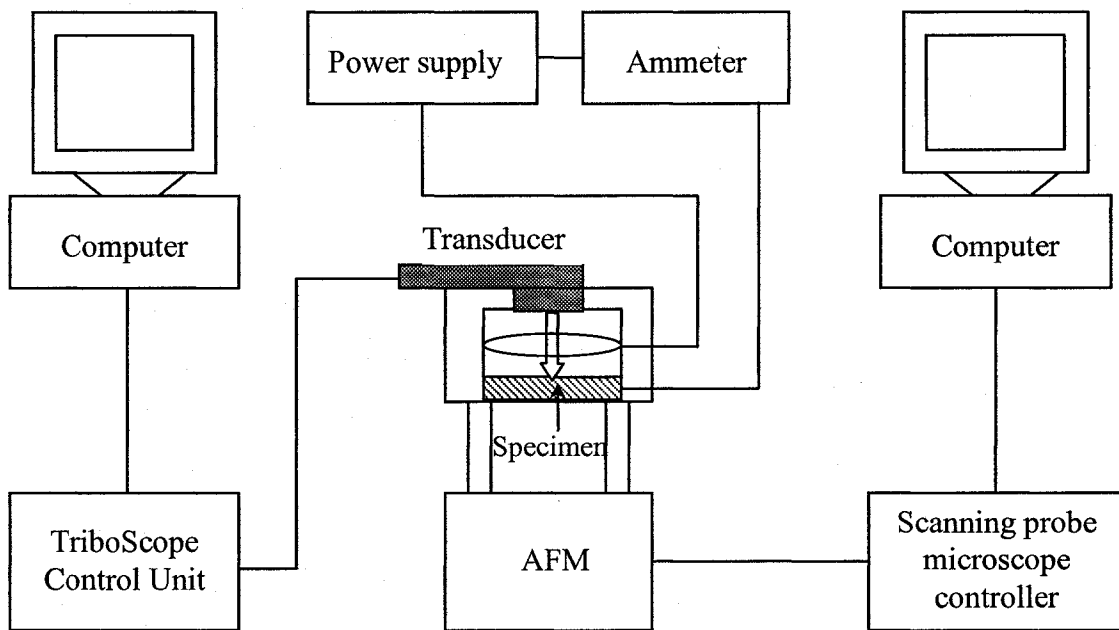
Nanoindentation tests were performed to determine the chemo-mechanical effect between electrochemical dissolution and the mechanical properties. A small electrochemical cell made from polymethyl methacrylate was designed to accommodate the operation procedure and the limitations imposed by the sample size. A schematic diagram is shown in **Figure 3-7 (a)**. The design was similar to that of Chiba and Seo [1, 2]. The bottom of the cell was the specimen in the shape of a thin cylinder with dimensions of 16 mm in diameter and 3.5 mm in thickness. Three screw holes were made for connection of the sample to the side wall of the cell. A two-electrode system was used, with the specimen as the working electrode and a platinum ring as the counter electrode. An O-ring prevented solution from leaking from the cell.

**Figure 3-7 (b)** shows the setup for the in situ nanoindentation tests. A nanoindentation apparatus (Hysitron Co., Ltd., Triboscope®) was connected with AFM (Digital Instruments, Nanoscope E) to control the displacement of the indenter on the specimen surface. A power supply and an ammeter were used to control the current applied to the specimen. Indentations were performed using a diamond cube corner tip with an included angle of 90°. The tip was attached to a tungsten rod for use in liquid.

This method can determine the mechanical properties on a smaller scale than the micro hardness tests. Nevertheless, a disadvantage was that the engaging time of the indenter was not controllable. Depending on the observation by eye and adjustment of the controller, engaging the indenter required at least a few minutes.



(a) Electrochemical cell



(b) Experimental setup

Figure 3-7. Schematic of the equipment used for in situ nanoindentation tests.

### 3.3 Separating the material losses from different processes

According to Equation (2-1), the total material loss in a slurry consists of four components. In order to understand the interaction of erosion and corrosion, experiments were conducted to separate the material losses due to the four individual processes. We rewrite the equation as:

$$W_t = W_{c0} + W_{e-c} + W_{e0} + W_{c-e} \quad (3-1)$$

in which the symbols have the same meaning as in Equations (2-1) to (2-3). To determine the individual material loss rates, weight loss tests were carried out under different test conditions, as follows [3].

- (a) The total material loss,  $W_t$ , was determined from tests conducted under designated conditions by the weight loss method.
- (b) The pure erosion rate,  $W_{e0}$ , was measured from tests carried out in flowing slurry at a potential of -0.850 V, i.e., under the cathodic protection (CP) condition. Under these conditions, the corrosion reaction was inhibited by the impressed current, and so the material losses due to corrosion reaction were insignificant. Hence, all the weight loss can be ascribed to the mechanical effect from pure erosion processes.
- (c) The corrosion component,  $W_c$ , was determined by electrochemical methods in flowing slurry, such as by extrapolation of polarization curves. Since  $W_c$  is the sum of  $W_{c0}$  and  $W_{e-c}$ , then at this stage, in line with Equation (3-1), the loss due to corrosion-enhanced erosion,  $W_{c-e}$ , can be obtained by subtracting  $W_c$  and  $W_{e0}$  from  $W_t$ .  $W_{c0}$  then can be measured using the weight loss method or the same electrochemical technique in tests carried out in solution without sand particles. Then, from the difference between  $W_c$  and  $W_{c0}$ , the erosion-enhanced corrosion,  $W_{e-c}$ , can be calculated.

In some experiments the effect of corrosion on erosion at different corrosion rates was determined. Under these conditions, erosion-enhanced corrosion was not a target parameter, and so emphasis was put on corrosion-enhanced erosion. The different corrosion rates were acquired by applying an impressed current using the potentiostat. Firstly, the total material loss was measured from tests carried out in slurry with applied current or potential. Simultaneously, the current-time curve was obtained, and the total corrosion rate,  $W_c$ , was calculated from Faraday's law. Then, by subtracting  $W_c$  and  $W_{e0}$  from  $W_t$  the corrosion-enhanced-erosion,  $W_{c-e}$ , was obtained.

### **3.4 Experimental procedures**

#### **3.4.1 Weight loss tests**

The weights of samples were measured before and after tests using an analytical balance (Scientech, SA510) with a precision of  $\pm 0.1$  mg, and the weight loss was calculated from the difference.

Before weighing a sample after erosion corrosion tests, the specimen surface was cleaned according to ASTM Standard G1-90 [4]. The solution used for cleaning was hydrochloric acid solution with hexamethylene tetramine as the inhibitor.

#### **3.4.2 Micro-hardness tests**

The Vickers micro-hardness of sample surfaces with and without applied anodic current was investigated. A small indenting load of 50 g was chosen to determine the hardness within a thin layer, and the time for applying the indenting load was 15 s. For the in situ micro-hardness tests, the samples were immersed in the test solution and a constant anodic current was applied to the sample. After the indent was made, the test solution was drained from the electrochemical cell and the sample surface was dried before measuring the diagonal length of the impression area. Only one

hardness measurement was made for each sample. The Vickers micro hardness,  $H_v$ , was calculated with the following equation [5]:

$$H_v = 1.854 \frac{P}{l^2} \quad (3-2)$$

where  $P$  is the applied indenting load (in kilograms-force) and  $l$  is the average diagonal length of the indenter impression (in millimeters).

### 3.4.3 Tensile test

In tensile tests the connection between the sample and the INSTRON machine was insulated by tapes. The sample that was immersed in the solution was sealed and an area of 5 cm<sup>2</sup> was exposed. At the beginning of the test, no load was applied to the sample. Rather, an anodic constant potential was impressed and the current-time curve was recorded. When the current density became stable, a tensile stress with crosshead speed of 0.5 mm/min was applied to the sample until the sample failed.

### 3.4.4 Electrochemical experiments

Electrochemical measurements were carried out using a Gamry 100/300 Electrochemical Measurement System (Gamry Instrument Inc.). For the majority of electrochemical tests, a conventional three-electrode system was used where SCE was the reference electrode and platinum wire the counter electrode.

#### 3.4.4.1 Corrosion potential

The corrosion potential ( $E_c$ ) was measured under the designed test conditions in order to investigate the effect of sand impingement on the corrosion of an electrode. The specimen was immersed in the test solution, and the change of  $E_c$  with time was recorded.

#### **3.4.4.2 Potentiostatic measurements**

In potentiostatic tests, a constant potential was applied directly to the sample, and the variation of current with time and test condition was recorded. The measurements were used in erosion corrosion tests, tensile tests and scratch tests, so as to determine the effect of the impingement, the strain and the scratch on the corrosion current.

#### **3.4.4.3 Galvanostatic measurements**

Galvanostatic measurements were made while the dependence of corrosion-enhanced erosion and the response of the mechanical properties to electrochemical dissolution were investigated. In these tests, a constant current with a selected current density value was applied to the sample.

#### **3.4.4.4 Potentiodynamic polarization**

Potentiodynamic polarization tests were carried out to characterize the corrosion behaviour of samples, determine the pitting corrosion and to investigate the effect of erosion on the corrosion behaviour. When  $E_c$  became stable, a potential scan with a scanning rate of 1 mV/s was started from approximately 300 mV more negative than  $E_c$ . For cyclic polarization tests, when the anodic current density reached 0.1 mA/cm<sup>2</sup>, the potential scan reversed and then stopped when it intersected with the original potential scanning curve.

#### **3.4.4.5 Polarization resistance**

Due to its reciprocal relationship to corrosion rate, linear polarization resistance can be used to characterize the corrosion resistance of metallic materials. In the present work, the technique was employed to investigate the effect of the sand impingement on the corrosion behavior of materials. After the  $E_c$  of the sample stabilized, the potential scan was started from -10 mV to +10 mV vs.  $E_c$  with a

scanning rate of 0.5 mV/s. Polarization resistance was calculated from the slope of the current curve.

#### **3.4.4.6 Electrochemical impedance spectrum**

EIS measurements were used to analyze the influence of solution velocity and sand particles on the electrochemical process, and their effect was quantified in terms of the equivalent circuit elements. For all the impedance measurements, the electrodes were subjected to a cathodic treatment at -1 V for 90 s to reduce films previously formed in air. Then, after the electrodes were passivated for 1 h in various designated conditions, impedance measurements were carried out at  $E_c$ . The frequency was scanned logarithmically from 100 kHz to 0.01 Hz with 10 points per decade. The peak-to-peak amplitude of the ac signal was 10 mV. After tests, the impedance data were analyzed with commercially available EIS 300 electrochemical analysis software from Gamry Instrument Inc., in which a non-linear least squares fitting Levenberg-Marquardt algorithm was used.

#### **3.4.4.7 Mott-Schottky measurements**

The erosion-enhanced corrosion and passive film stability were studied using Mott-Schottky analysis. Flat samples were used for the measurements. The specimens were pre-passivated at various potentials (film formation potential) for 1 h, and then the capacitance was determined by performing a potential scan in the anodic direction at 10 mV/s. An *ac* signal with a frequency of 1000 Hz and peak-to-peak magnitude of 10 mV were superimposed on the scanning potential. At high frequency, an equivalent series resistance-capacitance circuit was assumed and the capacitance values were calculated from the imaginary part of the impedance [6-9].

#### **3.4.4.8 Electrode scratch test**

Electrode scratch tests were performed using flat samples to simulate the effect of sand impingement on the breakdown and repassivation of the passive film in erosion corrosion processes. A constant potential was applied to the samples. When

the current stabilized, the sample surface was scratched with a pointed-tip PTFE rod and the resulting response of the current was recorded.

### 3.4.5 Nanoindentation tests

Ex situ and in situ nanoindentation tests were conducted to investigate the effect of electrochemical dissolution on the properties of the surface layers. Before the tests were performed, calibration was carried out to develop the correct tip area function. A triangular load function consisting of a 5 s loading segment and a 5 s unloading segment was employed, as shown in **Figure 3-8**. The peak indentation loads used in the tests were in the range of 200~2000  $\mu\text{N}$ .

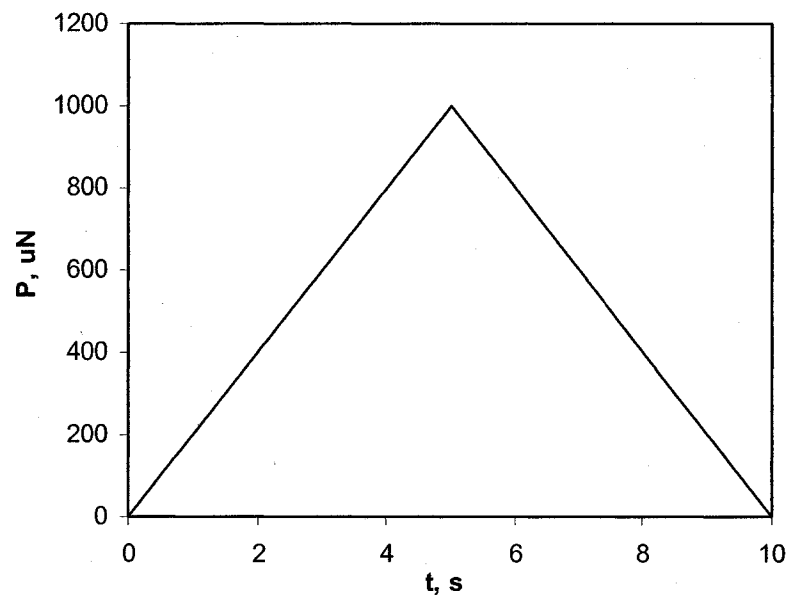


**Figure 3-8. Load function for nanoindentation tests with peak load of 1000  $\mu\text{N}$ .**

For ex situ tests, the setup was similar to **Figure 3-7** but without the power supply system. For in situ indentation tests, the tip can't be seen clearly through the side wall of the cell. Therefore the position of the tip was adjusted properly prior to setting up the cell. Then the tip that was connected to the transducer was moved away from the surface, the cell was put on, and solution was added to the cell. After the tip was repositioned on the surface, a constant current was applied to the specimen by the power supply, and the tip was engaged to perform the indentation tests. The indentation data were analyzed using TriboScope software (Hysitron Inc.).

### **3.5 Experimental calibrations**

#### **3.5.1 Sand degradation**

As pointed out by Hutchings [10], the particles suffer progressive degradation due to their repeated contact with the containing walls. The degradation takes the form of reducing the particle size by attrition and fracture, and the shape of the particles becomes gradually more rounded. Both factors reduce the abrasivity of the particles, and thus the erosion rate. **Figure 3-9** shows the change of the pure erosion rate with time. In the test, each erosion rate was obtained with a new polished sample but the slurry was not renewed. It was found that the erosion rate decreased with time and then became stable after degradation for around 2 h.

This effect was important for investigating the individual material losses during erosion corrosion. Since the erosion rate depended on test duration, the duration for all weight loss tests was identical within each series of tests.

#### **3.5.2 Calibrations for nanoindentation test**

Three calibrations were carried out before all nanoindentation tests were performed, z-axis advanced calibration, electrostatic force constant calibration, and

tip area function calibration. The first two calibrations were system calibrations and were conducted as directed in the manufacturer's manual. For the tip area function calibration, a series of indents were performed on the standard sample, fused quartz, and the tip area function was determined by regression using the software provided. After the calibrations, the standard sample was tested. **Figure 3-10** shows the hardness and reduced modulus value of fused quartz. The theoretical hardness and reduced modulus are 9.5 GPa and 69.6 GPa, respectively. When the indentation depth was lower than 30 nm, the data were more scattered. Beyond this depth, the data were stable and were consistent with theoretical values.

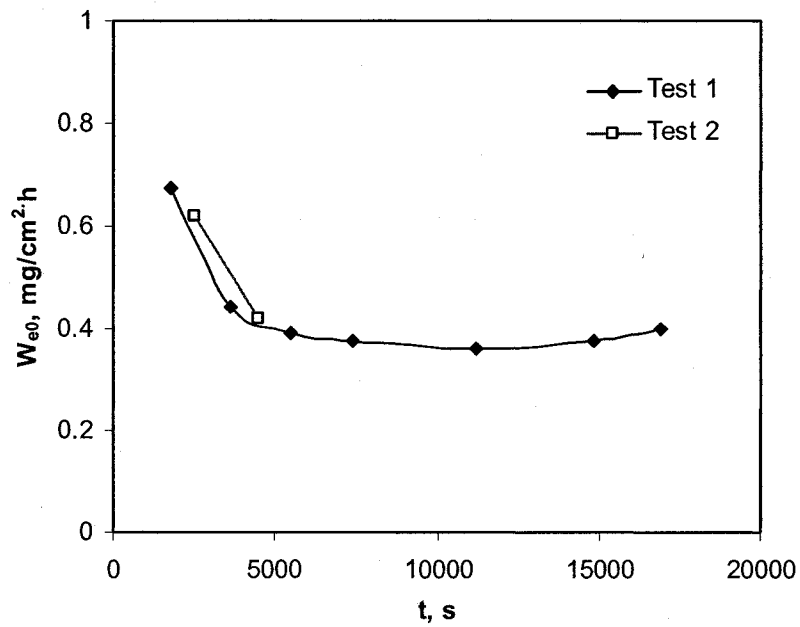


**Figure 3-9. Pure erosion rate of carbon steel A1045 with sand degradation.**

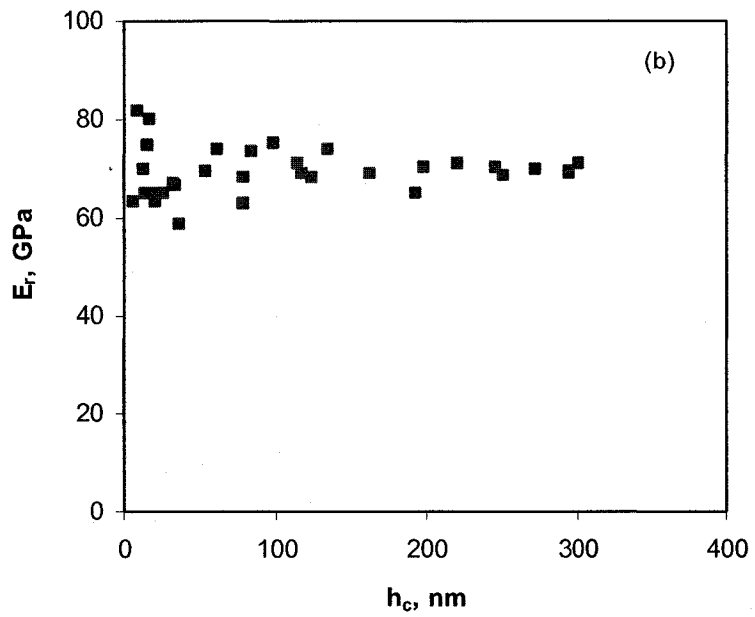
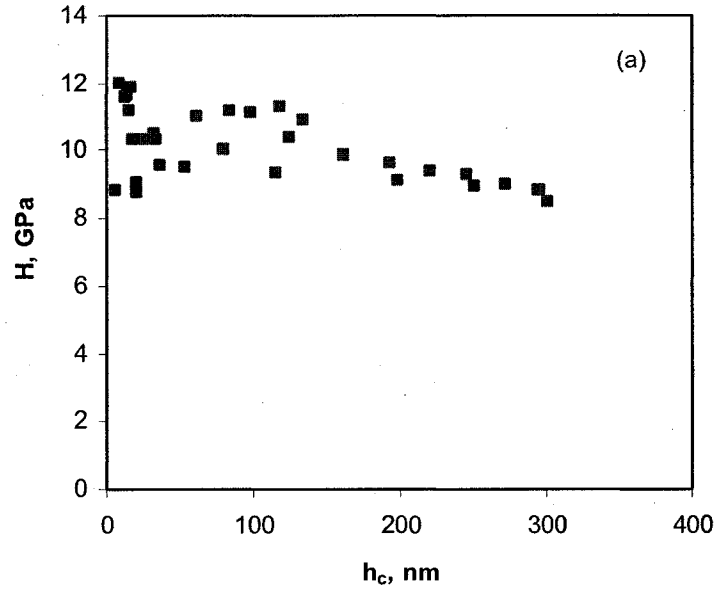


**Figure 3-10. Hardness (a) and reduced modulus (b) of fused quartz.**

## References

- [1] M. Chiba and M. Seo, *Corrosion Science* 44 (10) (2002) 2379.
- [2] M. Seo and M. Chiba, *Electrochimica Acta* 47 (1-2) (2001) 319.
- [3] ASTM Standard Designation: G119-93, *Standard Guide for Determining Synergism Between Wear and Corrosion*, 1993, p.139.
- [4] ASTM Standard Designation G1-90: *Standard practice for preparing, cleaning, and evaluating corrosion test specimens*, 1994, p.9.
- [5] W.D. Callister, *Materials science and engineering: an introduction*, 1994.
- [6] G. Bianchi, A. Cerquetti, F. Mazza, and S. Torchio, *Corrosion Science* 12 (1972) 495.
- [7] Y.F. Cheng and J.L. Luo, *Electrochimica Acta* 44 (1999) 2947.
- [8] J.G. Yu, J.L. Luo, and P.R. Norton, *Electrochimica Acta* 47 (2002) 1527.
- [9] A.W. Bott, *Current Separations* 17 (3) (1998) 87.
- [10] I.M. Hutchings, *The Erosion of Materials by Liquid Flow*, Cambridge, UK, MTI Publication No. 25, Material Technology Institute of the Chemical Process Industries, 1986.

## Chapter 4      Effect of Erosion on Corrosion

As discussed in Chapter 2, the corrosion systems can be categorized into non-passive and passive systems depending on whether or not a protective passive film forms on the metal surface. The corrosion behaviours of these two systems are distinct. As a result, it is reasonable to expect that the effect of erosion on corrosion behaviour would be different for passive systems and non-passive systems, and supporting experimental evidence is found in the literature [1, 2]. However, the difference in the response of a corrosion system to erosion has largely been ignored. Therefore, it is important to investigate the effect of erosion on corrosion in different corrosion systems to understand the interaction between erosion and corrosion.

In this chapter the effect of erosion on electrochemical reaction will be described and discussed for a non-passive corrosion system, and the impact of erosion on the electrochemical processes, the properties of the passive films, and pitting corrosion, will be studied for a passive corrosion system. Since this part of the work investigates aspects of corrosion behaviour, most of the experimental approaches are electrochemical techniques.

### 4.1 In a non-passive corrosion system

A corrosion system consisting of carbon steel A1045 and 0.1 M Na<sub>2</sub>SO<sub>4</sub> solution was chosen as an important industrial example of a non-passive system for the present erosion-corrosion study. **Figure 4-1** shows the potentiodynamic polarization curve for carbon steel A1045 obtained at a rotating velocity of 9000 rpm. The steel showed typical active dissolution behaviour during anodic polarization. The current increased continuously with potential, showing that no passivation occurred in

the present system. Hence, this system was suitable for the investigation of the impact of erosion on corrosion in a non-passive system.

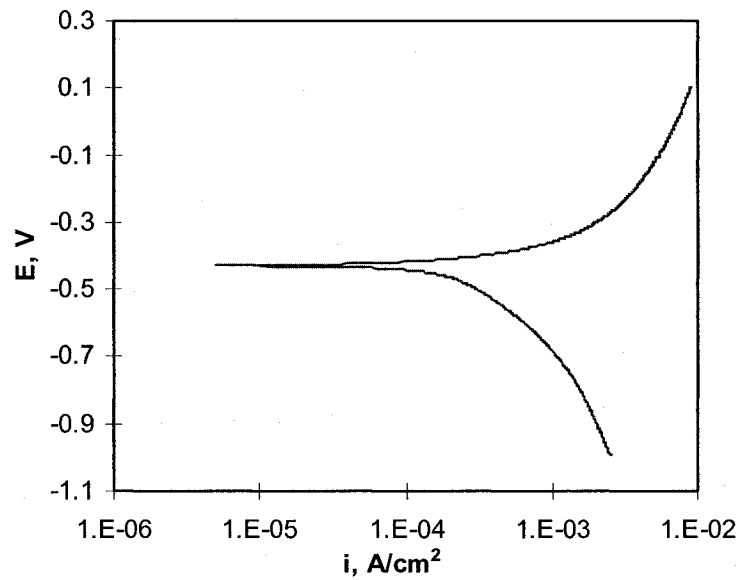


**Figure 4-1. Polarization curve for carbon steel A1045 rotating at 9000 rpm in 0.1 M  $Na_2SO_4$  solution.**

Before studying the interaction between erosion and corrosion, the synergistic effect between these processes in the corrosion system was determined. **Figure 4-2** shows the material loss from steel A1045 in a slurry of 35% sand/0.1 M  $Na_2SO_4$  solution at a rotating velocity of 9000 rpm. The corrosion rate was measured under  $E_c$  using the weight loss method when the sample was rotated at 9000 rpm in the absence of sand. The pure erosion rate was determined in 35% slurry under CP. The synergistic component was calculated by subtracting the corrosion and erosion components from the total weight loss that was measured in 35% slurry at  $E_c$ . A significant synergistic effect between erosion and corrosion was found, the proportion of which contributed as high as 51%. Therefore, in order to develop methods to control the material losses due to erosion-corrosion, it is necessary to investigate the interaction mechanism of these two processes.

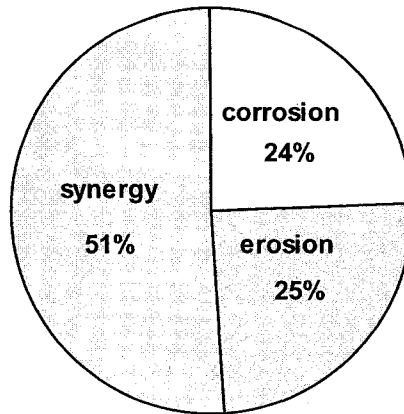


**Figure 4-2. Synergistic effect between erosion and corrosion for carbon steel A1045 in a slurry of 35% sand/0.1 M Na<sub>2</sub>SO<sub>4</sub> solution at 9000 rpm.**

#### **4.1.1 Experimental results**

##### **4.1.1.1 E<sub>c</sub> decay**

A series of electrochemical tests were conducted to investigate the effect of erosion on the corrosion behavior of carbon steel A1045 in a slurry. E<sub>c</sub> decay was tested first. Initially, the sample was immersed in still solution. After 6760 s the sample was rotated at 9000 rpm and then 35% sand was added at 10446 s. **Figure 4-3** shows the E<sub>c</sub> decay curve. E<sub>c</sub> decreased initially with time and then increased slightly until it reached a steady state. The initial decrease was attributed to the decrease in the content of dissolved oxygen. The agitation, however, increased the diffusion of oxygen. The resistance for the cathodic reaction decreased dramatically and E<sub>c</sub> increased correspondingly. The addition of 35% sand induced a transient rise in E<sub>c</sub> but sand impingement did not significantly affect the steady state E<sub>c</sub>.

##### **4.1.1.2 Potentiodynamic polarization**

E<sub>c</sub> will remain constant under two situations: when neither the anodic reaction nor the cathodic reaction is affected by erosion; and when both reactions are

influenced to an equal extent. To determine which case was true for the present system, the potentiodynamic polarization behavior of the test material in the slurries containing three concentrations of sand, 0%, 20% and 35% was examined at 6,000 rpm and 9,000 rpm. The results are shown in **Figure 4-4 (a)** and **(b)**, respectively. Neither the anodic nor cathodic current density was significantly affected by the impingement of the solid particles even in slurries with high sand concentration of 35%. Thus the impingement of solid particles had no apparent effect on the polarization behavior of the present system.

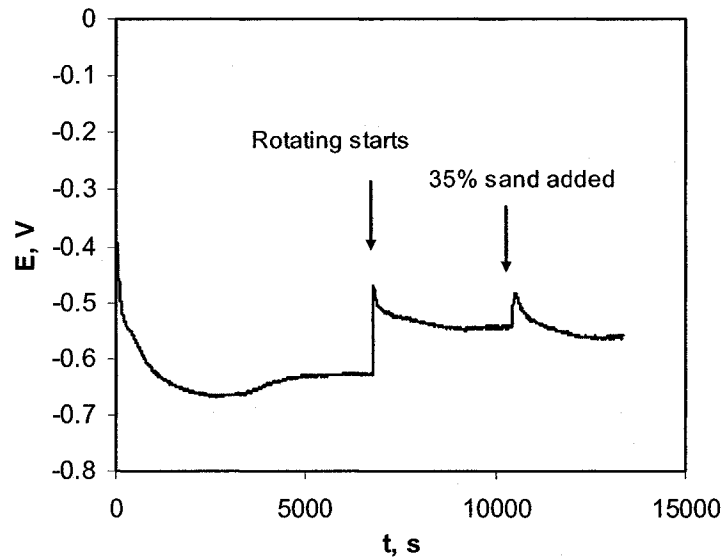


**Figure 4-3. Corrosion potential decay of A1045 steel in 0.1M Na<sub>2</sub>SO<sub>4</sub> solution.**

#### 4.1.1.3 Potentiostatic polarization

The results shown in **Figures 4-3** and **4-4** are contradictory to our expectations based on most prior reports. It is usually expected that when the flow velocity is held constant, the corrosion rate in the slurry erosion process increases with slurry concentration, and that in slurries with identical sand concentration the corrosion rate increases with slurry velocity. The validity of these experimental results was confirmed by two further electrochemical experiments carried out to determine the

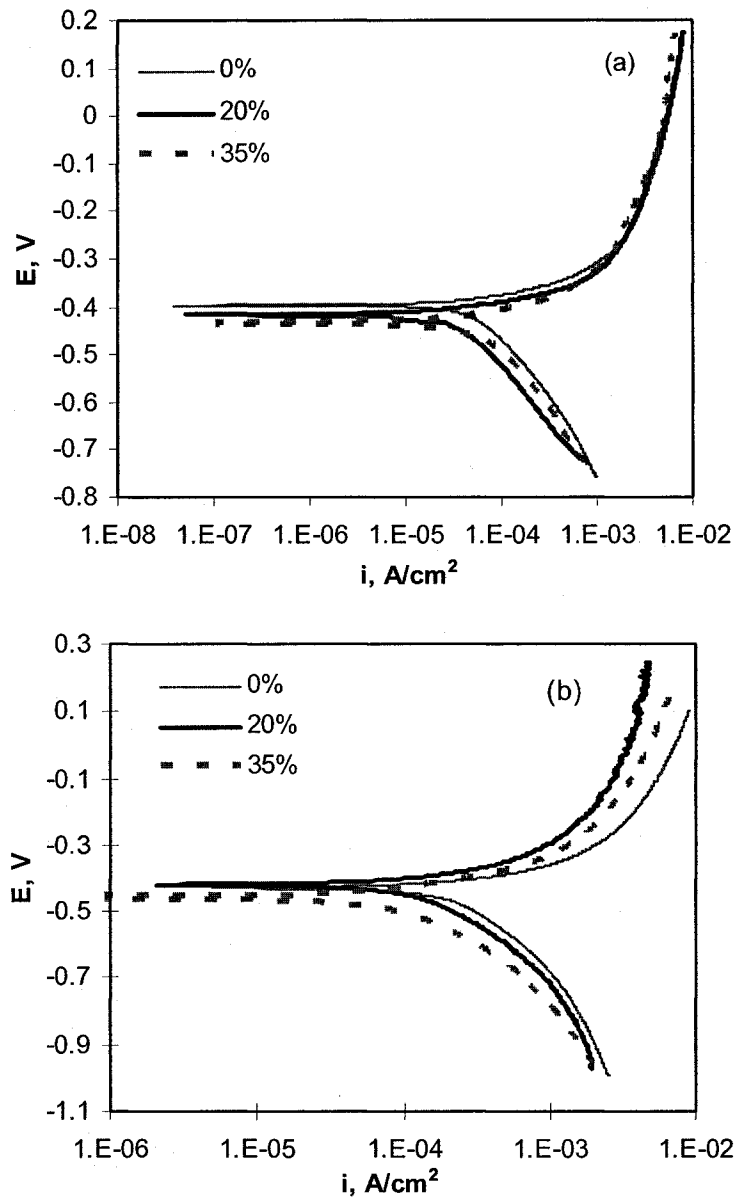


**Figure 4-4. Polarization behavior of carbon steel A1045 in 0, 20 and 35% slurries: (a) rotating at 6000 rpm and (b) 9000 rpm.**

impacts of flow velocity and sand impingement on corrosion behavior. The results from a potentiostatic test at an applied potential of -400 mV are shown in **Figure 4-5**. The test started in still solution, and after a period of time, the sample was rotated at 9000 rpm. At 6340 s 35% sand was added into the solution. When the sample started to rotate, the current density first dropped and then increased gradually. The

disturbance created as a result of sand addition also caused an immediate decrease in current which then gradually increased with time. The current response for sand addition was consistent with the results obtained from the polarization tests. The transient drop of current density after rotation and sand addition was associated with an immediate increase in cathodic reaction rate. The corrosion current then recovered after the transient change that arose after introduction of 35% sand. Consistent with the results shown in **Figure 4-5**, continuing sand impingement did not effect any significant change in corrosion current after stable conditions were re-established at the metal interface.

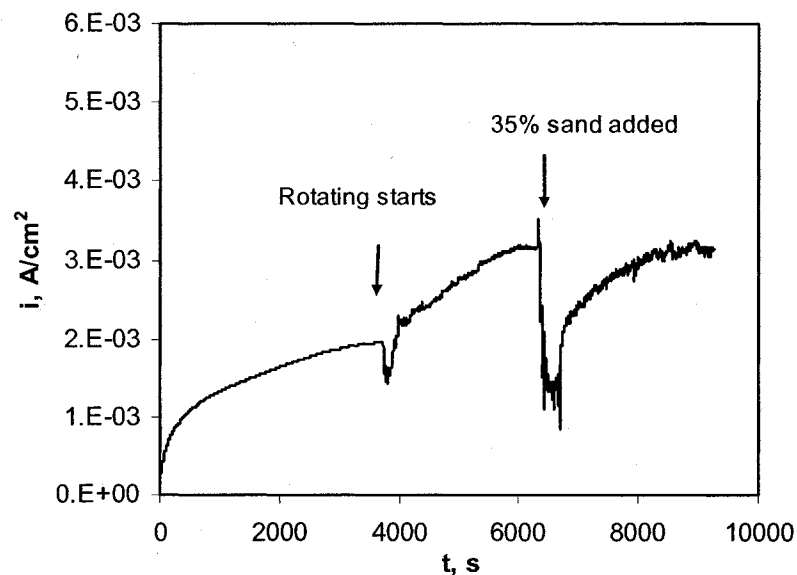


**Figure 4-5.** Current response of carbon steel A1045 arising from initiation of rotating and sand impingement at an applied potential of -400 mV.

#### 4.1.1.4 Polarization resistance

The polarization resistances were measured for carbon steel A1045 at rotation velocities of 3,000, 6,000 and 9,000 rpm and with sand concentrations of 0%, 20% and 35%. As shown in **Figure 4-6**, there were no obvious variations in polarization

resistance under the various conditions. No data were obtained for the condition of 3000 rpm and 35% sand, because the sand was incompletely agitated at such a low velocity.

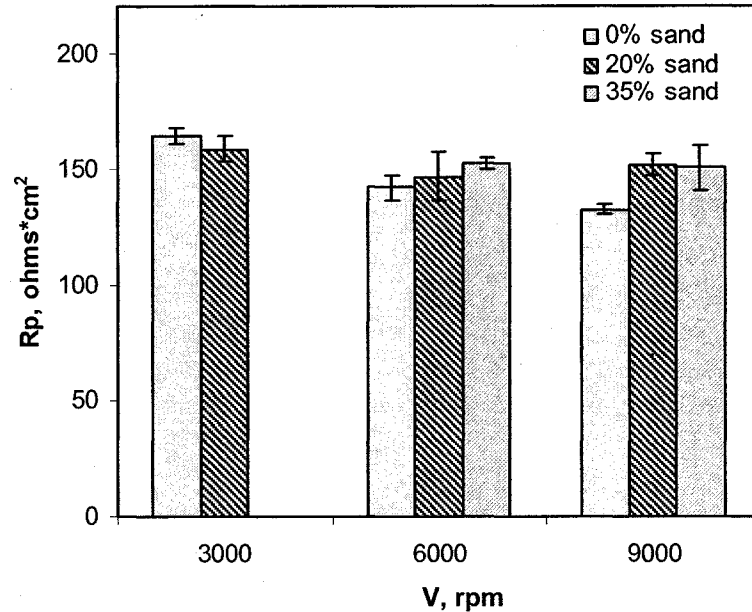


**Figure 4-6. Polarization resistances of carbon steel A1045 in slurries as a function of velocity and sand concentration.**

#### 4.1.2 Discussion

The experimental results showed that the impingement of sand particles had no significant effect on the corrosion behaviour of carbon steel in the present active dissolution system. This result was not expected, as it had not previously been pointed out in the literature for similar active systems [1, 2]. Hence, the current results require explanation. As mentioned in Section 2.1.1 of Chapter 2, the corrosion process includes both a mass transfer step and an electrode reaction step. The effect of erosion on corrosion can be analyzed from consideration of these two steps.

#### 4.1.2.1 Effect of erosion on mass transfer

Generally, accelerating the mass transfer rate has been accepted as explaining the promotive effect of erosion on corrosion process [1, 3, 4]. First, the disturbance of solid particles in flow field enhances the transport process of both reactants and corrosion products, and thus promotes the corrosion process. It has been reported that the mass transfer rate in a slurry, a two-phase flow system, is higher than that in solution, a single phase flow system [5]. However, comparison of the polarization curves at different velocities (**Figure 4-7**) shows that the current densities of the carbon steel in 0.1 M Na<sub>2</sub>SO<sub>4</sub> solution were very large, and thus the electrochemical reaction rate was not changed significantly when the velocity was increased. This suggested that mass transfer in solution at high flow velocity was not the rate-determining step. The system was controlled by active dissolution, although the uncompensated solution resistance did cause the curves to deviate from the Tafel linear relationship to a minor extent. Hence, for an active system, although the disturbance by sand accelerated mass transport at the interface, it did not affect the corrosion rate significantly.

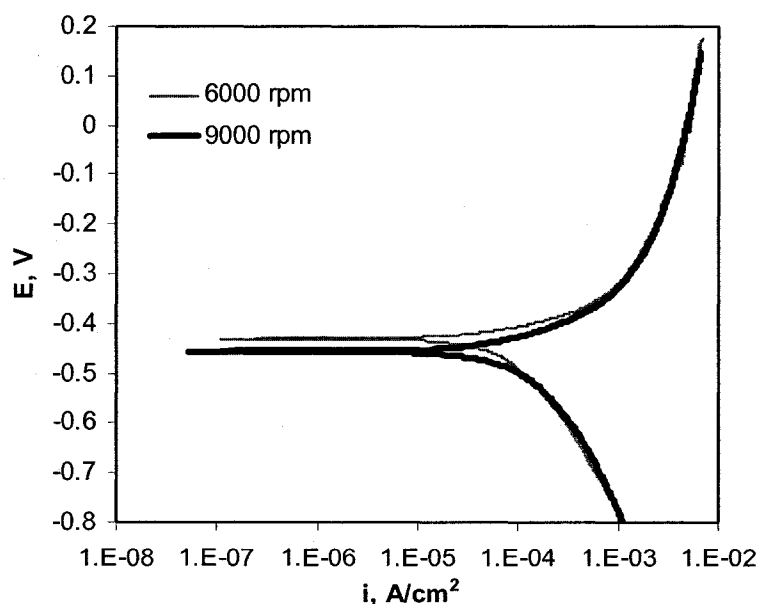


**Figure 4-7. Effect of rotating velocity on polarization behavior of carbon steel A1045 in a slurry containing 35% sand.**

#### 4.1.2.2 Effect of erosion on surface film

Another factor effecting corrosion rate is the removal of corrosion product by the impingement of solid particles on the electrode surface. In aqueous environments, especially in near neutral or alkaline solution, the dissolved metallic ions are readily hydrated, and so some corrosion product will deposit on the electrode surface. When deposited corrosion products form a strong coating they can retard the mass transfer process and thus reduce the corrosion rate. As discussed in Section 2.3.1.2 of Chapter 2, the impact of sand particles can break and remove the corrosion product or film, leading to exposure of fresh metal surface to the corrosive environment, and so the surface will suffer further severe damage due to corrosion. Scratch electrode tests were carried out to simulate this effect in the present system. The sample surface was scratched with a pointed-tip PTFE after the current density of the sample had stabilized. **Figure 4-8 (a)** shows the effect of scratching on the current of carbon steel A1045 at -400 mV, and **Figure 4-8 (b)** presents the typical morphology of the scratches. It was found that the scratching did not cause a significant change in the transient current response. The current responses to scratching illustrated in the small figure embedded in **Figure 4-8 (a)** showed that the current density decreased immediately after scratching and then increased. The small initial drop was attributed to accelerated oxygen diffusion caused by the scratching process. To eliminate the influence of oxygen, the scratch test was repeated with air bubbled to the electrode surface. **Figure 4-9** shows the current response of carbon steel at 20 mV vs.  $E_c$ . Again, there was no apparent current increase upon scratching. Thus the dissolution rate of the steel remained unchanged despite scratching. This effect was attributed to the nature of the corrosion products. The corrosion products formed in this active dissolution system could be very loose, non-protective, and even soluble, so the removal of corrosion products by the impingement of solid particles did not strongly affect the already rapid dissolution rate.

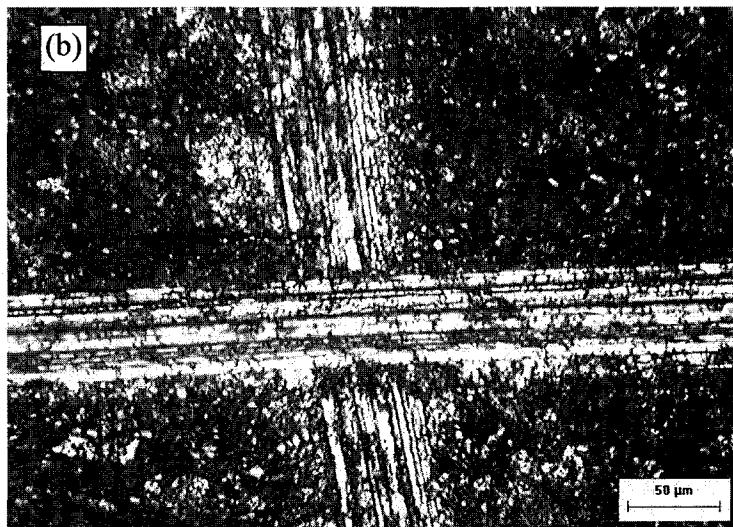
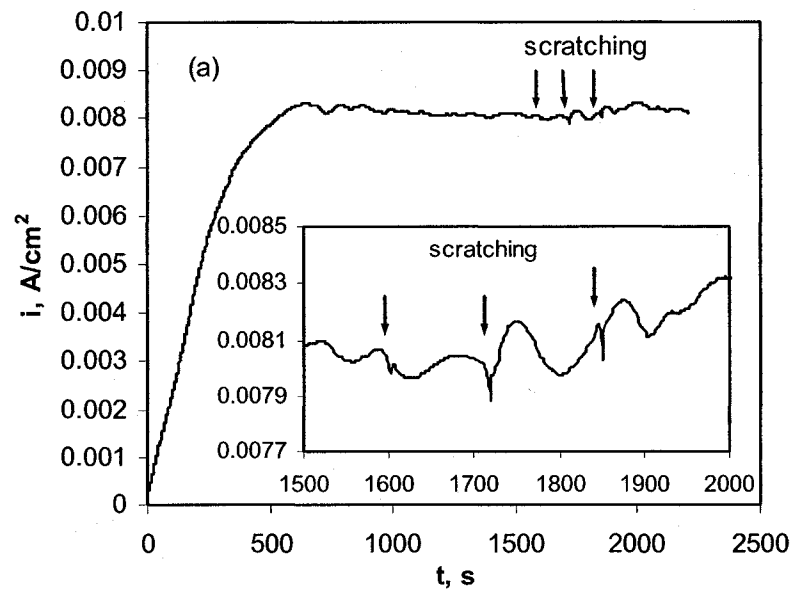


**Figure 4-8. Effect of scratching on carbon steel A1045 under constant potential: (a) Current density at -400 mV, (b) Micrograph of the sample after scratching.**

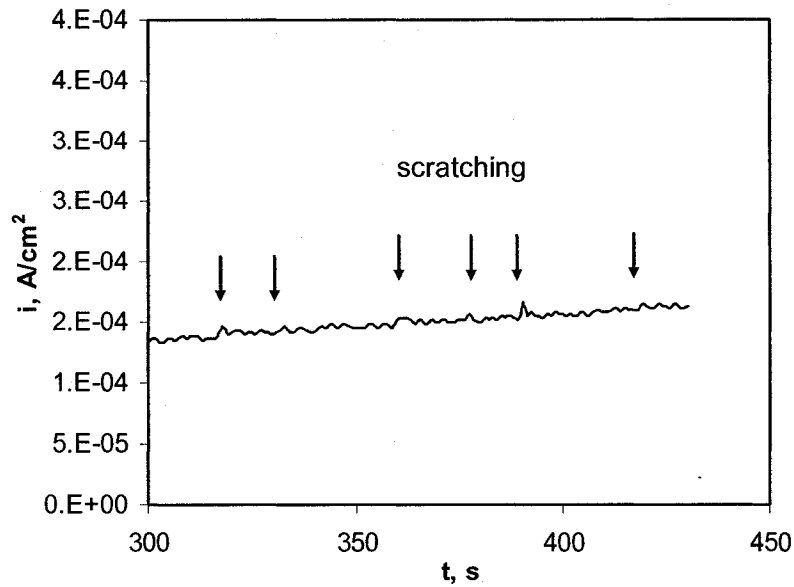


Figure 4-9. Current response for carbon steel A1045 in scratch test at 20 mV vs.  $E_c$  with air bubbled at sample surface.

#### 4.1.2.3 Effect of deformation on electrode reaction

In addition to the influence on mass transfer process and corrosion product, the deformation effect from erosion on the electrode reaction was also considered [6]. The effect of deformation processes has also been analyzed from a thermodynamic perspective [7, 8]. When a metal is corroding in aqueous solution, as a stress is applied to the electrode the anodic dissolution current density can be expressed as [8]

$$i_{a,\sigma} = k_{\sigma} i_a \quad (4-1)$$

where  $i_{a,\sigma}$  is the anodic dissolution current density in the presence of stress, and  $k_{\sigma}$  is a stress factor that characterizes the influence of stress on anodic dissolution rate. When the applied stress causes elastic deformation, it will result in a volume change of the metallic electrode, and the elastic energy will be stored in the electrode. Meanwhile, if plastic deformation is caused by the applied stress, the density of crystalline defects such as vacancies and dislocations will increase, and thereby the

plastic strain energy is stored in the metallic electrode. Hence, the stress factor can be expressed as [8]

$$k_{\sigma} = k_e k_p \quad (4-2)$$

where  $k_e$  and  $k_p$  are elastic stress factor and plastic stress factor, respectively.

By substituting the mechanical property parameters into the expressions for  $k_e$  and  $k_p$  [8], it was calculated that  $k_e = 1.03$  and  $k_p = 1.08$  for carbon steel A1045, and so the value for the stress factor  $k_{\sigma}$  was 1.11. These values mean that the possible maximum influence of stress factor on the corrosion rate of carbon steel A1045 is no more than 11%. Mao et al. [7] calculated  $k_{\sigma} = 1.1$  for steel X80, and Lu and Luo [8] also found that  $k_{\sigma}$  was less than 1.20 for austenitic stainless steels. These theoretical results were consistent with the experimental observations, and indicated that there was only a minor effect of applied stress on the anodic dissolution rate.

The above results showed that impingement of the sand does not significantly alter the corrosion behavior of the carbon steel. This interesting phenomenon has not been reported previously in the literature regarding erosion-corrosion study [9]. However, there are reported data supporting this finding, although no clear conclusions have previously been drawn. For example, Madsen [2] measured the polarization curves of type 316 stainless steel, steel A514 and REM 500 in 0.06 M  $\text{Na}_2\text{SO}_4$  solution and the results showed that the passive current of stainless steel 316 increased dramatically with the slurry concentration, while for A514 and REM 500, which showed active dissolution in the slurry, there was no apparent dependence of corrosion rate on slurry concentration. Zheng et al. [1] investigated the polarization behaviour of stainless steel 321, 316L, F5 and carbon steel X60 in 10 wt%  $\text{H}_2\text{SO}_4$  + 15 wt% corundum sand. The first three steels showed passive behaviour and the last one showed active dissolution behaviour in the slurry. As a result, the passive current density of the first three steels increased with the velocity but the anodic current density of X60 was not affected by the velocity. Also, the impingement of solid particles did not appear to change the polarization behaviour of cast iron [10].

### 4.1.3 Summary

The electrochemical tests, the scratch and tensile simulation tests, and the theoretical estimations based on thermodynamics showed that in the non-passive corrosion system, when the corrosion was controlled by active dissolution of metallic material, the erosion process did not have any significant acceleration effect on the corrosion rate. This was because (a) the mass transfer step was not the rate-determining step, (b) the corrosion products formed on the surface were not protective, and (c) the deformation or residual stresses caused by impingement of sand did not affect the corrosion behaviour in any significant way.

The present report is the first time the effect of erosion on corrosion in an active system has been discussed. Understanding the interaction between erosion and corrosion is of importance because corrosion systems controlled by active dissolution are very common in industrial applications where most metallic materials are non-passive, and the high flowing environment makes mass transfer resistance insignificant. Thus, the present investigation has wide significance for analyzing material losses arising from erosion-corrosion in industrial processes.

## 4.2 In a passive corrosion system

A corrosion system consisting of carbon steel A1045 and a  $\text{H}_3\text{BO}_3 + \text{Na}_2\text{B}_4\text{O}_7 \cdot 10\text{H}_2\text{O}$  solution was chosen for investigation of erosion-corrosion in passive systems. The reason for choosing this system was that researchers have reported several results on passivation of this system, which provided valuable background and complementary information for the present erosion-corrosion study. **Figure 4-10** presents the potentiodynamic polarization curve for the passive system at a rotating velocity of 9000 rpm. The carbon steel showed typical passive behaviour during anodic polarization. When the potential was 100 mV higher than  $E_c$ , the electrode surface was passivated and the current was substantially independent of potential. At around 0.93 V, the current increased quickly with potential, which was attributed to the evolution of oxygen from the solution. With a stable and wide passive zone, this system was suitable for investigation of erosion-corrosion in a passive system.

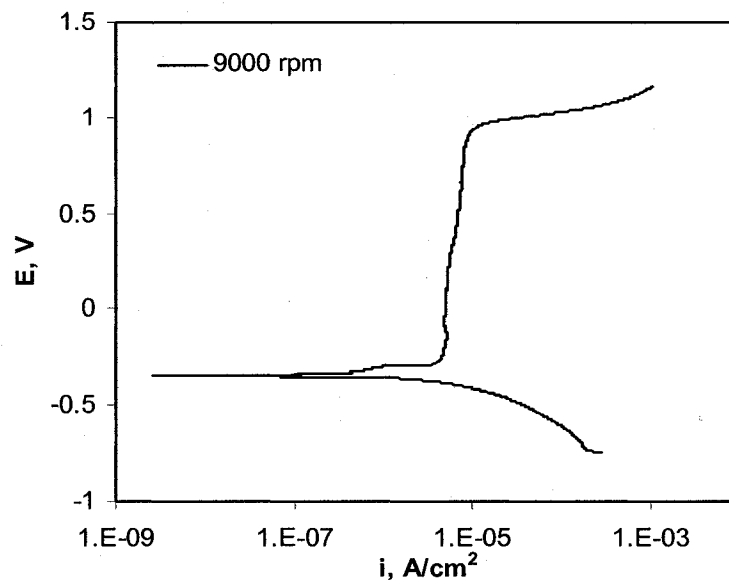


**Figure 4-10. Polarization curve of carbon steel A1045 in borate buffer solution.**

#### 4.2.1 Effect of erosion on passivation of carbon steel

It has been reported that the removal of surface passive film in passive corrosion systems can result in a dramatic increase in corrosion rate [11-13]. When the concentration or velocity of the slurry is sufficiently high, impingement of solid can even eliminate the passive zone [14].

However, many investigations on passive systems in erosion-corrosion processes have focused on the increment of weight loss with slurry parameters. Few studies paid attention to the influence of mechanical degradation on the electrode reaction kinetics and properties of passive films [15, 16]. The electrochemical impedance spectroscopy, a very useful technique for determining the fundamental parameters relating to the electrode reactions and properties of the passive film, has been widely employed in metal corrosion studies, but has limited application in erosion-corrosion studies [17].

For these reasons, in this part of the work the effect of erosion on corrosion behaviour was investigated using an electrochemical impedance spectroscopy and then analyzed based on the equivalent electrical circuit.

##### 4.2.1.1 Experimental results

###### 4.2.1.1.1 $E_c$ measurement

In addition to the direct impingement effect of sand particles on the electrode surface, the influence of media flowing over the surface also was investigated. **Figure 4-11** shows the  $E_c$  decay curve for carbon steel A1045 in borate solution. The test commenced using a still solution. After  $E_c$  reached a steady value, the sample was rotated at a velocity of 9000 rpm.  $E_c$  increased when the sample was rotated. This was attributed to an increase in the diffusion rate of dissolved oxygen in solution, resulting in a decrease in the resistance for the cathodic reaction. However, the addition of 35%

sand into the flowing solution induced a dramatic drop in  $E_c$ , suggesting a significant effect of particle impingement on the anodic process.

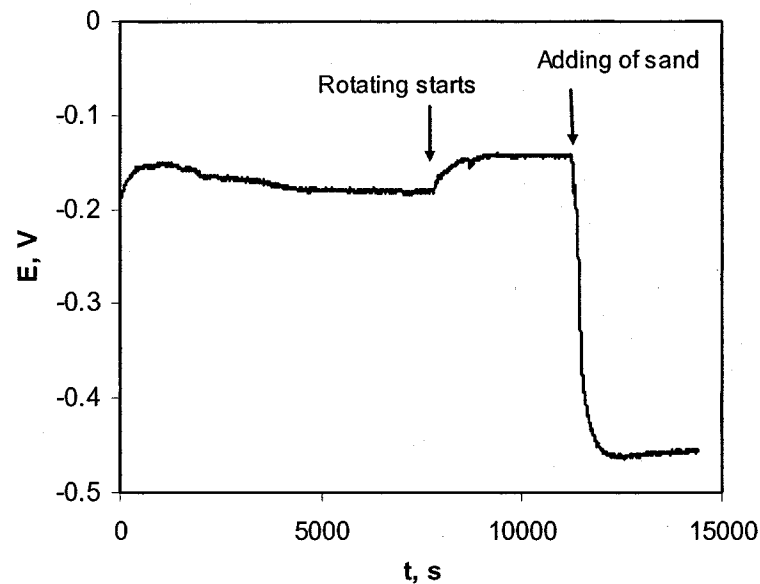


**Figure 4-11. Corrosion potential decay of carbon steel A1045 in the borate solution.**

#### 4.2.1.1.2 Potentiostatic curve measurements

Potentiostatic curves were obtained to investigate the effect of solution velocity and sand impingement on corrosion behavior of the carbon steel. **Figure 4-12** presents the current curves of A1045 at an applied potential of 200 mV in borate solution. When no sand particles were present, the current decreased with time and reached a stable value after a period of time, indicating the formation of a passive film. There was no important dependence of the steady state currents of the carbon steel on velocity. In contrast, the current increased with time initially and then rapidly attained stable values in flowing sand slurry. This behaviour was similar to that of the active system shown in **Figure 4-5**, suggesting a role of active dissolution in the present electrode process. Further, the current increased with slurry concentration, which clearly demonstrated that there was an effect of erosion on corrosion.

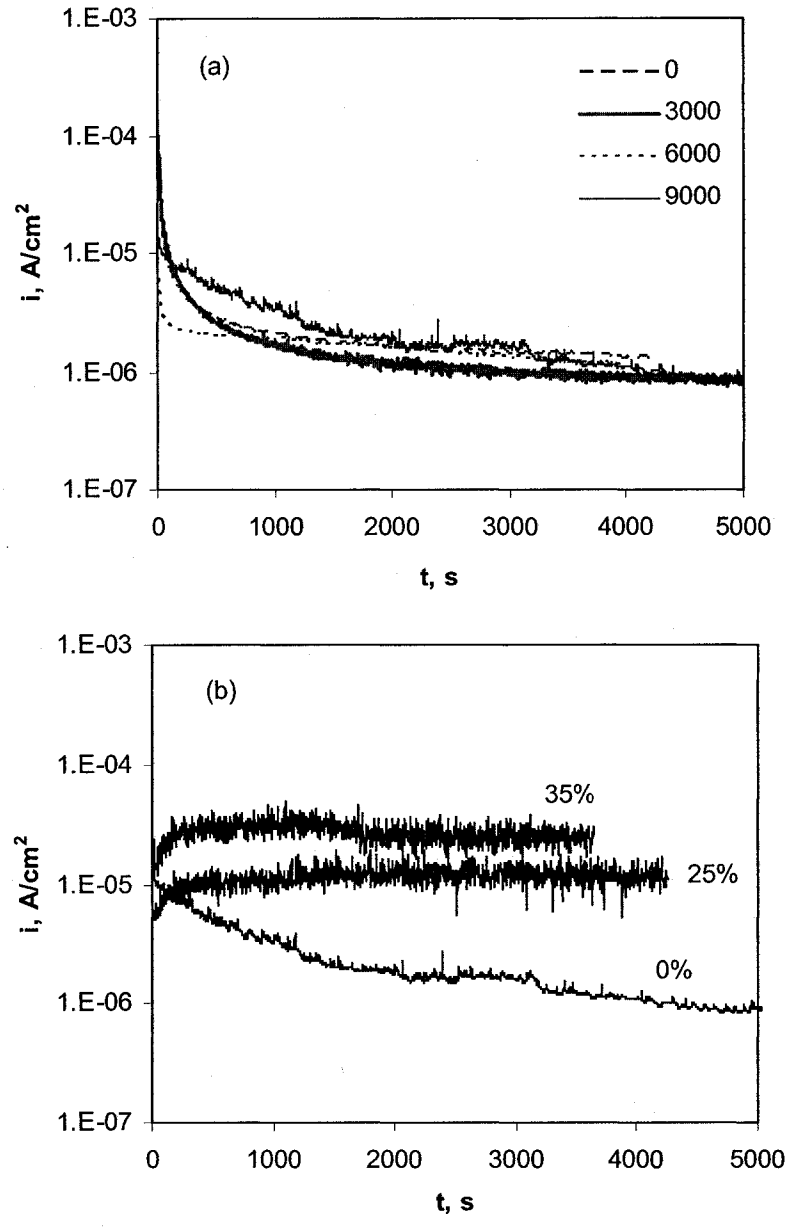


**Figure 4-12. Potentiostatic curves for carbon steel A1045 at an applied potential of 200 mV in borate solution: (a) as a function of velocity; (b) as a function of sand concentration at 9000 rpm.**

#### 4.2.1.1.3 Polarization curve measurements

**Figure 4-13 (a)** shows the potentiodynamic polarization curves obtained in solution at different velocities. The corrosion potential of carbon steel A1045 increased slightly with an increase in velocity. For the anodic reaction, there was no apparent dependence of passive current on solution velocity, in agreement with the potentiostatic test results. Thus, the influence of solution flowing on the electrode process was mainly on the cathodic reaction, which can be observed from the shifting of the cathodic polarization curves.

The polarization curves obtained in the slurries with different sand concentrations at a constant rotating velocity of 9000 rpm are shown in **Figure 4-13 (b)**. The cathodic reaction rate was almost independent of sand concentration, consistent with the result shown in **Figure 4-13 (a)** where the cathodic reaction rate did not increase markedly as the rotating velocity was raised from 6000 rpm to 9000 rpm. On the other hand, the passive current density of the carbon steel increased with slurry concentration monotonically and significantly, which explained the dramatic decrease of  $E_c$  in **Figure 4-11** and the higher current in **Figure 4-12 (b)**. The increase in passive current was directly attributed to the damaging effect of sand impinging on the passive film. However, the polarization curves in the slurry still showed a stable passive region in which the measured current did not increase with potential, and the potential range of the passive region did not depend on the sand concentration. This suggested that the anodic electrode process did not transform to a purely active dissolution process, although the breaking down and repair of the passive film was repeated on the electrode surface. From the view point of statistics, the electrode can be regarded as being covered by a passive film.

#### 4.2.1.1.4 Scratch tests

Scratch tests were conducted in still solution under 200 mV to simulate the impingement process and to understand the damaging effect of sand particles' impinging on passive film. The obtained current curve is shown in **Figure 4-14**.

When the current density had stabilized, the sample surface was scratched after 620 s, 710 s and 725 s. The current density increased immediately after each scratching and decreased subsequently. Similar to sand impingement, the scratching ruptured the

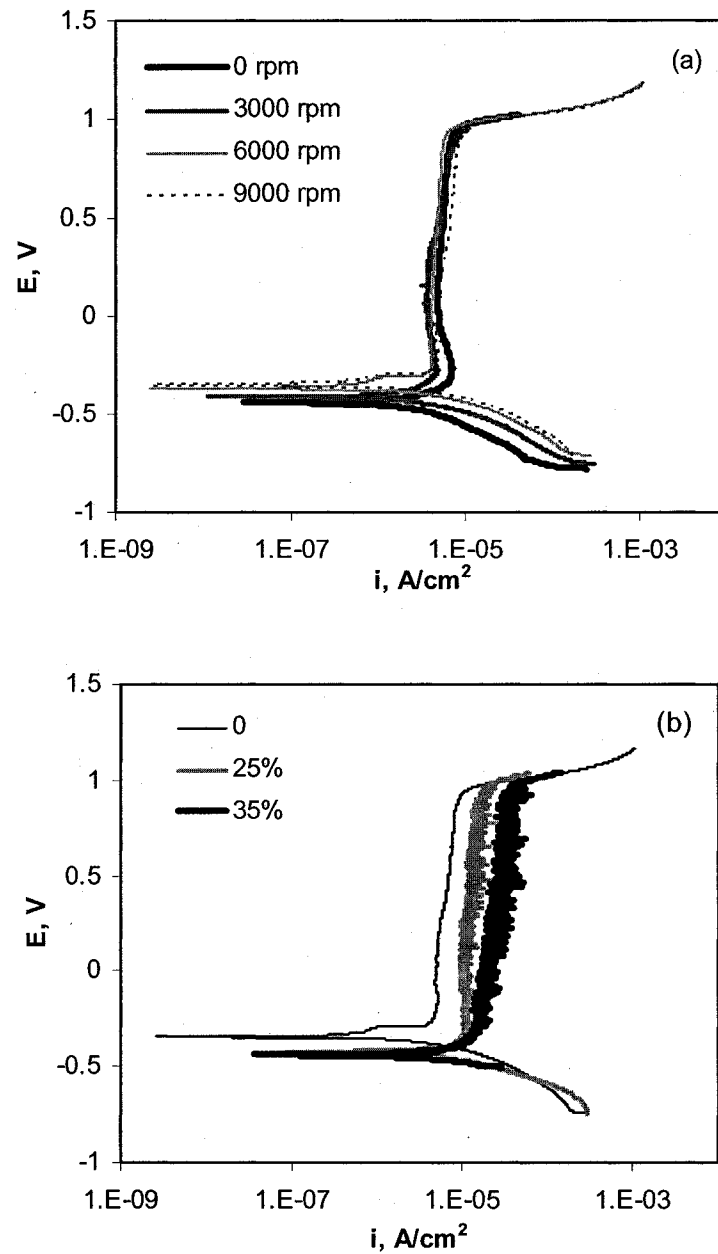


**Figure 4-13. Potentiodynamic polarization curves of carbon steel A1045 in borate solution: (a) in flowing solution at different velocities; (b) in slurries with different sand concentrations at 9000 rpm**

passive film formed on the electrode surface and thereby exposed fresh metal to the corrosive environment. This resulted in a sudden but temporary increase in the electrochemical dissolution rate. The current density decreased gradually with time owing to the re-passivation process of the passive film. The effect of chloride ions will be discussed later.

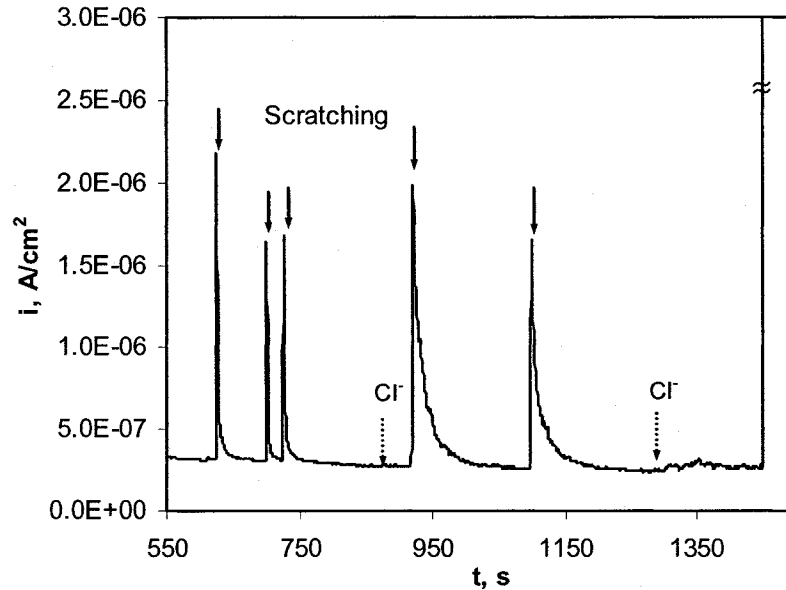
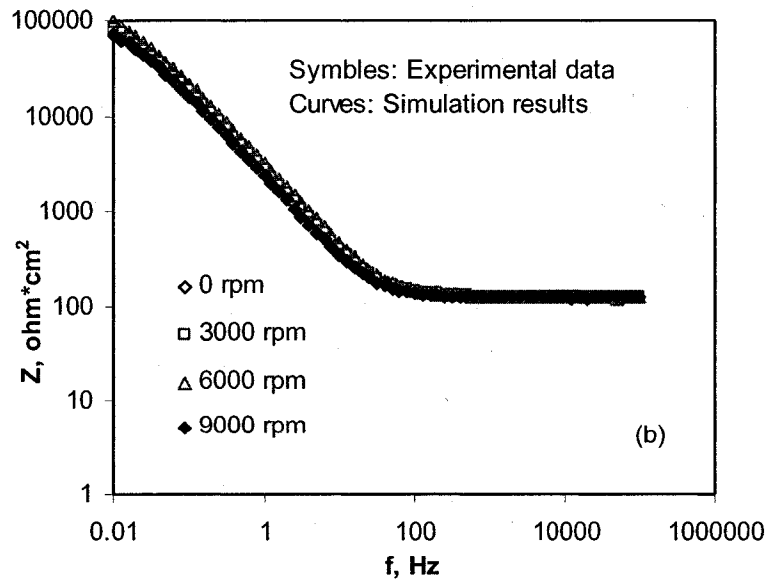
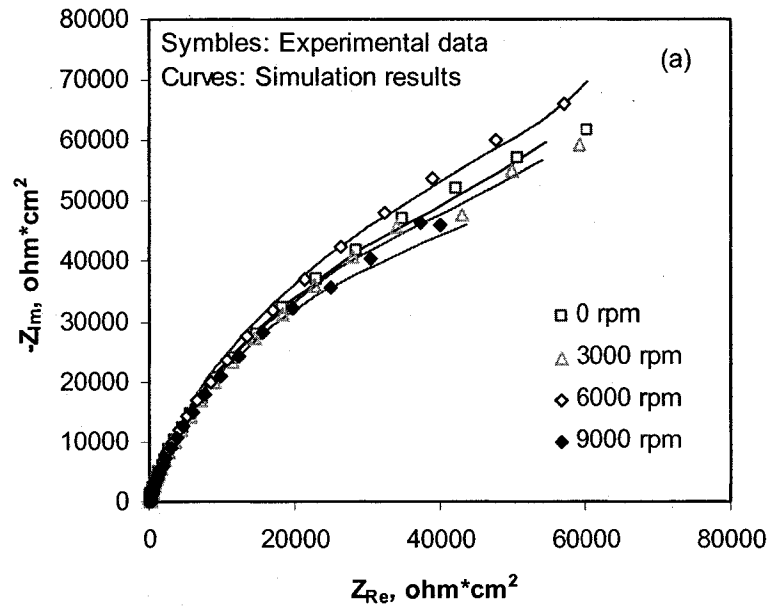


**Figure 4-14. Current density curves for carbon steel A1045 in borate solution during scratch test at an applied potential of 200 mV.**

#### 4.2.1.1.5 Electrochemical impedance measurements

The impedance spectrum technique was employed to investigate the electrochemical process. The experimental data were modeled using an equivalent electrical circuit, and the effect of erosion on corrosion was analyzed in terms of their impact on the circuit elements. **Figure 4-15** shows the impedance data obtained in solution at different flowing velocities under  $E_c$ , and the data are plotted as Nyquist and Bode diagrams. Each Nyquist plot comprised part of a distorted semicircle. The diameters of the circles appeared to be independent of the solution velocity. Since the diameter of the semicircle was determined by the charge transfer resistance of the electrode, this result was consistent with the potentiodynamic polarization

measurements, and showed that the flowing velocity of the media did not influence the kinetics of the electrode reaction in the present system. On the Bode plot, the impedance showed capacitive behaviour at frequencies of around 1 Hz: the slope of the logarithm of the impedance vs. frequency was close to -1 and the phase angle was close to  $90^\circ$ . Similar spectra also have been reported for iron [18], stainless steel [19] and chromium [20].



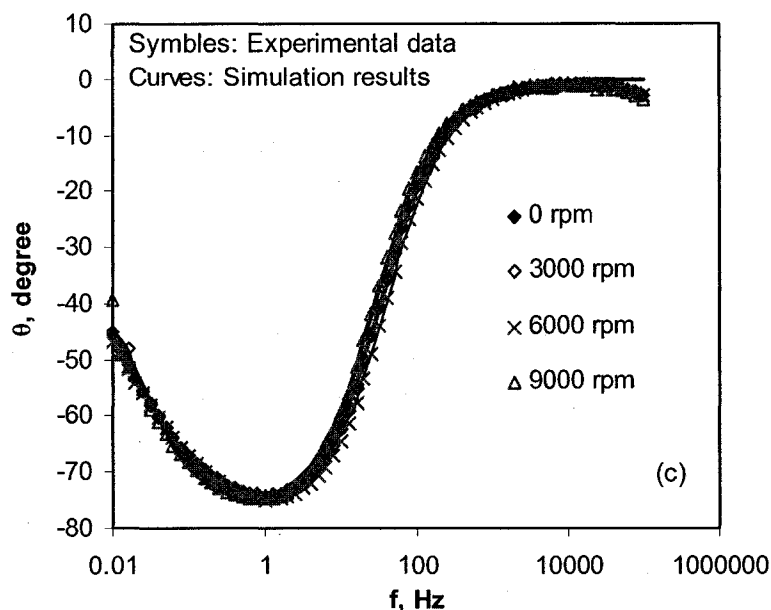
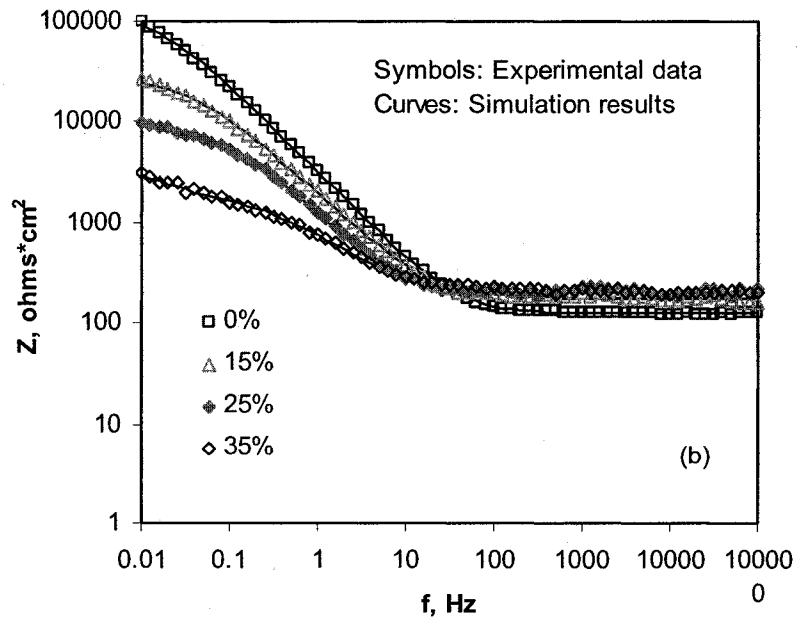
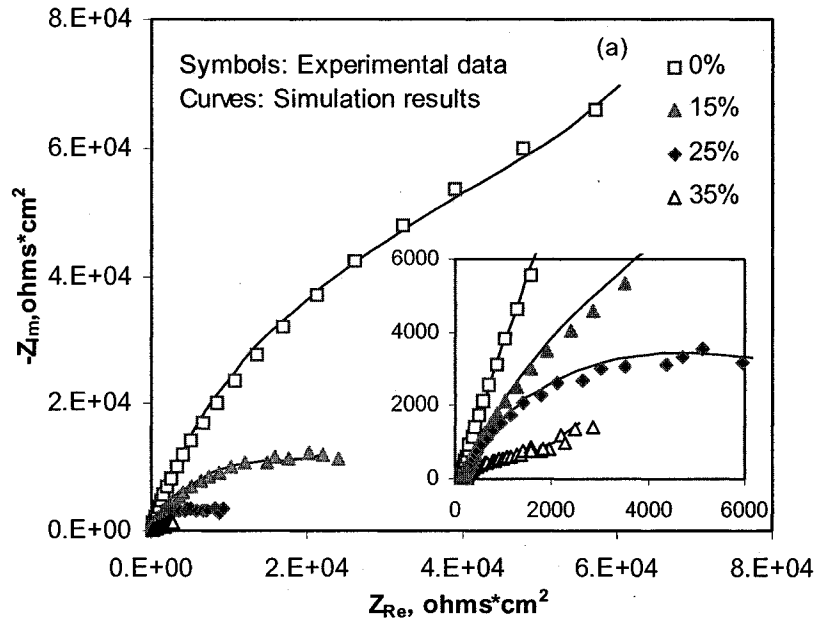


**Figure 4-15. Nyquist plots (a) and Bode plots (b & c) for carbon steel A1045 in borate solution at different velocities.**

The impedance data obtained at  $E_c$  in slurries with different sand concentrations at a rotating velocity of 6000 rpm (**Figure 4-16**) are similar to those obtained in flowing solutions, and the Nyquist plots in the slurry were again parts of distorted semicircles. The diameter of the semicircles, however, decreased markedly with increased sand concentration. On the Bode plot, the impedance and the phase angle at low frequency decreased with an increase in the sand concentration, indicating a transition from capacitive to resistive behaviour.

Several equivalent circuits were tried to fit the obtained impedance data. The equivalent circuit proposed by Martini and Muller [21] for the passive film on iron in borate solution was found to provide the best fit. As shown in **Figure 4-17**, the circuit consisted of two resistors,  $R_{sol}$  and  $R_f$ , and two constant phase elements (CPE),  $CPE_1$  and  $CPE_2$ . As discussed by Martini and Muller [21], choosing this circuit was a compromise that provided a reasonable fit of the experimental data while maintaining the number of circuit elements at a minimum, and associating every element to an appropriate physical meaning in terms of the electrochemical reaction. In the circuit,  $R_{sol}$  represented the electrolyte resistance;  $CPE_1$  was related to the ionic species'

transport across the film;  $R_r$  represented the charge transfer resistance at the electrode and  $CPE_2$  was related mainly to the film capacitance. The curves fit with this equivalent circuit are also shown in **Figure 4-15** and **Figure 4-16**. The simulated curves fitted the experimental data very well, which showed that this equivalent circuit was suitable for describing the electrochemical process in the present flowing solution and slurry.



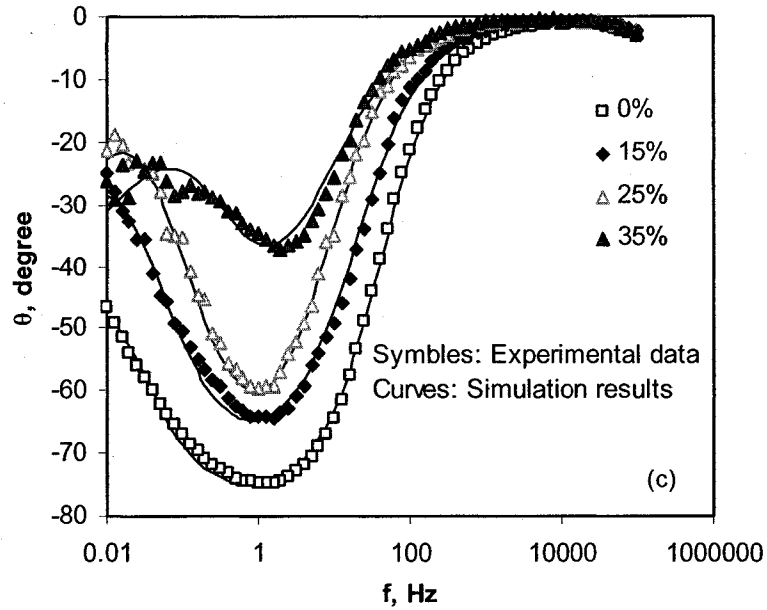


Figure 4-16. Nyquist plots (a) and Bode plots (b & c) for carbon steel A1045 in slurries with different sand concentrations at 6000 rpm.

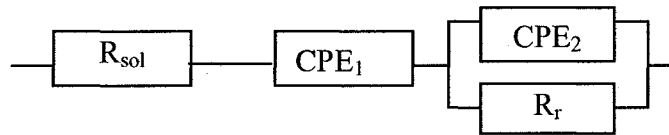


Figure 4-17. Equivalent circuit for the carbon steel/borate solution system.

For CPE, the impedance  $Z_{CPE}$  is defined by [22]:

$$Z_{CPE} = b(j\omega)^{-a} \quad (4-3)$$

where  $b$  is a constant, and  $a$  is defined as  $a = 1 - 2\beta'/180$  where  $\beta'$  is the depression angle. The exponent  $a$  can reflect the deviation of the passive film from an ideal capacitor, and its value always lies between 0.5 and 1. For  $a = 1$ , the CPE describes an ideal capacitor; for  $a = 0.5$ , the CPE represents a Warburg impedance with diffusion character.

Tables 4-1 and 4-2 present the parameters determined by fitting the impedance data with the equivalent circuit. On this basis, the effect of erosion on the corrosion behaviour was analyzed through comparing values for the equivalent circuit elements under different experimental parameters. Figure 4-18 shows the charge resistance, the reciprocal of the passive film capacitance, and the exponents of CPE<sub>1</sub> ( $a_1$ ) and CPE<sub>2</sub> ( $a_2$ ) as a function of flowing velocity. As expected from the impedance data, these fitted electrochemical parameters were approximately independent of velocity. The mean value of  $a_2$  was 0.866, from which the depression angle was calculated to be 12°, which meant that the passive film behaved as a capacitor in the present system.

**Table 4-1. Equivalent circuit parameters as a function of velocity.**

Velocity, RPM	$R_{sol}$ ohms*cm <sup>2</sup>	$R_r$ ohms*cm <sup>2</sup>	CPE <sub>1</sub> F/cm <sup>2</sup>	CPE <sub>2</sub> F/cm <sup>2</sup>	$a_1$	$a_2$
0	127.008	71032.5	0.000356	9.35E-05	0.894	0.86158
3000	129.53	75631.2	0.000363	9.29E-05	0.9036	0.8641
6000	131.7015	74686.5	0.000268	8.23E-05	0.8985	0.86645
9000	125.622	67599.1	0.000501	0.000104	0.9067	0.8683

**Table 4-2. Equivalent circuit parameters as a function of sand concentration.**

Sand	$R_{sol}$ ohms*cm <sup>2</sup>	$R_r$ ohms*cm <sup>2</sup>	CPE <sub>1</sub> F/cm <sup>2</sup>	CPE <sub>2</sub> F/cm <sup>2</sup>	$a_1$	$a_2$
0	131.7015	74686.5	0.000268	8.23E-05	0.8985	0.86645
15%	164.9655	23023.35	0.001263	0.000122	0.8304	0.8273
25%	195.552	7304.85	0.003354	0.000183	0.77745	0.85788
35%	201.033	1113.525	0.002534	0.000414	0.5715	0.77275

The electrochemical parameters fitted using the above equivalent circuit are shown in **Figure 4-19** as a function of sand concentration. Impingement of solid particles significantly reduced the charge transfer resistance, which corresponded to an increase in passive current. In addition, the reciprocal of the film capacitance decreased linearly with the sand concentration. The capacitance for a parallel-plate capacitor is defined as [23]:

$$C = \frac{\epsilon_0 \epsilon A_c}{d_c} \quad (4-4)$$

where  $A_c$  is the capacitor surface area and  $d_c$  the thickness of the capacitor. Hence, for the present system, the reciprocal of the film capacitance was proportional to the thickness of the passive film. The decrease in reciprocal capacitance with increase in slurry concentration suggested that impingement of sand decreased the effective thickness of the passive film formed on the electrode surface [18]. However, Equation (4-4) shows that an increase in electrode surface can also result in an increase in capacitance. Consequently, it was necessary to also determine whether there was a comparable change in area of the work electrode. During the slurry erosion process the impingement of sand particles resulted in a larger working electrode area. From the change of solution resistance it was clear that the proportional increase in area was considerably less than the substantial decrease in the reciprocal capacitance. Therefore, with the assumption that the passive film formed in flowing solution and slurry had similar dielectric constants, it was reasonable to infer that the thickness of the passive film decreased with flowing slurry concentration.

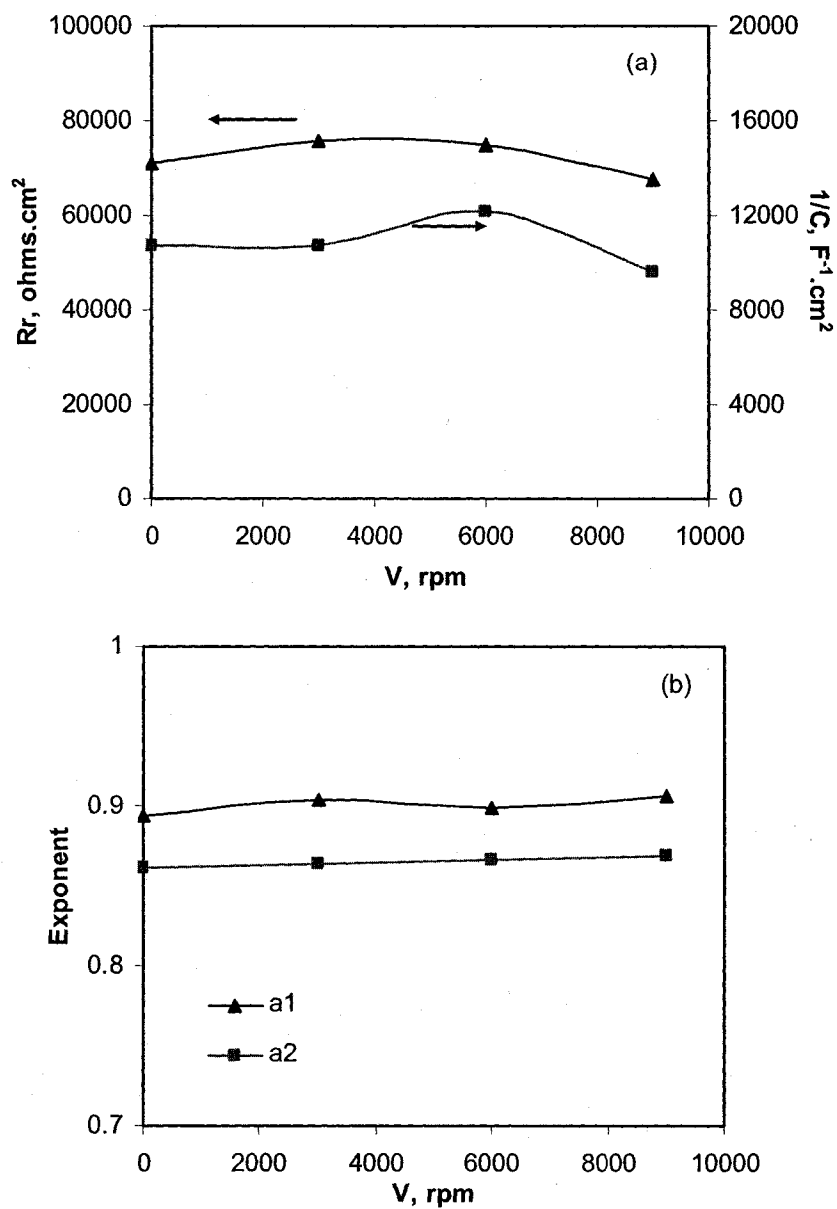
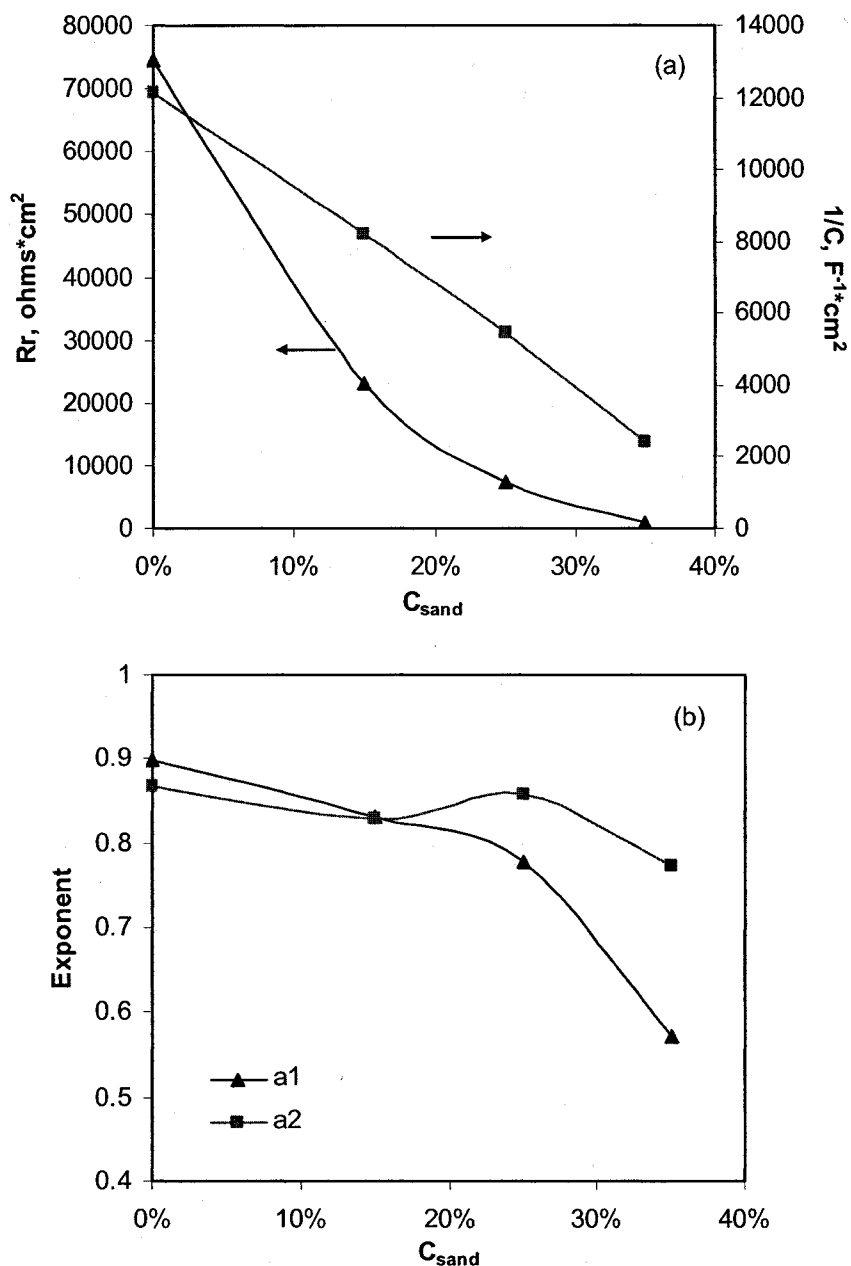


Figure 4-18. Electrochemical parameters fitted with the equivalent circuit as a function of velocity: (a)  $R_r$  &  $1/C$  ; (b)  $a_1$  &  $a_2$ .



**Figure 4-19. Electrochemical parameters fitted with the equivalent circuit as a function of sand concentration: (a)  $R_r$  &  $1/C$  ; (b)  $a_1$  &  $a_2$ .**

From **Figure 4-19 (b)** it was seen that the value of  $a_1$  decreased with an increase in sand concentration, suggesting greater deviation of the passive film from an ideal

capacitor in concentrated slurry. Also the behaviour of  $CPE_1$  deviated from a pure resistor because the charge carrier can accumulate at some area within film and cause difference in phase degree. Since  $a_1$  was associated with the ionic flux across the film, its decrease reflected that the ionic diffusion in the passive film became more important with an increase in sand concentration. This was related to the increased passive current and/or the degradation of the passive film. Juttner et al. [24] believed that  $a_2$  was influenced by surface inhomogeneities or surface active sites. At these sites, the charge transfer can take place preferentially. This led to a non-linear distribution of metal ions and induced a diffusion effect [25]. As a result, a frequency dispersion evolved and caused a decrease in  $a_2$ . Thus, the slight decrease of  $a_2$  with sand concentration suggested an increase in inhomogeneities within the passive film, but the reason for the exceptionally high value of  $a_2$  at 25% slurry was not clear.

#### **4.2.1.2 Discussion**

##### **4.2.1.2.1 Effect of erosion on corrosion and passive film**

The electrochemical test results showed that in the solution free of solid particles the velocity did not influence the passive current of carbon steel. The shape of the anodic part of the polarization curves shown in **Figure 4-13** showed that the carbon steel exhibited self-passivation behaviour in the test environment, and so the corrosion rate was controlled by the anodic reaction. In a passive system, the anodic reaction consists of three processes: mass transport in aqueous solution, mass transportation in the passive film, and charge transfer reaction on the electrode. Since the experimental results showed that the anodic reaction was independent of the solution velocity, it can be concluded that mass transfer in the aqueous solution was not the rate-determining step. As a result, the solution flowing did not influence the corrosion rate of carbon steel in the present passive system.

Martini and Muller's [21] investigations on iron in borate solution support this interpretation. However, others have obtained contrary results. Zhao et al.'s [26]

study showed that the passive current density of stainless steel 430 and 316 increased with flowing velocity in 0.5 M NaCl solution. Brown et al. [27] found the passive current of stainless steel 304 decreased with increasing velocity in the laminar flow region, while under turbulent flow conditions it stabilized in deaerated and low ozone concentration solutions. The dependence of passive current on velocity found by these authors can be attributed to the different nature and formation processes of the respective passive films.

In the slurry erosion processes, sand impingement increased the corrosion rate of carbon steel immersed in borate solution. This process can be understood as follows. Firstly, the sand particles with high kinetic energy were destructive and directly caused the breakdown of the passive film, which mainly comprises iron oxide and hydroxide [28, 29]. The exposure of fresh metal surface to corrosive slurry then increased the corrosion current. At the same time, new passive film was forming on the electrode surface. As simulated by the scratch test, the passive film on the present electrode surface was broken down and repaired repeatedly in flowing slurry. The frequency of impingement, which was related directly to the sand concentration, influenced the corrosion behaviour, as shown in **Figure 4-13 (b)**.

In the meantime, the properties of the passive film were also influenced by the slurry erosion process. Despite undergoing the repeated breakdown and repair processes, the electrode could be regarded as covered by a passive film, from both a macro and average point of view. The rupture frequency increased with an increase in slurry concentration, and so the repassivation time was reduced. As a result, the passive film formed in flowing slurry became thinner with increasing sand concentration, which was consistent with the capacitance measurements shown in **Figure 4-19 (a)**. The thinner passive film resulted in a higher electric intensity across the passive film. According to Sato [30], the ionic current through the passive film was related to the passive current and increased markedly with the electric field strength. Moreover, the potential difference across the Helmholtz double layer increased with a decrease in film thickness [31], and the consequent higher electric intensity also accelerated the corrosion rate. On the other hand, repeated sand

impingement led to microplastic deformation of the metal surface layer, and resulted in the presence of a higher density of dislocations, defects, and deformation energy in the surface layer. The passive film formed on such a deteriorated metal surface had a more disordered structure and poorer properties when compared with those formed on surfaces not subjected to sand impingement [32, 33]. The decrease of  $a_2$  was associated with the deteriorated structure and properties of the passive film.

#### **4.2.1.2.2 System dependence of erosion-enhanced corrosion**

It was interesting to compare the experimental results for the passive corrosion system and non-passive corrosion system: the  $E_c$  test curves in **Figures 4-3** and **4-11**, the potentiodynamic polarization curves in **Figures 4-4** and **4-13 (b)**, the potentiostatic curves in **Figures 4-5** and **4-12 (b)**, and the scratch test results in **Figures 4-9** and **4-14**. There were distinct differences between the response of the passive corrosion system and the non-passive corrosion system to erosion, in particular no significant increase in corrosion rate for the non-passive system compared to an obvious increase in corrosion rate for the passive system, showing that erosion-enhanced corrosion was dependent on the corrosion system.

The system dependence of erosion-enhanced corrosion can be understood from consideration of the impact of erosion on the basic reaction steps during corrosion. Sand impingement exhibited same influence for both systems on mass transport in the aqueous phase and the electrode reaction on the surface. Therefore, the differences stemmed from the effect on mass transport within the solid phase, i.e., the film on the electrode surface. In a passive system, the impact of solid particles decreased the mass transportation resistance within the passive film by impairing and/or deteriorating the film properties. In an active system, by contrast, no effective film was formed on the electrode, although some corrosion product deposited on the surface. As a result, there was no apparent effect from sand impingement.

#### 4.2.1.3 Summary

- (1) In the carbon steel/borate solution passive system, mass transfer in the fluid media was not the rate-determining step for the electrode reaction. Thus in a solution free of solid particles the electrochemical reaction parameters were independent of the rotation velocity.
- (2) The corrosion rate of carbon steel was increased by erosion through impairing and deteriorating the passive film. The effect of erosion was characterized using the parameters in equivalent circuit. The charge transfer resistance and reciprocal of film capacitance decreased significantly with slurry concentration, indicating that the erosion deteriorated the passivation of carbon steel.
- (3) The effect of erosion on corrosion was dependent on whether the corrosion system was passive or not.

#### 4.2.2 Study on erosion-enhanced corrosion by Mott-Schottky analysis

During erosion-corrosion passive films on the metal surface experience repeated breakdown and repassivation. For a system displaying self-passivation behavior, the repassivity ability of the passive film can strongly affect the corrosion kinetics, and thus the rate of erosion-enhanced corrosion. Therefore, aspects of erosion-enhanced corrosion can be studied by examining the repassivity behaviour of metals.

Although many models and theories have been proposed to explain the passivation of materials, a satisfactory description of the phenomenon is still lacking. The point defect model (PDM) [34-36] was developed by Macdonald et al. to qualitatively describe the growth and breakdown of passive film from a microscopic perspective. This model is based on the assumption that the passive film contains a high concentration of point defects, such as oxygen vacancies and metal cation vacancies. The growth and breakdown of the passive film involves the migration in the film of these point defects, which are also the charge carriers, under the influence of an electrostatic field. Thus, the key parameters in determining the kinetics of film growth are the density and diffusivity of the defects in the film. By employing Mott-Schottky analysis, Sikora et al. [37], Cheng et al. [38], and Ahn and Kwon [39] have determined the defect density and diffusivity for the passive films formed on tungsten and iron.

The primary aim of this part of the work was to understand the erosion-enhanced corrosion using a similar approach, by determining the diffusivity and density of point defects within the film. To fulfill this objective, the passivation behaviour and erosion-enhanced corrosion of the carbon steel were first investigated in three different aqueous environments, and then Mott-Schottky analysis was applied to the three systems to determine the defect density of the passive films. Finally, in conjunction with the PDM, the defect diffusivities within the passive films were calculated and correlations were made between defect flux, film growth and erosion-enhanced corrosion.

The test systems consisted of carbon steel A1045 and borate solutions with three different concentrations, 0.3 M  $\text{H}_3\text{BO}_3$  + 0.075 M  $\text{Na}_2\text{B}_4\text{O}_7 \cdot 10\text{H}_2\text{O}$ , denoted as 0.3 M solution, 0.1 M  $\text{H}_3\text{BO}_3$  + 0.025 M  $\text{Na}_2\text{B}_4\text{O}_7$ , denoted as 0.1 M solution, and 0.03 M  $\text{H}_3\text{BO}_3$  + 0.0075 M  $\text{Na}_2\text{B}_4\text{O}_7$ , denoted as 0.03 M solution. The solution pH was 8.4 for all the solutions.

#### **4.2.2.1 Results and discussion**

##### **4.2.2.1.1 Passive behavior in the three solutions**

Figure 4-20 shows the potentiodynamic polarization curves for carbon steel A1045 in 0.3 M, 0.1 M and 0.03 M solution in still solution and at a rotating velocity of 9000 rpm. The carbon steel showed good passivation behavior in all three solutions, independent of the flow conditions.  $E_c$  decreased slightly with increase in solution concentration, due to retardation of the cathodic reaction. One reason for this phenomenon was that the higher concentration of salts decreased the oxygen content in solution. In still solution, before the electrode was passivated, an active current peak occurred at around -200 mV in 0.3 M solution, which was attributed to oxidation of  $\text{Fe}^{2+}$  to  $\text{Fe}^{3+}$  ions in the passive film [40, 41]. In 0.1 M and 0.03 M solution, however, the current increased gradually with potential during the early stage of passivation and no current peak was observed. Similar self-passivation behavior was observed in all the solutions as the electrode rotated at 9000 rpm. The passive currents of carbon steel in all three solutions were comparable in magnitude, except that there was a small decrease in the most dilute solution.

There are few published studies describing the passivation in solutions with different salt concentrations. Oblonsky et al. [42] compared the passive behavior of iron in a 0.01 M and 0.136 M borate buffer solution, and found that the passivation below 0.4 V in the dilute borate buffers was associated with dissolution during the early stages of passivation. They also concluded that the films formed in solution with different salt concentrations had similar average oxidation states, i.e., the valence

state of iron was predominantly  $\text{Fe}^{3+}$  with 4~10%  $\text{Fe}^{2+}$  at high potentials (0.4 V), and 14~20%  $\text{Fe}^{2+}$  at lower potentials. Hence, it was believed that the chemical composition of the passive film was not dependent on the concentration of the borate solution.

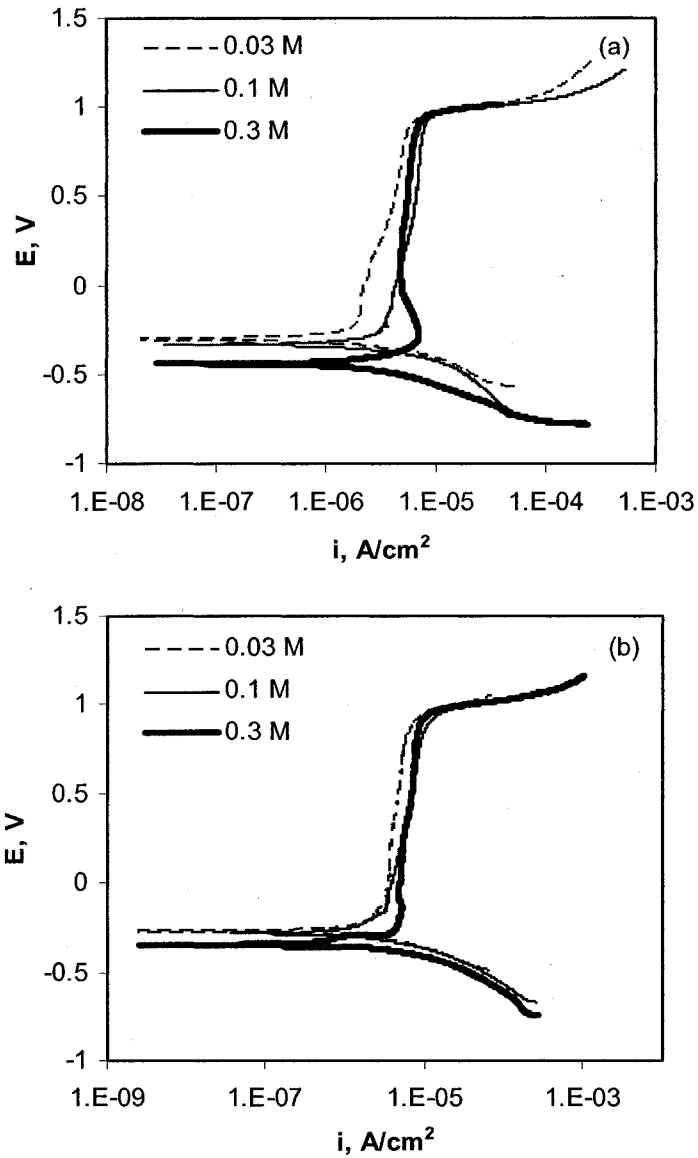


**Figure 4-20. Potentiodynamic polarization curves for carbon steel A1045 in borate solutions: (a) in still solution, (b) rotating at 9000 rpm.**

#### 4.2.2.1.2 Resistance to erosion-enhanced corrosion

Potentiostatic tests were carried out to compare the resistance to erosion-enhanced corrosion of the passive films formed in the three solutions. **Figure 4-21** shows the current curves in the 0.3 M solution at 200 mV and 800 mV. The current increased immediately with the addition of silica sand, and rapidly reached a new

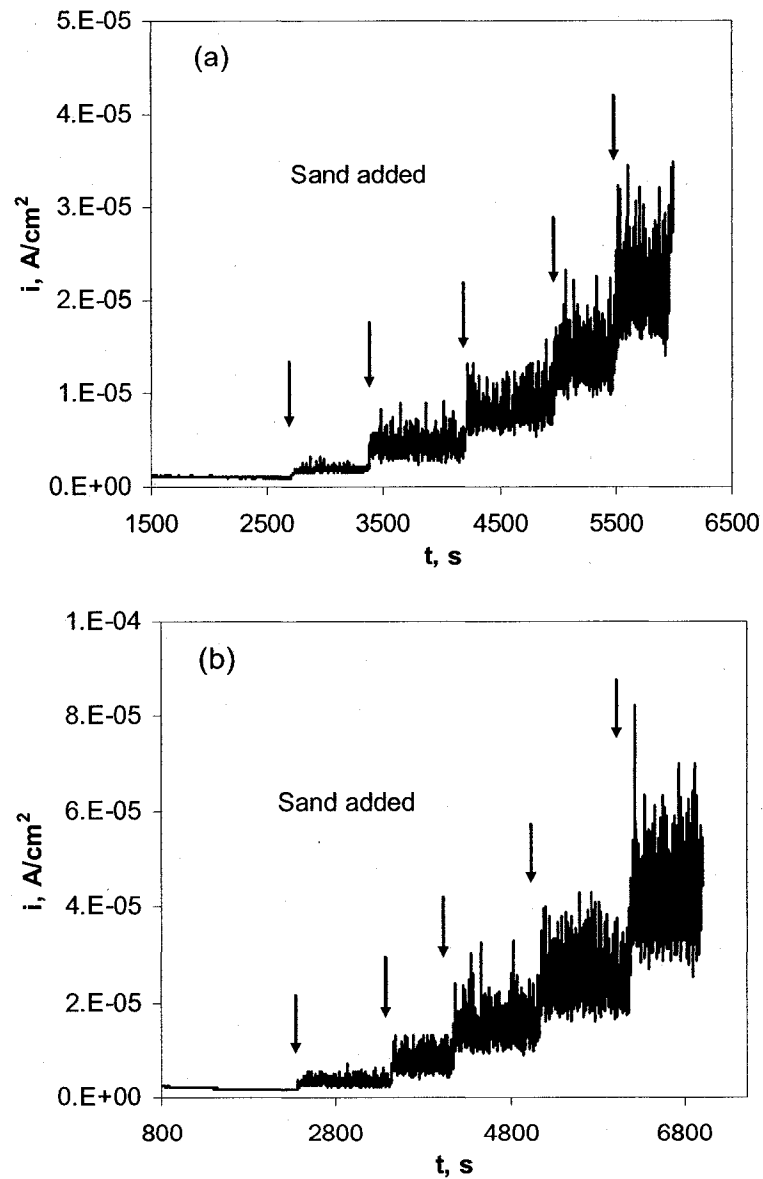


**Figure 4-21.** Potentiostatic curves for carbon steel A1045 rotating at 9000 rpm in the 0.3 M solution at a potential of 200 mV (a) and 800 mV (b).

stable value. The current curves in the 0.1 M and 0.03 M solution gave similar results, but the stable currents were different at each slurry concentration level. **Figure 4-22** shows the current density as a function of sand concentration in the 0.3 M, 0.1 M and 0.03 M solution under applied potentials of 200 mV and 800 mV. The current increased significantly with sand concentration. Under either potential the dependence of the current density on sand concentration was more profound in the dilute solution than in the concentrated solution, suggesting that there was reduced resistance to erosion-enhanced corrosion in the dilute solution system.

**Figure 4-22** shows that the dependence of current density on sand concentration can be fitted using a power relationship. Each of the exponentials was found to be greater than 1, which was unexpected. In the slurry erosion-corrosion processes, sand particles impinge on the surface layer of the sample, and each sand impingement event results in a current peak [15]. The average current density over the whole sample surface is between the peak value and the passive current value. **Figure 4-23** schematically presents the transient current increase caused by sand impingement. If the damaged area of the passive film caused by a sand impingement can re-heal before the next sand impingement, i.e. every impingement event is separated and does not overlap, then the relationship between the current and the sand concentration will be linear. This is the case when the sand concentration is low. However, as the concentration of sand increases, there is interaction or overlap of each impingement event, as shown in **Figure 4-23 (b)**. The passive film is damaged before it has healed from the previous breakdown. As a result, for each impingement event, only part of the consequent increase in current contributes to the total current density, and this fraction decreases with increasing sand concentration [43]. In other words, current overlap occurs, and so the efficiency of sand impingement in promoting current will decrease with increase in sand concentration. In the limiting case, the current density won't increase with further increase in sand concentration. Consequently, when a power relation is used to fit the dependence of the current on sand concentration under these conditions, the exponent value will be less than 1.

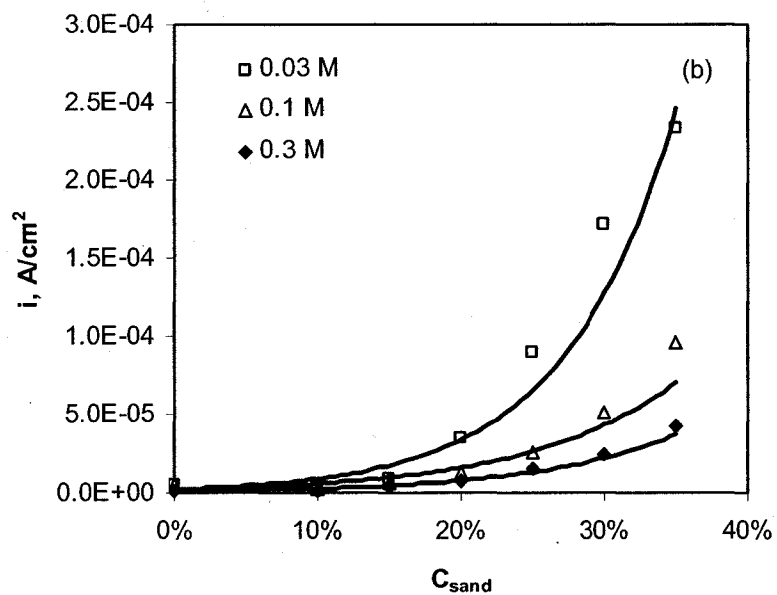
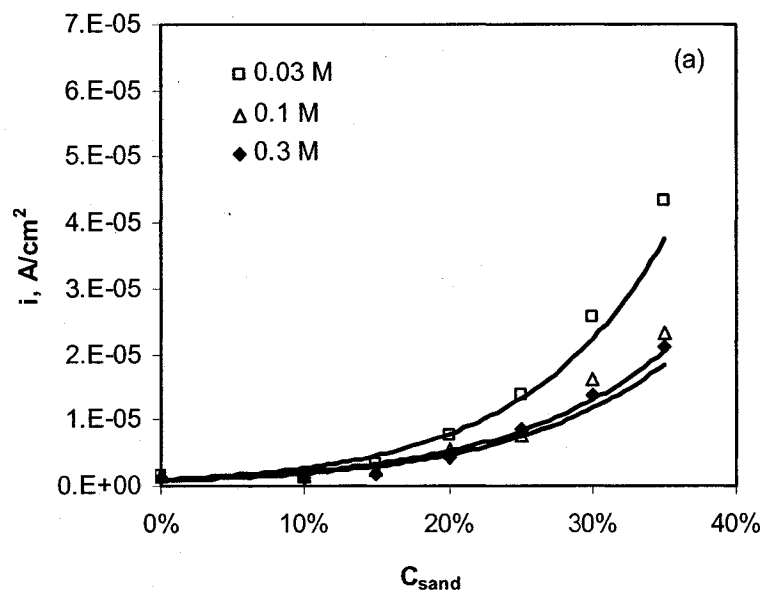
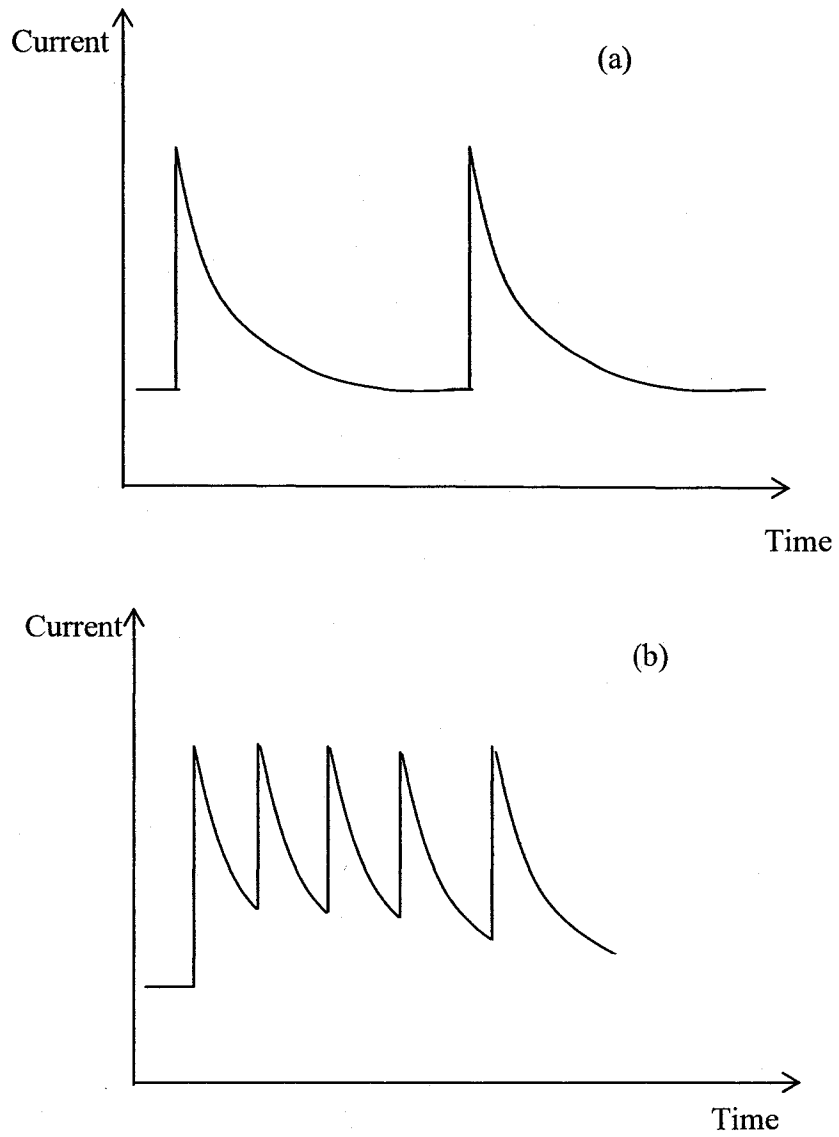


Figure 4-22. Current densities of carbon steel A1045 as a function of sand concentration at a potential of 200 mV (a) and 800 mV (b).



**Figure 4-23. Schematic transient current peak arising from sand impingement: (a) with lower sand concentration, (b) with higher sand concentration.**

Therefore, there must be other factors affecting the process, to account for the high exponents shown in **Figure 4-22**. The probable reason was from a special

dependence of impingement frequency on sand concentration in the present RCE electrochemical cell. In order to confirm this interpretation, the pure erosion rates with different sand concentrations were determined by applying a cathodic potential of  $-0.85$  V to the samples. The results are shown in **Figure 4-24**. The curve also bowed upward, in a similar manner to the curves shown in **Figure 4-22**. According to Hutchings's study [44], the dependence of the pure erosion rate decreased with slurry concentration due to interference between particles. Since pure erosion rate was proportional to sand impingement frequency, the power relation between the impingement frequency on the electrode and the sand concentration in the present setup was believed to be different from that in Hutchings's pipe loop. Thus, it was estimated that the special dependence of impingement frequency on sand concentration in the present cell resulted in the deviation of the relationship between current density and sand concentration.

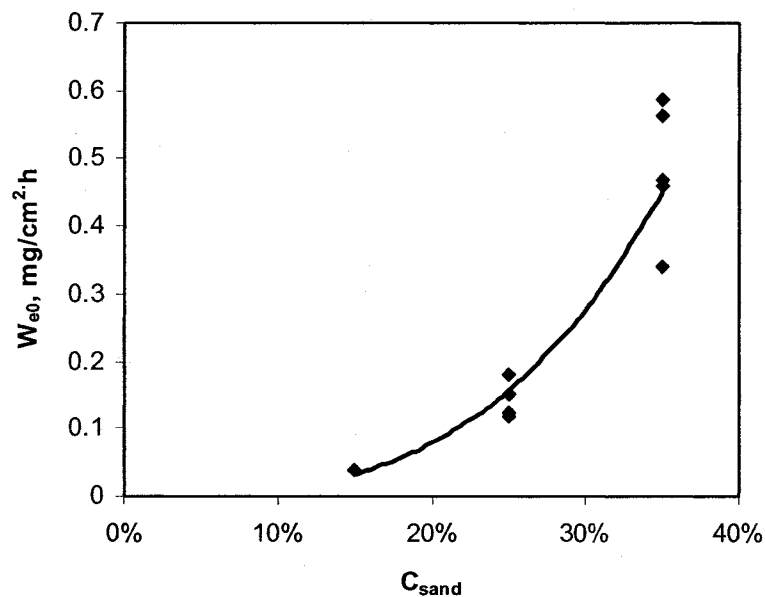


**Figure 4-24. Pure erosion rate as a function of sand concentration at a rotation velocity of 9000 rpm.**

Replotting the current density data in **Figure 4-22** as a function of pure erosion rate, as shown in **Figure 4-25**, led to a different relationship. Consistent with the

analysis, the exponents were each less than 1 when the relationship between the current density and the pure erosion rate was fitted by a power equation.

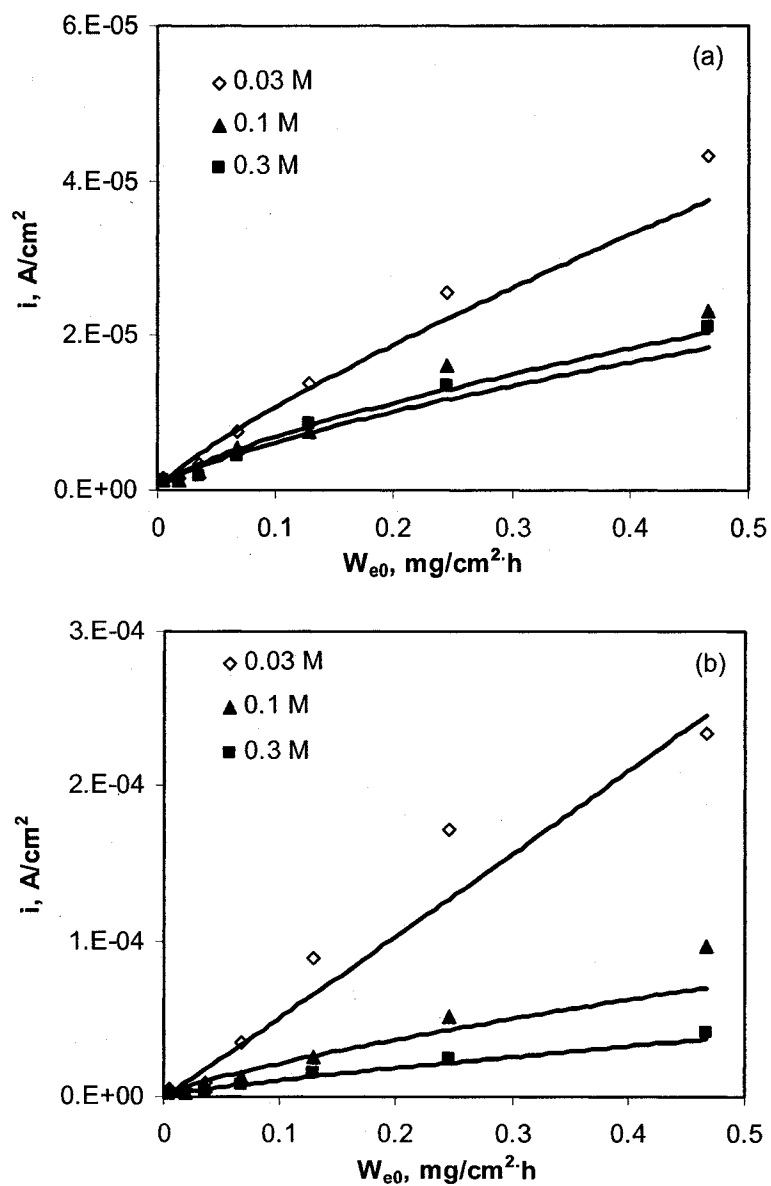


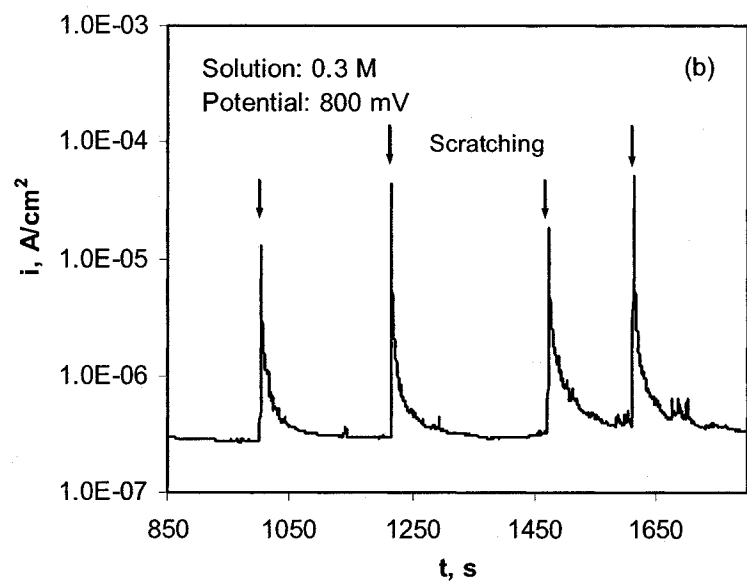
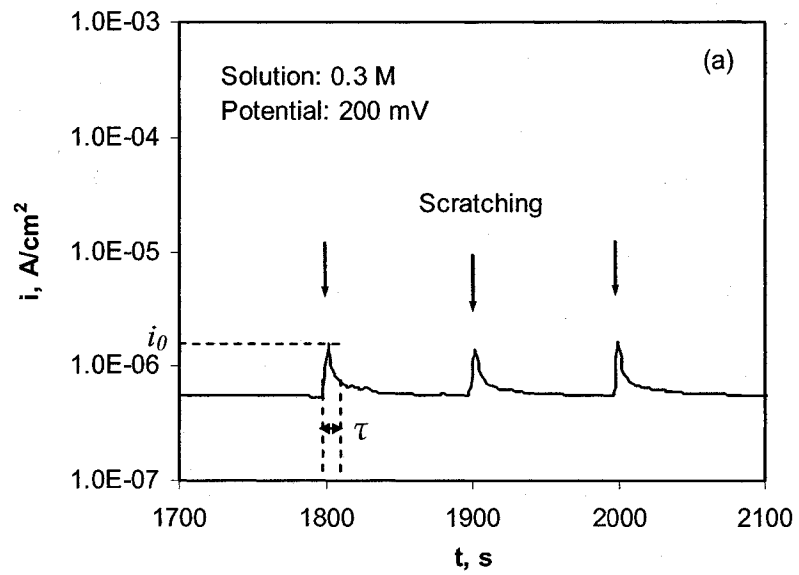
Figure 4-25. Current densities of carbon steel A1045 as a function of pure erosion rate in borate solutions at 200 mV (a) and 800 mV (b).

The exponents decreased with increased solution concentration, indicating poorer resistance to erosion-enhanced corrosion of the passive film in dilute solution. In order to investigate the cause for this behavior, scratch tests were performed in the three solutions to simulate the impingement of sand particles in the slurry. **Figure 4-26** shows the current response of the carbon steel to scratching in the 0.3 M, 0.1 M, 0.03 M solution at potentials of 200 mV and 800 mV. As the passive film was broken down by scratching the current density increased dramatically, but the passive film was re-healed over time and the current density gradually recovered. The peak current value,  $i_0$ , and the current decay constant,  $\tau$ , the time for the current to recover to 36.8% of the peak value, described the repassivation behavior. By comparing the current responses shown in **Figure 4-26**, it can be seen that both  $i_0$  and  $\tau$  increased with either increasing potential or decreasing solution concentration.

It was believed that the peak value and decay constant in flowing solution were different from those in still solution. However, it was reasonable to assume that even in flowing solution  $i_0$  and  $\tau$  increased with increasing potential or decreasing solution concentration for the present system. In slurries with the same given sand concentration and the same flowing velocity, the impingement frequency of sand particles on the electrode surface should have been the same. The current in the systems with larger  $i_0$  and  $\tau$  were higher, as shown in **Figures 4-22** or **4-25**. According to Lu and Luo [45], the relation of current to the intensity of particle impingement can be expressed as

$$i = i_p + i_0 \cdot \frac{\tau A_e}{1 + \tau A_e} \quad (4-5)$$

where  $i_p$  is the passive current density in a solution free of solid particles, and  $A_e$  the intensity of particle impingement. According to this equation,  $i$  will increase with either  $i_0$  or  $\tau$ . Therefore, although the electrode showed comparable passive behaviour in solutions with different concentrations, its resistance to erosion-enhanced corrosion was significantly different.



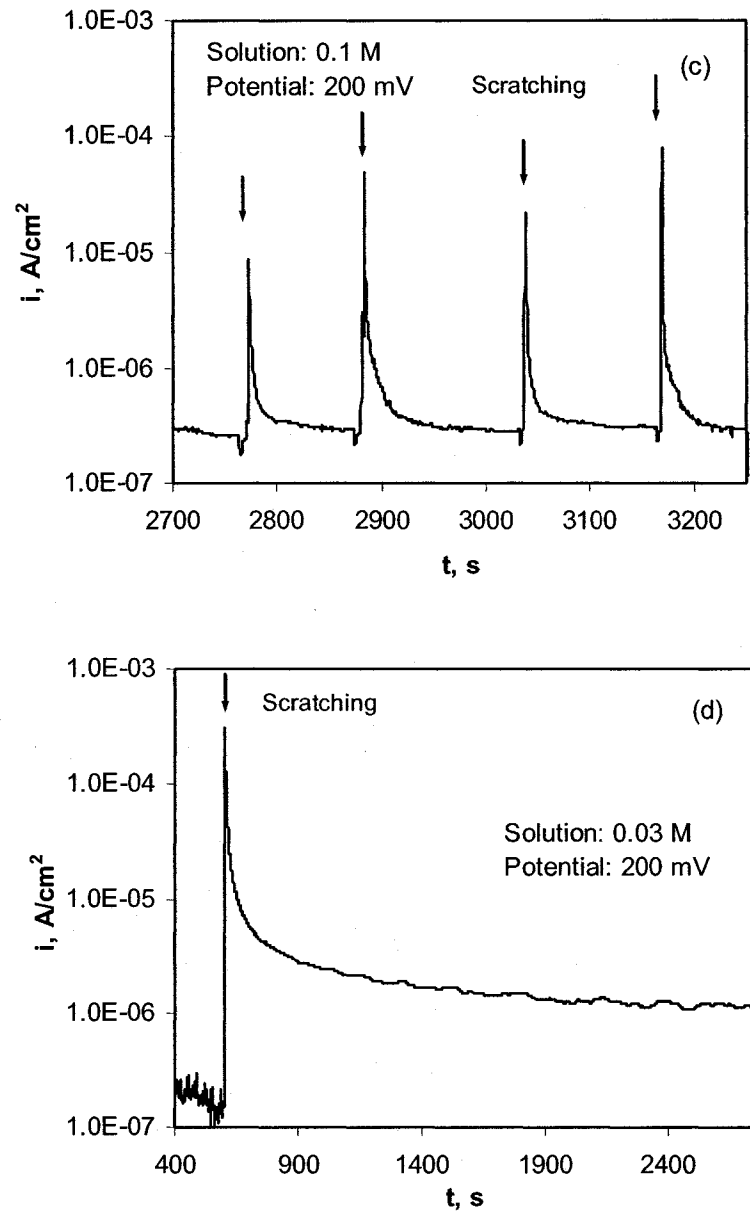
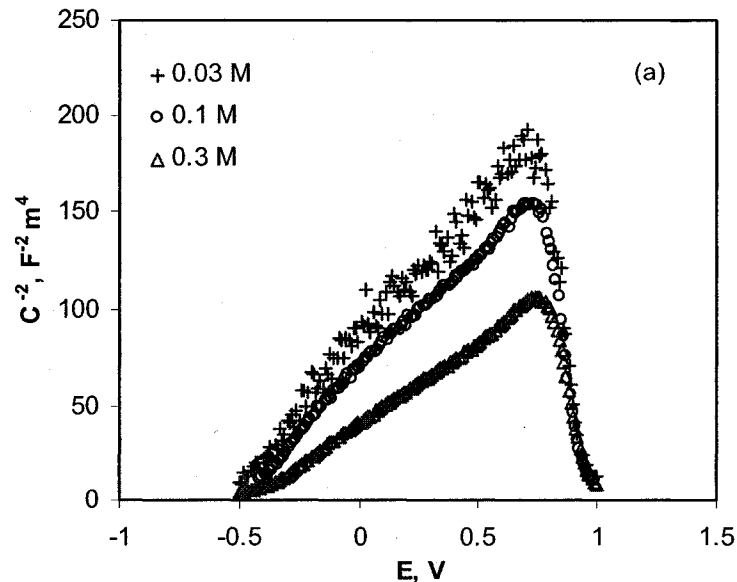


**Figure 4-26. Current density curves for carbon steel A1045 in borate solutions in scratch test at an applied potential of 200 mV and 800 mV.**

#### 4.2.2.1.3 Mott-Schottky analysis

Higher values for  $i_0$  and  $\tau$  led to poor resistance to erosion-enhanced corrosion of the passive film. To better understand the reasons for this effect, the two critical parameters for the growth of passive film, defect density and defect diffusivity, were determined.

The passive film formed in the three solutions was investigated using the Mott-Schottky analysis method. **Figure 4-27** shows the Mott-Schottky plots for the passive films formed on carbon steel A1045 in the 0.3 M, 0.1 M and 0.03 M solution at 200, 400 and 800 mV. In the potential range -0.3~0.7V, a linear relationship between  $1/C^2$  and  $E$  was found in all solutions, and the positive slopes in this range showed that all the passive films formed on the carbon steel were n-type semiconductors. At lower film formation potentials or in dilute solutions, break points occurred above and below which the Mott-Schottky plot showed different slopes, as shown by the straight lines drawn in **Figures 4-27 (b) and (c)**. This phenomenon was reported to be related to non-uniform donor distribution within the film [46, 47]. The peaks in Mott-Schottky plots for each of the films indicated an inversion from an n-type to a p-type semiconductor.



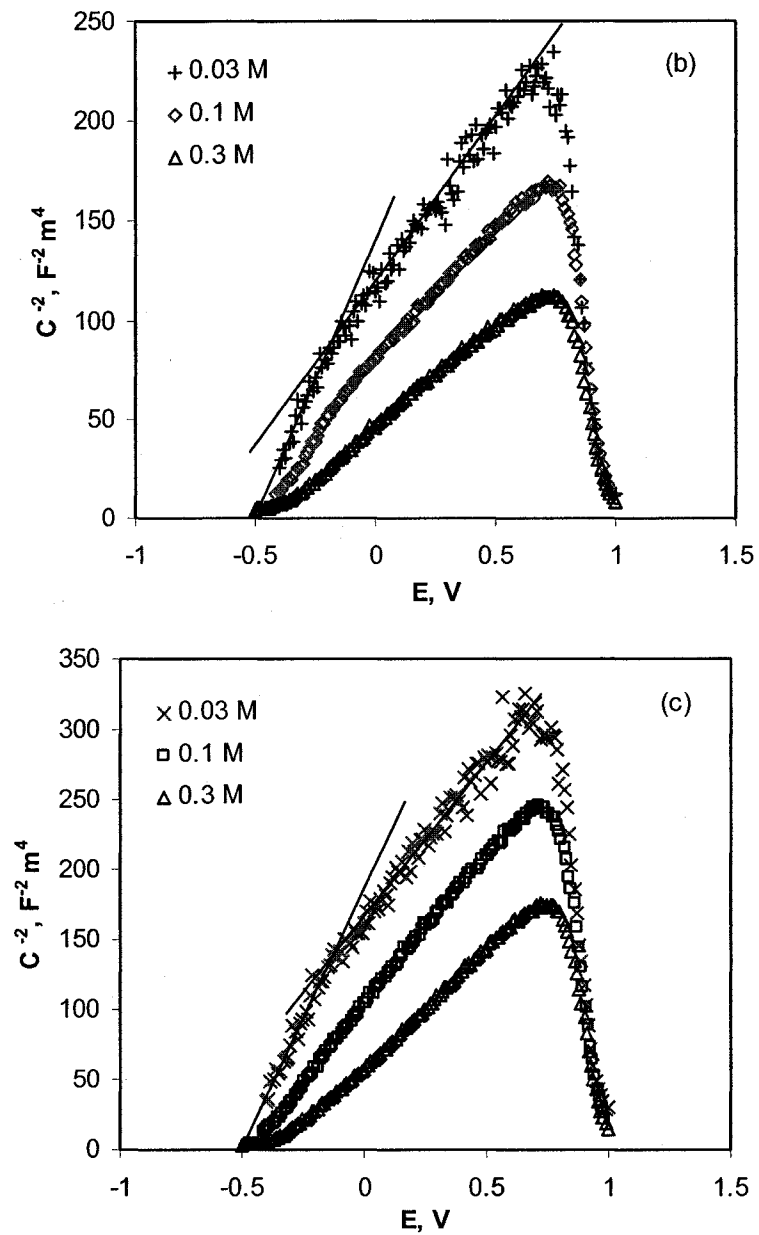


**Figure 4-27. Mott-Schottky plots for carbon steel A1045 in the 0.03 M, 0.1 M and 0.3 M solution. The electrode was pre-passivated for 1 h at 200 mV (a), 400mV (b) and 800 mV (c).**

The validity of Mott-Schottky analysis was based on the assumption that the capacitance of the space charge layer was much smaller than the double layer capacitance. Since the two layers were in series, the total impedance was the sum of their reciprocals. Hence, the capacitance determined was mainly from the contribution of the space charge layer. This assumption was reasonable, provided that the frequency was sufficiently high (on the order of kHz) [48, 49].

It was noted that the passive films formed in dilute solution had higher slopes at all the film formation potentials. According to Equation (2-15), the donor density was calculated from this slope, where the average slopes were used. **Figure 4-28** shows the calculated donor densities for the films formed at various potentials in the three solutions. The dielectric constant of the passive film was taken as 15.6 [50]. For all three solutions, the donor density decreased with increase in the formation potential. These results were consistent with other reports [37, 38, 51].

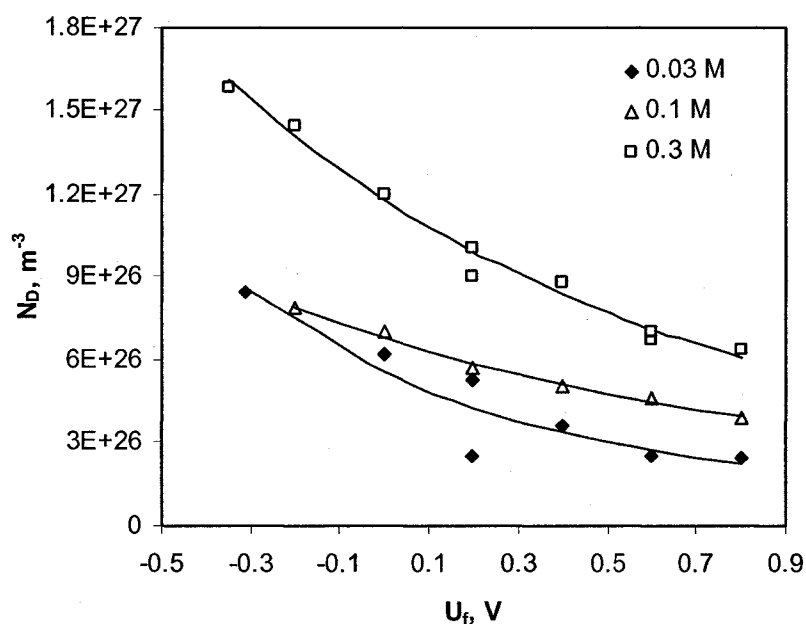


**Figure 4-28. Donor densities of carbon steel A1045 as a function of film form potential in the 0.3 M, 0.1 M and 0.03 M borate solution.**

Regarding the donor species, Macdonald et al. [52, 53] suggested that the donors were the defects in the passive film, including cation vacancies, anion vacancies, and cation interstitials, and the major donors in an n-type oxide film formed on iron were the oxygen vacancies. The relationship between the donor density,  $N_D$ , and the film formation potential,  $U_f$ , can be described by the expression [37]:

$$N_D = \omega_1 \exp(-b_0 U_f) + \omega_2 \quad (4-6)$$

where  $\omega_1$ ,  $\omega_2$  and  $b_0$  are constants that are to be determined from the experimental data. The values of exponents used in fitting curves to the experimental data are also shown in **Figure 4-28**, from which the required parameters can be determined. The donor density increased with solution concentration at constant potential.

Sikora et al. [37] also demonstrated that  $\omega_2$  in Equation (4-6) was related to the diffusivity of the point defects,  $D_0$ , by the following equation, based on the Nernst-Planck transport equation:

$$D_0 = -\frac{J_0}{2K_0\omega_2} \quad (4-7)$$

where  $J_0$  is the steady state flux of donors, and  $K_0 = F\varepsilon_L/(RT)$ ,  $\varepsilon_L$  the mean electric field strength within the passive film, and  $R$  the gas constant. Since the current flow was mainly due to the flux of oxygen vacancies, the relationship between  $J_0$  and passive current at the steady state was expressed by [37]

$$J_0 = -\frac{i_p}{2e} \quad (4-8)$$

where  $i_p$  can be determined from polarization curves.

Thus, it was possible to determine the diffusivity of the defects in the passive film,  $D_0$ , by combining Equation (4-6), (4-7) and (4-8)

$$D_0 = \frac{i_p RT}{4eF\omega_2\varepsilon_L} \quad (4-9)$$

The value of  $\epsilon_L$  determined by Smialowska and Kozlowski [54] was  $3.9 \times 10^6$  V/cm for the passive film grown on iron, and  $3.5 \times 10^6$  V/cm by Haupt et al. [55] for the passive film on iron in 1 M NaOH solution. Thus it was reasonable to assume that  $\epsilon_L$  for the passive films formed on carbon steel A1045 in the borate solutions was approximately  $4.0 \times 10^6$  V/cm. The calculated diffusivities of the oxygen vacancies in the passive films formed in the three solutions as well as other parameters are listed in **Table 4-1**. No significant difference was found for the diffusivities in the passive films formed in the three solutions. All diffusivities were in the order of  $10^{-16}$  cm<sup>2</sup>/s. This result was quite consistent with the diffusivity determined by Cheng et al. [38] for carbon steel A516-70 in 0.02 M H<sub>3</sub>BO<sub>3</sub> + 0.005 M Na<sub>2</sub>B<sub>4</sub>O<sub>7</sub> · 10H<sub>2</sub>O solution, which was estimated to be  $2.94 \times 10^{-16}$  cm<sup>2</sup>/s. The diffusivity of oxygen vacancies determined by Sikora et al. [37] for WO<sub>3-x</sub> passive film was  $5.3 \times 10^{-15}$  cm<sup>2</sup>/s with  $\epsilon_L = 2.48 \times 10^6$  V/cm. Ahn and Kwon [39], however, found the donor diffusivity in the passive film formed on pure iron in borate solution to be  $1.69 \times 10^{-20}$  cm<sup>2</sup>/s. This large deviation may be attributed to the surface charge approach used in their work.

**Table 4-3. Defect diffusivities and other parameters for the passive films formed in the borate solutions.**

Solution	$i_p$ ( $\mu\text{A}\cdot\text{cm}^{-2}$ )	$\omega_1$ ( $10^{26} \text{ m}^{-3}$ )	$\omega_2$ ( $10^{26} \text{ m}^{-3}$ )	$b_0$ (V)	$D_0$ ( $10^{-16} \text{ cm}^2\cdot\text{s}^{-1}$ )
<b>0.3 M</b>	<b>4.81</b>	<b>10.19</b>	<b>1.569</b>	<b>1.018</b>	<b>3.07</b>
<b>0.1 M</b>	<b>4.96</b>	<b>5.392</b>	<b>1.410</b>	<b>0.934</b>	<b>3.53</b>
<b>0.03 M</b>	<b>2.92</b>	<b>4.548</b>	<b>1.006</b>	<b>1.633</b>	<b>2.91</b>

#### 4.2.2.1.4 Correlation between defect flux, film growth and erosion-enhanced corrosion

The experimental results showed that, although carbon steel A1045 exhibited comparable passive behaviour in borate solutions having different concentrations, its resistance to erosion-enhanced corrosion was significantly different. In dilute solutions, the efficiency of each impingement event in enhancing corrosion current was increased through elevating the peak current value and the decay constant. In this case, the repassivation process, i.e. the growth rate of the passive film on the metal surface, strongly influenced the corrosion rate of the electrode. The Mott-Schottky analysis demonstrated that the donor diffusivities in the films formed in the solutions with different concentrations were comparable, while the donor density increased with solution concentration.

Since no reports concerning the dependence of donor density on solution concentration were found in the literature, additional tests were carried out to confirm the above experimental results. **Figure 4-29** shows the donor density as a function of solution concentration when the electrode was pre-passivated for 1 h at 800 mV. The x-axis shows the concentration of boric acid, to which borate was added at a fixed ratio to boric acid of 0.25. It was observed that the donor density increased linearly with solution concentration, consistent with the results shown in **Figure 4-28**.

The effect of solution concentration on the repassivation rate here should not be misunderstood as a direct relationship between concentration of reactant and reaction rate. The passivation process did not directly involve the borate or boric ions, as only the concentrations of  $H^+/OH^-$  influenced the formation reaction of the passive film [56, 57]. The pH values of the solutions were measured and no variation was found. This was a consequence of buffering, where a fixed ratio of acid to its salt determined a constant pH value. Therefore, the different passivation rates were not attributable to the concentration effect as expected from the reaction kinetic equation. Other factors needed to be considered to understand this result.

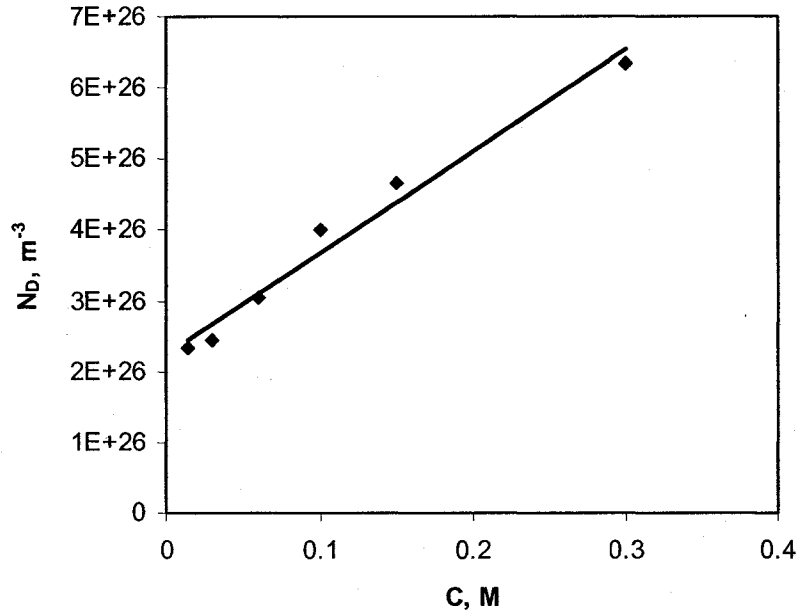


**Figure 4-29. Dependence of donor density on borate solution concentration. The electrode was pre-passivated at 800 mV for 1h in the solutions.**

When a metallic electrode was exposed to solution, an electric double layer formed on the metal/solution interface. According to the Stern double layer theory, the electric double layer consisted of a compact layer and a diffusion layer. Generally, the thickness of the diffusion layer decreased with an increase in ion concentration. Hence, the diffusion layer in concentrated solution would be thinner than that in dilute solution. As a result, the potential drop across this layer would be sharper in concentrated solution, leading to higher electric field intensity. This effect can result in a higher reaction rate, and thus higher film growth rate at the beginning stage of film formation. Due to the higher film growth rate, there was limited time for the atoms/ions to diffuse to the 'right' position, more defects were generated in the passive film, and the donor density increased correspondingly. After formation of the passive film had been initiated on the electrode surface, subsequent growth was determined by the flux of oxygen vacancies in the film. According to PDM the

oxygen vacancies must be transported from the metal/film interface to the film/solution interface, and the film growth kinetics can be expressed by [34]

$$\frac{dL}{dt} = \frac{\Omega}{Nv} J \quad (4-10)$$

where  $L$  is the thickness of the film,  $t$  the time,  $\Omega$  the molar volume per cation,  $Nv$  Avogadro's number, and  $J$  the flux of the vacancies. In line with the generalized form of Fick's first law, in an electric field the diffusion rate of charged species was influenced not only by the concentration gradient but also by the potential gradient [34],

$$J = J^c + J^p \quad (4-11)$$

where  $J^c$  and  $J^p$  are the fluxes due to concentration gradient and potential gradient, respectively. The term related to the potential gradient can be written as [34]:

$$J^p = -2KD_oN_D \quad (4-12)$$

Since the diffusivities were comparable for each condition within the present systems, the higher donor density led to higher  $J^p$  and thus higher film growth rate. The faster film growth rate resulted in a smaller decay constant, as shown by the tests in the concentrated solution.

Based on the above analysis, during the erosion processes the passive film was damaged by impact of sand particles, which caused an immediate increase in the current. In concentrated solutions, the initiation and growth rate of the passive film were higher owing to the thinner diffusion double layer and the higher donor density of the formed passive film. As a consequence, the electrodes in concentrated solutions were rapidly repassivated and so exhibited better resistance to erosion-enhanced corrosion. It is worthy to point out that the thickness of the diffusion layer in flowing solution decreased significantly when compared with that in still solution. Thus the effect of solution concentration on the diffusion layer was attenuated to some extent.

The reason for the higher peak current caused by scratching the film immersed in the dilute solution was still not clear at this stage.

The erosion-corrosion tests were conducted in flowing solution, while the Mott-Schottky capacitance was measured in still solution. Therefore, in order to verify the above analysis, the Mott-Schottky capacitance tests were also performed in flowing 0.03 M solution using the erosion-corrosion setup, after pre-passivating the sample for 1 h. The capacitance data were somewhat scattered. However, the calculated donor densities showed good agreement with those determined in still solution, as shown in **Figure 4-30**. Therefore, it is reasonable to believe that the above analysis applied to the experimental data obtained in the still solution can also be applied to the flowing conditions.

The donor densities of the films formed in all the solutions decreased with increasing film formation potential, which was attributed to the oxidation of  $\text{Fe}^{2+}$  to  $\text{Fe}^{3+}$  with increasing formation potential [58]. Studies of related systems have shown that the  $\text{Fe}^{2+}$  content decreased with increasing film formation potentials [42].

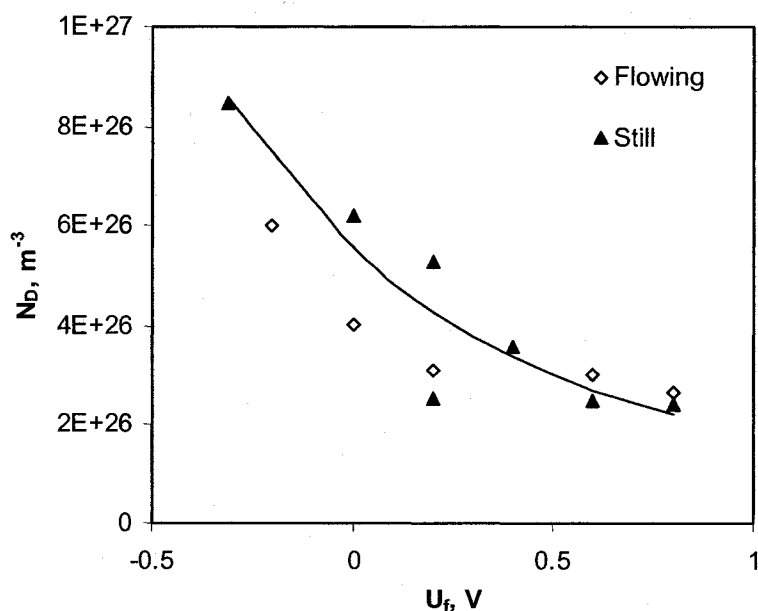


**Figure 4-30. Donor densities determined for carbon steel A1045 in flowing solution and still solution.**

#### 4.2.2.2 Summary

The electrochemical response of carbon steel A1045 to slurry erosion and the electronic properties of the passive films formed in the solutions with different borate concentrations were investigated in this part of the work. Although the polarization curves suggested that the carbon steel showed comparable passive behavior in the three different solutions, the resistance to erosion-enhanced corrosion increased significantly with solution concentration. In the scratch tests, the peak current and decay constant were higher in dilute solutions than in concentrated solutions. Mott-Schottky analysis, in conjunction with PDM, revealed that the diffusivities of the defects within the passive film formed in the solutions with different concentrations were similar, while the defect density increased with solution concentration. According to PDM, the higher donor density resulted in higher diffusion flux and thus higher film growth rate. Improved resistance of the electrode to erosion-enhanced corrosion resulted from higher repassivation rate.

### 4.2.3 Effect of sand impingement on pitting corrosion

In a passive corrosion system, pitting corrosion is one of the most serious prevailing corrosion forms due to its insidious feature and quick propagation rate, especially in solutions containing halide ions. Burstein et al. [15, 16] developed a novel technique for measurement of the current transients during erosion of stainless steel 304L in chloride solution. However, the impact of erosion on the overall pit development process, involving initiation, propagation and repassivation, is still not well understood.

#### 4.2.3.1 Experimental results and discussion

##### 4.2.3.1.1 Pitting induction time measurements

Figures 4-14 and 4-26 shows that, although every impingement event caused a local breakdown of the passive film, no specific area was always undergoing active dissolution and developed into a local corrosion pit. Typically, pitting corrosion occurred more readily in an environment containing halide ions. Therefore chloride ions were introduced into the slurry to investigate the effect of erosion on pitting corrosion. Firstly, attempts were made to measure the pitting induction time in the flowing solution and 10% slurry at a velocity of 6000 rpm and an applied potential of 200 mV, as shown in Figure 4-31. Chloride ions were added to make the overall  $\text{Cl}^-$  concentration 0.003 M. The salt was added to the flowing solution at 1300 s and to the slurry at 6100 s. For the flowing solution free of sand particles, no substantial increase in current occurred upon addition of  $\text{Cl}^-$ , indicating that no pitting corrosion took place. For the 10% slurry, however, the current was boosted up essentially immediately upon the addition of  $\text{Cl}^-$  so that the induction time for pitting corrosion was too short to be determined under these conditions.

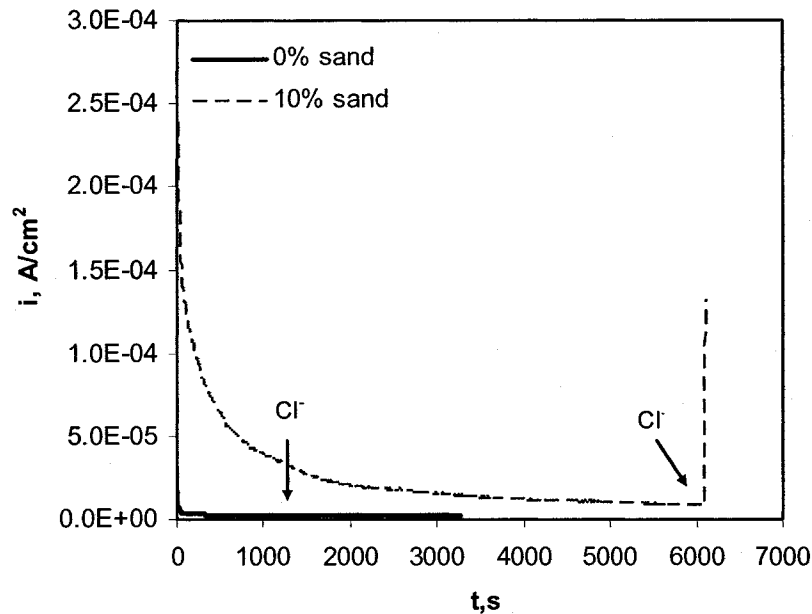


**Figure 4-31. Potentiostatic current curves for carbon steel A1045 at an applied potential of 200 mV and a rotation velocity of 9000 rpm.**

#### 4.2.3.1.2 Pitting potential measurements

The polarization curves for carbon steel in 15% slurry with different chloride concentrations were determined at a velocity of 6000 rpm to determine the pitting potential, and the results are shown in **Figure 4-32**. The passive region shrank upon increasing concentration of chloride in the slurry. The potential corresponding to the sudden increase of current was regarded as the pitting potential,  $E_b$ , as marked in the figure.  $E_b$  decreased markedly with increased chloride concentration. **Figure 4-33** shows the pitting potential as a function of chloride concentration for flowing solution free of solid particles and 15% slurry. According to the literature [59-61], the relationship between pitting potential and chloride concentration can be described by:

$$E_b = \alpha_0 - \beta_0 \log C_{cl^-} \quad (4-13)$$

where  $\alpha_0$  and  $\beta_0$  are experimental parameters, and  $C_{cl^-}$  is the concentration of chloride ions. From the figure, the test data for slurry and flowing solution were fitted well

using this equation. The pitting potential in the slurry at the same  $\text{Cl}^-$  concentration was lower than that in solution without sand.

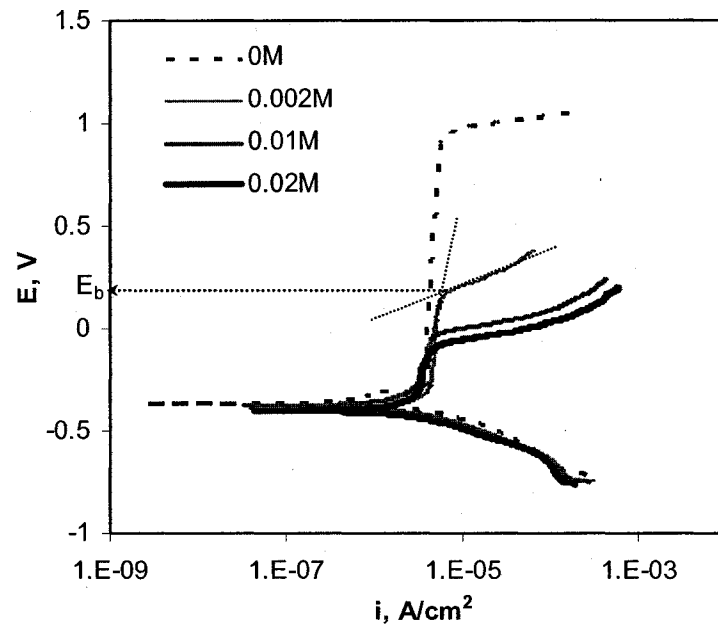


**Figure 4-32. Potentiodynamic polarization curves for carbon steel A1045 in 15% slurry containing different  $\text{Cl}^-$  concentrations at rotation velocity of 6000 rpm.**

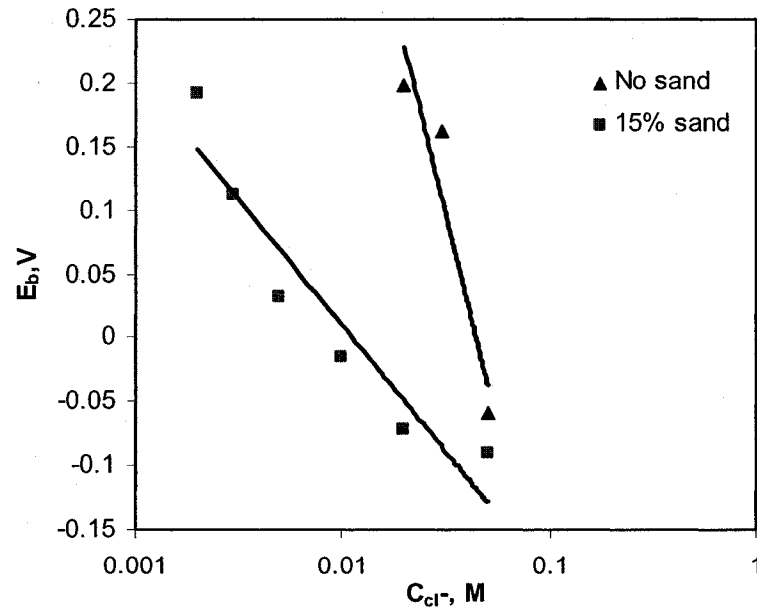


**Figure 4-33. Pitting potentials of carbon steel A1045 as a function of  $\text{Cl}^-$  concentration at rotation velocity of 6000 rpm.**

**Figure 4-34** shows the cyclic polarization curves for carbon steel A1045 in slurry with different sand concentrations and constant 0.05 M concentration of chloride ions at a velocity of 6000 rpm. Consistent with the potentiodynamic polarization test results, the pitting potential decreased as solid particles impacted the electrode surface. However, increasing the sand concentration further mainly influenced the passive current density, without a significant influence on decreasing the pitting potential. **Figure 4-35** shows the pitting potentials as a function of sand concentration at 6000 rpm for the slurries containing 0.002 M and 0.05 M Cl<sup>-</sup>. When the slurry concentration increased the pitting potential decreased slightly.

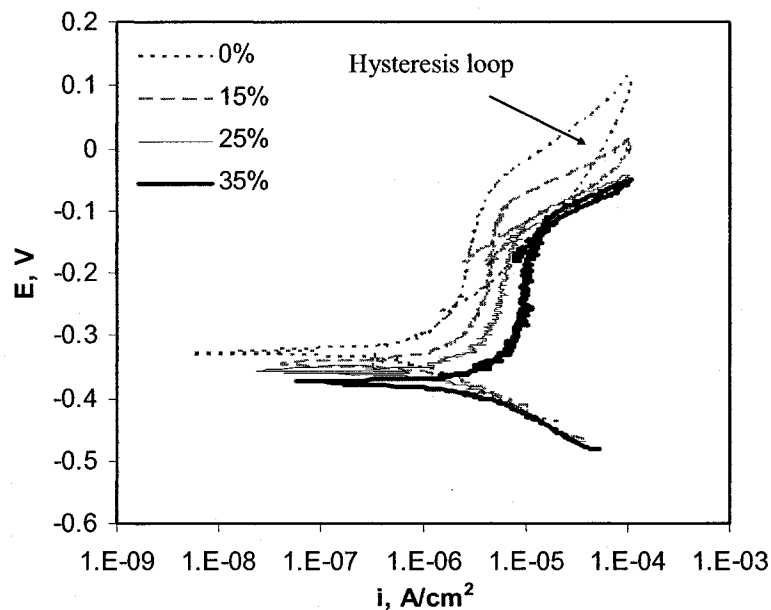


**Figure 4-34.** Cyclic polarization curves for carbon steel A1045 in slurry containing 0.05 M Cl<sup>-</sup> at a rotation velocity of 6000 rpm.

For pitting corrosion, the size of the area within the hysteresis loop formed by the potential curves in cyclic polarization, as marked in **Figure 4-34**, was related to the capacity of the electrode to recover from pitting corrosion, i.e. the repassivation ability of the electrode. A smaller area of hysteresis loop corresponded to better repassivation ability. The areas of hysteresis loops in **Figure 4-34** were calculated by integrating the cyclic polarization curves, and the results are shown in **Figure 4-36**. It

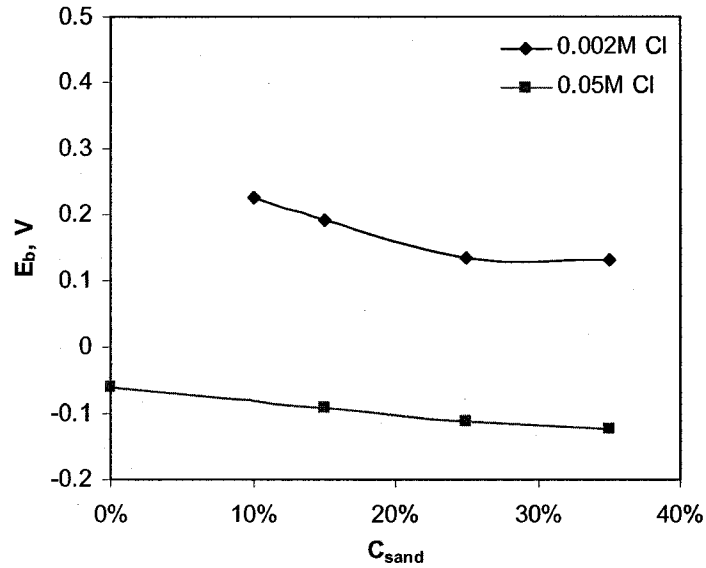


**Figure 4-35. Pitting potentials of carbon steel A1045 as a function of slurry concentration at rotation velocity of 6000 rpm.**

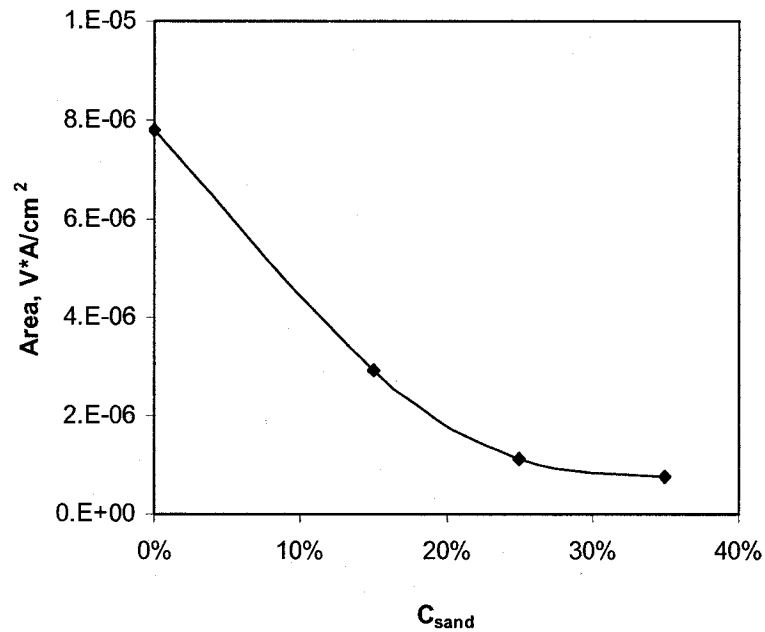


**Figure 4-36. Areas of hysteresis loops in Figure 4-35 as a function of slurry concentration.**

was somewhat surprising to find that the hysteresis loop area decreased with slurry concentration, suggesting better repassivation ability of the electrodes subjected to

sand impingement. The protective potential, the potential value at the intersection of the forward and backward potential scan curves, was much lower for flowing solution than those for slurries, confirming that the corrosion pits could recover more easily in slurry than in solution.

The above tests showed that the impact of solid particles at the surface decreased the pitting potential, but improved the repairing ability of the corrosion pits. This indicated a difference between the nature of pitting corrosion in slurry and that during general pitting corrosion. According to the most widely accepted theory for the pitting corrosion, the development of pitting corrosion involved the initiation of pits, and the growth of a metastable pit to a stable pit or the repassivation of the pit. Thus, the effect of erosion on pitting corrosion can be analyzed by considering the initiation, growth and repassivation of corrosion pits.

Generally, pitting corrosion occurs at 'weak sites' in passive films such as defect points and damaged points. The impact of solid particles facilitated the initiation of pitting corrosion, because the points damaged by the impingement became the 'weak sites'. In these areas, chloride ions were adsorbed preferentially, which impeded the formation of passive film. As a result, the repassivation process of the damaged electrode surface was retarded [62]. This viewpoint was confirmed by the scratch test results shown in **Figure 4-14**. In solutions free of chloride ions, the repassivation time for each scratch were around 50 s. However, when  $\text{Cl}^-$  was added into the solution to make the overall  $\text{Cl}^-$  concentration 0.001 M, the repassivation time increased to around 180 s. With further increase in  $\text{Cl}^-$  concentration to 0.002 M after 1270s, the corrosion at damaged area accelerated and the current fluctuated. Scratching the electrode surface in this case caused the current to increase dramatically and no further repassivation occurred. Although the influence of  $\text{Cl}^-$  on repassivation in flowing slurries was different from that in still solutions, it was believed that the impingement of solid particles created 'weak sites' where chloride ions were adsorbed, which resulted in the initiation of pitting corrosion. This explained the increase of current in **Figure 4-31** and the decrease of pitting potential in **Figures 4-32, 4-33 and 4-34**. Meanwhile, as mentioned in Section 2.2.1, with

repeated sand impingement on the electrode, the passive films formed on the surface had more defects and then became more susceptible to pitting corrosion. In addition, as seen in **Figure 4-35**, an increase in impingement frequency did not lead to a further substantial decrease in the pitting potential.

According to Pistorius and Burstein [63], the applied polarization potential in the nucleation process of pits influenced the dissolution rate of the metal. With an increase in potential, the sites that were not activated at lower potentials became activated to form corrosion pits. When there were more active sites, the effect of potential on the electrochemical dissolution of the electrode was more profound. This effect was supported by the polarization curves shown in **Figure 4-34**. When the potential was higher than the pitting potential, the current density increased. However, the rates of increase, which can be defined as the slope of the potential scanning curves between  $E_b$  and the reversal potential, were dependent on slurry concentration. **Figure 4-37** shows the rates of current increase as a function of slurry concentration with 0.05 M Cl<sup>-</sup>. The rate increased markedly with slurry concentration. In concentrated slurry, the impingement frequency was higher, and thus more sites were initiated to form corrosion pits above the pitting corrosion potential. For each pit, the local current increased with potential, and as a result the overall current increase rate was higher.

In the growth period, however, the impingement of particles impeded the development of metastable pits to stable corrosion pits. As discussed in Chapter 2, the metastable pits experienced an auto-catalytic process in an occluded environment to develop into stable pits. The hydrolysis of dissolved metal cations raised the acidity of the solution within the pits, resulting in higher dissolution rates of metal [64, 65]. Finally, this site developed into a corrosion pit. In flowing slurry, the colliding of solid particles with the electrode surface impaired the occluded environment and reduced the acidity of the local solution. As a result, the auto-catalytic effect was alleviated and the bottoms of pits maintained active dissolution. Thus a simple relationship was developed between the potential and current density. When the

potential scan was reversed, the dissolution of metal electrode decreased correspondingly.

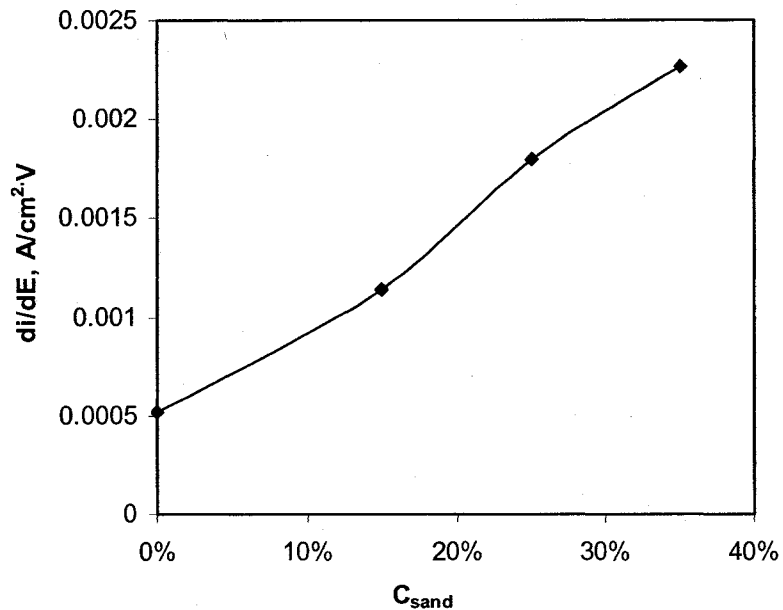


**Figure 4-37. Slope of potential polarization curve as a function of sand concentration in slurries containing 0.05 M Cl<sup>-</sup>.**

#### 4.2.3.1.3 Potentiostatic measurements

The above analysis was confirmed by potentiostatic tests. **Figure 4-38** shows the current response of carbon steel A1045 to chloride ions and sand impingement at a potential of 200 mV and a rotation velocity of 6000 rpm. Initially no sand was added into the solution. As the current density stabilized, chloride ions were added to the solution to increase the overall concentration to 0.003 M. Then sand was added to make the overall slurry concentration 10%, 15% and 20%. The current density increased with slurry concentration, but even in 15% and 20% slurry the current density reached a stable and finite value. From the pitting potential shown in **Figure 4-33**, however, it can be seen that in a 15% slurry containing 0.003 M Cl<sup>-</sup> the pitting potential was much lower than 0.2 V. Thus, the conditions were not suitable for establishment of a stable and relatively low current value if an auto-catalytic process

occurred during pitting corrosion in the slurries. More potentiostatic test results summarized in **Figure 4-39** further showed that auto-catalytic process was minor.

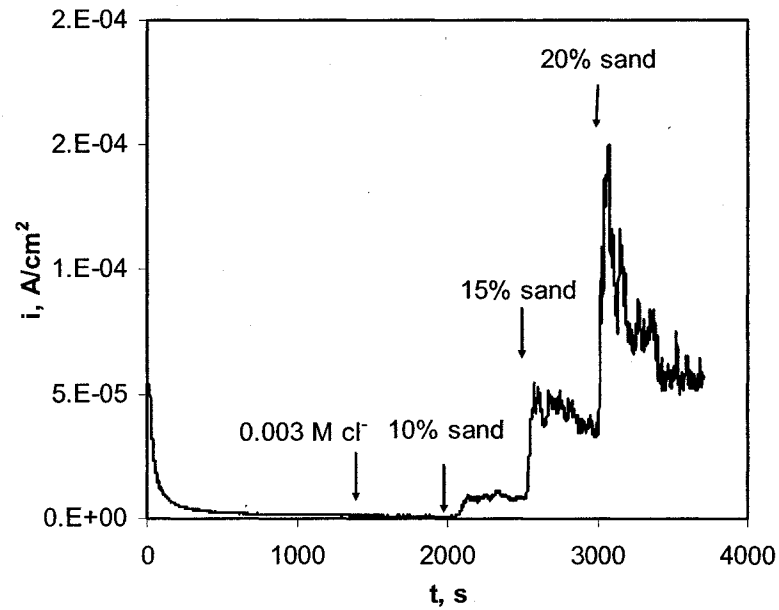


**Figure 4-38.** Current response of carbon steel A1045 to chloride ions and sand impingement at potential of 200 mV and rotation velocity of 6000 rpm.

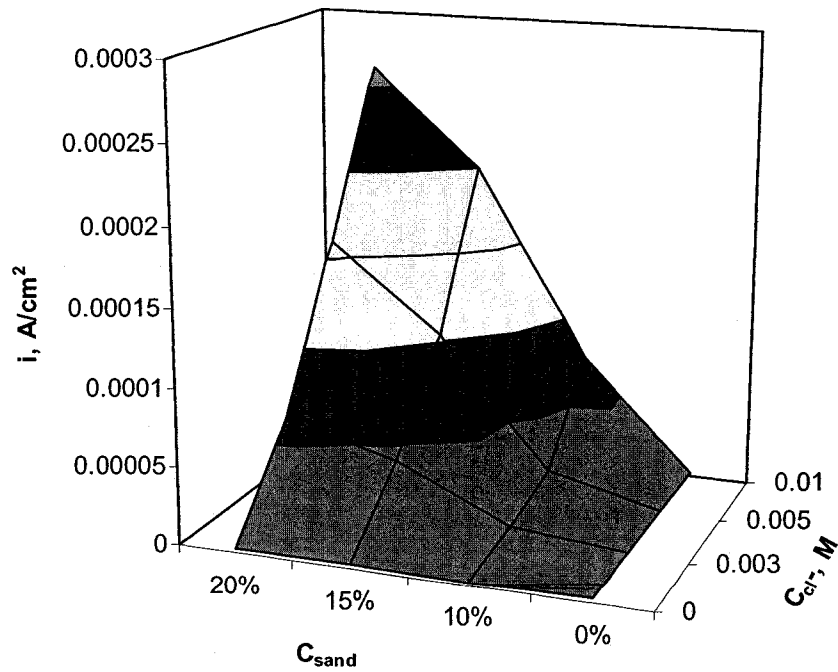


**Figure 4-39.** Current densities of carbon steel A1045 as a function of slurry concentration and chloride ions at 200 mV and rotation velocity of 6000 rpm.

#### 4.2.3.1.4 Surface morphology

From the above analysis, it can be seen that the effect of erosion on pitting corrosion was not monotonic. On the one hand, erosion facilitated the generation of 'pits' by damaging to the passive film, and so resulted in high local current density. On the other hand, erosion impeded the propagation of these pits through impairment of the occluded environment and alleviation of the auto-catalytic process. Most of the 'pits' showed active dissolution. Even if some of them developed into relatively stable pits, the size of these pits could not be as deep, big and occluded as those formed in flowing solution without sand. In other words, erosion made the localized corrosion more 'open' and 'generalized'. This can explain the small hysteresis loop area shown in plots from experiments in slurries, shown in **Figure 4-34**.

**Figure 4-40** shows the surfaces under optical microscopy after potentiodynamic polarization when the velocity was 6000 rpm, the slurry concentration was 15% and the chloride concentration was 0.02 M. The pits readily occurred at the 'head' of the comet-shaped groove caused by sand particle impingement, confirming the initiation effect of erosion on pitting corrosion. Moreover, the sizes of pits produced in slurries were almost half of those formed in flowing solution, although the number of pits was much larger. This suggested that the local current density within the pits formed in slurries was lower than that in solution.

#### 4.2.3.1.4 Synergy between erosion and chloride

In addition, an interesting feature shown in **Figure 4-39** was a synergistic effect between sand erosion and  $\text{Cl}^-$  in developing pitting corrosion. Singly increasing the sand or  $\text{Cl}^-$  concentration did not result in a much higher corrosion current, but the effect of increasing both led to much more severe corrosion. This phenomenon can be understood by their roles in pitting corrosion development. Without the presence of  $\text{Cl}^-$ , the pits caused by sand impingement became repassivated rapidly. Without the presence of sand particles, it was difficult for  $\text{Cl}^-$  to impair the passive film and

initiate corrosion pits. When these two effects were both present, however, the development of pitting corrosion was accelerated significantly.

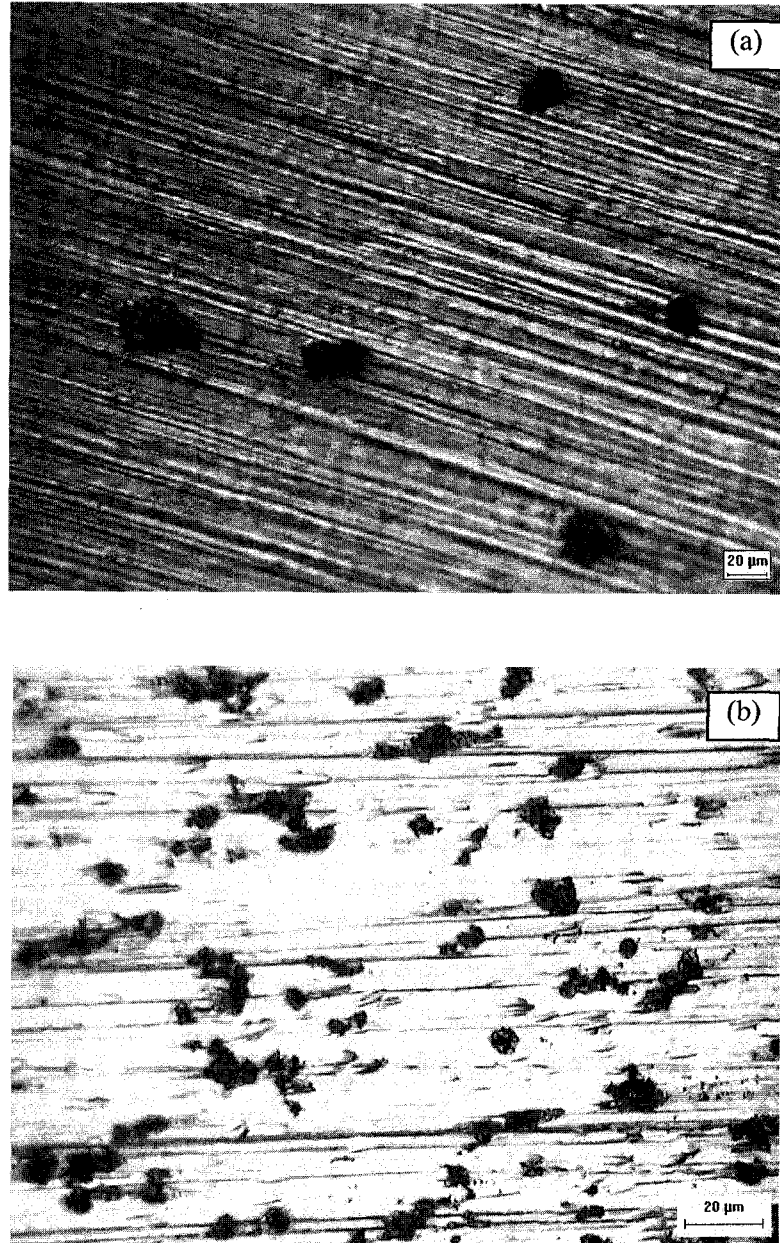


**Figure 4-40. Morphology of carbon steel A1045 after anodic polarization as the Cl<sup>-</sup> concentration was 0.02 M and rotation velocity was 6000 rpm: (a) in solution (b) in 15% slurry.**

### 4.2.3.2 Summary

In a slurry containing chloride ions, the effect of erosion on pitting corrosion of carbon steel A1045 was not monotonic. The impingement of erosion particles promoted the initiation of pitting corrosion by breaking down the passive film, but impeded the propagation of metastable pits to stable corrosion pits by impairing the occluded environment for pitting corrosion development.

### References

- [1] Y.G. Zheng, Z.M. Yao, X.Y. Wei, and W. Kei, *Wear* 186 (2) (1995) 555.
- [2] B.W. Madsen, *Wear* 123 (1988) 127.
- [3] B. Poulson, *Wear* 235 (1999) 497.
- [4] E. Heitz, *Corrosion* 47 (2) (1991) 135.
- [5] S. Zhou, M.M. Stack, and R.C. Newman, *Corrosion Science* 38 (1996) 1071.
- [6] H.H. Huang, *Biomaterials* 23 (2002) 59.
- [7] S.X. Mao, B. Gu, N.Q. Wu, and L. Qiao, *Philosophical Magazine A* 81 (7) (2001) 1813.
- [8] B.T. Lu and J.L. Luo, in *The 2nd Environment-Induced Cracking in Materials, (EICM-2), Banff, Alberta, Canada, 2004,*
- [9] H.X. Guo, B.T. Lu, and J.L. Luo, in *43 rd Annual conference of metallurgists of CIM, Hamilton, Ontario, Canada, 2004, p.525.*
- [10] A. Neville, M. Reyes, T. Hodgkiess, and A. Gledhill, *Wear* 238 (2000) 138.
- [11] A. Neville and T. Hodgkiess, *Wear* 233-235 (1999) 596.
- [12] A. Neville and X. Hu, *British Corrosion Journal* 37 (1) (2002) 43.
- [13] A. Neville and B.A.B. McDougall, *Wear* 8836 (2001) 1.
- [14] V. Rajagopal and I. Iwasaki, *Corrosion* 48 (1992) 132.
- [15] G.T. Burstein and K. Sasaki, *Electrochimica Acta* 46 (2001) 3675.
- [16] G.T. Burstein and K. Sasaki, *Corrosion Science* 42 (2000) 841.
- [17] P. Ponthiaux, F. Wenger, D. Drees, and J.P. Celis, *Wear* 256 (2004) 459.
- [18] J.G. Yu, J.L. Luo, and P.R. Norton, *Electrochimica Acta* 47 (2002) 1527.

- [19] S.S. El-Egamy, W.A. Badawy, and H. Shehata, *Corrosion Prevention & Control* (2) (2000) 35.
- [20] T.P. Moffat and R.M. Latanision, *Journal of the Electrochemical Society* 139 (1992) 1869.
- [21] E.M.A. Martini and I.L. Muller, *Corrosion Science* 42 (2000) 443.
- [22] J. Flis, Y. Tobiya, K. Mochizuki, and C. Chiga, *Corrosion Science* 39 (1997) 1757.
- [23] W.D. Callister, *Materials science and engineering: an introduction*, 1994.
- [24] K. Juttner, W.J. Lorenz, W. Paatsch, M. Kendig, and F. Mansfeld, *Werkst. Korros.* 36 (1985) 120.
- [25] J. Hitzig, J. Titz, K. Jutter, and e. al., *Electrochimica Acta* 29 (1984) 287.
- [26] X.Z. Zhao, N. Cui, J.L. Luo, and S. Chiovelli, *British Corrosion Journal* 37 (1) (2002) 63.
- [27] B.E. Brown, H.H. Lu, and D.J. Duquette, *Corrosion* 48 (12) (1992) 970.
- [28] E.B. Castro and J.R. Vileche, *Electrochimica Acta* 38 (1993) 1567.
- [29] W. Kozlowski and J. Flis, *Corrosion Science* 28 (1988) 787.
- [30] N. Sato, ed., *Passivity and its breakdown on iron and iron base alloys*, NACE, ed. R.W. Staehle H. Okada, Houston, 1976, p.1.
- [31] A.M. Kuznetsov, R.R. Dogonadze, and *Izv. Akad. Nauk SSSR, Ser. Him.*, 1964, No.12, p2140; English Translation, Consultants Bureau, New York, (1964) 2024.
- [32] Z. Szklarska-Smialowska, *Corrosion* 27 (1971) 223.
- [33] A. Barbucci, G. Cerisola, and P.L. Cabot, *Journal of the Electrochemical Society* 149 (12) (2002) B534.
- [34] C.Y. Chao, L.F. Lin, and D.D. Macdonald, *Journal of the Electrochemical Society* 128(6) (1981) 1187.
- [35] D.D. Macdonald, *Journal of the Electrochemical Society* 139 (1992) 3434.
- [36] L. Zhang and D.D. Macdonald, *Electrochimica Acta* 43 (7) (1998) 679.
- [37] E. Sikora, J. Sikora, and D.D. MacDonald, *Electrochimica Acta* 41 (6) (1996) 783.

- [38] Y.F. Cheng, C. Yang, and J.L. Luo, *Thin Solid Films* 416 (2002) 169.
- [39] S.J. Ahn and H.S. Kwon, *Journal of the Electrochemical Society* 579 (2) (2005) 311.
- [40] M. Bucher, P. Schmuki, and H. Bohmi, *Journal of the Electrochemical Society* 145 (1998) 378.
- [41] M.E. Vela, J.R. Vilche, and A.J. Ariva, *Journal of Applied Electrochemistry* 16 (1986) 490.
- [42] L.J. Oblonsky, A.J. Davenport, M.P. Ryan, H.S. Isaacs, and R.C. Newman, *Journal of the Electrochemical Society* 144 (7) (1997) 2398.
- [43] J. Li, Y.G. Zheng, J.Q. Wang, Z.M. Yao, Z. Wang, F, and W. Ke, *Wear* 186-187 (1995) 562.
- [44] I.M. Hutchings, *The Erosion of Materials by Liquid Flow*, Cambridge, UK, MTI Publication No. 25, Material Technology Institute of the Chemical Process Industries, 1986.
- [45] B.T. Lu and J.L. Luo, in *The 16th International Corrosion Congress*, Beijing, China, 2005, Sept 19-24, p.Paper No. 12.
- [46] J. Schoonman, K. Vos, and G. Blasse, *Journal of the Electrochemical Society* 128 (1981) 1154.
- [47] Y.F. Cheng and J.L. Luo, *Electrochimica Acta* 44 (1999) 2947.
- [48] R. Degryse, W.P. Gomes, F. Cardon, and J.T. Vennik, *Journal of the Electrochemical Society* 122 (5) (1975) 711.
- [49] A.W. Bott, *Current Separations* 17 (3) (1998) 87.
- [50] A.M.P. Simoes, M.G.S. Ferreira, B. Rondot, and M. Da Chunha Belo, *Journal of Electrochemistry Society* 137 (1990) 82.
- [51] S.J. Ahn and H.S. Kwon, *Electrochimica Acta* 41 (6) (2004) 3347.
- [52] D.D. Macdonald and M. Urquidi-Macdonald, *Journal of the Electrochemical Society* 137 (1990) 2395.
- [53] J. Liu and D.D. Macdonald, *Journal of the Electrochemical Society* 148 (2001) B425.

- [54] Z.S.Z. Smialowska and W. Kozlowski, in *Passivity of metals and Semiconductors*, Elsevier, 1983, p.89.
- [55] S. Haupt, C. Carinski, U. Collisi, H.W. Hoppe, and H.H. Strhbolw, *Surface and Interface Analysis* 9 (1986) 357.
- [56] I. Diez-Perez, P. Gorostiza, F. Sanz, and C. Muller, *Journal of the Electrochemical Society* 148 (8) (2001) B307.
- [57] B. Krishnamurthy, R.E. White, and H.J. Ploehn, *Electrochimica Acta* 46 (2001) 3387.
- [58] N. Sata, K. Kudo, and R. Nishinura, *Journal of the Electrochemical Society* 123 (1976) 1419.
- [59] Y.F. Cheng, M. Wilmott, and J.L. Luo, *Bulletin of Electrochemistry* 17 (10) (2001) 433.
- [60] E. Mccafferty, *Journal of the Electrochemical Society* 137 (12) (1990) 3731.
- [61] Y.M. Zeng, J.L. Luo, and P.R. Norton, *Electrochimica Acta* 49 (2004) 703.
- [62] J.D. Kim and S.I. Pyun, *Electrochimica Acta* 40 (12) (1995) 1863.
- [63] P.C. Pistorius and G.T. Burstein, *Philosophical Transactions of the Royal Society* A341 (1992) 53.
- [64] T.P. Hoar, *Transactions of the Faraday Society* 33 (2) (1937) 1152.
- [65] T. Suzuki, M. Yanabe, and Y. Kitamura, *Corrosion* 29 (1973) 18.

## Chapter 5      Effect of Corrosion on Erosion

When corrosion takes place on an electrode surface, even with a very limited rate, the erosion rate can be accelerated significantly [1, 2]. From the nature of the corrosion reaction, the influence of anodic dissolution on erosion represents essentially the effect of corrosion on erosion. Therefore, most work for this subject was carried out in an active system, because the anodic dissolution of metals occurs freely in corrosion of active systems.

From the tests result shown in **Figure 4-2**, the synergistic effect in the carbon steel/sodium sulphate solution system was observed to be as high as 51% of the total weight loss. This synergistic component was the sum of the erosion-enhanced corrosion and corrosion-enhanced erosion. However, from the analysis performed in Section 4.1, the erosion-enhanced corrosion was not substantial in this system. Consequently, the significant synergistic effect was attributed to the corrosion-enhanced erosion, which played an important role in the total material loss.

The investigation on corrosion-enhanced erosion in the literature has been reviewed in Chapter 2. Limitations and discrepancies existed in explaining the significant effect of corrosion on erosion. Recently, a chemo-mechanical effect has been applied to the research areas where the interaction of mechanical action and chemical/electrochemical reaction was involved [3-5]. A preliminary attempts have also been made to understand the corrosion-enhanced erosion by the chemo-mechanical effect [6]. On this basis, in the present work the erosion-enhanced corrosion was investigated firstly in the active system with and without solid particles, and finally experiments was designed to provide direct experimental support to the chemo-mechanical effect.

## 5.1 Effect of anodic current on erosion in sand slurry

### 5.1.1 Total weight losses and corrosion-enhanced erosion

Erosion tests were conducted with different corrosion rates to study the effect of corrosion on erosion and to determine the quantitative relationship between the synergistic effect and corrosion parameters. The total weight losses measured in 0.1 M Na<sub>2</sub>SO<sub>4</sub> containing 25% and 35% sand with constant anodic currents are illustrated in **Figure 5-1**, and the total weight losses in tap water containing 35% sand are shown in **Figure 5-2**. The weight loss due to electrochemical corrosion,  $W_c$ , was calculated from the applied current density with Faraday's law, because under such galvanostatic condition the corrosion rate was controlled by the impressed current density. The wastages of pure mechanical erosion  $W_{e_0}$  have been experimentally measured under CP condition. The sum of the corrosion rate and pure erosion rate was also shown in **Figure 5-1**. Obviously, the total weight losses were always greater than the sum of the erosion and corrosion. Based on the fact that the uniform corrosion rate in the slurry-erosion tests was controlled by the applied current, the synergistic effect was entirely attributed to the corrosion-enhanced erosion.

### 5.1.2 Possible effect from solution

It has been known that the erosion rate can be influenced by three categories of parameters. The first one is the hydrodynamic parameters of the erodent, such as the impingement velocity; the second one is the slurry properties, such as the hardness, shape, and concentration of the sand particle; and the third category is the mechanical properties of the target material. Thus, the effect of corrosion on erosion can be analyzed from consideration of these factors.

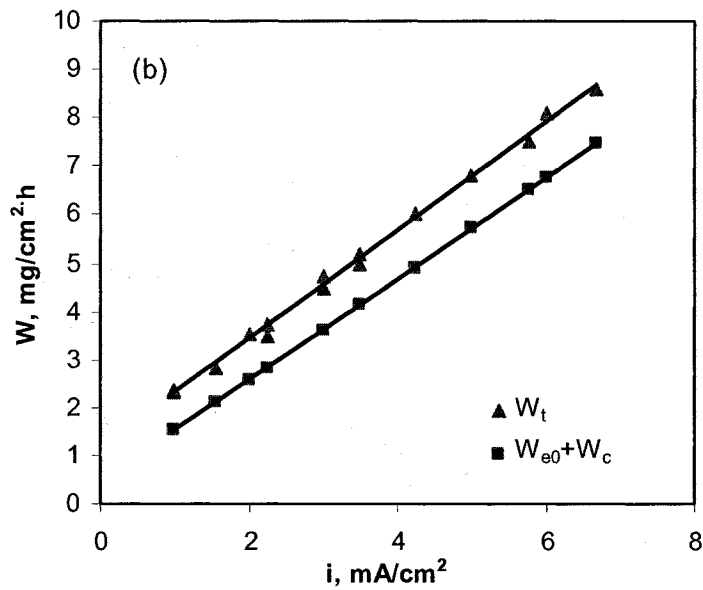
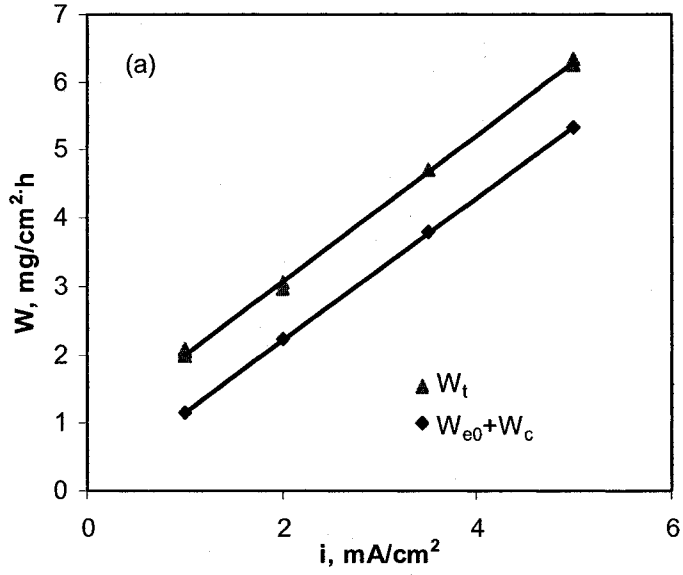
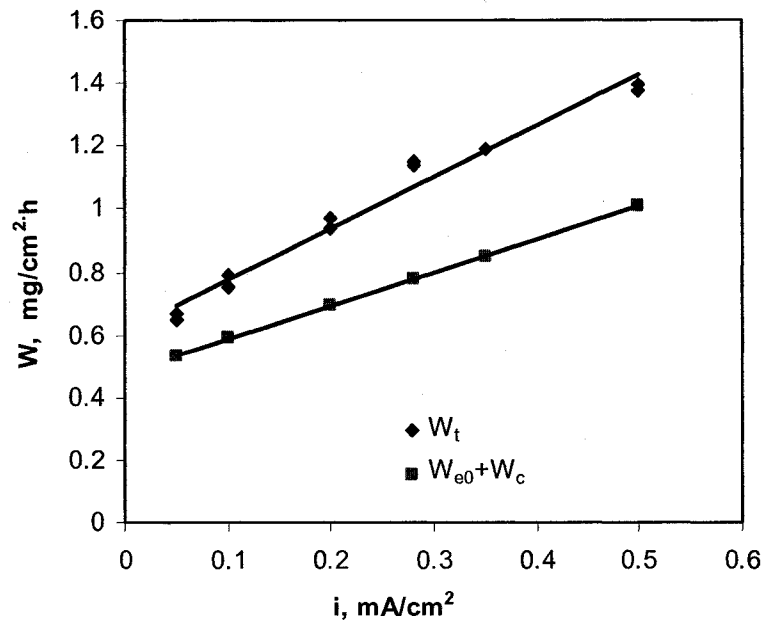


Figure 5-1. Weight loss of carbon steel A1045 as a function of anodic current density in 0.1 M Na<sub>2</sub>SO<sub>4</sub> solution: (a) in 25% slurry; (b) in 35% slurry.



**Figure 5-2. Weight loss of carbon steel A1045 as a function of anodic current density in tap water with 35% sand.**

The corrosion reaction occurred on the electrode (target material) surface, and thus its influence, if there was one, on the first two aspects was expected to be indirect. During the anodic reaction, the metallic elements entered the solution in form of ions or compounds. At the same time, the cathodic reaction can alter the pH value of the solution. Both of these reactions could change the physical and chemical properties of the solution. Changes in the solution, however, cannot affect the properties of the sand particles. On the other hand, according to the test data summarized by Hutchings [7] some physical properties of the solution, such as viscosity, can affect the erosion process. Thus, there existed some possibility to influence the hydrodynamic property of sand particles by altering solution properties. To examine the possible effect of the change in solution physical properties on the erosion process, erosion experiments under CP condition were conducted in a newly prepared  $\text{Na}_2\text{SO}_4$  solution, a used  $\text{Na}_2\text{SO}_4$  solution, and in tap water. The used  $\text{Na}_2\text{SO}_4$  solution was the one in which the sample was corroded at -400 mV for 1 h. **Figure 5-3** shows the pure erosion rates of carbon steel A1045 in the three solutions.

The pure mechanical erosion rate was approximately independent of the type of solution. It meant that the effect due to a change in a solution physical property, as a result of corrosion process on the erosion, was negligible.

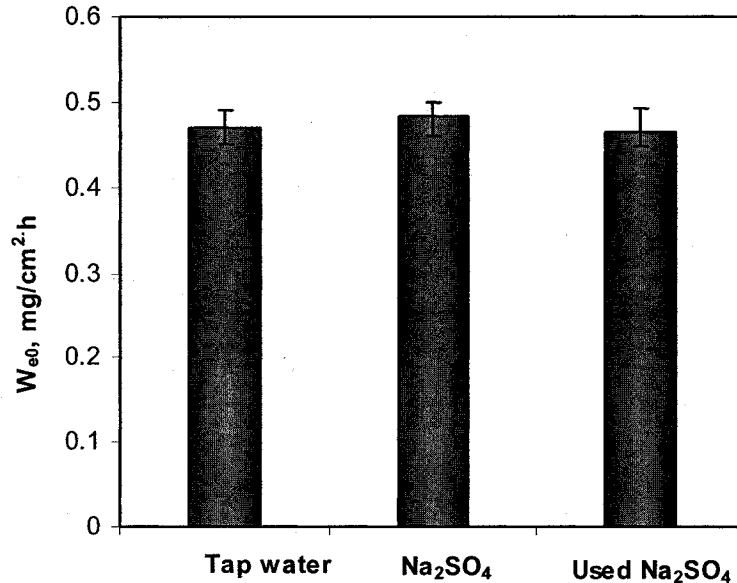


**Figure 5-3. Pure erosion rates of carbon steel A1045 in tap water, new and used Na<sub>2</sub>SO<sub>4</sub> solution with 35% sand.**

As a consequence of the above analysis, the facilitation of corrosion on erosion stemmed from a corrosion-induced mechanical property degradation of the electrode.

### **5.1.3 Chemo-mechanical model for corrosion-enhanced erosion**

Based on the experimental results and analysis, it was believed that the corrosion process accelerated the erosion rate through degrading the mechanical property of the target material. This effect has been termed chemo-mechanical effect in the literature. Before the relationship between the corrosion-enhanced erosion and corrosion parameters was developed, two dependences needed to be clarified: one was the dependence of erosion rate on the mechanical property of metallic material, and the other was the dependence of the mechanical property on the corrosion rate.

### 5.1.3.1 Dependence of erosion rate on mechanical property

Mechanical properties can influence the erosion resistance of materials, but none of them has been found to possess a general relationship with the erosion rate. However, due to the extensive investigation background and measurement convenience, hardness was chosen as the mechanical parameter to relate to the erosion rate, although there still are some contradictory conclusions on its effect [8, 9].

To obtain different hardnesses, some A1045 specimens were heated at 500 °C, 850 °C and 1025 °C in flowing argon and kept for 1 h, followed by furnace cooling to room temperature. **Figure 5-4** shows the Vicker's hardness of A1045 samples after heat treatment. The hardness of the sample decreased with an increase in the heating temperature, which can be ascribed to the grain growth during heat treatment.

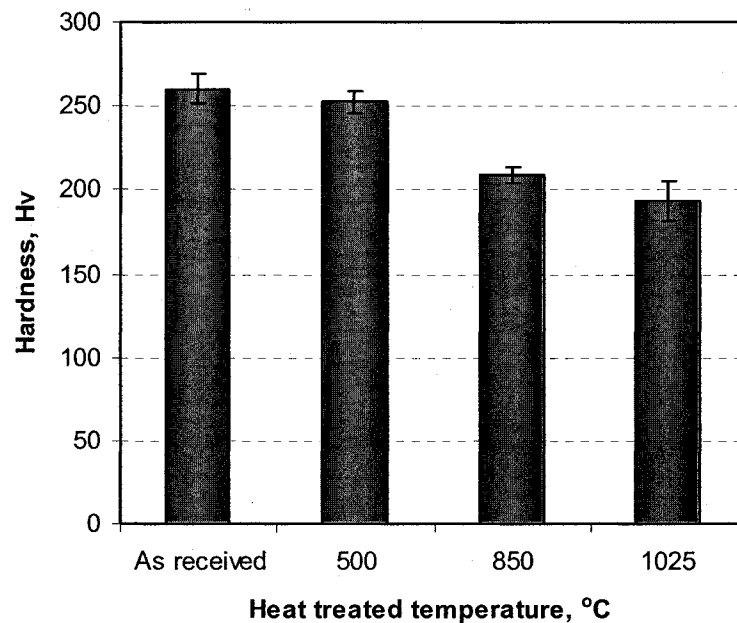


**Figure 5-4. Vicker's hardness of carbon steel A1045 as a function of heat treated temperatures.**

After heat treatment, the pure erosion rates for each type of samples were measured in 25% slurry with a rotating velocity of 9,000 rpm, and the result is shown in **Figure 5-5**. Obviously, the erosion resistance decreased with the drop of hardness. This test result was consistent with the test data summarized by Hutchings [7, 10], Oka et al.[11] and Heitz [12].

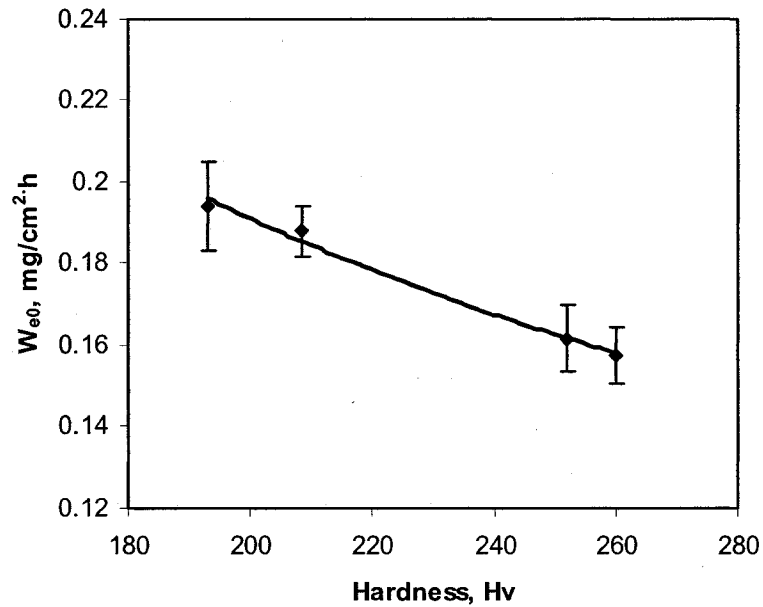


**Figure 5-5. Dependence of pure erosion rate of carbon steel A1045 on Vicker's hardness in 25% slurry.**

The correlation between the hardness and the mechanical erosion rate of the carbon steel can be approximately formulated by the following empirical expression [11, 13, 14],

$$W_{e0} = \kappa H\nu^{-\nu} \quad (5-1)$$

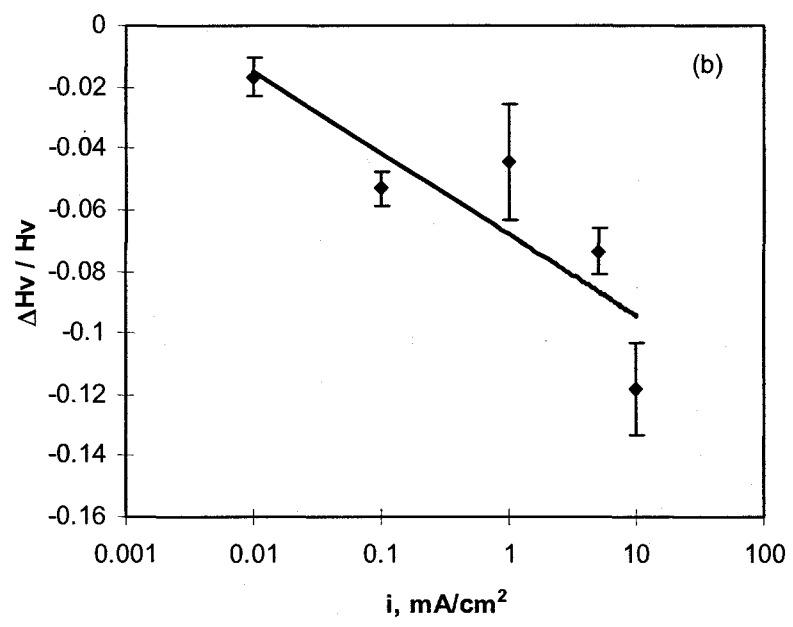
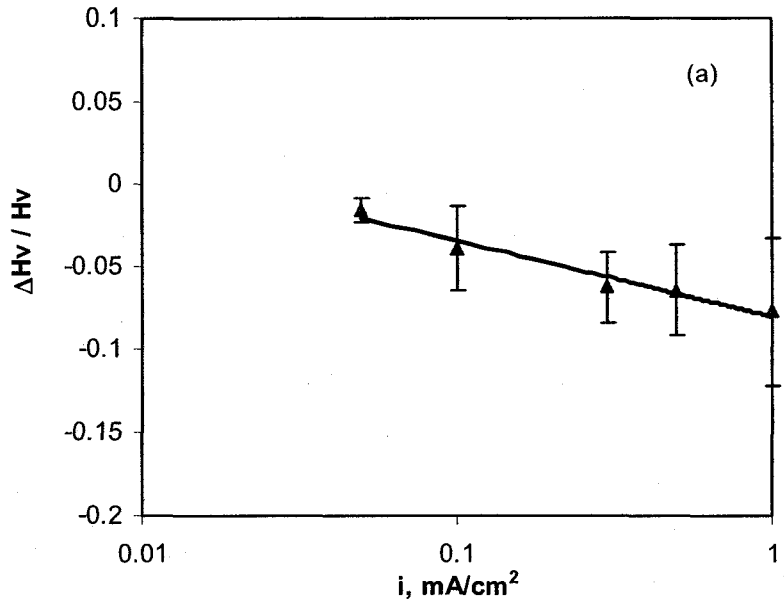
where  $\kappa$  and  $\nu(> 0)$  are experimental constants.

### 5.1.3.2 Relation of mechanical property to corrosion

Based on the theories of non-equilibrium thermodynamics and dislocation kinetics, a theoretical model for corrosion-promoted plasticity has been developed [6]. In line with this model, the hardness of a metallic electrode decreases when anodic dissolution is applied. The relative hardness degradation can be correlated to the anodic current density. The equation was presented in Chapter 2, and is rewritten as follows,

$$\frac{\Delta H_v}{H_v} = -B \log \left[ \frac{i_a}{i_{th}} \right] \quad (2-10)$$

Although some experimental evidence about the chemo-mechanical effect has been reported for different metallic materials [3, 6, 15-18], this phenomenon is not accepted extensively. In the present investigation, the dependence of sample hardness on applied anodic current density was measured in four solutions, and the results are shown in **Figure 5-6**. In the tests, indentations were made immediately after the anodic current was imposed. Since the anodic current at the surface can only affect the mechanical property within a thin surface layer, a small indenting load of 50 g was used. A great scatter band of the test data was observed because the impression area produced by the indenter was small and its shape was irregular. In spite of the scattered test data, it still can be found that the surface hardness degraded with increasing anodic current density. A linear relationship between the hardness degradation and the logarithm of average anodic current density was found. This was consistent with the results reported by Lu and Luo [6].



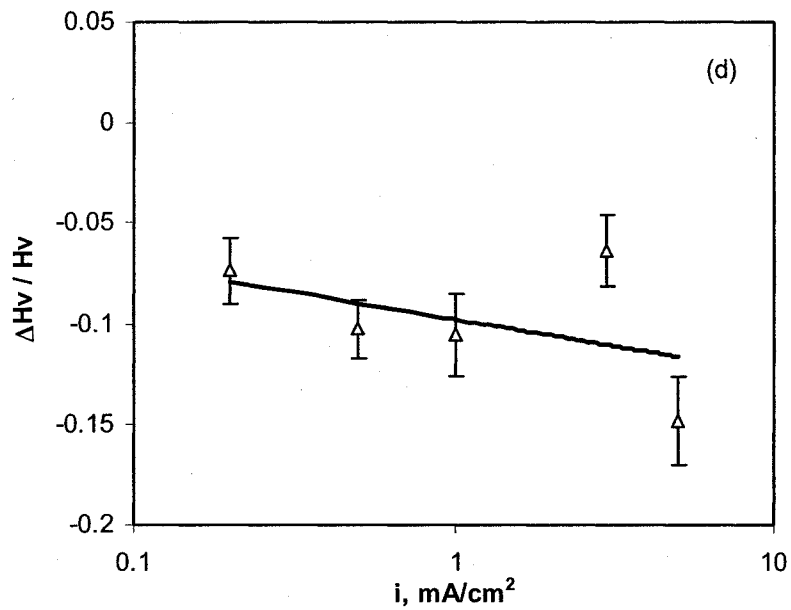
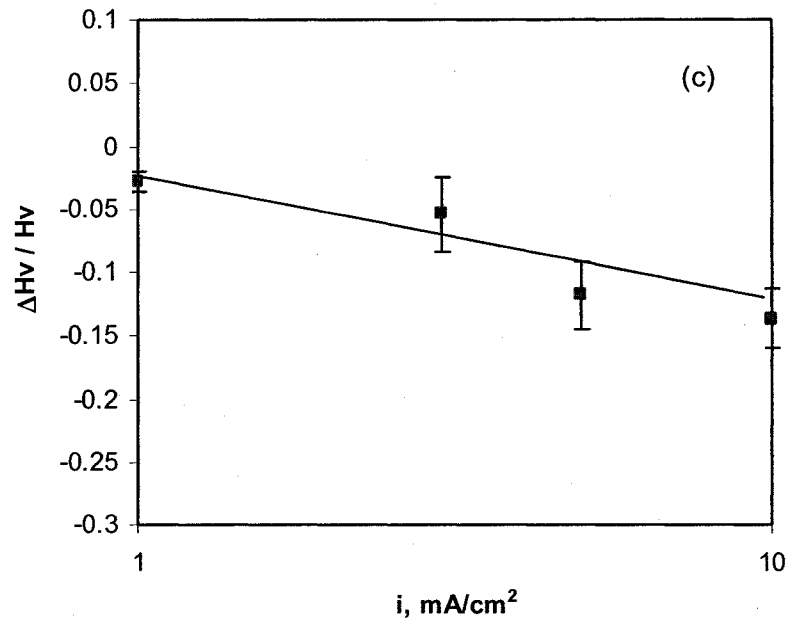


**Figure 5-6. Hardness degradation of carbon steel A1045 caused by applied anodic current: (a) in tap water, (b) in 1 M NaHCO<sub>3</sub> solution, (c) in 0.001 M Na<sub>2</sub>SO<sub>4</sub> solution, and (d) in 0.1 M Na<sub>2</sub>SO<sub>4</sub> solution.**

### 5.1.3.3 Dependence of synergistic effect on corrosion

From the experimental results, when the anodic dissolution took place on electrode surface, the hardness of the electrode layer decreased, thus resulting in an increase in erosion rate. In the case where the mechanical property degradation in surface layer was the mechanism for corrosion-enhanced erosion, with the aid of Equation (5-1), the wastage caused by the corrosion-enhanced erosion can be formulated as [6]:

$$\begin{aligned} W_{c-e} &= \kappa(Hv^*{}^{-\nu} - Hv^{-\nu}) = W_{e0} \left[ \left( \frac{Hv^*}{Hv} \right)^{-\nu} - 1 \right] \\ &= W_{e0} \left[ \left( 1 + \frac{\Delta Hv}{Hv} \right)^{-\nu} - 1 \right] \approx -\nu W_{e0} \left( \frac{\Delta Hv}{Hv} \right) \end{aligned} \quad (5-2)$$

Substituting Equation (2-10) into Equation (5-2) can give the following relationship:

$$\frac{W_{c-e}}{W_{e0}} = Z \log \left( \frac{i_a}{i_{th}} \right) \quad (5-3)$$

where  $Z = \nu B$ . According to this equation, the normalized corrosion-enhanced erosion rate,  $W_{c-e}/W_{e0}$ , increases with anodic dissolution rate. Since the material losses due to the electrochemical corrosion under the galvanic conditions were controlled by the applied current density when the electrode potential was far away from  $E_c$ , the wastage due to the corrosion-enhanced erosion can be calculated from the test data given in **Figure 5-1** with the equation

$$W_{c-e} = W_t - W_c - W_{e0} \quad (5-4)$$

The relationship between the applied anodic current density and the wastage ratio  $W_{c-e}/W_{e0}$  is shown in **Figure 5-7**. At the same time, similar experiments and calculation methods were employed for the samples heat-treated at 1025 °C and the results are shown in **Figure 5-8**. As predicted with the above analysis, the values of  $W_{c-e}/W_{e0}$  can be approximately formulated as a linear function of the logarithm of

anodic current density. These results indicated the erosion can be enhanced by the chemo-mechanical effect when corrosion occurred simultaneously.

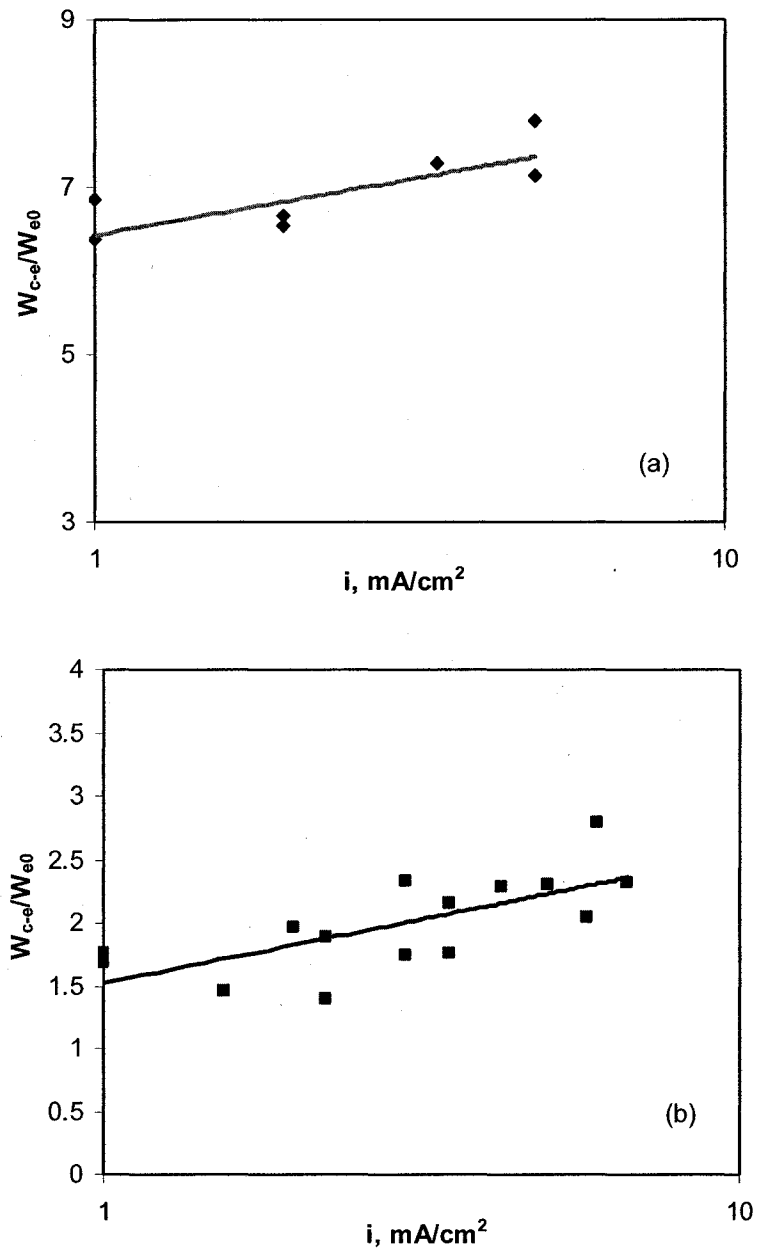


**Figure 5-7. Normalized corrosion-enhanced erosion as a function of anodic current density in slurries containing 25% sand (a) and 35% sand (b).**

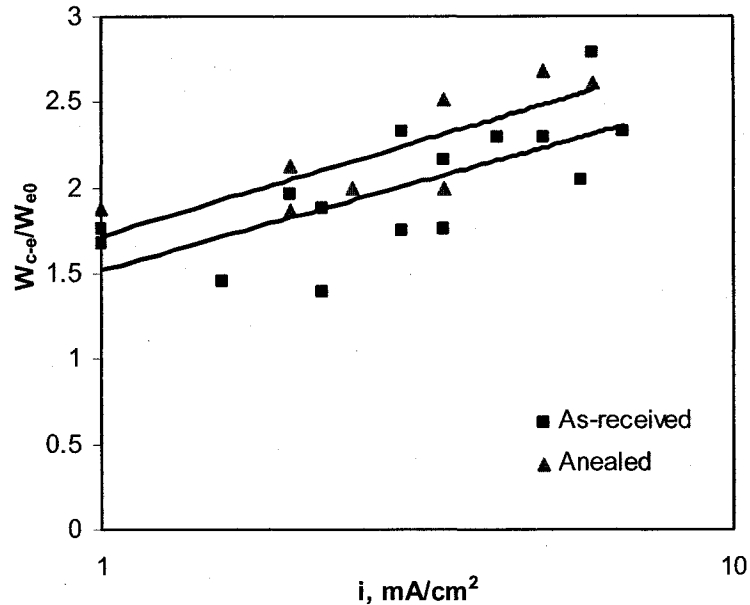


**Figure 5-8. Normalized corrosion-enhanced erosion for as-received and annealed carbon steel A1045 in 35% slurry.**

However, the corrosion-enhanced erosion rate estimated with Equations (5-1), (2-10) and (5-3) were much lower than those experimentally determined. Two reasons could be attributed to this phenomenon. First, the load used in the hardness measurement might be too high, resulting in an indentation depth greater than that of the layer affected by the anodic current. As mentioned in the literature review, the anodic current applied can only affect the mechanical properties of a very thin layer on the specimen surface. Therefore, the hardness degradation could be underestimated when the load used in the micro-hardness measurement was too high. Second, it was possible that there were some synergistic mechanisms other than anodic dissolution-induced erosion resistance degradation during the erosion-corrosion process. Both of these processes could lead to a higher erosion rate than theoretically predicted. More work was necessary to understand the effect of corrosion on erosion.

#### 5.1.4 Summary

- (1) In the carbon steel/sodium sulphate solution system, corrosion significantly accelerated the erosion rate so that the total weight loss was much higher than the sum of corrosion rate and pure erosion rate.
- (2) The surface hardness of A1045 electrode decreased with applied anodic current density and the drop of hardness due to corrosion was a linear function of the logarithm of the average anodic current density.
- (3) The wastage of carbon steel A1045 caused by the corrosion-enhanced erosion increased with the anodic current density and was a linear function of the logarithm of the average anodic current density, showing that the mechanical property degradation induced by the anodic dissolution was an important synergistic mechanism in erosion-corrosion.

## 5.2 Corrosion-enhanced erosion in flowing solution

### 5.2.1 An interesting experimental phenomenon

As described in Chapter 3, to separate the individual material loss in an erosion-corrosion process, the pure corrosion rate  $W_{c0}$  needed to be determined. Usually, two methods were used to estimate  $W_{c0}$  in a corrosive solution without solid particles. One was measuring the weight loss of the sample directly after the test, denoted as  $W_m$ . The other one was calculating the corrosion rate with the Faraday's secondary law, denoted as  $W_f$ , and we have

$$W_f = M \frac{i_a}{nF} \quad (5-5)$$

where  $M$  is the molar weight of the metal.

In corrosive environments free of solid particles, when cavitation was not significant, it was usually believed that the mass losses were dominated by corrosion. Therefore, the corrosion rates measured using these two methods were believed to be consistent with each other, and so these two methods were often used equivalently in erosion-corrosion studies [19-21]. However, it was found from our experimental results that the mass loss rates experimentally measured with the traditional weight loss method, effectively the total weight loss of the sample, were always higher than that calculated with Faraday's law if the flowing velocity of solution was sufficiently high.

This phenomenon suggested the existence of an additional material loss in flowing corrosive liquids free of solid particles. Several researchers also found similar phenomena, but little attention has been paid to it and no further investigation was performed [22-25]. Efirid et al. [25] pointed out that this part of the material losses may result from the flowing of liquid. Weight loss measurements included the material loss from the flow effect while electrochemical measurements did not, but how the flowing liquid resulted in this extra material loss was still unknown.

Sankaran [24] attributed this difference to the flow-induced-corrosion because it depended on velocity. However, the nature of such a “flow-induced corrosion” was not pointed out. If it was an electrochemical process, its contribution to the material losses would be able to be calculated with Faraday’s secondary law. Obviously, the mechanism behind this extra material loss was still unknown.

In this part of work, an attempt was made to get some insight into this phenomenon and to understand the mechanism behind it.

### 5.2.2 Phenomenon analysis

In order to clarify the special experimental phenomenon, the ratio values of the measured weight loss rate to the calculated one,  $W_m/W_f$ , are present in **Figure 5-9** for different conditions. The tests were carried out with an applied current density of 2 mA/cm<sup>2</sup>. For case (a), the solution was still and without sand. The ratio was very close to unity, suggesting that the corrosion obeyed Faraday’s law under this condition. For case (c), the test was conducted in 35% silica sand slurry at a rotating velocity of 9000 rpm. The ratio was much higher than unity, which was not unexpected because the erosion effect from sand impingement in the flowing slurry can cause substantial mechanical damage to the sample. This part of the material loss cannot be calculated with Faraday’s law. For case (b), however, the ratio was still much higher than unity, although the test was performed in solution at a rotating velocity of 9000 rpm in the absence of sand. It suggested an extra material loss in addition to the pure corrosion.

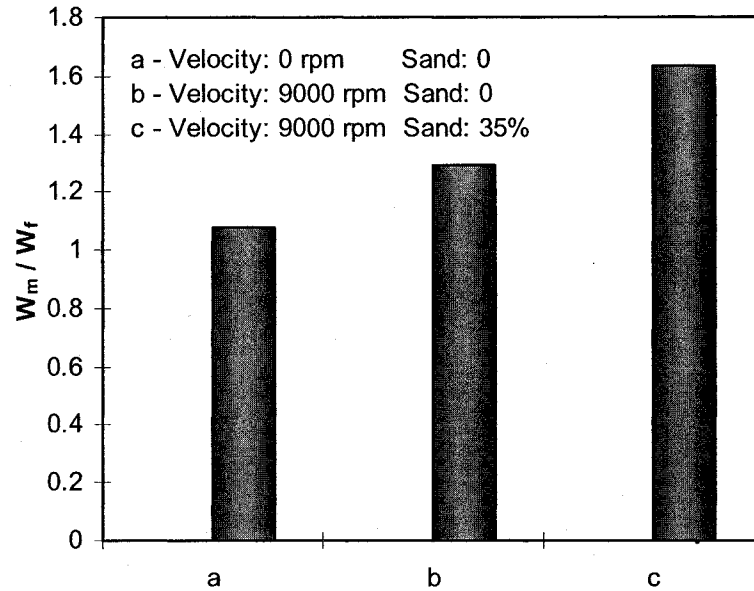


**Figure 5-9. Ratio of  $W_m/W_f$  for carbon steel A1045 at an applied current density of 2 mA/cm<sup>2</sup>.**

The error from uncompensated cathodic current was estimated. According to the potentiodynamic curves measured in the test solution at a rotating velocity of 9000 rpm, as shown in **Figure 5-10 (a)**, the polarization potential corresponding to the applied current density of 2 mA/cm<sup>2</sup> was about -302 mV. This potential was 126 mV above the corrosion potential, -428 mV. With this level of polarization, the anodic current density was usually much higher than the cathodic one, and the dissolution process of the metal was almost identical to the applied current density [26]. Also, Ives et al. [27] studied the oxygen cathodic reactions rate using a rotating gold disc electrode and found that the oxygen reduction rate increased significantly with rotating velocity only when the potential was lower than -350 mV(SCE). Hence the cathodic reduction rate at -302mV under flowing condition might be close to that under still solution condition. In **Figure 5-10**, the extrapolation method was used to estimate the cathodic current, but it is necessary to be pointed out that this method may result in overestimation. However, even if the cathodic reduction rate was estimated from point A in **Figure 5-10 (a)**, the possible maximum cathodic current density came around 0.18 mA/cm<sup>2</sup>. Then we have

$$i = i_a - |i_c| = 2 \text{ mA/cm}^2 \text{ with } |i_c| = 0.18 \text{ mA/cm}^2,$$

where  $i$  is the total current density present on the electrode surface,  $i_a$  and  $i_c$  are the anodic and cathodic current density respectively. Then

$$\frac{W_m}{W_f} = \frac{i_a}{i} = \frac{i + |i_c|}{i} = 1.09$$

This means that the maximum error arising from uncompensated cathodic reduction could not be higher than 10%, whereas the ratio of  $W_m$  to  $W_f$  for case (b) in **Figure 5-9** was 1.29, i.e, the difference in the value  $W_m$  from  $W_f$  did not result from error induced by an uncompensated cathodic reduction reaction. On the other hand, from **Figure 5-10 (b)** when the rotating velocity was higher than 3000 rpm, the oxygen reduction rate, which could be obtained from points C, D, and E, did not change markedly with velocity. At the same time, the anodic polarization behavior of carbon steel was almost the same in this range of velocity. Thus, the values of  $W_m/W_f$  should have appeared very close. However, in this velocity range, there existed a linear relationship between  $W_m/W_f$  and velocity, which will be shown later.

The above analysis suggested the difference between the measured mass loss and the calculated value did not come from error caused by the cathodic reduction reaction. Moreover, the additional weight loss was not caused by flow-induced corrosion because the flow-induced corrosion was essentially an electrochemical process accelerated by flowing of solution [28-30] and its contribution can be reflected in the corrosion current enhanced by flowing of corrosive media. Therefore, the extra weight loss can be regarded as a non-Faraday material loss resulting from a mechanical damage mechanism other than an electrochemical process.

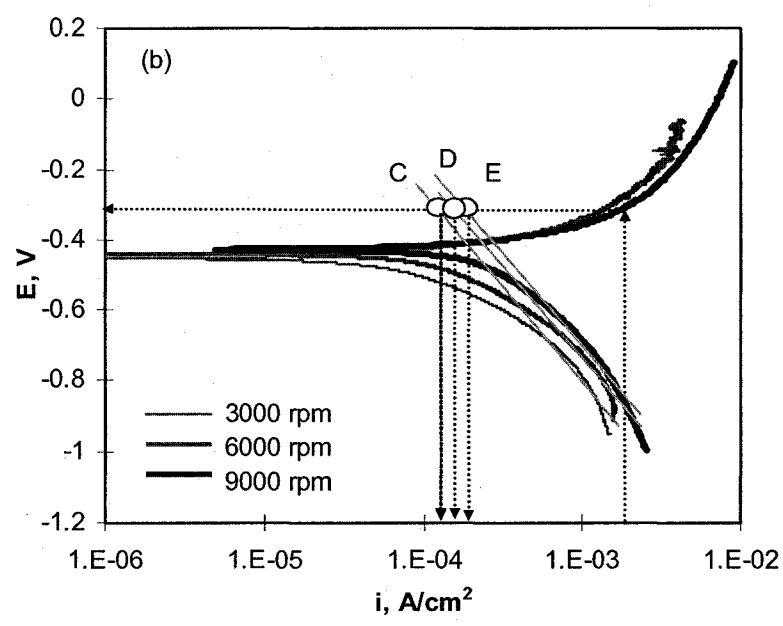
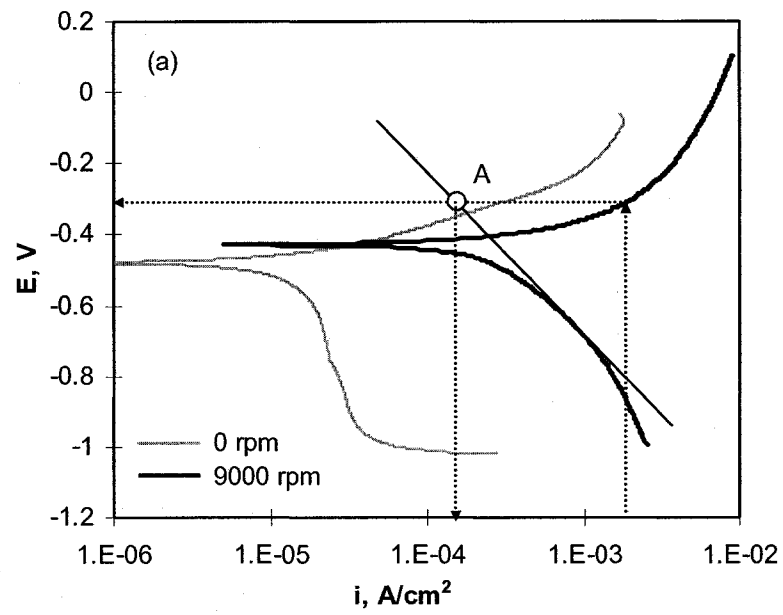


**Figure 5-10. Polarization behavior of carbon steel A1045 in 0.1 M Na<sub>2</sub>SO<sub>4</sub> solution at different rotating velocities.**

The flow velocities adopted in the present experiments were too low to induce cavitation erosion. This was verified by the experiments performed in the flowing solution under CP. The result showed that the mass loss was below the detection limit of the balance (0.0002 g) after the test was conducted at a rotating velocity of 9000 rpm for 10 h. Such a mass loss rate ( $<0.003\text{mg/cm}^2\cdot\text{h}$ ) was much lower than the difference between the calculated value and the experimental measured value. Thus, the extra material loss could not be attributed to a pure mechanical erosion mechanism.

Actually, the measured weight loss was always the total weight loss. Thus, in accordance with Equation (2-1) through (2-3), the measured weight loss can be described by

$$W_m = W_{c0} + W_{e0} + W_{c-e} + W_{e-c} \quad (5-6)$$

All terms related to electrochemical corrosion,  $W_{c0}$ , and  $W_{e-c}$  if present, were controlled by the applied current density, i.e.,

$$W_f = W_{c0} + (W_{e-c}) \quad (5-7)$$

The pure erosion rate was approximately zero without cavitation or impingement from solid particles.

$$W_{e0} \approx 0 \quad (5-8)$$

Then only one term in Equation (5-6) was left, i.e.  $W_{c-e}$ . Thus,

$$W_m = W_f + W_{c-e} \quad (5-9)$$

Therefore, it was the wastage component of  $W_{c-e}$  which resulted in the extra mass loss. Since Faraday's law cannot formulate its relation to anodic current density,  $W_{c-e}$  was not directly caused by the electrochemical process. In addition,  $W_{c-e}$  was absent when the corrosion process was inhibited, as indicated by the weight loss test under CP. Therefore, this weight loss component can be termed as corrosion-induced

erosion, which occurred in the corrosive solution free of solid particles when the flow velocity was sufficiently high.

### 5.2.3 Factors affecting the corrosion-induced erosion

#### 5.2.3.1 Effect of velocity

Figures 5-11 and 5-12 show the mass loss ratio  $W_m/W_f$  and the corrosion-induced erosion rate  $W_{c-e}$  as a function of rotating velocity with an applied current density of 2 mA/cm<sup>2</sup> and 1.5 mA/cm<sup>2</sup>, respectively. There existed a critical velocity to induce the corrosion-induced erosion. When the rotating velocity was below the critical velocity, around 2000 rpm,  $W_m/W_f$  and  $W_{c-e}$  were nearly independent of velocity, the ratio was very close to unity, and there was no apparent synergistic effect. However, when the velocity was higher than the critical velocity,  $W_{c-e}$  appeared significant and increased linearly with velocity. It suggested that this part of the weight loss depended heavily on the hydrodynamic conditions. For a concentric cylinder system, the inner Reynolds number can be estimated with the following equation

$$\text{Re} = \frac{r_i \cdot \omega \cdot d_i}{\nu} \quad (5-10)$$

where  $r_i$  is the inner cylinder radius, i.e., the outer radius of the sample for the present system,  $\nu$  is the kinematic viscosity of the solution, and  $d_i$  is the difference between the outer and inner radii, which is the distance between the sample surface and the cell wall. The rotating velocity of 500~9000 rpm approximately corresponded to a Reynolds number of  $8.2 \times 10^3 \sim 1.5 \times 10^5$  for the present system. Since the critical Reynolds number for transition from laminar flow to turbulent flow was no higher than 2000 for the rotating cylinder system, the flow pattern in this whole range of velocity was turbulent flow [31, 32]. Thus the critical velocity for  $W_{c-e}$  here cannot be attributed to the transition from laminar flow to turbulent flow.

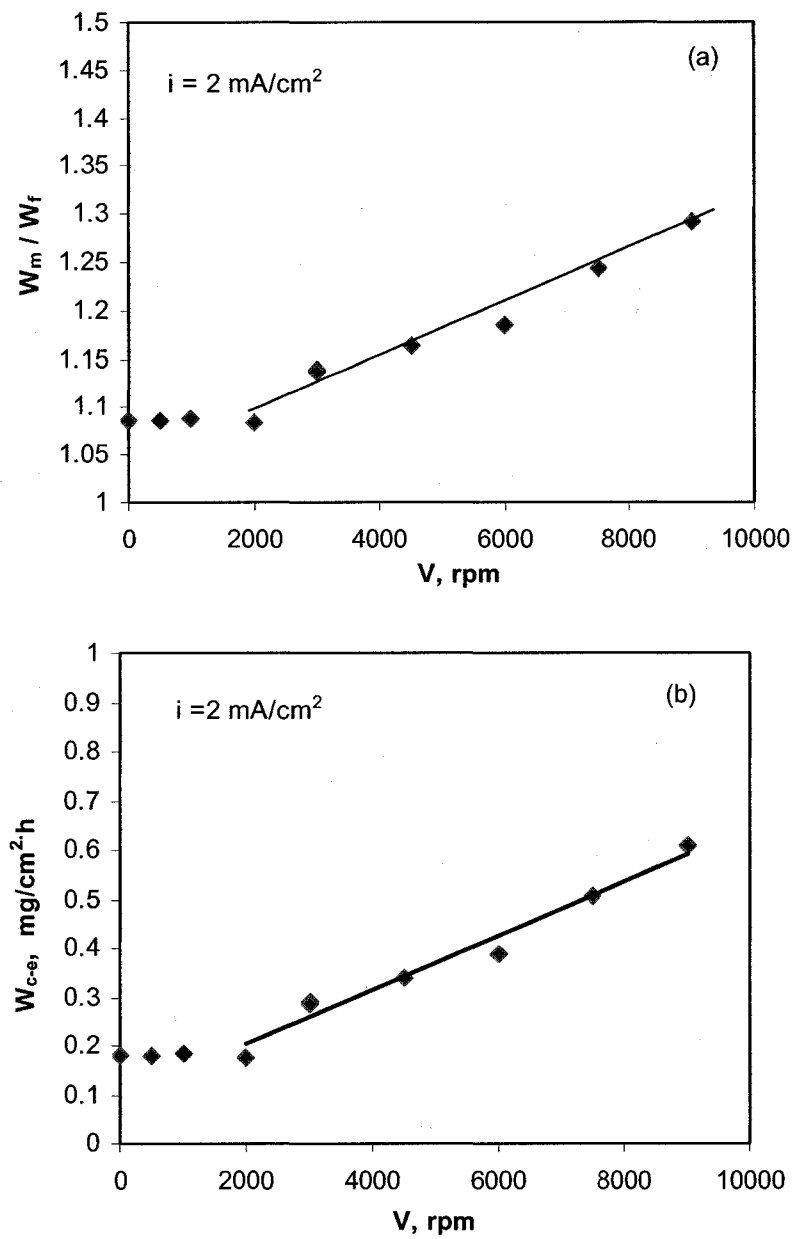
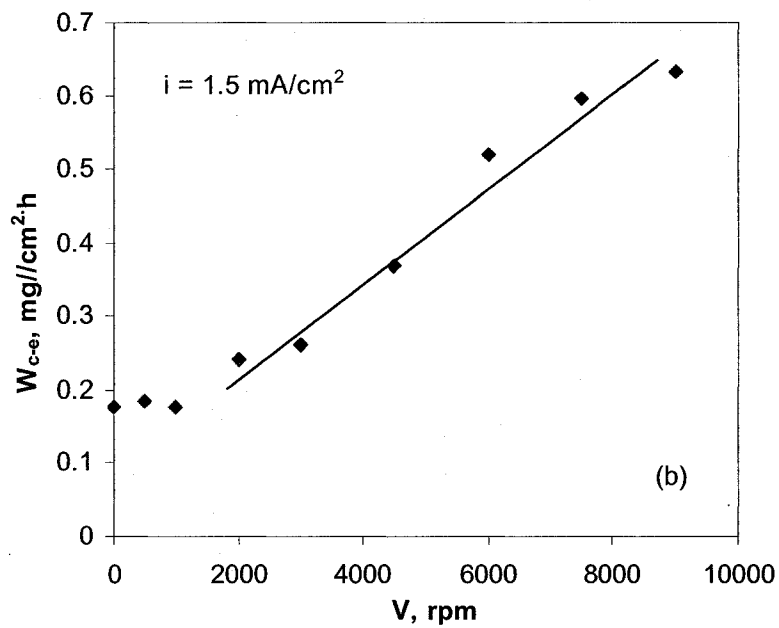
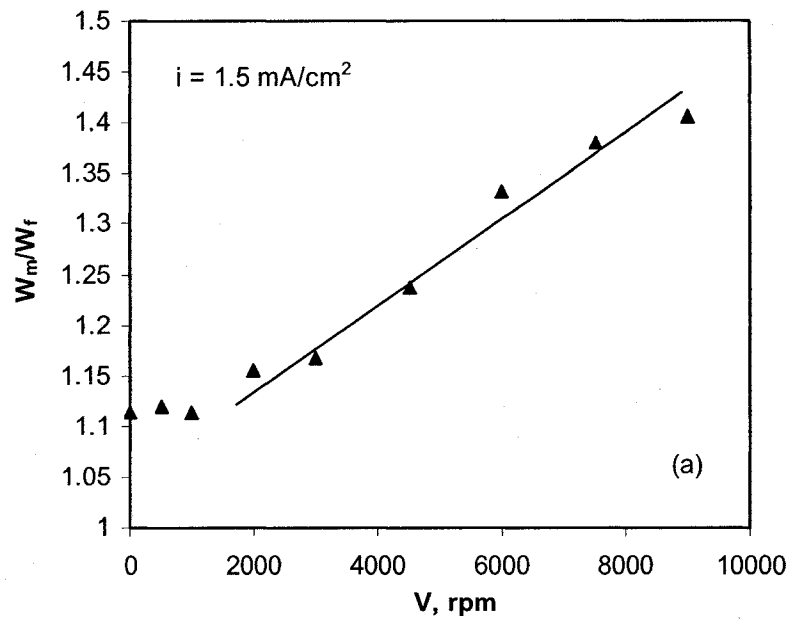


Figure 5-11. Dependence of corrosion-induced erosion on rotating velocity with an applied current density of  $2 \text{ mA/cm}^2$  : (a)  $W_m / W_f$  vs. velocity, (b)  $W_{c-e}$  vs. velocity.



**Figure 5-12. Dependence of corrosion-induced erosion on rotating velocity with an applied current density of  $1.5 \text{ mA/cm}^2$ : (a)  $W_m/W_f$  vs. velocity; (b)  $W_{c-e}$  vs. velocity.**

### 5.2.3.2 Effect of anodic current density

The dependence of  $W_{c-e}$  on the anodic current density at different flowing velocities is demonstrated in **Figure 5-13**. The corrosion-induced erosion wastage increased with the applied anodic current density. This observation confirmed again that  $W_{c-e}$  was not solely caused by a pure mechanical damage process. It is worthy to note that  $W_{c-e}$  can be approximately expressed as a linear function of the logarithm of anodic current density.

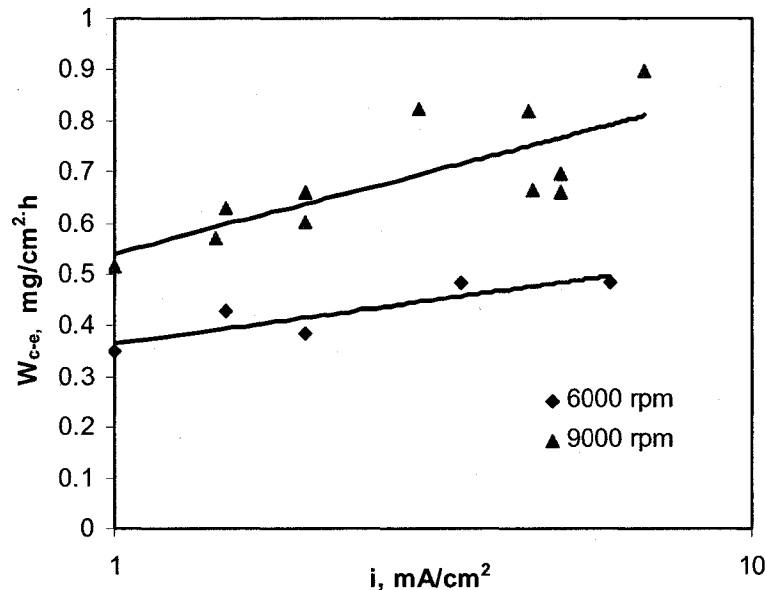


**Figure 5-13. Dependence of corrosion-induced erosion on current density in 0.1 M Na<sub>2</sub>SO<sub>4</sub> solution.**

### 5.2.3.3 Effect of hardness

Carbon steel samples with different hardnesses were adopted in the present experiments to understand the effect of mechanical properties on the corrosion-induced erosion. Some samples that were annealed at 1050°C for 1 h were used. **Figure 5-14** shows  $W_m / W_f$  and  $W_{c-e}$  as a function of velocity for the as-received sample and the annealed sample. With constant applied current density the corrosion-induced erosion rate for annealed sample was higher than that for as-received sample. This test result was similar to that shown in **Figure 5-8**. It implied that  $W_{c-e}$  may be

related to certain corrosion-induced mechanical property degradation in the surface layer since it can be enhanced by a decrease in hardness.

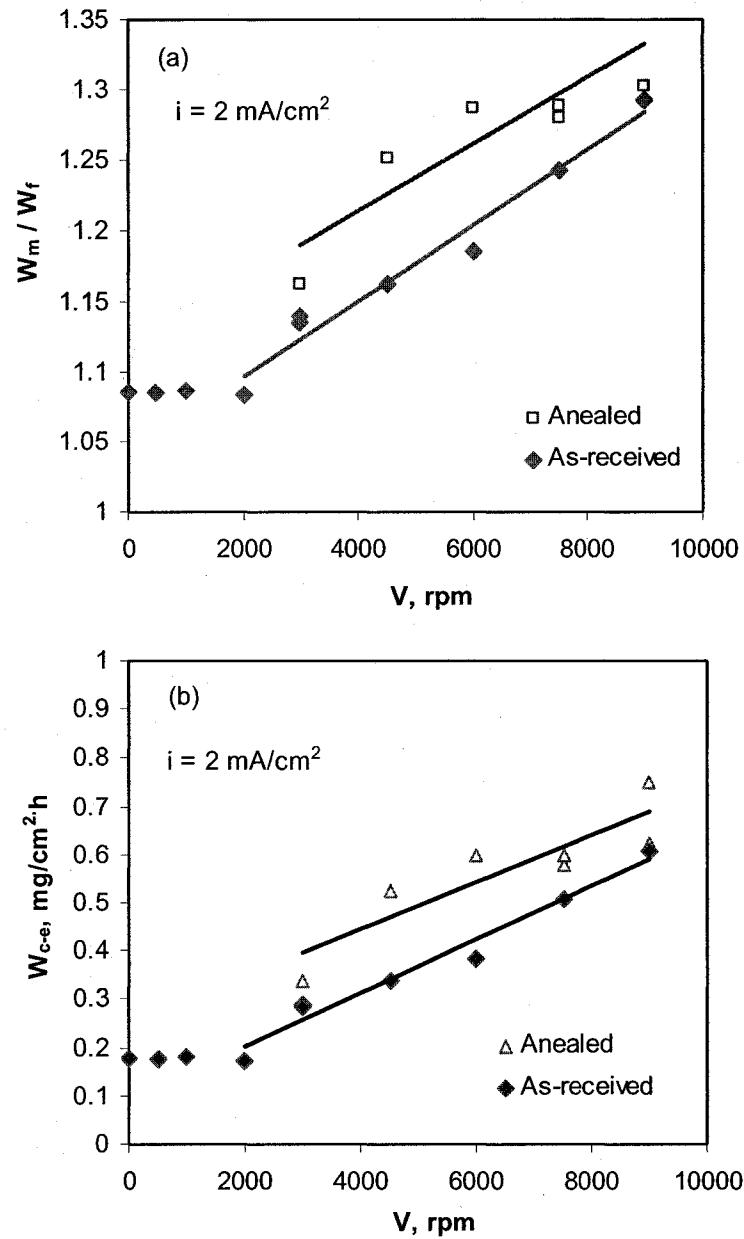


**Figure 5-14. Corrosion-induced erosion as a function of velocity for as-received and annealed carbon steel A1045 samples in 0.1 M Na<sub>2</sub>SO<sub>4</sub> solution: (a)  $W_m / W_f$  vs. velocity; (b)  $W_{c-e}$  vs. velocity**

#### 5.2.3.4 Effect of solution pH

Since  $W_{c-e}$  resulted from the interaction between the electrochemical process and the mechanical process, it could be affected by the electrode reaction. Based on this concern, the effect of solution pH was investigated. Weight loss tests were carried out in solutions with different pH (4, 7 and 10) under the same flow velocity and applied current density. The results are shown in **Figure 5-15**.  $W_{c-e}$  was found to be the highest in acidic solution, and the lowest in neutral solution. However, the difference between the loss rates in these solutions was not marked. It implied  $W_{c-e}$  may result from a mechanical degradation in the surface layer caused by the anodic dissolution. In other words, the anodic dissolution rate seemed to be an important factor controlling this non-Faraday material loss, while the effect of solution pH, at least in the present corrosion system, was not significant.

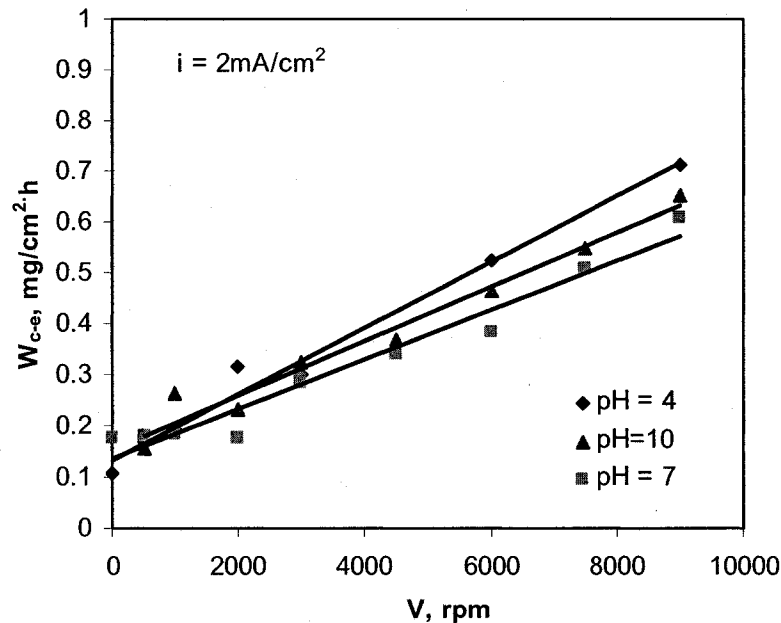


**Figure 5-15. Corrosion-induced erosion of carbon steel A1045 as a function of rotating velocity in solution with different pH.**

#### 5.2.4 Discussion

In view of slurry erosion-corrosion,  $W_{c-e}$  is related to the mechanical damage directly. If we remove the solid particle from the slurry gradually, the wastage of pure mechanical erosion will be reduced, and therefore  $W_{c-e}$  will decrease. In the limiting case, when there are no solid particles present in the solution and the cavitation is negligible, it is reasonable to expect that the mechanical damage and hence  $W_{c-e}$  to diminish to zero. However, the experimental observations in this work demonstrated the presence of  $W_{c-e}$  in flowing corrosive solutions free of solid particles.

In regard to the mechanism of material removal, the corrosion-induced erosion in flowing corrosive solution was analogous to the corrosion-enhanced erosion in flowing slurry. Both of them arose from the synergistic effect between corrosion and erosion, and showed similar dependence on media velocity and material properties. Furthermore, their dependence on applied current density was also compared in **Figure 5-16**. The anodic current density exhibited similar impact on the corrosion-induced erosion in flowing electrolyte and on the corrosion-enhanced erosion in flowing slurry. This implied the similarity in mechanisms of these two kinds of phenomena. Hence, the mechanism that has been proposed for the synergistic effect in flowing slurry would give some indications to help understand the corrosion-induced erosion in flowing solution. In this part of the work the chemo-mechanical model was taken into account.

The experimental results have shown that the corrosion-induced erosion disappeared when the sample was under CP. Under such conditions, the corrosion was inhibited and no hardness degradation occurred. At the same time, the corrosion-induced erosion was enhanced by an increase in the anodic current density or by a decrease in the hardness. Therefore, it was reasonable to assume that  $W_{c-e}$  can be expressed as

$$W_{c-e} = \kappa'(-\Delta Hv)^m \quad (5-11)$$

where  $\kappa'$  and  $m$  ( $>0$ ) are experimental constants, and their values depend on the material properties and the hydrodynamic parameters. The experimental results shown in **Figure 5-5** indicated that  $m$  was close to 1 for carbon steel A1045 with a velocity of 9000 rpm. Then,

$$W_{c-e} \approx -\kappa' \Delta H v \quad (5-12)$$

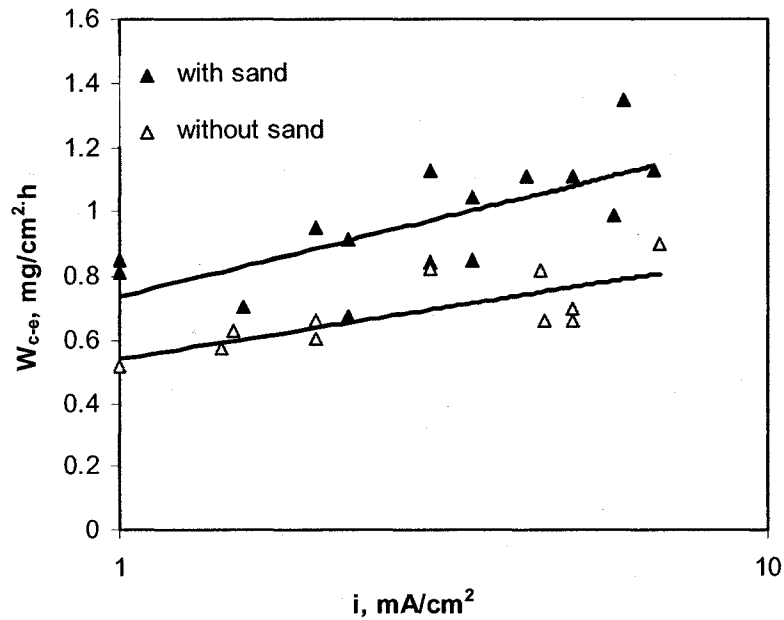


**Figure 5-16. Corrosion-induced erosion as a function of current density in 35% slurry and in solution at velocity of 9000 rpm.**

**Figure 5-17** shows the dependence of the corrosion-induced erosion on the hardness degradation at a rotating velocity of 9000 rpm.  $W_{c-e}$  and  $\Delta H v$  approximately followed a linear relationship, consistent with Equation (5-12). The fitted line should intersect the origin, which made the line slightly deviated from the best fitted line of the data.

Considering the chemo-mechanical effect and inserting Equation (2-10) into Equation (5-12), we have

$$W_{c-e} = -\kappa' \Delta H v = \kappa' B H v \log \left( \frac{i_a}{i_{th}} \right) \quad (5-13)$$

Let  $A_0 = \kappa' B H v$ , then

$$W_{c-e} = A_0 \log \left( \frac{i_a}{i_{th}} \right) \quad (5-14)$$

This expression was very similar to the equation for corrosion-enhanced erosion in slurry. Accordingly, the corrosion-induced erosion rate in solution increased linearly with the logarithm of the anodic current density. This relationship is consistent with the experimental results shown in Figures 5-13 and 5-16. It indicated that mechanical surface damage like erosion on a metallic surface can be induced by anodic dissolution in a flowing solution.

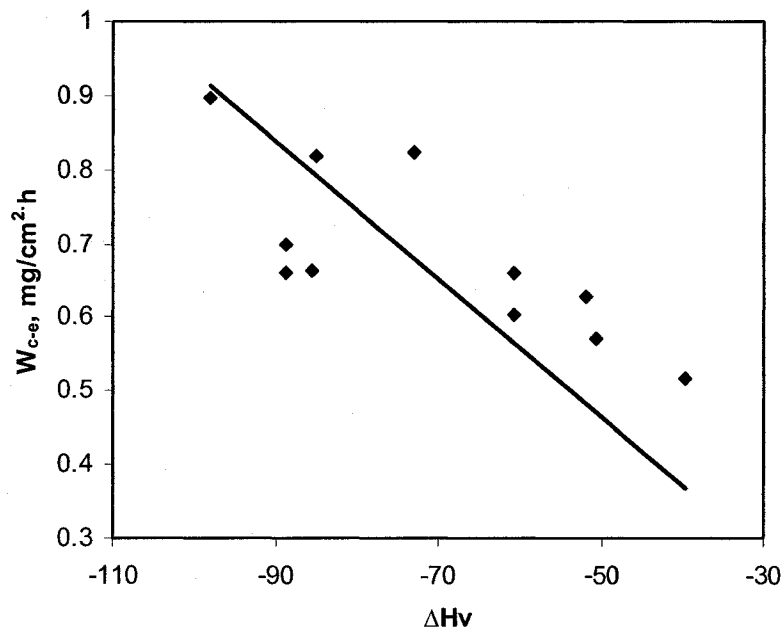


**Figure 5-17. Dependence of corrosion-induced erosion on hardness degradation where  $W_{c-e}$  was measured in flowing solution at 9000 rpm.**

Equation (5-14) showed the corrosion-induced erosion was a linear function of the logarithm of anodic current density. Also, we knew that Faraday's wastage was a

linear function of anodic current density, as indicated by Equation (5-5). Thus, we can have

$$\frac{W_m}{W_f} = \frac{W_f + W_{c-e}}{W_f} = 1 + \frac{nF}{AM} \frac{\log(i_a / i_{th})}{i_a} \quad (5-15)$$

According to this equation,  $W_m / W_f$  reaches its maximum value when  $i_a = e_0 \cdot i_{th}$ , and the second order derivative value for  $i_a = e_0 \cdot i_{th}$  is negative, where  $e_0$  is 2.718. Thus,  $W_m / W_f$  increases with  $i_a$  monotonously for  $0 < i_a < e_0 \cdot i_{th}$  and decreases with  $i_a$  for  $i_a > e_0 \cdot i_{th}$ . Fitting the experimental data in **Figure 5-13** showed that  $i_{th}$  was much smaller than  $0.1 \text{ mA/cm}^2$ . Hence, the applied current densities were much higher than  $e_0 \cdot i_{th}$ . Hence, for the present experimental data  $W_m / W_f$  will decrease with  $i_a$  according to Equation (5-15). **Figure 5-18** shows the value of  $W_m / W_f$  as a function of anodic current density. Consistent with the analysis,  $W_m / W_f$  diminished with the anodic current density.

The corrosion-induced erosion in various conditions can be schematically understood by **Figure 5-19**. Under CP (**Figure 5-19 (a)**), no corrosion occurred on the surface. The atoms in the crystal pack together compactly and the interatomic bonding was strong so that the atoms on the surface can not be removed by the flowing solution if the flowing velocity was not high enough to induce cavitation erosion. As corrosion occurred in a still solution (**Figure 5-19 (b)**), some metal atoms entered into solution as ions through the electrochemical dissolution, and produced supersaturated vacancies in the surface layer, which may weaken the interatomic bonding [4, 16, 18]. This was well demonstrated by the hardness measurements shown in **Figure 5-5**. Because the external force was absent in the still solution, the non-Faradayic material removal cannot take place. Once sufficient mechanical forces due to a hydrodynamic effect were present, the atoms were removed before discharging, and this part of material loss came as corrosion-induced erosion. This might be the process occurring in a flowing corrosive solution, as illustrated in **Figure 5-19(c)**.

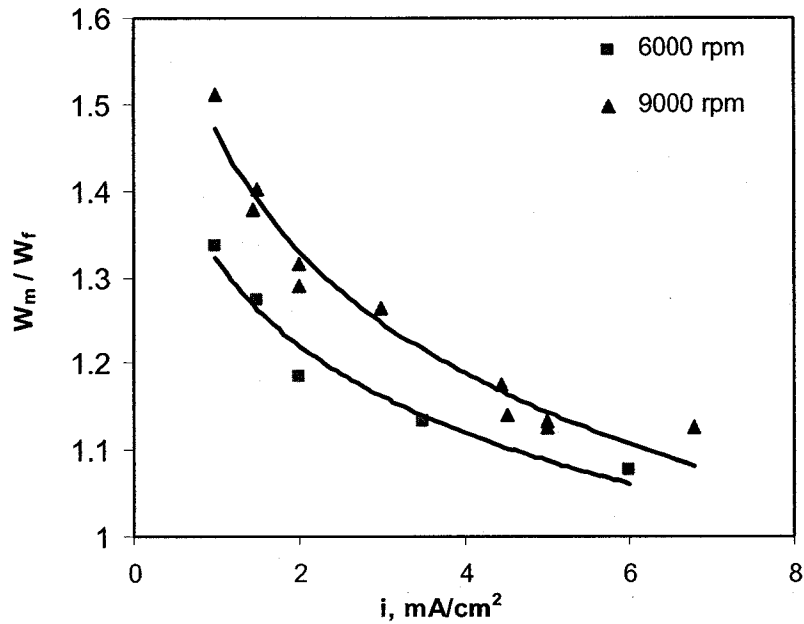


Figure 5-18. Effect of current density on the wastage ratio  $W_m / W_f$  for carbon steel A1045 in 0.1 M  $\text{Na}_2\text{SO}_4$  solution.

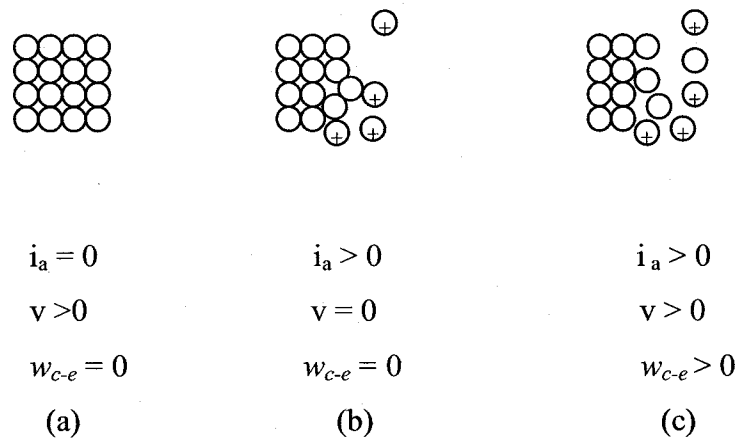


Figure 5-19. Schematic for corrosion-induced erosion: (a) under cathodic protection, (b) in still solution, (c) in flowing solution.

The above analysis was proposed to provide some lucidness to help understand the extra material loss in the flowing corrosive solution. Considering that the mechanical force, such as the wall shear stress, caused by turbulent flow was rather

low, the interatomic bonding between the atoms within the surface layer has to be weak enough so that the corrosion-induced erosion can occur.

### **5.2.5 Summary**

In a flowing corrosive solution free of solid particles, when the flow velocity was sufficiently high the mass loss rates obtained from traditional weight loss measurements were higher than those calculated with Faraday's law. This extra material loss was not a pure mechanical degradation, since under CP, no weight loss was detected. It did not come from the error of cathodic reduction either because the corrosion was completely controlled by the applied current. This material mass loss increased with both flow velocity and applied current density, but decreased with surface hardness. Analysis showed that this material loss arose from a synergistic effect between corrosion and erosion, and thus can be regarded as corrosion-induced erosion. Based on its similarity to the corrosion-enhanced erosion in a slurry, the chemical-mechanical model, proposed for slurry erosion-enhanced corrosion, was tentatively applied to understand the underlying mechanism behind. According to this model, the corrosion-induced erosion resulted from a surface mechanical property degradation caused by the anodic dissolution process on the surface.

## **5.3 Investigation of chemo-mechanical effect by nanoindentation**

### **techniques**

As discussed in Section 5.1 and 5.2, the chemo-mechanical model successfully predicted the linear relationship between the corrosion-enhanced erosion and the logarithm of anodic current density. However, the values of corrosion-enhanced erosion estimated from the theory were much lower than those experimentally determined. One possible reason that could account for this phenomenon was the load used in the hardness measurement was too high to precisely estimate the hardness degradation of the surface layer. Based on this concern, nanoindentation, a technique that allowed determining mechanical properties on a much smaller scale, was employed to further estimate the hardness degradation induced by anodic dissolution.

#### **5.3.1 Introduction**

Since corrosion happens only on the material surface, the corrosion-induced degradation of mechanical properties was expected to be limited within a very thin surface layer and decay quickly inwards towards the bulk material. This could be the reason why anodic-enhanced creep was more readily observed in thin foil or wires [3, 33]. Therefore, the nanoindentation technique was used to further understand the response of mechanical properties to corrosion on a submicron or nanometric scale.

Conventionally, the nanoindentation tests were performed in air [34, 35]. Recently Seo and Chiba [36-38] developed an in situ nanoindentation technique to study the mechanical properties of the passive film during an electrochemical reaction process. This method combined the nanoindentation technique and electrochemical measurements, thereby enabling the determination of the instantaneous response of surface mechanical properties to electrochemical dissolution.

In this part of the work, the in situ nanoindentation technique was employed to investigate the influence of an electrochemical process on the mechanical properties

of the material surface layer. The material used was pure iron along with a 0.01 M  $\text{Na}_2\text{SO}_4$  solution.

### 5.3.2 Nanoindentation tests in air and in liquid

**Figure 5-20** shows the typical indentation images obtained from tests performed in air with peak a load of 200, 600 and 800  $\mu\text{N}$ . By comparing this picture and **Figure 3-1 (b)**, it can be found that the craters produced by the indentation were much smaller than the average grain size of the sample. Therefore, the possibility of making indents in a grain boundary would be very small.

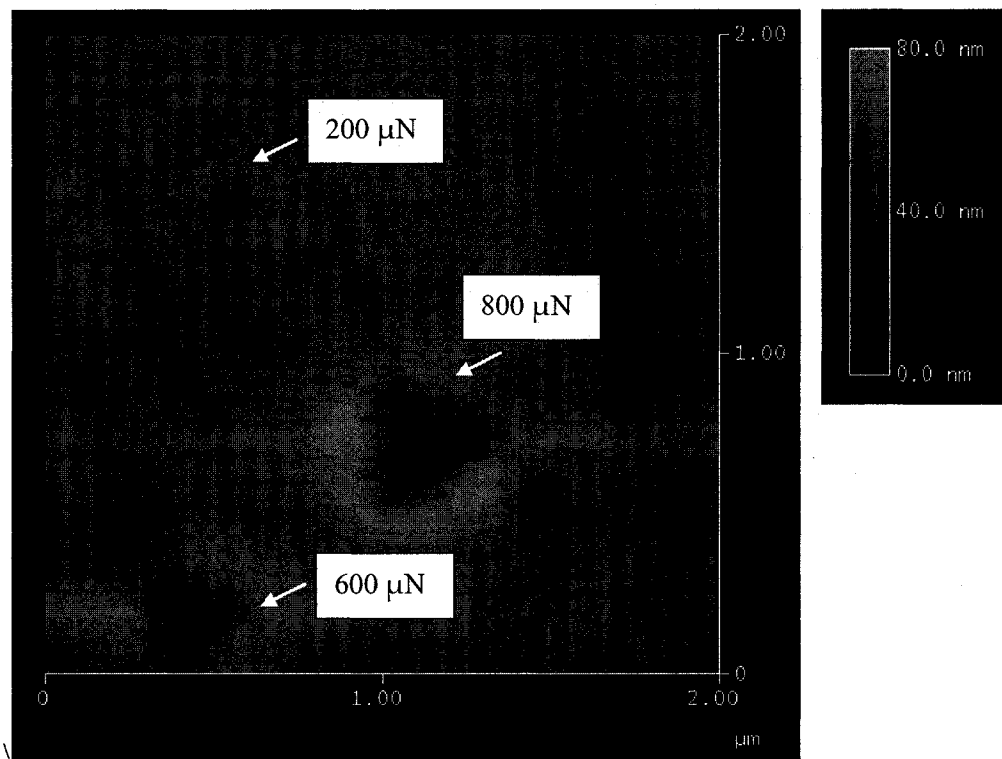


**Figure 5-20.** Typical nanoindentation image on pure iron sample.

**Figure 5-21 (a)** shows the load-depth curves measured in air with a maximum load in the range of 200~2000  $\mu\text{N}$ . With the analysis method mentioned in Chapter 2, the hardness data were determined, as presented in **Figure 5-21(b)**. The hardness tended to decrease with an increase in the indentation depth. Similar results were also

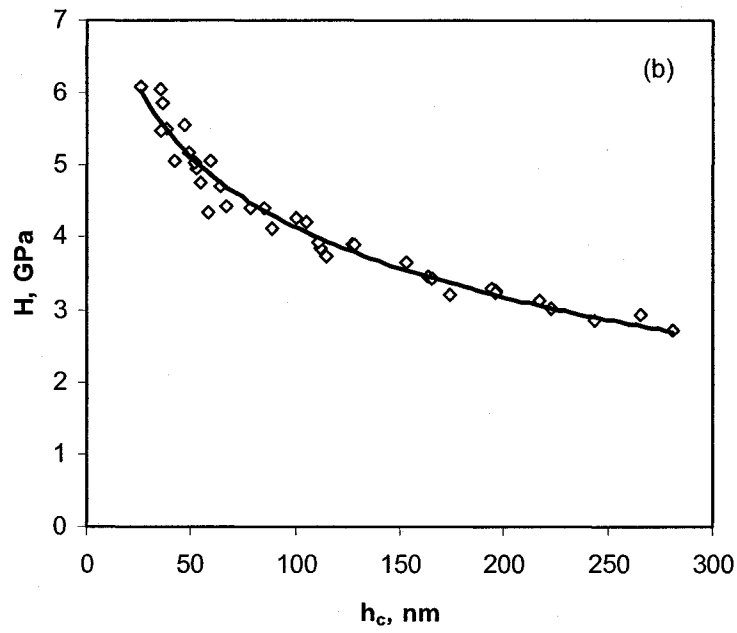
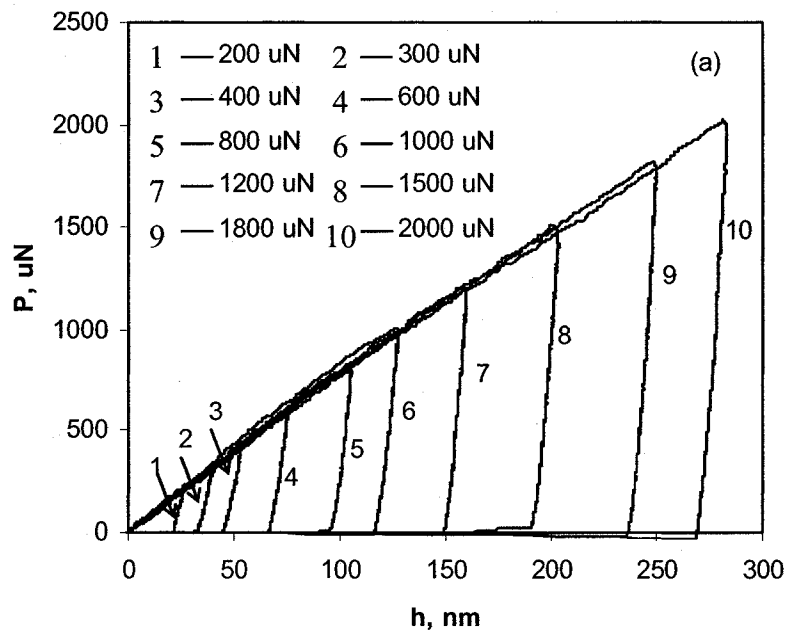
reported for single crystal copper and silver [39, 40]. This phenomenon has been known as the indentation size effect. In the range of small indentation depths, usually smaller than 5  $\mu\text{m}$ , metallic materials showed an increase in hardness with a decrease in indentation depth. It has been pointed out that this effect was due to the geometrically necessary dislocations (GNDs) caused by the large strain gradients inherent in small indentations [41, 42]. Taking the effect of GNDs into account, Nix and Gao [43] formulated the depth dependence of hardness as follows.

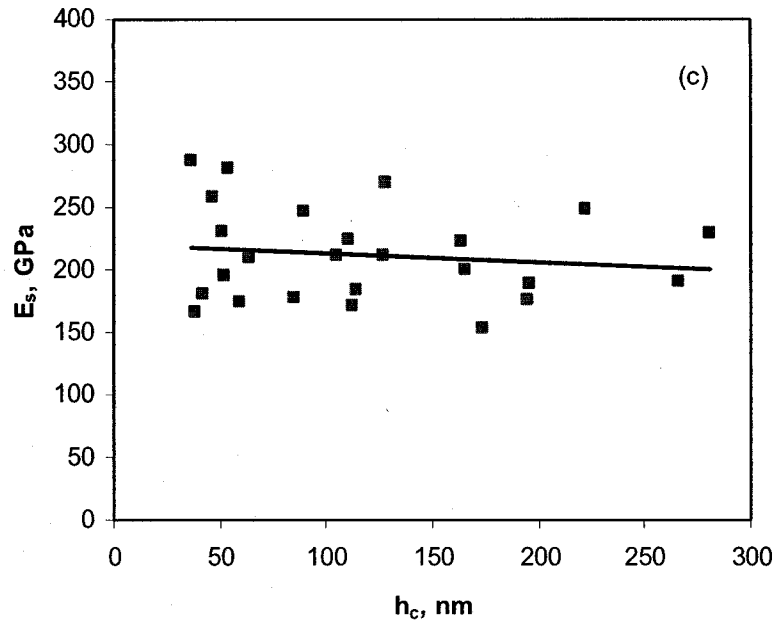
$$\frac{H}{H_0} = \sqrt{1 + \frac{h^*}{h_c}} \quad (5-16)$$

where  $H_0$  is the hardness of the bulk material, and  $h^*$  is a length that characterizes the depth dependence of hardness. Rearranging this equation gives

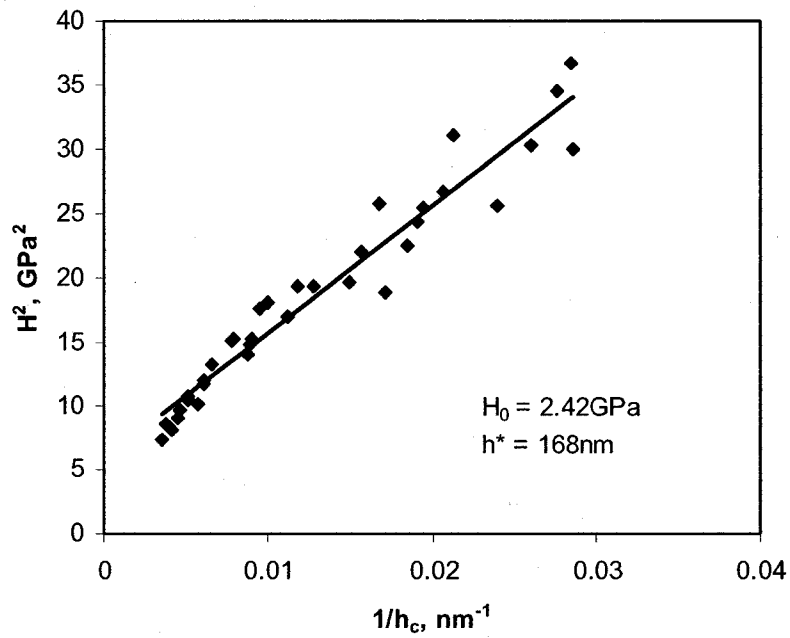
$$H^2 = H_0^2 \cdot h^* \cdot \frac{1}{h_c} + H_0^2 \quad (5-17)$$

Clearly, there was a linear relationship between the square of hardness and the reciprocal of indentation depth. Replotting the hardness data in **Figure 5-22**, the straight line confirmed the validity of Equation (5-17). From the fitted line,  $H_0$  was 2.42 GPa and  $h^*$  is 168 nm. Meanwhile, the hardness measured by Vickers hardness tests was found to be 193.7 Hv. Converting the unit to MPa gave a hardness of 1.90 GPa. Hence, the hardness values obtained with the nanoindentation method were higher than those measured with the traditional micro-hardness test. A similar result was also reported by Qian et al. [44]. The overestimation of nanoindentation was due to the pile-up phenomenon during the indentation process; the details can be found in reference [45].





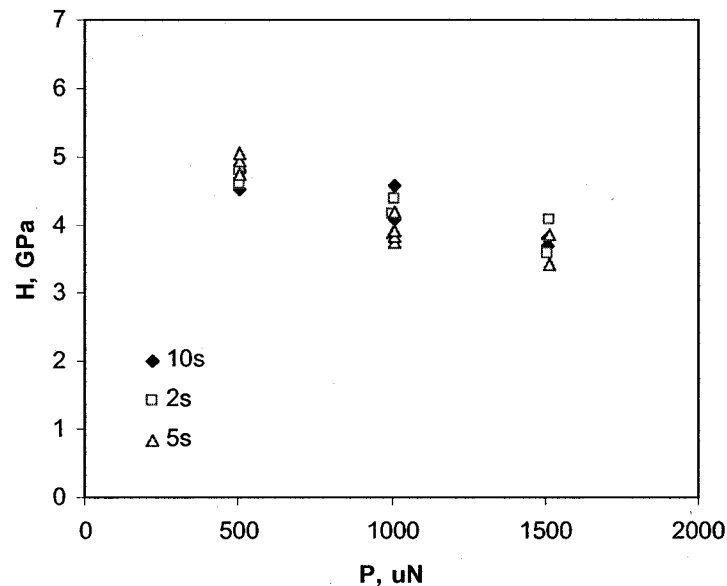
**Figure 5-21. Mechanical properties of iron measured in air at the maximum load of 200-2000  $\mu\text{N}$ : (a) Load-depth curves, (b) Hardness vs. contact depth; (c) Modulus vs. contact depth.**



**Figure 5-22. Depth dependence of hardness for pure iron, plotted according to Equation (5-17).**

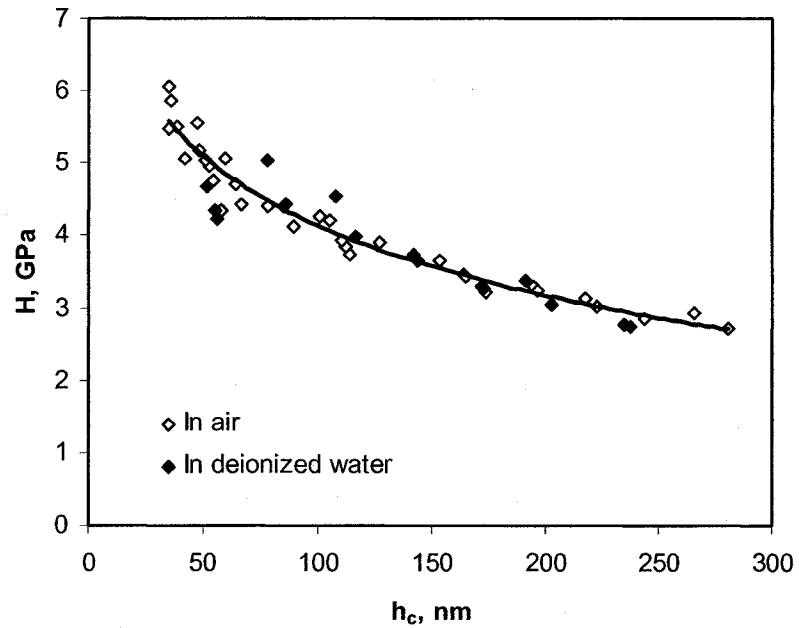
**Figure 5-21 (c)** presents the elastic modulus of iron as a function of contact depth. From Equation (2-17), the reduced modulus can be directly fitted from the load-depth curve. The elastic modulus was calculated by substituting  $E_i = 1140$  GPa,  $\nu_i = 0.07$  and  $\nu = 0.29$  to Equation (2-18). Also,  $\alpha = 0.75$  for the indenter used in the present investigation. From the figure, the modulus data were pretty scattered, which may be ascribed to different crystallographic orientations.

In the above tests, the load function with a loading and unloading time of 5 s was used at all loads. It means that the loading rate was different for each load. To understand the effect of loading/unloading rate on test results, the nanoindentation tests with 2 s and 10 s were also carried out. **Figure 5-23** shows the results with applied loads of 500, 1000 and 1500  $\mu\text{N}$ . No marked differences were observed. Theoretically, an increase in loading rate leads to dislocations to glide difficultly and results in small plastic deformations. Hence, as the loading rate increases, the penetration depth will decrease [46]. This effect was negligible for the present samples, which suggest that the loading rate effect was not important in the tests shown in **Figure 5-21**.



**Figure 5-23. Effect of loading/unloading rate on nanoindentation hardness of pure iron.**

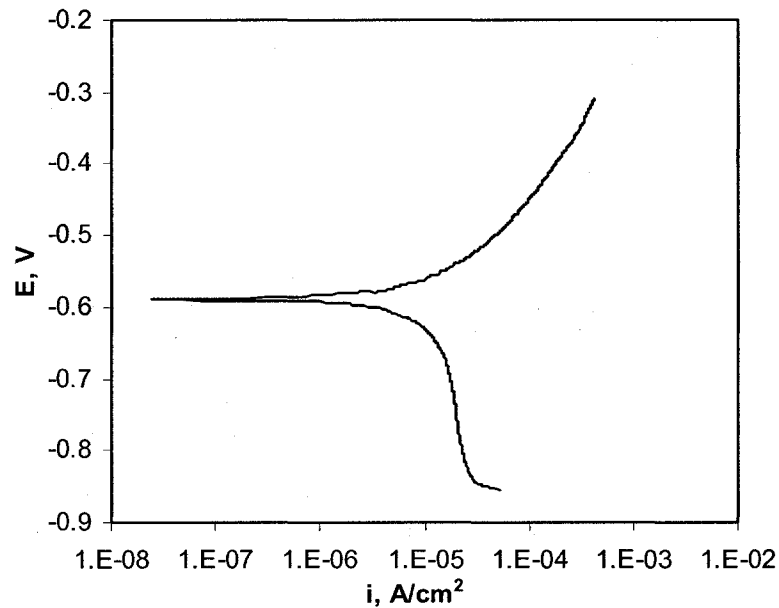
Most previous nanoindentation measurements in the literature were carried out in air. In the present in situ nanoindentation tests, however, liquid phase had to be involved to apply current to the sample. Thus, the effect of the liquid phase on the measurement results was considered. Nanoindentation measurements were conducted in deionized water to clarify this concern. The reason for choosing deionized water was to avoid influence from corrosion reactions. **Figure 5-24** presents the comparison results of test values in air and in deionized water. It can be seen that the presence of liquid phase did not affect the nanoindentation measurements. Therefore, the influence from the liquid phase can be ignored.



**Figure 5-24. Comparison of nanoindentation test results in air and in deionized water.**

### 5.3.3 Effect of anodic dissolution on surface hardness

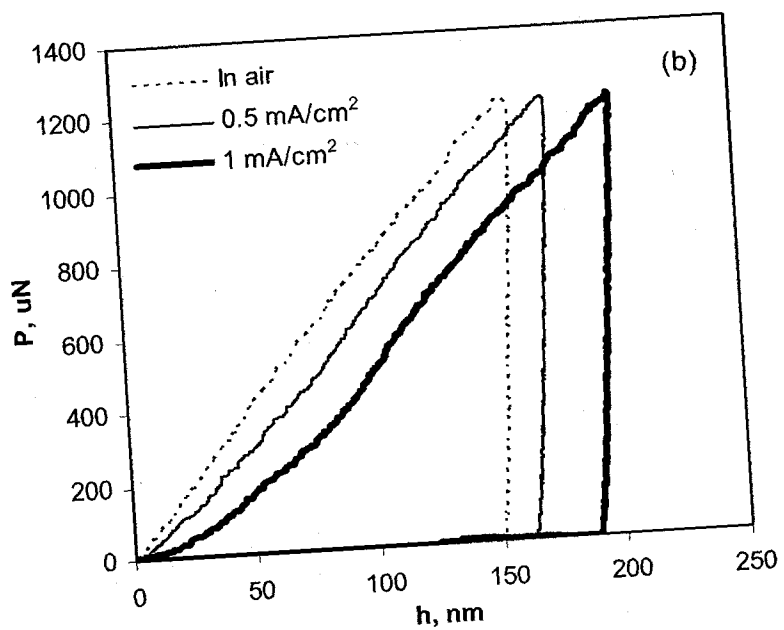
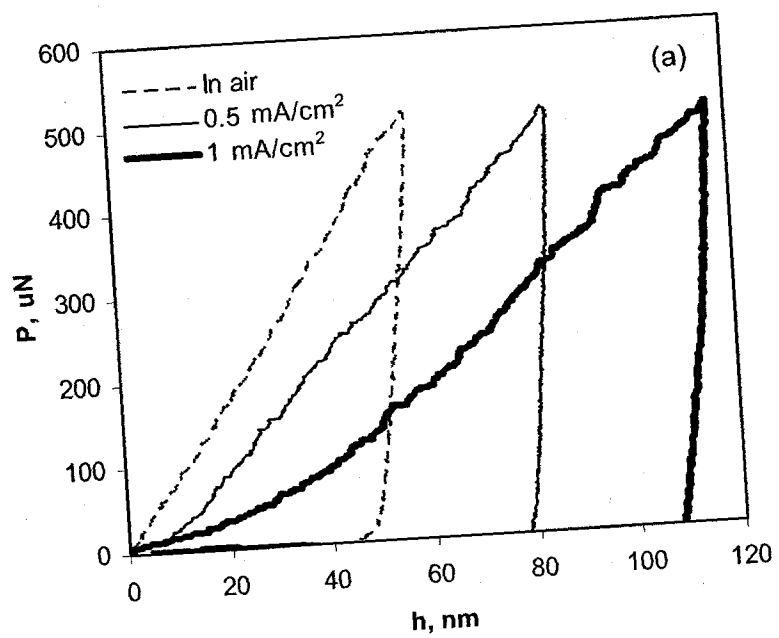
Before performing in situ nanoindentation tests, the corrosion behaviour of iron in 0.01 M Na<sub>2</sub>SO<sub>4</sub> solution was investigated. **Figure 5-25** shows the potentiodynamic polarization curve. In the anodic polarization zone, the pure iron specimen exhibited typical active dissolution behaviour. Hence, the anodic dissolution rate can be controlled by applying impressed current.



**Figure 5-25. Potentiodynamic polarization curve for pure iron in 0.01 M Na<sub>2</sub>SO<sub>4</sub> solution.**

#### 5.3.3.1 Surface hardness degradation

Anodic currents of 0.5 mA/cm<sup>2</sup> and 1 mA/cm<sup>2</sup> were applied with a power supply, and in the mean time the nanoindentation technique was carried out on the sample surface. **Figure 5-26** shows the effect of anodic dissolution on the load-depth curves in 0.01 M Na<sub>2</sub>SO<sub>4</sub> solution under a peak load of 500, 1200 and 1800 μN. For the same load, the penetration depth of indentation increased when the anodic current was applied to the specimen. Then according to Equations (2-16), (2-19) and (2-20), a higher indentation depth will result in a lower value in hardness.



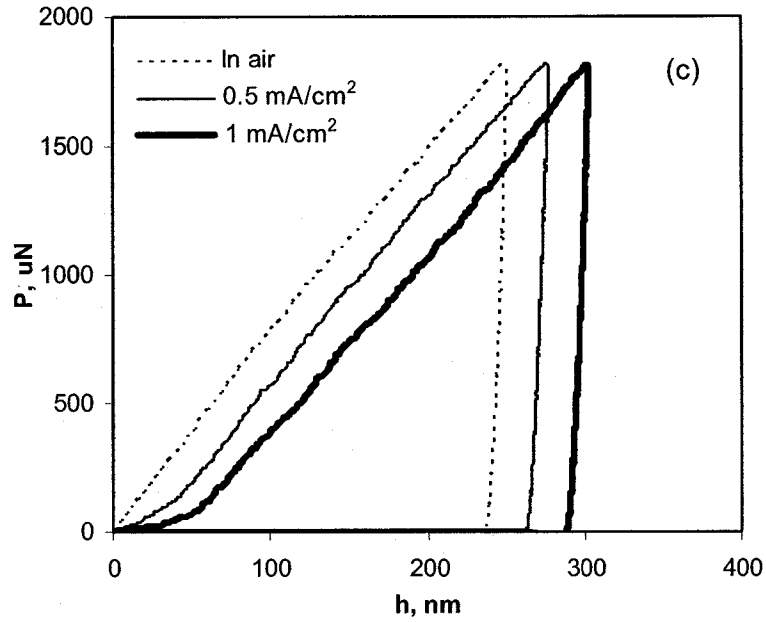


**Figure 5-26. Effect of anodic current on load-depth curves of iron: (a)  $P_{\max}=500 \mu\text{N}$ ; (b)  $P_{\max}=1200 \mu\text{N}$ ; (c)  $P_{\max}=1800 \mu\text{N}$ .**

**Figure 5-27** shows the hardness of the pure iron with different anodic dissolution densities. Although the experimental data were quite scattered, it can still be seen that the hardness degraded more with a higher anodic dissolution rate. In addition, in line with Equations (2-16) and (2-17), when the penetration depth and the contact area increase the modulus of the pure iron will decrease. **Figure 5-28** shows the effect of anodic current on the modulus of the specimen. The modulus of the specimen also diminished with an increase in applied anodic current.

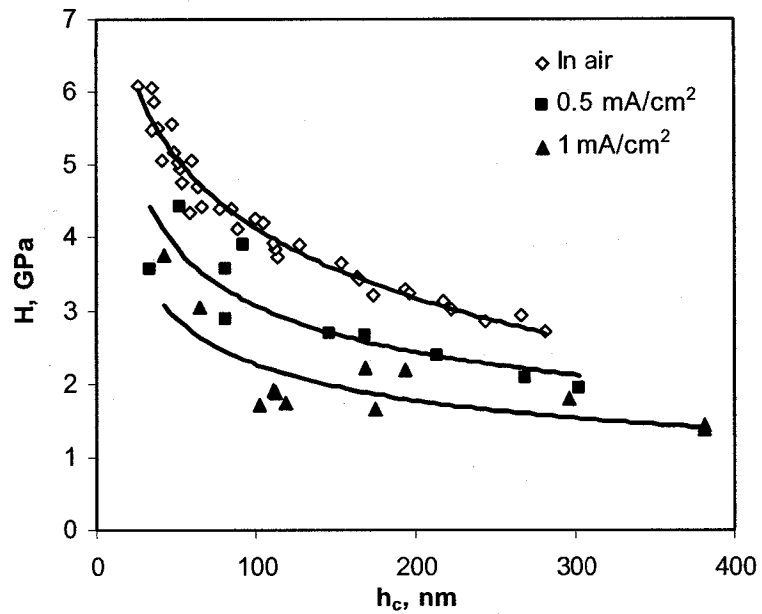


Figure 5-27. Effect of anodic current on the surface hardness of iron.

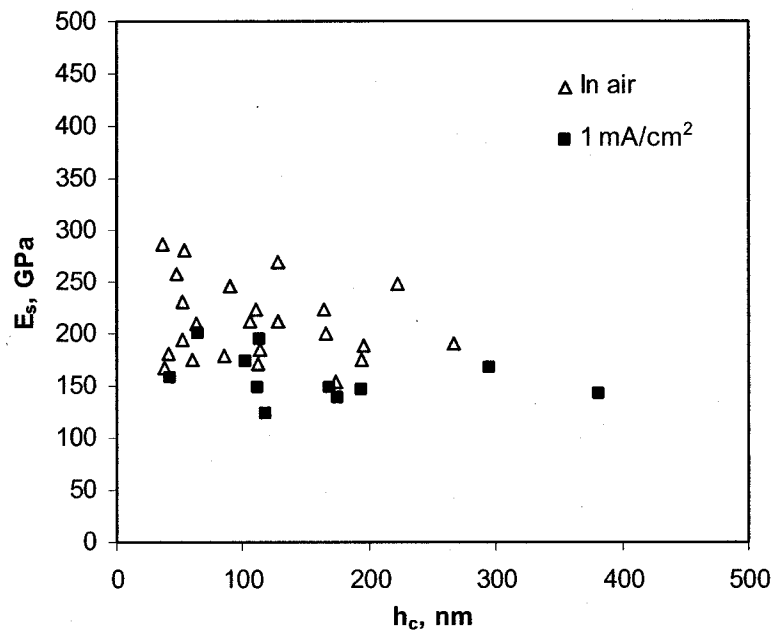
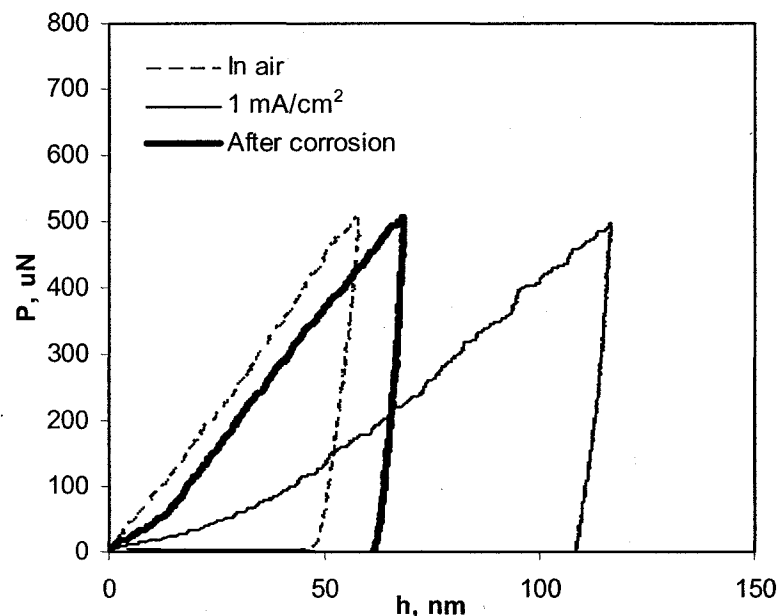


Figure 5-28. Effect of anodic current on the elastic modulus of iron.

Before any analysis associated with the above experimental phenomenon was carried out, the influence from corrosion products and/or surface change needed to be considered, because it was possible that the hardness change in **Figure 5-27** arose from the effect of a corrosion product deposited on the sample surface or other surface change, such as roughness. To clarify this problem, after the hardness with applied current was measured the anodic current was shut off and nanoindentations were conducted on the corroded specimen surface. In this case, the hardness of the specimen was measured after corrosion, which can be regarded as an ex situ test. **Figure 5-29** shows the in situ and ex situ load-depth curves with a current density of  $1 \text{ mA/cm}^2$  and peak load of  $500 \text{ }\mu\text{N}$ . Although the penetration depth of indentation measured after cutting off the current decreased significantly, it did not entirely recover to the value tested in air. **Figure 5-30** shows comparison for the surface hardness tested in situ and ex situ. Apparently, after corroding with  $1 \text{ mA/cm}^2$  the hardness of the material did not recover to its original value, showing the possible effect of a corrosion product on measurement of surface hardness. Nevertheless, the hardness with an applied current was still much lower than the corroded surface. This suggested that only a small part of the hardness degradation, if any, was attributed to the corrosion products and/or surface change. This confirmed the anodic dissolution-induced hardness degradation. The contribution of the corrosion product and/or surface change to hardness measurement was difficult to determine at this moment. In fact, it was arbitrary to entirely ascribe the hardness degradation determined in ex situ tests to the effect of corrosion products and/or surface change, because this decrease could also possibly be caused by some hysteresis effect of anodic dissolution, which will be discussed later.

In despite of some uncertainty due to corrosion products etc., the above experimental results showed clearly that the presence of anodic current at the surface can cause degradation of mechanical properties in the surface layer. This phenomenon can be understood from the electrochemical dissolution process. Although the most energetically favourable dissolution atoms are from kink sites, the anodic overvoltage could favour dissolution directly from ledge sites [47]. This

nonuniform dissolution might inject vacancies into the subsurface of materials. Then, a subsurface with a supersaturation of vacancies can form, as demonstrated by Jones et al. [4, 16, 18]. As a large amount of vacancies were generated in the subsurface, the inter-atomic bonds of the metal surface layer were attenuated. Such changes deteriorated the mechanical properties of materials, such as tensile strength, modulus and fatigue life [48-51]. Furthermore, Meletis et al. [52] calculated the binding energies between vacancies and dislocations and then proposed that the vacancies generated during electrochemical dissolution were attracted to dislocations and increased their mobility. Pickering and Wagner [53, 54] also proposed that the generated vacancies, especially divacancies, which had a much more rapid diffusion rate, can form during the preferential dissolution of some metal elements in alloys. Accordingly, the resistance of a material to plastic deformation can be reduced, thus resulting in a lower hardness.



**Figure 5-29. Comparison of the load-depth curves for iron measured by in situ and ex situ tests at  $P_{\max} = 500 \mu\text{N}$ .**

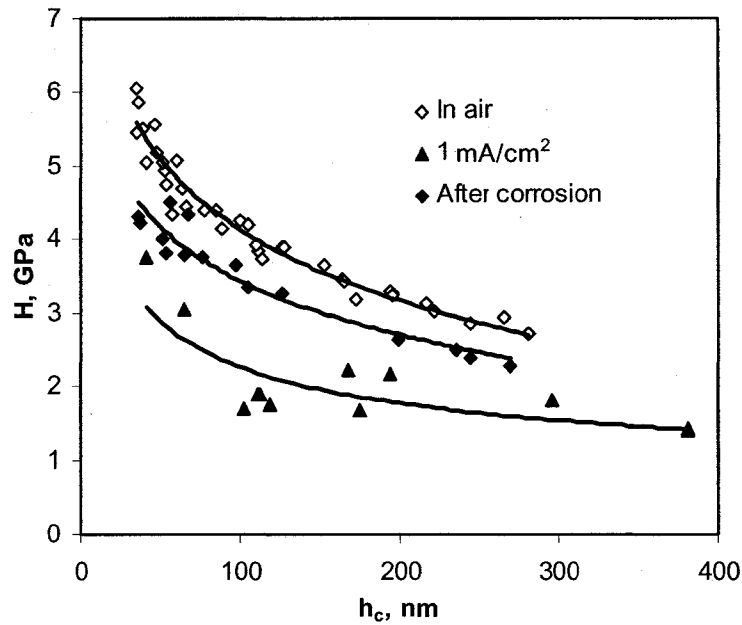


**Figure 5-30. Comparison of the surface hardness of iron measured in air and in solution by in situ and ex situ tests.**

As mentioned in Chapter 2, the vacancy generation induced by anodic dissolution has been applied to explain several experimental phenomena that involved the coexistence of electrochemical dissolution and mechanical deformation, although there are still some discrepancies about it.

Another interesting phenomenon, the long-term degradation of cementitious materials [55, 56], may provide some elucidation to understand the above discussed chemo-mechanical effect. Under permanent aqueous environmental conditions, it has been found that one of the main mechanisms for concrete degradation is leaching, particularly calcium leaching due to an aggressive solution. The main consequences of leaching on the concrete microstructure are an increase of porosity and, at the macrolevel, a decrease of the mechanical properties of the material with time. Ultimately, the collapse of concrete structures is caused by the superposition of both deterioration mechanisms, even if the individual degradation processes are not critical for the structural integrity.

### 5.3.3.2 Hysteresis effect of hardness degradation

Although the generation of vacancies was used to understand the degradation of material mechanical properties due to electrochemical dissolution, the effect on diffusion kinetics was still unknown. In creep tests, Revie and Uhlig reported a lag time with a magnitude of several to tens of minutes [3]. In order to understand this phenomenon further the hysteresis effect in the hardness test was also investigated in the present work. Considering the difficulty in measuring hardness with the nanoindentation technique with a controlled time because of the tip engagement process, micro hardness tests were carried out for this purpose. In the tests, the original hardness before anodic dissolution,  $H$ , was measured first with a Vicker hardness tester. Then, an anodic current of  $10 \text{ mA/cm}^2$  was applied to the sample for 20 min in  $0.1 \text{ M H}_2\text{SO}_4$  solution. After corrosion, the hardness of the sample as a function of time,  $H_t$ , was immediately measured in air. **Figure 5-31** shows the dependence of the ratio  $H_t/H$  on time for five similar samples. Due to the low indentation load the data were rather scattered. However, a hysteresis effect with a lag time around 10 min was observed. This phenomenon further supported the mechanism of vacancy diffusion. It also suggested that the diffusion rate of vacancies can be much higher than that estimated from extrapolation of elevated temperature data.

In Section 5.1.3.2 (**Figure 5-6**), due to the optical observation requirement the micro-hardness was tested immediately after the current was imposed. Thus, the hardness degradation in the surface layer might be underestimated because of the hysteresis effect. As for the nanoindentation tests, the data measured with and after corrosion could be regarded as stable values owing to the slow tip engagement process. Therefore, the decreased hardness in **Figure 5-30** was mainly attributed to the effect of corrosion products and/or other surface changes resulting from anodic dissolution, rather than the hysteresis effect.

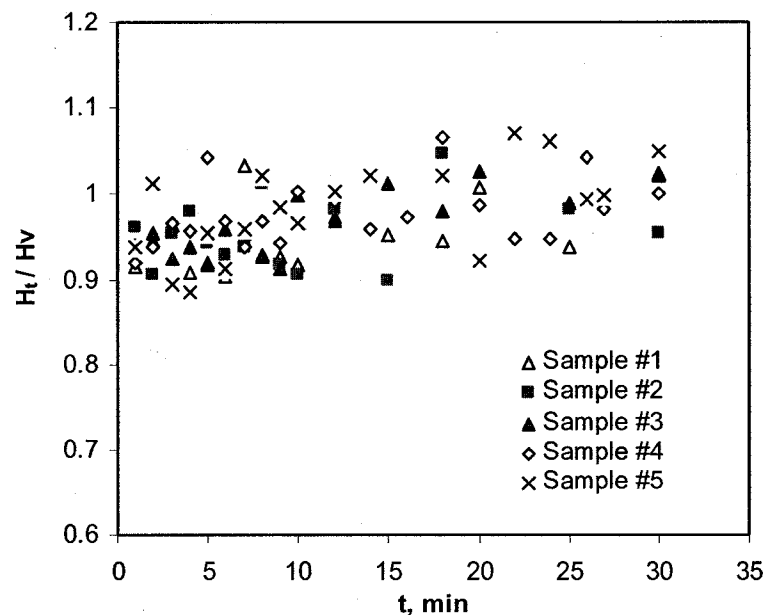


**Figure 5-31. Hardness degradation as a function of time after electrochemical dissolution.**

### 5.3.3.3 Decline of hardness degradation with depth

Owing to the fact that the anodic dissolution reaction occurred on the material surface, it was expected that its influence on material properties was mainly limited to a thin surface layer. From the vacancy analysis, the concentration of vacancies was expected to decrease with depth because it was directly related to the anodic dissolution of atoms. This suggested that the influence of anodic current on the mechanical properties measured by the nanoindentation technique declined with indentation depth, as indicated by the curves present in **Figures 5-32** and **5-33**. The hardness and modulus data in these two figures were obtained by fitting the curves in **Figures 5-27** and **5-28**. In **Figure 5-32**, the effect of anodic dissolution on hardness was characterized by the hardness ratio  $H'/H$  and the hardness difference  $H'-H$  as a function of indentation depth.  $H$  and  $H'$  are the hardnesses measured in air and under the action of anodic current respectively. Similar comparison results for the modulus are shown in **Figure 5-33**. Both the hardness difference and the modulus

difference decreased with depth while both the hardness ratio and the modulus ratio increased with the indentation depth consistently. In addition, the dependence of hardness degradation on the indentation depth was further confirmed by the comparison between the hardness values measured with the nanoindentation and microhardness techniques. **Figure 5-32** indicates that the maximum hardness degradation measured with the nanoindentation technique was more than 30% whereas the hardness degradation measured with the microhardness technique was only 10-15%.

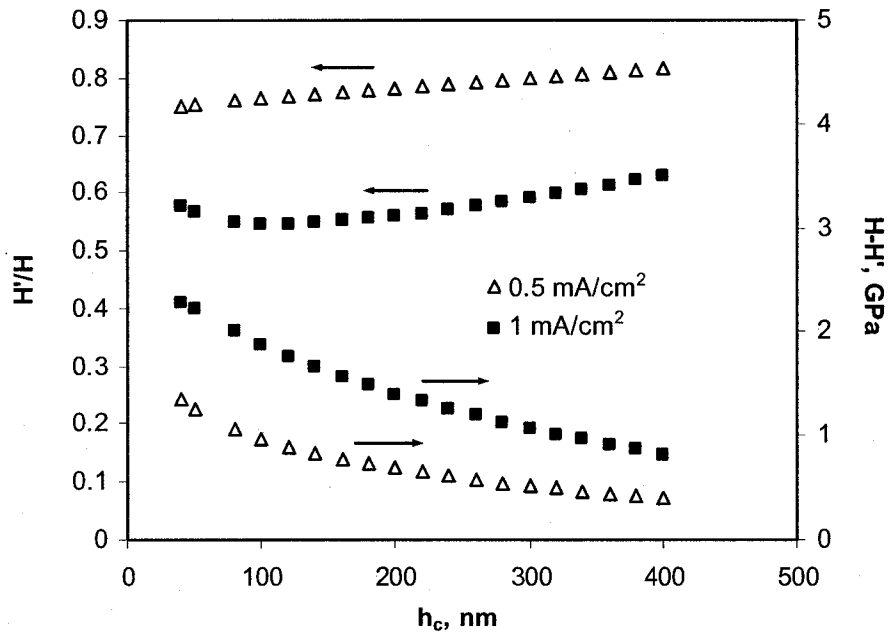


**Figure 5-32. Hardness ratio and difference as a function of contact depth for pure iron in 0.01 M Na<sub>2</sub>SO<sub>4</sub> solution.**  
(Data were obtained by fitting the experimental data in Figure 5-27).

Additionally, it can be observed from **Figure 5-27** that the indentation size effect still existed as anodic dissolution occurred on the material surface, which can influence the measured hardness curve. According to Equation (5-16), we have the following equation for the metal surface with anodic current:

$$H' = H'_0 \sqrt{1 + \frac{(h^*)'}{h_c}} \quad (5-18)$$

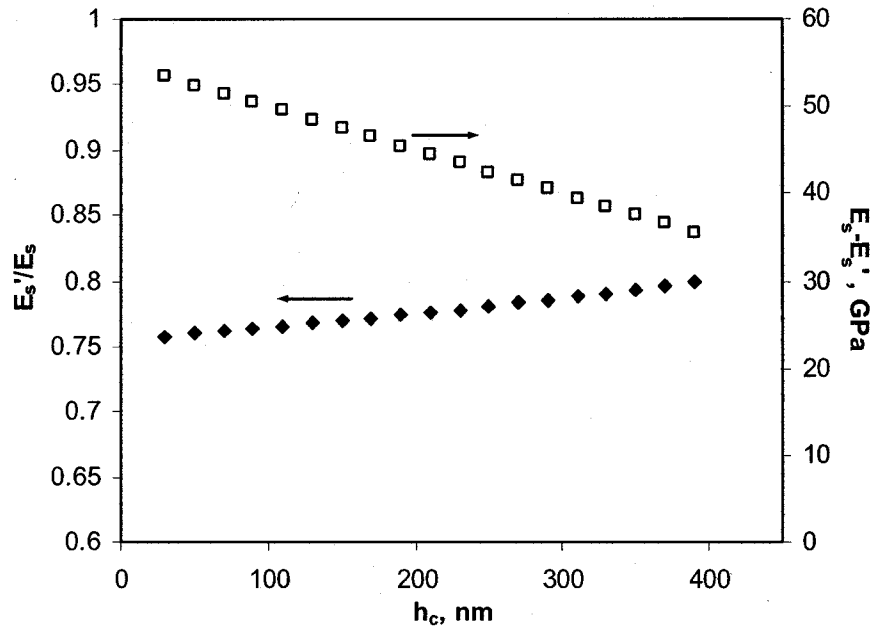


**Figure 5-33. Modulus ratio and difference as a function of contact depth for pure iron in 0.01 M Na<sub>2</sub>SO<sub>4</sub> solution with an applied current of 1mA/cm<sup>2</sup>.**  
(Data were obtained from fitting the experimental data in Figure 5-28)

where  $H'_0$  and  $(h^*)'$  are the true material hardness and the character length with applied current, respectively. If the character length is assumed to be approximately held unchanged, i.e.

$$(h^*)' = h^* \quad (5-19)$$

then in line with Equation (5-16) and Equation (5-18) we have

$$\frac{H'}{H} = \frac{H'_0}{H_0} \quad (5-20)$$

In this situation, the  $H'/H$  in **Figure 5-30** could represent the real ratio of the hardness with and without anodic dissolution. However, from the analysis of Nix et al. [34] the character length  $h^*$  can be expressed by

$$h^* = \frac{81}{2} \bar{b} \eta^2 \tan^2 \phi \left( \frac{\mu_0}{H_0} \right)^2 \quad (5-21)$$

where  $\bar{b}$  is Burgers vector,  $\eta$  a constant for the Taylor relation,  $\mu_0$  the shear modulus, and  $\phi$  the angle between the indenter surface and the plane of the sample surface. When vacancies develop within the surface layer during anodic dissolution,  $\mu$  and  $H_0$  will decrease; meanwhile the equivalent  $b$  value will also alter because the disorder in arrangement of atoms in the surface layer will be enhanced. Therefore, the relationship between  $H'/H$  and  $h_c$  will become very complicated. The geometric effect from indentation size was inevitably inevitable at this stage.

#### 5.3.4 Effect of cathodic reaction on surface hardness

For comparison, the effect of cathodic current on surface hardness was also investigated. From the potentiodynamic curve in **Figure 5-25**, the cathodic current density corresponding to a potential of -0.85 V (SCE) was applied to the iron sample and at the same time the surface hardness was measured. **Figure 5-34** shows the results. The surface hardness was independent of the applied cathodic current. In neutral solution, the cathodic reaction under CP potential was the reduction of dissolved oxygen,



For this process the metallic electrode only provided locations for the reaction to take place, rather than direct participation. The packing of the metal atoms or the inter-atom bonds may not change with the reaction occurring. Therefore, the mechanical properties of the surface layer were not influenced by cathodic current arising from reduction of oxygen.

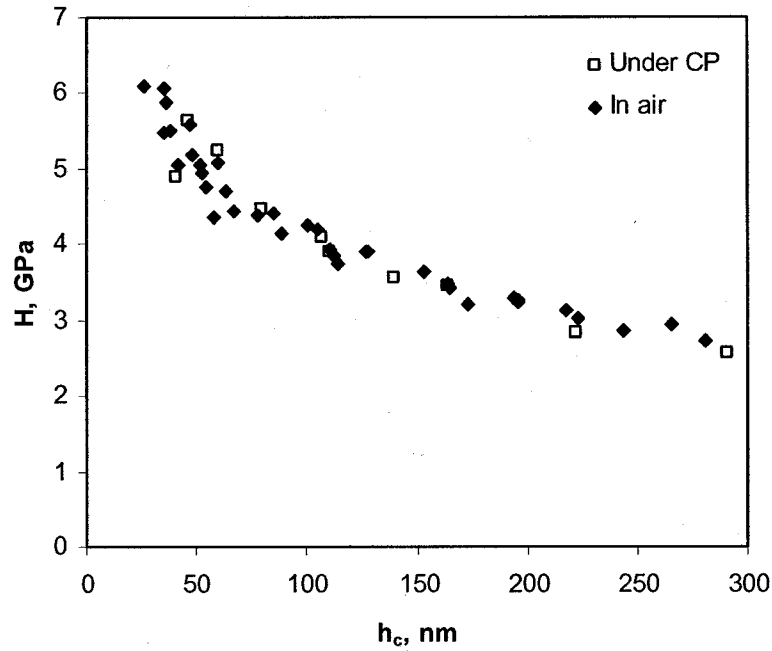


**Figure 5-34. Effect of cathodic current on the surface hardness of iron.**

However, further increasing the applied cathodic current density led to different results. **Figure 5-35** shows the ex situ hardness test results for the hydrogen-charged specimen, which was charged for 5800s in a borate buffer solution with a current density of  $2 \text{ mA/cm}^2$ . When the contact depth was less than 80 nm, no apparent effect was found, while for a contact depth larger than 80nm the hardness became much higher than that of the uncharged sample. For the cathodic current up to  $2 \text{ mA/cm}^2$ , the formation reaction of hydrogen dominated the cathodic reaction,



As a result, many hydrogen atoms penetrated into the electrode surface layer and caused internal stress, which could decrease ductility and thus influenced the hardness of the surface layer. This phenomenon is known as hydrogen embrittlement [57], which differs from the cause for the decrease in hardness during anodic dissolution.

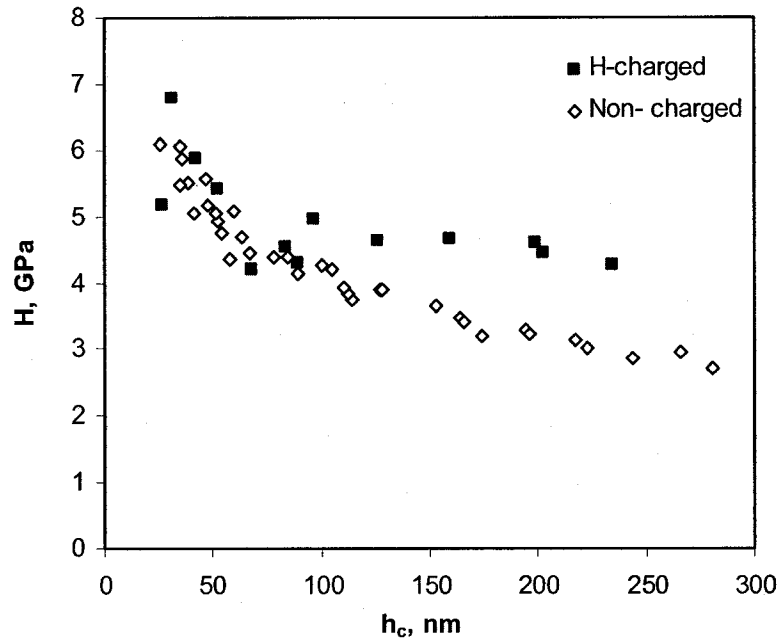


Figure 5-35. Effect of hydrogen charging on the surface hardness of iron.

### 5.3.5 Summary

- (1) The presence of anodic dissolution reduced the hardness and elastic modulus of iron within the surface layer.
- (2) The effect of anodic dissolution on mechanical properties declined with increasing distance from the surface.
- (3) The property degradation resulting from anodic dissolution can be attributed to the generation of vacancies in the metal surface layer.
- (4) Cathodic current from the reduction of oxygen did not influence the surface hardness of iron while hydrogen penetration increased the surface hardness for the present system.

## 5.4 Other effect of corrosion on erosion

From the nanoindentation experiment results the hardness degradation on the metal surface can be as high as to 40% when anodic corrosion took place on the electrode. In view of the change in this material property, the influence was substantial. However, the calculation value for  $W_{c-e}/W_{e0}$  with this hardness degradation was still lower than the experimental data. **Figure 5-36** shows the comparison results of the experimental corrosion-enhanced erosion data and the theoretical prediction with the chemo-mechanical model under different conditions. It needs to point out that the exponential in Equation (5-1) was tested to be smaller than 1 from **Figure 5-5**. In the literature regarding erosion models, the exponential was often estimated to be 1.26 [11]. With this exponent and the parameters estimated from the nanoindentation test,  $W_{c-e}/W_{e0}$  was also calculated and is shown in **Figure 5-36**. It was seen that the calculation values were closer to the experimental data. However, the deviation is still not negligible.

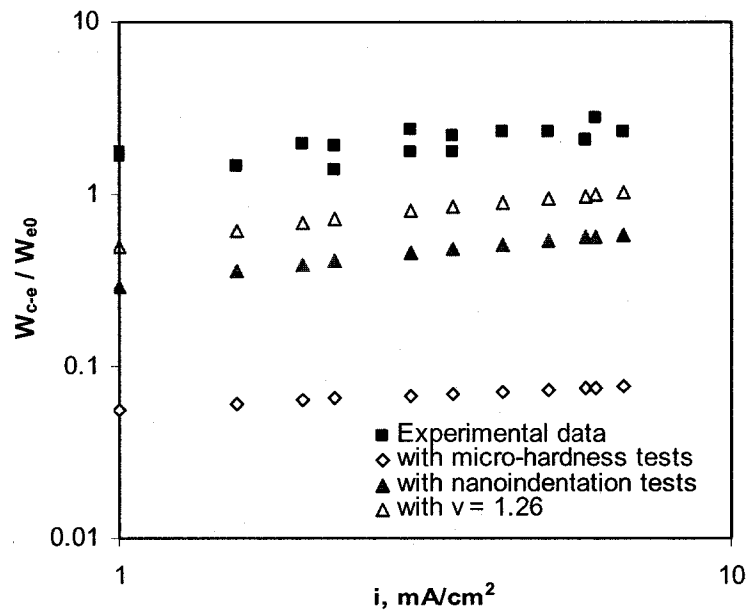


**Figure 5-36. Comparison of the experimental corrosion-enhanced erosion data and the calculated values with chemo-mechanical model under different conditions.**

The experimental results and analysis so far indicated that the chemo-mechanical effect could be a very important mechanism by which corrosion accelerated the erosion rate both in flowing slurry and solution. However, other processes would also be responsible for the corrosion-enhanced erosion. Therefore, further preliminary investigation was preliminarily carried out to check other possible mechanisms.

If the chemo-mechanical effect can be thought of as an in situ effect of corrosion on erosion, then some other ex situ effect could be associated with the significant corrosion-enhanced erosion. Hence, a test was designed to check the ex situ effect. After polishing, the carbon steel samples were corroded in 0.1 M  $\text{Na}_2\text{SO}_4$  for different times with a current density of  $1 \text{ mA/cm}^2$  and thereafter were cleaned in the standard solution to take off the corrosion product. Then the pure erosion rates of these corroded samples were measured under CP. **Figure 5-37** shows the pure erosion results for the uncorroded sample and the corroded samples with different times. The corroded samples had higher pure erosion rates than the uncorroded one.

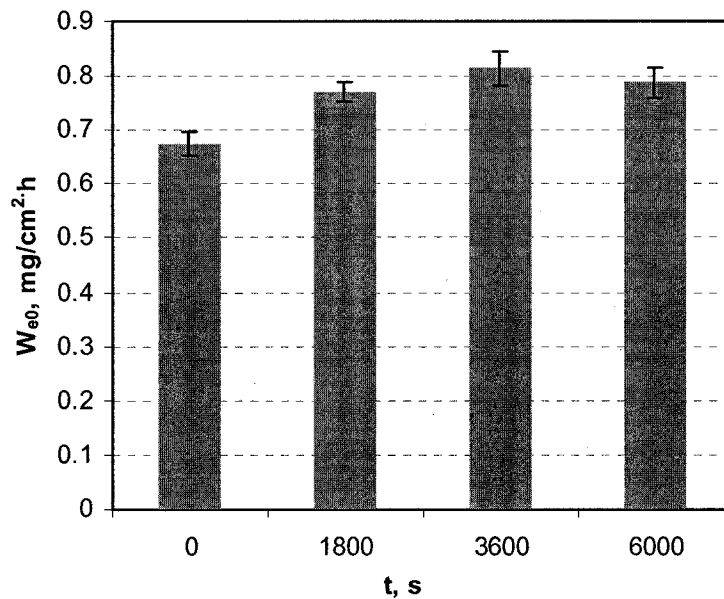


**Figure 5-37. Pure erosion rates of the corroded and uncorroded carbon steel samples (x-axis represents the corrosion time).**

Since the pure erosion rate was measured a long enough time after it was corroded, it can be expected that the chemo-mechanical effect was not involved in this test. The higher erosion rate can be understood from the difference between the corroded and uncorroded samples. On one hand, corrosion would help to remove the hardened layer that resulted from polishing. All the samples for weight loss tests were polished through 240, 320, 400 and 600 grit. A hardened layer can be established during this polishing process. Then in a solution with anodic current applied, this layer can be dissolved to a different extent depending on the corrosion time. According to the literature and the test result shown in **Figure 5-5**, without the protection of the hardened layer the pure erosion rate of the sample will increase. However, the strain hardening exponent of carbon steel A1045 is 0.12 [58]. Thus, such a hardened layer removal effect can not be expected to be very high. Also, the hardened layer removal effect was emphasized in this test, considering the erosion-corrosion test condition. In an erosion-corrosion test, the work hardening process and the corrosion dissolution process take place simultaneously, and thus the hardened layer removal effect will not be as significant as in the present test.

On the other hand, the physical properties of the corroded surface could be inferior, such as surface roughness, which could result in a higher friction coefficient. The friction coefficients of the samples were investigated with nano-scratch tests, where the same setup for nanoindentation tests was used. **Figure 5-38** shows the friction coefficients of iron under loads of 100, 200, 300 and 400  $\mu\text{N}$  in air, in solution and after corrosion. The friction coefficient increased with an increase in normal load. This phenomenon was attributed to the geometry of the diamond tip by Chiba and Seo [59]. The friction coefficients increased as the sample was immersed in 0.1 M  $\text{Na}_2\text{SO}_4$  solution. After the sample was corroded with  $0.5 \text{ mA/cm}^2$  for 10 min, the coefficient increased further. A higher coefficient means a larger lateral force on the target surface, which can result in a larger material loss. Yin and Li [60] also related the larger material loss of copper in a 3.5%  $\text{NaCl}$  solution than in a 0.1 M  $\text{HNO}_3$  solution to its higher friction coefficient in the former solution. Therefore, during the erosion-corrosion process, increasing the friction coefficient between the

sand particles and the material would be one of the mechanisms by which corrosion accelerated the erosion rate.

The above experiments were an attempt to understand the high corrosion-enhanced erosion beyond the chemo-mechanical effect. Further investigation and quantitative measurement were desirable to explain the deviation found between the experimental data and the theoretical prediction of the chemo-mechanical model.

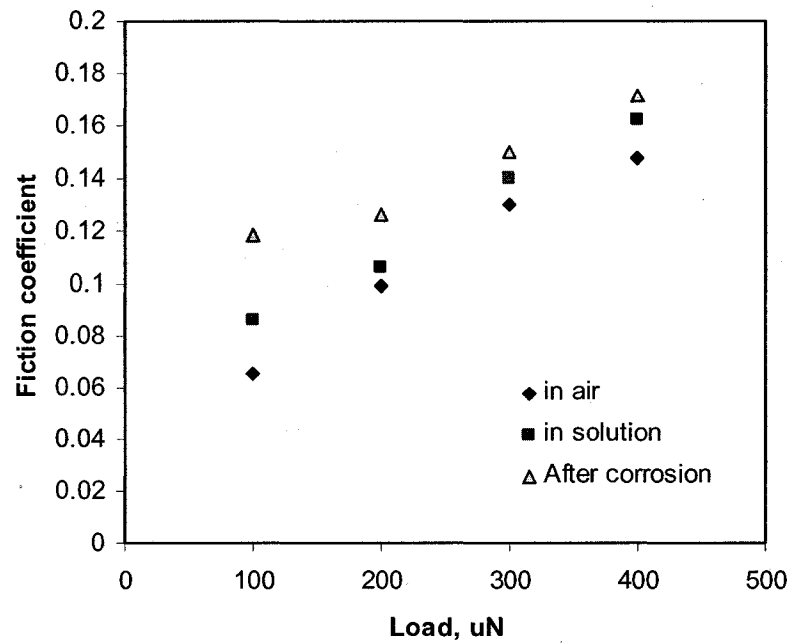


**Figure 5-38. Friction coefficients of iron in air, in solution and after corrosion.**

## 5.5. The corrosion-enhanced erosion in passive system

The corrosion-enhanced erosion in a passive system was also investigated. Compared with the corrosion-enhanced erosion in an active system, the formation, growth and breakdown of the passive film in the passive system were involved in the interaction between corrosion and erosion, and thus made the mechanism more complicated.

In a passive system, the corrosion rate cannot be controlled directly by applying impressed current to the sample. Thus, potential was taken as the parameter to investigate the effect of corrosion on erosion. Carbon steel A1045 and borate solution were used. Weight loss tests were carried out under different potentials in 35% slurry at a velocity of 9000 rpm, and the current was recorded. Then, with the pure erosion rate determined under CP and the pure corrosion rate calculated from the passive current in the borate solution free of sand, the weight loss rate due to various processes can be determined. **Figure 5-39** illustrates the weight loss distribution of carbon steel A1045 in borate solution at a velocity of 9000 rpm under 600 mV. Although the pure corrosion rate was only 0.2% of the total weight loss, it can be found that it has a substantial effect on the erosion rate such that the percentage of the corrosion-enhanced erosion was as high as 35%. **Figure 5-40** shows the percentage of corrosion-enhanced erosion under different potentials. At all the potentials the corrosion-enhanced erosion made substantial contribution to the total material loss with a percentage of around 30%. Thus, in the passive system the corrosion-enhanced erosion was still a very important material loss process.

**Figure 5-41** shows the total weight loss as a function of passive potential, and the corresponding normalized corrosion-enhanced erosion is also presented. From the figure, the total weight loss and the corrosion-enhanced erosion showed an independence of potential. In fact, this observation is consistent with the experimental results obtained from the active corrosion system. In the passive system, the corrosion current in the passive zone as approximately maintained as a constant. Considering the relationship between

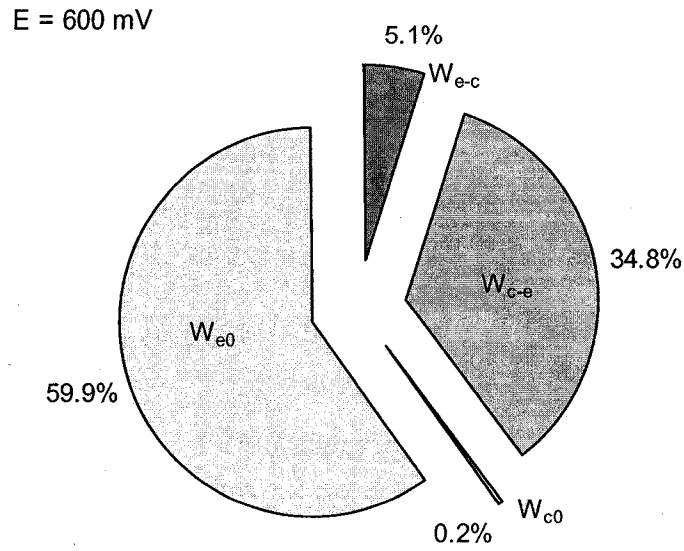


**Figure 5-39. The weight loss distribution of carbon steel A1045 in borate solution at velocity of 9000 rpm under 600 mV.**

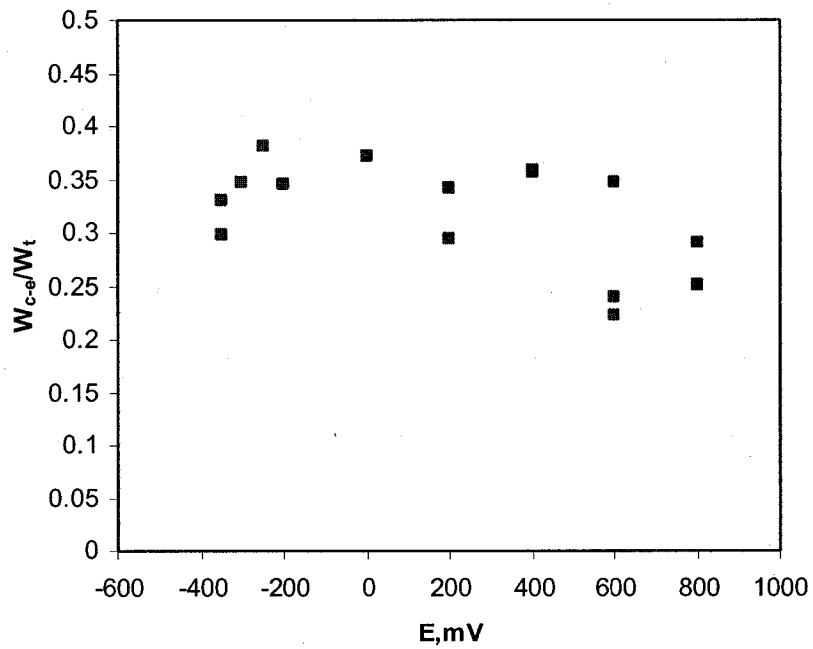


**Figure 5-40. The percentage of corrosion enhanced erosion as a function of passive potential in borate solution at velocity of 9000 rpm.**

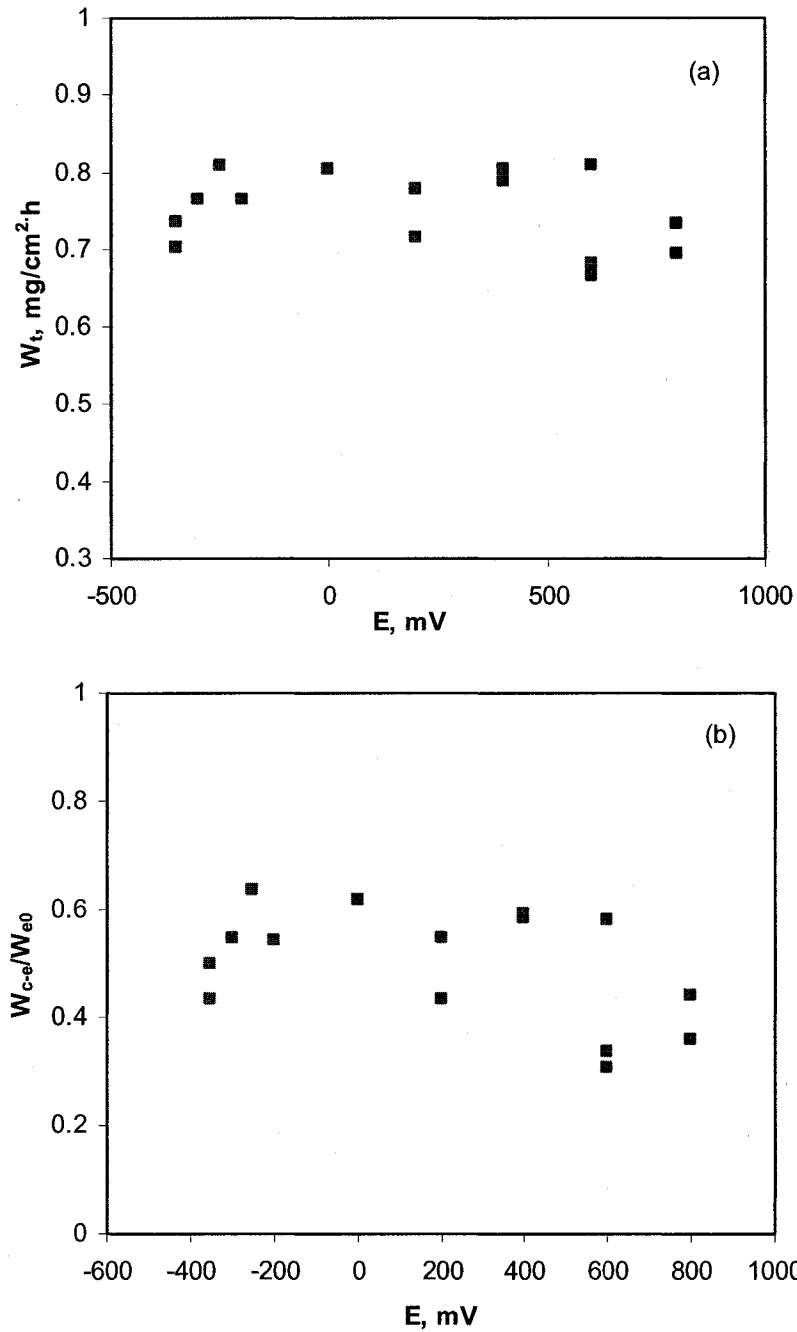


**Figure 5-41. The total weight loss (a) and normalized corrosion-enhanced erosion (b) as a function of passive potential in borate solution at a rotating velocity of 9000 rpm.**

corrosion-enhanced erosion and corrosion current density described by Equation (5-3), this independence was unexpected. **Figure 5-42** plots the corrosion-enhanced erosion data for the passive system and the non-passive system together. It was seen that the data measured in the passive system approximately followed the same trend as those in the active system. Further, since pure erosion rate, pure corrosion and corrosion-enhanced erosion rate showed independence of potential, the total loss rate maintained constant. The contribution from erosion-enhanced corrosion was limited, although it increased with potential.

Therefore, from a macroscopic view point, the mechanism for the action of corrosion on erosion in the passive system was similar to that in the active system. The material degradation process proposed for the active system can be applied to an investigation in a passive system.

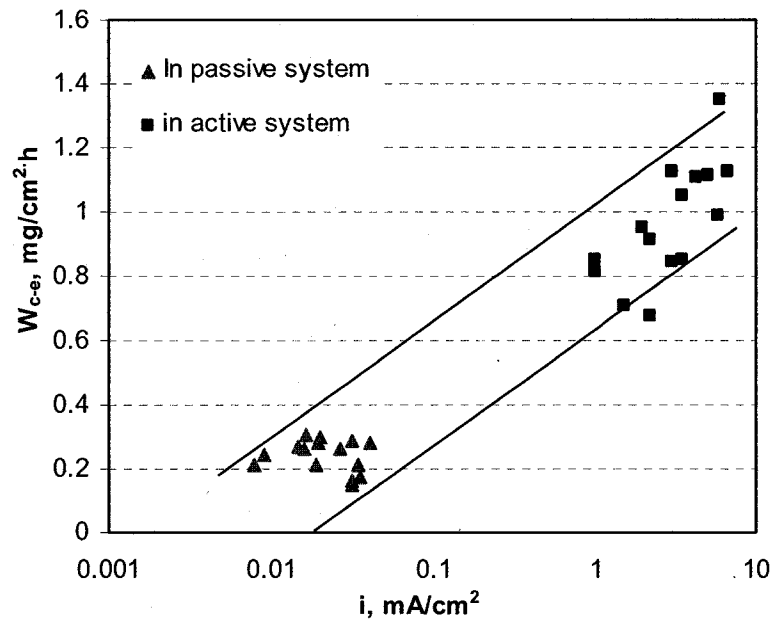


**Figure 5-42. Comparison of the normalized corrosion enhanced-erosion data for passive system and non-passive system.**

## References

- [1] Y. Li, G.T. Burstein, and I.M. Hutchings, *Wear* 186 (2) (1995) 515.
- [2] M. Matsumura, Y. Oka, H. Hiura, and M. Yano, *ISIJ Int.* 31 (2) (1991) 168.
- [3] R.W. Revie and H.H. Uhlig, *Acta Metallurgy* 22 (1974) 619.
- [4] D.A. Jones, A.F. Jankowski, and G.A. Davidson, *Metallurgical and Materials Transactions* 28A (1997) 843.
- [5] T. Magnin, A. Chambreuil, and B. Bayle, *Acta Materials* 44 (4) (1996) 1457.
- [6] B.T. Lu and J.L. Luo, *Journal of Physical Chemistry B* 110 (9) (2006) 4217.
- [7] I.M. Hutchings, *The Erosion of Materials by Liquid Flow*, Cambridge, UK, MTI Publication No. 25, Material Technology Institute of the Chemical Process Industries, 1986.
- [8] A. Neville and X. Hu, *Wear* 250-251 (2001) 1284.
- [9] G.I. Laird, *Transactions of the American Foundrymen's Society* 99 (1991) 339.
- [10] I.M. Hutchings, *Wear* 70 (1981) 269.
- [11] Y.I. Oka, M. Matsumura, and T. Kawabata, *Wear* 162-164 (1993) 688.
- [12] E. Heitz, *Corrosion* 47 (2) (1991) 135.
- [13] I. Finnie, *Wear* 19 (1972) 81.
- [14] G.L. Sheldon and A. Kanhere, *Wear* 21 (1972) 195.
- [15] E.M. Gutman, *Mechanochemistry of Materials*, Great Abington, Cambridge, UK, Cambridge International Science Publishing, 1998.
- [16] D.A. Jones and A.F. Jankowski, *Scripta Metallurgica et Materialia* 29 (1993) 701.
- [17] K. Lian and E.I. Meletis, *Corrosion* 52 (5) (1996) 347.
- [18] D.A. Jones, *Corrosion* 52 (5) (1996) 356.
- [19] M.M. Stack and N. Pungwiwat, *Wear* 256 (5) (2004) 565.
- [20] Y.G. Zheng, Z.M. Yao, X.Y. Wei, and W. Kei, *Wear* 186 (2) (1995) 555.
- [21] A. Neville, T. Hodgkiess, and H. Xu, *Wear* 233-235 (1999) 523.
- [22] T. Amarnath, T. Namboodhiri, and S.N. Upadhyay, *Canadian Journal of Chemical Engineering* 80 (2002) 456.

- [23] J.F. Lu, Synergy Between Erosion and Corrosion of Carbon Steel in Slurry, University of Alberta, 2004.
- [24] S.R. Sankaran, Erosion Corrosion in Simulated Oil Sand Slurry Transportation, Master Thesis of University of Alberta, 2004.
- [25] K.D. Efird, Corrosion (2000) Paper No.00052.
- [26] D. Talbot and J. Talbot, Corrosion science and technology, CRC Press, (1998) 99.
- [27] M.B. Ives, Y.C. Lu, and J.L. Luo, Corrosion Science 32 (1) (1991) 91.
- [28] B. Poulson, Corrosion Science 23 (4) (1983) 391.
- [29] J. Weber, British Corrosion Journal 27 (3) (1992) 193.
- [30] J.A. Wharton and R.J.K. Wood, Wear 256 (5) (2004) 525.
- [31] M. Eisenberg, C.W. Tobias, and C.R. Wilke, Journal of the Electrochemistry Society 101 (1954) 306.
- [32] T. Mizushima, in, New York, Academic Press, 1971, p.No. 87.
- [33] B. Gu, W.Y. Chu, L.J. Qiao, and C.M. Hsiao, Corrosion Science 36 (8) (1994) 1437.
- [34] W.D. Nix, Materials Science and Engineering A 234 (1997) 37.
- [35] B. Bhushan, ed., Handbook of Micro/Nano Tribology, CRC Press, New York, 1995, p.321.
- [36] M. Chiba and M. Seo, Corrosion Science 44 (10) (2002) 2379.
- [37] M. Seo and M. Chiba, Electrochimica Acta 47 (1-2) (2001) 319.
- [38] M. Seo, M. Chiba, and K. Suzuki, Journal of Electroanalytical Chemistry 473 (1-2) (1999) 49.
- [39] Q. Ma and D.R. Clarke, Journal of Materials Research 10 (1995) 853.
- [40] K.W. McElhane, J.J. Vlassak, and W.D. Nix, Journal of Materials Research 13 (5) (1998) 1300.
- [41] N.A. Flick and J.W. Hutchinson, Journal of the Mechanics and Physics of Solids 41 (1993) 1825.
- [42] N.A. Flick, G.A. Muller, M.F. Ashby, and J.W. Hutchinson, Acta Metallurgica et Materialia 42 (1994) 475.

- [43] W.D. Nix and H. Gao, *Journal of Mechanics and Physics Solids*, 46 (3) (1998) 411.
- [44] L.M. Qian, M. Li, Z.G. Zhou, H. Yang, and X.Y. Shi, *Surface and Coatings Technology* 195 (2-3) (2005) 264.
- [45] W.C. Oliver and G.M. Pharr, *Journal of Materials Research* 19 (1) (2004) 3.
- [46] T.H. Fang and W.J. Chang, *Applied Surface Science* 252 (5) (2005) 1863.
- [47] A. Jones, *Metallurgy Transaction A* 16 (1985) 1133.
- [48] C.H. Caceres and B.I. Selling, *Materials Science and Engineering A* 220 (1996) 109.
- [49] N. Chawla and X. Deng, *Materials Science and Engineering A* 390 (2005) 98.
- [50] A. Hadrboletz and B. Weiss, *International Materials Reviews* 42 (1997) 1.
- [51] C. Tekmen, I. Ozdemir, U. Cocen, and K. Onel, *Materials Science and Engineering A* 360 (2003) 365.
- [52] E.I. Meletis, K. Lian, and W. Huang, in *Proceeding of Corrosion-Deformation Interactions*, Les Ulis, France, 1993, p.69.
- [53] H. Pickering, *Journal of the Electrochemical Society* 117 (1970) 8.
- [54] H. Pickering and C. Wagner, *Journal of the Electrochemical Society* 114 (1967) 698.
- [55] C.L. Bellego, B. Gerard, and G. Pijaudier-Cabot, *Journal of Engineering Mechanics* (3) (2000) 266.
- [56] D. Kuhl, f. Bangert, and G. Meschke, *International Journal of Solids and Structures* 41 (2004) 15.
- [57] L. Raymond, ed., *Hydrogen embrittlement: prevention and control*, ASTM STP 962, American Society for Testing and Materials, Philadelphia, 1988, p.217.
- [58] W.D. Callister, *Materials science and engineering: an introduction*, 1994.
- [59] M. Chiba and M. Seo, *Electrochimica Acta* 50 (2004) 967.
- [60] S. Yin and D.Y. Li, *Materials Science and Engineering A* 394 (2005) 266.

## Chapter 6      Summary and Future Work

### 6.1 Main conclusions

As stated in Chapter 2, the objective of the present work was to clarify the interaction between erosion and corrosion in a slurry process, providing useful information for industrial applications and academic research. The following main conclusions can be made on the basis of the separate investigations of the effect of erosion on corrosion and the effect of corrosion on erosion:

(1) In the non-passive corrosion system, comprising carbon steel/sodium sulphate solution, as the corrosion is controlled by active dissolution of metallic material, erosion has no significant acceleration effect on corrosion rate. This is because (a) erosion cannot promote corrosion by accelerating the mass transfer step, since mass transfer is not the rate-determining step; (b) erosion cannot increase corrosion by the mechanism of removing a protective film due to the non-protective corrosion products formed on the metal surface; (c) the deformation or residual stresses caused by impingement of sand does not significantly affect the corrosion behaviour.

(2) In the passive corrosion system, the corrosion rate of carbon steel A1045 is increased by erosion by impairing and deteriorating the protective passive film. The effect of erosion can be characterized using the parameters in an equivalent circuit. The charge transfer resistance and the reciprocal of film capacitance decrease significantly with slurry concentration, indicating that the erosion process deteriorates the passivation of carbon steel. Mott-Schottky analysis, in conjunction with PDM, reveals that the diffusivities of the defects within the passive film formed in borate

solutions with different ion concentrations are comparable, while the defect density increases with solution concentration. According to PDM, the higher donor density results in higher diffusion flux and thus higher film growth rate. With higher film growth rate, the resistance of electrode to erosion-enhanced corrosion is improved.

(3) In the effect of erosion on pitting corrosion, erosion promotes initiation of pitting corrosion by breaking down the passive film, but impedes the propagation of metastable pits to stable corrosion pits by impairing the occluded environment for pitting corrosion development.

(4) The surface hardness of a carbon steel A1045 electrode decreases as a linear function of the logarithm of the average applied anodic current density. Nanoindentation analysis shows that the effect of anodic dissolution on mechanical properties declines with increasing distance from the surface. The property degradation resulting from anodic dissolution can be attributed to the generation of vacancies in the metal surface layer. Through this chemo-mechanical effect, corrosion enhances the erosion rate, and there is a linear relationship between the corrosion-enhanced erosion and the logarithm of average anodic current density.

(5) In a flowing corrosive solution free of solid particles, when the flow velocity is sufficiently high the mass loss rates obtained from traditional weight loss measurements are higher than those obtained from calculations using Faraday's law. Experimental analysis showed that this material loss arises from corrosion-induced erosion.

## **6.2 Contribution to knowledge**

The present work included determination and analysis of erosion-corrosion of carbon steel in different corrosion environments. Valuable insights have been gained

into the mechanism of the synergistic effect between erosion and corrosion. Further, the synergistic effect between mechanical factors and electrochemical factors will be applicable in related research areas, such as stress corrosion cracking and corrosion fatigue. The main contributions to knowledge are summarized as follows.

### **(1) Proposed corrosion system dependence of erosion-enhanced corrosion**

Based on experimental results and analysis, the corrosion system dependence of the synergistic effect between erosion and corrosion, especially the effect of erosion on corrosion, has been proposed. Due to the distinctly different corrosion behavior of passive corrosion systems and non-passive systems, which are attributed to the impact of protective passive films formed on metal surfaces, erosion impingement has different effects on corrosion processes. In non-passive corrosion systems, erosion cannot affect the corrosion rate significantly as the electrode reaction is the rate-determining step, while in passive corrosion systems, the corrosion rate, corresponding to the passive current, increases markedly with erosion intensity. Although some supportive experimental results can be found in the previous literature, this system dependence was ignored widely. A clear understanding on the dependence of the effect on the corrosion system has now been established. The data will enable more systematic investigations into the interaction of erosion and corrosion.

### **(2) Further verification and development of an erosion-corrosion model**

As anodic current is applied to the metallic electrode surface, the mechanical properties of the metal surface degrade and, therefore, result in a higher creep rate, a lower yield/tensile stress and lower surface hardness. To date, this phenomenon has been recognized as a chemo-mechanical effect. In some research areas involving the interaction corrosion and mechanical deformation, this effect has been applied to understanding of the material failure process. However, its application in the erosion-corrosion area was only recently proposed by the author's group. In the present work,

experiments were carried out to verify this chemo-mechanical model. To further understand the deviation between the predicted results and experimental data, a new technique, the in situ nanoindentation test, has been used. The differences between the predicted values and experimental data were considerably reduced. Through the nanoindentation tests, the decline of the chemo-mechanical effect with depth towards the bulk material was also determined for the first time.

### **(3) Analysis of a new experimental phenomenon**

In a flowing solution without the presence of solid particles, the measured weight loss rate was higher than that calculated from the anodic current using Faraday's law. This phenomenon was mentioned briefly in previous publications, but no systematic experimental investigations or the mechanistic studies were conducted. In the present work, based on the analogy between this phenomenon and the erosion-corrosion process in a flowing slurry, the root cause inducing the additional material loss was analyzed. The result showed for the first time that corrosion-enhanced erosion can still occur without impingement of solid particles in solution, provided that the flow velocity is sufficiently high.

### **(4) Electrochemical perspective provided into erosion-corrosion studies**

In passive systems, erosion accelerates corrosion by impairing the passive film. By using electrochemical impedance analysis techniques, the effect of erosion on the electrode reaction processes was characterized by the change in the elements of an equivalent circuit. The results showed the deterioration effects of erosion on passive films. Further, Mott-Shottky analysis, in conjunction with PDM, connected the repassivation process of passive films with the resistance of electrodes to erosion-enhanced corrosion. These investigations provided an electrochemical perspective applied to erosion-corrosion studies.

### 6.3 Contribution to literature

Based on the experimental results and analysis conducted in this work, the following papers have been published, accepted for publication or are in preparation.

- (1) H.X. Guo, B.T. Lu and J.L. Luo, Synergistic effect of erosion-corrosion of A1045 carbon steel in Na<sub>2</sub>SO<sub>4</sub> solution, 43<sup>rd</sup> Annual Conference of Metallurgists of CIM, Hamilton, Canada (2004) 525.
- (2) H.X. Guo, B.T. Lu and J.L. Luo, Study on passivation and resistance to erosion-enhanced corrosion by Mott-Schottky analysis, *Electrochimica Acta*, accepted.
- (3) H.X. Guo, J.L. Luo and B.T. Lu, Effect of erosion on passivation and pitting corrosion of carbon steel in borate solution, *Corrosion Science*, submitted
- (4) H.X. Guo, B.T. Lu and J.L. Luo, Interaction of mechanical and electrochemical factors in erosion-corrosion of carbon steel, *Electrochimica Acta*, 2005, 51: 315.
- (5) H.X. Guo, B.T. Lu and J.L. Luo, Non-Faraday material loss in flowing corrosive solution, *Electrochimica Acta*, 2006, 51: 5341.
- (6) H.X. Guo, B.T. Lu and J.L. Luo, Response of surface mechanical properties to electrochemical dissolution determined by in-situ nanoindentation technique, *Electrochemistry Communication*, 2006, 8: 1092.
- (7) H.X. Guo, J.L. Luo, F. King, Erosion-corrosion behaviour of TiC reinforced alloys, *Wear*, in preparation.

### 6.4 Suggestions for future work

The investigations conducted in the present work have greatly enhanced understanding of erosion-corrosion interactions. Nevertheless, some experimental phenomena and mechanisms are still not clear, and further experimental investigations are required to more fully elucidate these phenomena. Based on the

results acquired from this research, the following suggestions are made for future work.

**(1) Erosion-enhanced corrosion in non-passive systems**

The effect of erosion on corrosion has been investigated with carbon steel/sodium sulphate solution. The results showed no profound influence on corrosion rate from erosion as the electrode reaction is the rate-controlling step. More active corrosion systems should be investigated. The ratio of mass transfer limited rate to electrode reaction rate can be considered as a parameter for selecting systems to be studied. With regard to the influence of erosion on mass transfer, knowledge of fluid mechanics and mass transfer in multi-phase flow will be required.

**(2) The chemo-mechanical effect**

The chemo-mechanical effect is a very interesting phenomenon and worthy of further study. A more ideal system, preferably consisting of single crystal metal and a solution from which a corrosion product will not deposit on the metal surface, can be chosen. The research can place emphasis on the effect of different anodic current densities and the time effect of anodic current. Such research will provide fundamental understanding of the effect of corrosion on metallic materials' mechanical properties.

**(3) The effect of corrosion on erosion in passive systems**

Preliminary studies on the effect of corrosion on erosion in the passive system were carried out in this work. The special situation in which there is both damage and repair of passive film will influence the process. A jet impingement apparatus will be more suitable for this study than the present rotating electrode system, since the impingement frequency can be controlled more accurately.

## **Appendix: Erosion-Corrosion of TiC Reinforced Alloys**

In Chapter 4 and 5, the erosion-corrosion behaviour of carbon steel and the interaction between corrosion and erosion were investigated. Although there exists ferrite and pearlite in the carbon steel, the difference between these two components is not as great as in metal matrix composites. Therefore, the carbon steel was treated as a homogeneous material in the investigation. In the present chapter, the erosion-corrosion behaviour of several metal matrix composites was studied. It was found that some mechanism proposed in chapter 4 and 5 is able to be applied to MMC. On the other hand, a specific process for MMC, which cannot apply to homogeneous materials, was reported.

### **A.1 Introduction**

As has been introduced in Chapter 2, the metal matrix composites consist of a ductile metal matrix and hard particles phases. Due to their excellent mechanical properties, especially the high hardness, MMCs have been considered as promising candidate materials for protection against erosion/wear in various industrial applications. Unfortunately, as the application environment of MMCs involves a corrosion reaction, serious material loss and premature material failure were reported [1, 2].

Similar to the significant synergistic effect found in steels, during erosion-corrosion process of MMCs the interaction between these two processes results in severe material loss. Considering the different phase compositions and their roles in material mechanical properties and corrosion reactions, the synergistic effect could be more complicated than or different from that for steels. Thus, in the present work, the erosion-corrosion of several MMCs was investigated and the mechanism for the interaction was analyzed by electrochemical tests and surface characterization. In addition, an interesting experimental phenomenon regarding the effect of chloride on

the erosion-corrosion was reported. During analysis, some conclusions drawn from the erosion-corrosion of steels was attempted to be applied to MMCs.

Two MMCs, Nikro 143 and Nikro 128, were taken as test material, and their chemical compositions are listed in **Table 1**. These materials are used as cutting blades to slice polymer during polyethylene pellet production in NOVA Chemicals, Canada. The MMC test materials were solution-annealed at 850 C° for 3 h in vacuum. Some samples were used in the solution-annealed condition, denoted as 143A and 128A, while others were age-hardened at 480 C° for 6 h, denoted as 143H and 128H, respectively.

**Table 1. Chemical composition of Nikro 143 and Nikro 128 (wt%).**

	TiC	Cr	Co	Ni	Mo	Fe
Nikro 128	30	13.5	9	4	5	Balance
Nikro 143	30	-	9	15	6	Balance

## **A.2 Results and Discussion**

### **A.2.1 The synergistic effect between erosion and corrosion**

#### **A.2.1.1 The pure erosion rate**

Various weight loss rates due to the corresponding process were investigated separately in order to understand the role of each process in the total erosion-corrosion behaviour. Firstly, the weight loss due to a pure mechanical damage effect was measured in 35% silica sand slurry under CP condition, as shown in **Figure 1**. With the same heat treatment, alloys 143 were more erosion-resistant than alloys 128; for same type of alloy, the aged one had better erosion resistance than the annealed one. In the mean time, the hardness of each alloy was tested in Rockwell hardness

scale C. **Figure 2** illuminated the dependence of pure erosion rate on material hardness. It can be found that the erosion rate decreased with an increase in hardness.

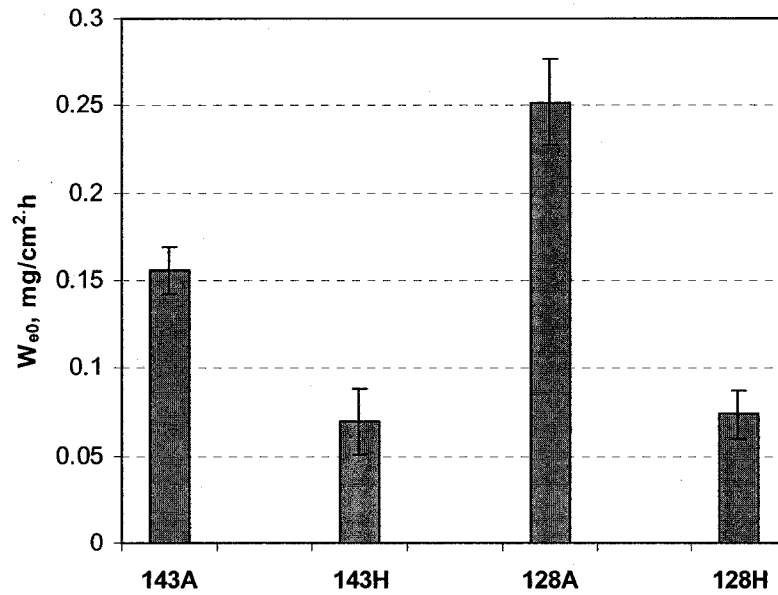


**Figure 1.** Pure erosion rates of alloys in 0.1 M Na<sub>2</sub>SO<sub>4</sub> with 35% sand at arotating velocity of 9000 rpm.

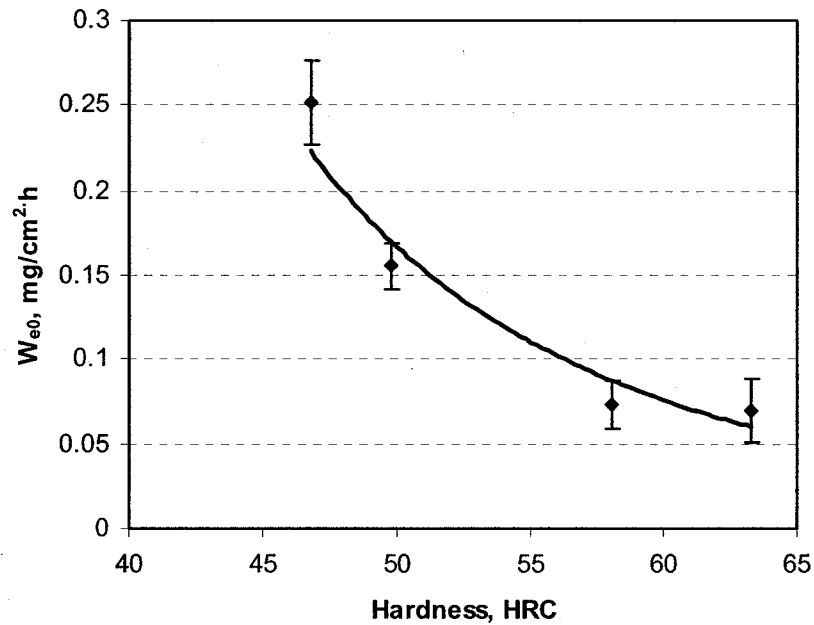


**Figure 2.** Dependence of pure erosion rate on hardness of Nikro alloys.

Although there exist some contradictory conclusions about the relationship between erosion rate and material hardness, the results observed in **Figure 2** was in agreement with the results measured with the carbon steel shown in **Figure 5-5**. The correlation between the erosion resistance and the hardness of base metal might depend on the erosion mechanism, the microstructure and composition of material. It might be difficult to find a general relation between hardness and erosion rate for all materials, but for materials with similar microstructure and composition, when the erosion process is dominated by the same mechanism, it is possible to find certain relationships between these two parameters. The alloys used in the present work were similar in composition and microstructure, except the content of chromium, and the erosion mode was the same. Hence, the dependence of erosion rate on hardness was found.

#### **A.2.1.2 The pure corrosion behavior**

The corrosion behaviour of alloys in solution and silica sand slurry was studied by potentiodynamic polarization scanning. **Figure 3** shows the polarization curves of the four alloys in 0.1 M Na<sub>2</sub>SO<sub>4</sub> solution at a rotating velocity of 9000 rpm. It can be observed that alloys 128, with high Cr content, showed passive behaviour, while alloys 143 showed active dissolution behaviour. It can be estimated from the polarization curves that the corrosion rate of alloys 128 at E<sub>c</sub> are much lower than those of alloys 143.

During annealing, the MMC samples were solution-annealed at 850C° for 3 h in vacuum. This heat treatment can result in a large grain size of intermetallic composite. By contrast, the hardened samples were age-hardened at 480C° for 6 h, which would result in small size and evenly-distributed intermetallic composite. For corrosion reactions, usually the grain boundary with high energy suffered more severe attack. In addition, there existed residual interstress within the hardened sample. Both of these factors could deteriorate the corrosion resistance of alloys, which might be the reason for the lower E<sub>c</sub> of 143H than that of 143A. As for alloys 128, the excellent

passive behaviour from chromium attenuated the difference brought by heat treatment, and led to very similar corrosion behaviour.

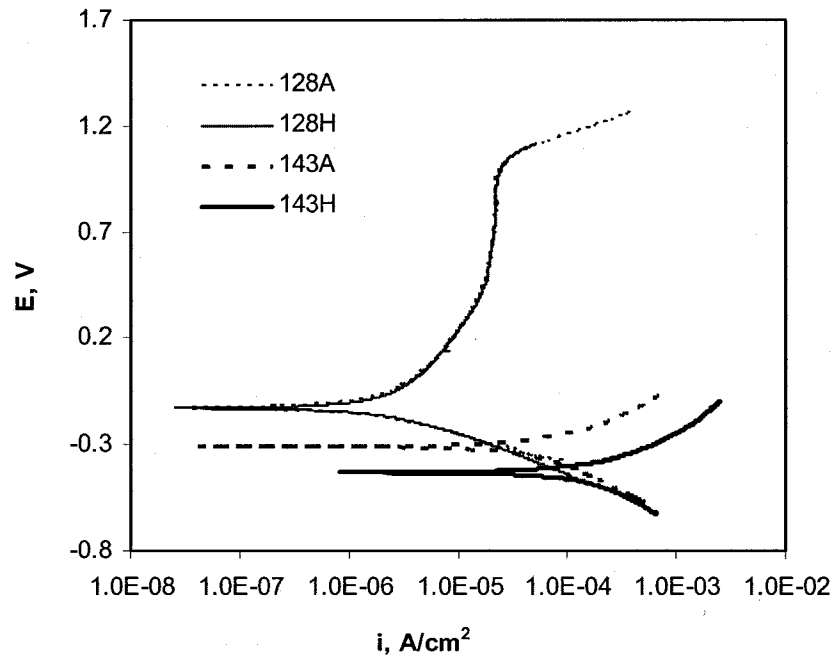


**Figure 3. Potentiodynamic polarization curves of alloys in 0.1 M Na<sub>2</sub>SO<sub>4</sub> solutions at a rotating velocity of 9000 rpm.**

#### A.2.1.3 The synergistic effect

The pure erosion rates due to the mechanical process have been determined, and the pure corrosion rates can also be estimated from **Figure 3** with the Tafel extrapolation technique. Therefore, once the total material loss rate due to erosion-corrosion process is measured, the synergistic component and then the relative contribution of each wastage component to the total material loss can be determined. To accomplish this, weight loss tests were conducted in sand-containing solutions at  $E_c$ . **Figure 4** shows the total weight loss rates obtained in 35% slurry at a rotating velocity of 9000 rpm. For comparison, the pure weight loss and the pure corrosion rates are also presented in the figure. Apparently, for each alloy, the total weight loss was higher than the sum of the pure erosion rate and pure corrosion rate, indicating a

synergistic effect existing between erosion and corrosion. Due to higher hardness, alloys 143 exhibited better pure erosion resistance than alloys 128. On the other hand, alloys 128 had much better corrosion resistance than alloys 143 owing to the 13.5% chromium-content in the alloy. As both erosion and corrosion occurred on the metal surface, however, it can be clearly found that the total material loss of alloys 128 was much lower than alloys 143.

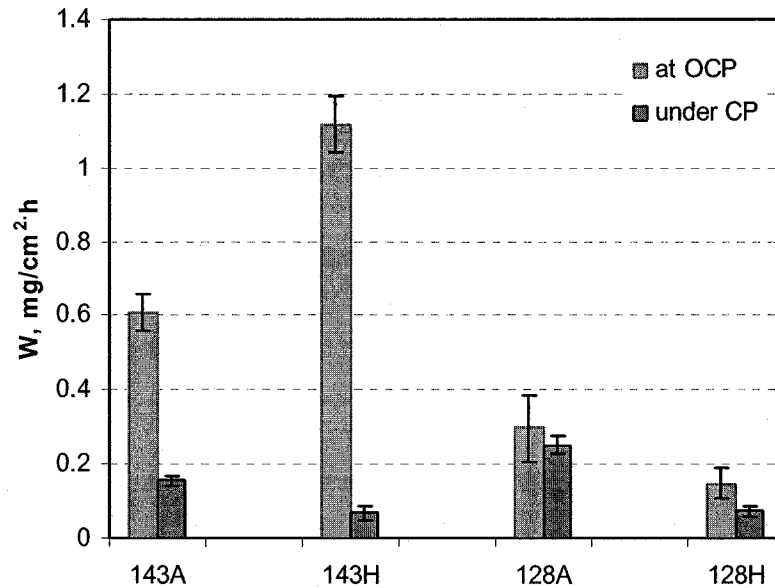


**Figure 4. Comparison of pure erosion rate, pure corrosion rate and erosion-corrosion rate.** (Pure erosion: 0% sand, 9000 rpm, under CP; Erosion-corrosion: 35% sand, 9000 rpm, under  $E_c$ , and pH=7.)

The percentages of material loss due to corrosion, erosion and synergy were calculated and are shown in **Figure 5** to illustrate the contribution of each component clearly. The important synergistic effect was more directly found for 128H and alloys 143, suggesting that the interaction of erosion and corrosion played a key role for the overall material loss.

By comparing the results for alloys 143 and 128, it was interesting to find that the synergy seemed to increase with corrosion rate, while by comparing the annealed

and hardened alloys the synergy was found to decrease with erosion rate. This suggests that the synergistic effect will be more significant for a material with higher erosion resistance and lower corrosion resistance. Based on this consideration, a parameter was constructed to be equal to the ratio of pure corrosion to pure erosion. **Figure 6** shows the dependence of synergy percentage on this parameter. As expected, the synergy increases with this parameter. This relationship should depend on the interaction mechanism of erosion and corrosion. This contention needed further verification with more experimental data from different alloys.

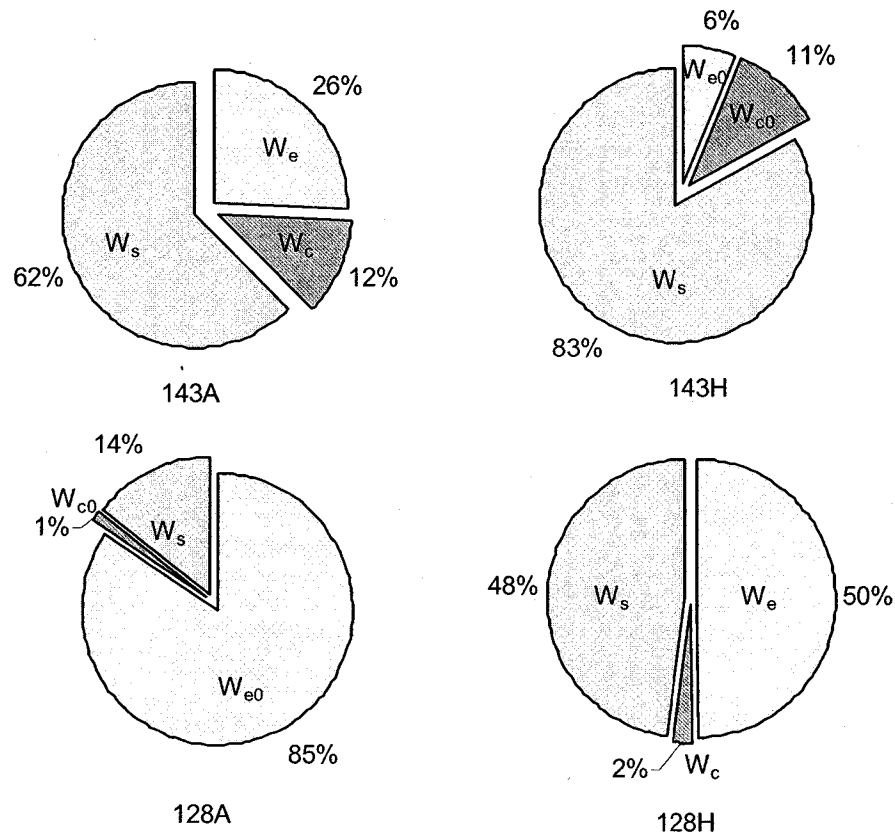


**Figure 5. Relative contribution of each component,  $W_{c0}$ ,  $W_{e0}$  and  $W_s$  to the total material loss in 0.1M  $Na_2SO_4$  solutions/35% sand with rotating velocity of 9000 rpm.**

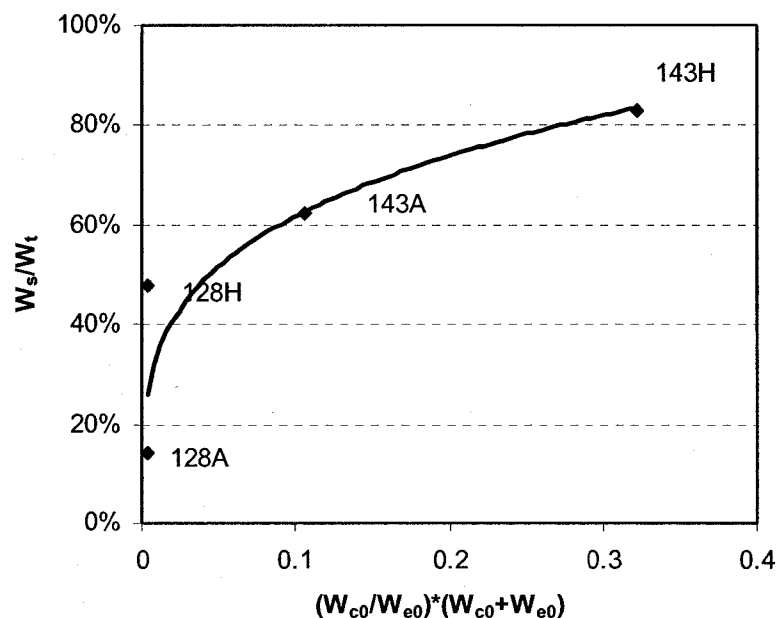


**Figure 6. Dependence of synergy component on pure erosion and pure corrosion.**

## **A.2.2 Interaction mechanism for erosion and corrosion**

### **A.2.2.1 Effect of erosion on corrosion**

The above test results showed that the synergistic effect was important in the erosion-corrosion process of MMCs. Due to the different mechanisms involved the interaction between erosion and corrosion process needed to be analyzed from the influence of erosion on corrosion and the influence of corrosion on erosion

The corrosion behaviour of the alloys was investigated in solutions with and without 35% sand to understand the effect of erosion on corrosion, and the results are shown in **Figure 7**. For 143A, its corrosion potential decreased apparently, while its corrosion rate only increased slightly. For 143H, the addition of sand did not significantly alter either corrosion potential or corrosion current density. Conversely, for both annealed and hardened 128 alloys, the corrosion potential shifted to the negative potential and the passive current increased apparently due to the addition of sand in the test solution.

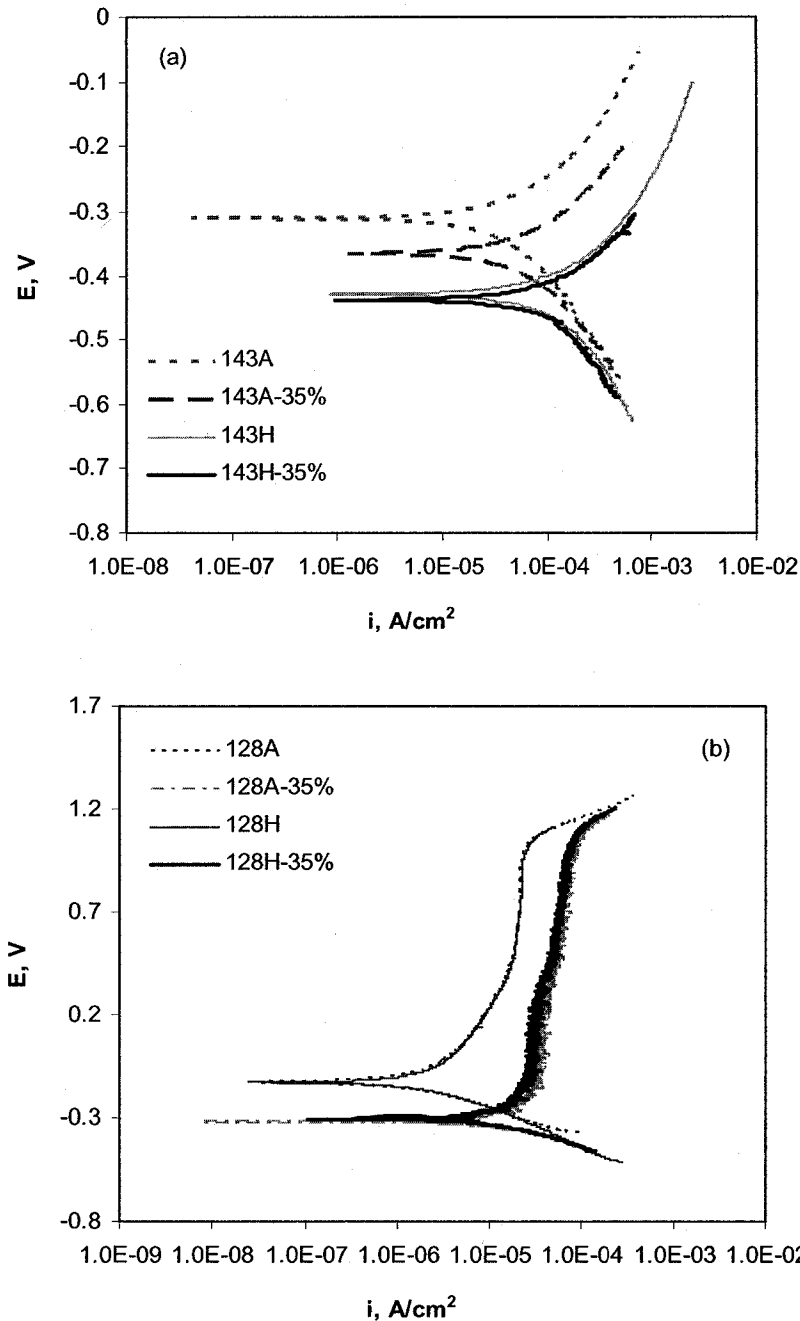


**Figure 7. Potentiodynamic curves for (a) 143 alloys and (b) 128 alloys in 0.1 M Na<sub>2</sub>SO<sub>4</sub> solutions (pH = 7) without and with 35% sand at the rotating velocity of 9000 rpm.**

The different response of corrosion to erosion process for these alloys suggests the dependence of the impact of erosion on the corrosion system. This observation

was consistent with the investigation results shown in Chapter 4 where the effect of erosion on corrosion for carbon steel in 0.1 M Na<sub>2</sub>SO<sub>4</sub> solution (an active corrosion system) [3] and borate solution (a passive corrosion system) was analyzed. Accordingly, the proposed dependence of erosion-enhanced corrosion on the corrosion system can also be applied to MMCs. In non-passive systems, the corrosion product adsorbed on the surface is not protective and, therefore, its removal by impingement of solid particles cannot affect the dissolution rate significantly. In passive systems, however, the passive film has an ability to inhibit corrosion. When this film is damaged by the impingement of solid particles during an erosion-corrosion process, fresh metal surface is exposed to solution and suffers from severe damage. Therefore, a much more significant effect of erosion can be found in passive systems than in active systems.

#### **A.2.2.2 The chemo-mechanical effect**

With regard to the effect of corrosion on erosion, a chemo-mechanical effect has been employed in Chapter 5 to explain the acceleration effect of corrosion dissolution on erosion rate for carbon steel [4, 5]. According to this effect, the corrosion-enhanced erosion in slurry resulted from the anodic dissolution-induced hardness degradation in the surface layer, and a linear relationship between the corrosion-enhanced erosion and the logarithm of anodic current has been found in the carbon steel/Na<sub>2</sub>SO<sub>4</sub> solution system, which was consistent with the prediction of the model. For the present alloys, the erosion-corrosion as a function of corrosion parameter (applied anodic current for alloys 143 and passive potential for alloys 128) was also tested. **Figure 8** presents the measured results for the MMC samples in 35% slurry at a rotating velocity of 9000 rpm. For the non-passive 143A and 143H, the total erosion-corrosion rate increased with applied current density. This was consistent with the experimental results for the carbon steel in sodium sulphate solution, which was shown in **Figure 5-1**. For the passive 128A and 128H, no apparent dependence of erosion-corrosion rate on passive potential was found. Also, this observation was

in agreement with the results tested for the carbon steel in borate buffer solution, as shown in Figure 5-43.

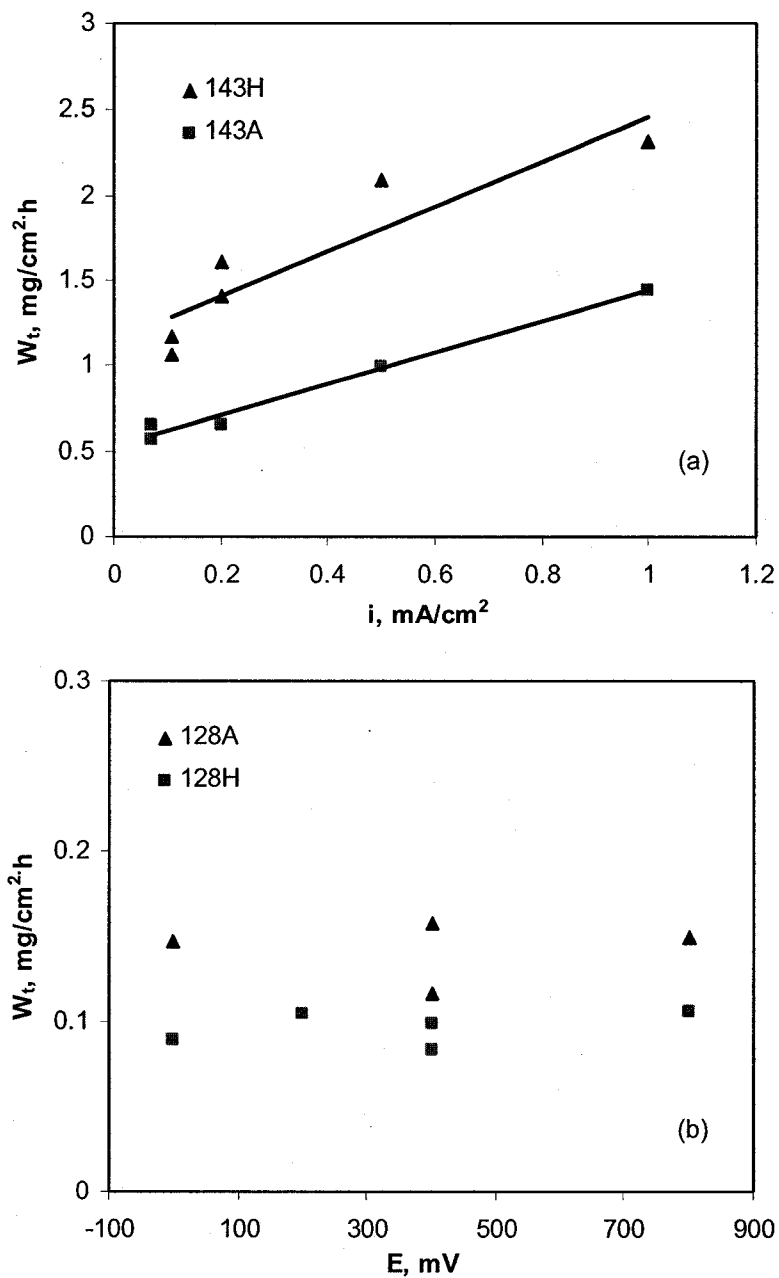


**Figure 8. Dependence of erosion corrosion rate on potential in 35% slurry at 9000 rpm: (a) Alloys 143; (b) Alloys 128.**

It seemed that the experimental results obtained for the present MMCs were quite similar to those for carbon steel A1045. However, as the corrosion enhanced-erosion (or normalized corrosion enhanced-erosion) was calculated and plotted as a function of applied current density, the half-logarithm dependence was not found. Considering the phase composition difference between carbon steel and Nikro alloys, this phenomenon was unexpected. Carbon steel consists of ferrite and pearlite, but the difference between the corrosion resistances of these two phases was not so marked as the difference between titanium carbide and Nikro metal matrix. In the development of the chemo-mechanical model, the phase heterogeneity was not considered and the metallic electrode was treated as a homogeneous material. As a consequence, for the particle reinforced material, this model might not give a good prediction. This, however, cannot exclude the possibility for this mechanism to work during the erosion-corrosion process of MMCs. Upon considering the interaction of chemical/electrochemical and mechanical processes in nature, the chemo-mechanical mechanism was still believed to work for the present corrosion system. Nevertheless, based on the phase composition of the present alloys, other mechanisms rather than the chemo-mechanical effect might dominate the impact of corrosion on erosion.

#### **A.2.2.3 The microscope observation and corrosion-enhanced erosion**

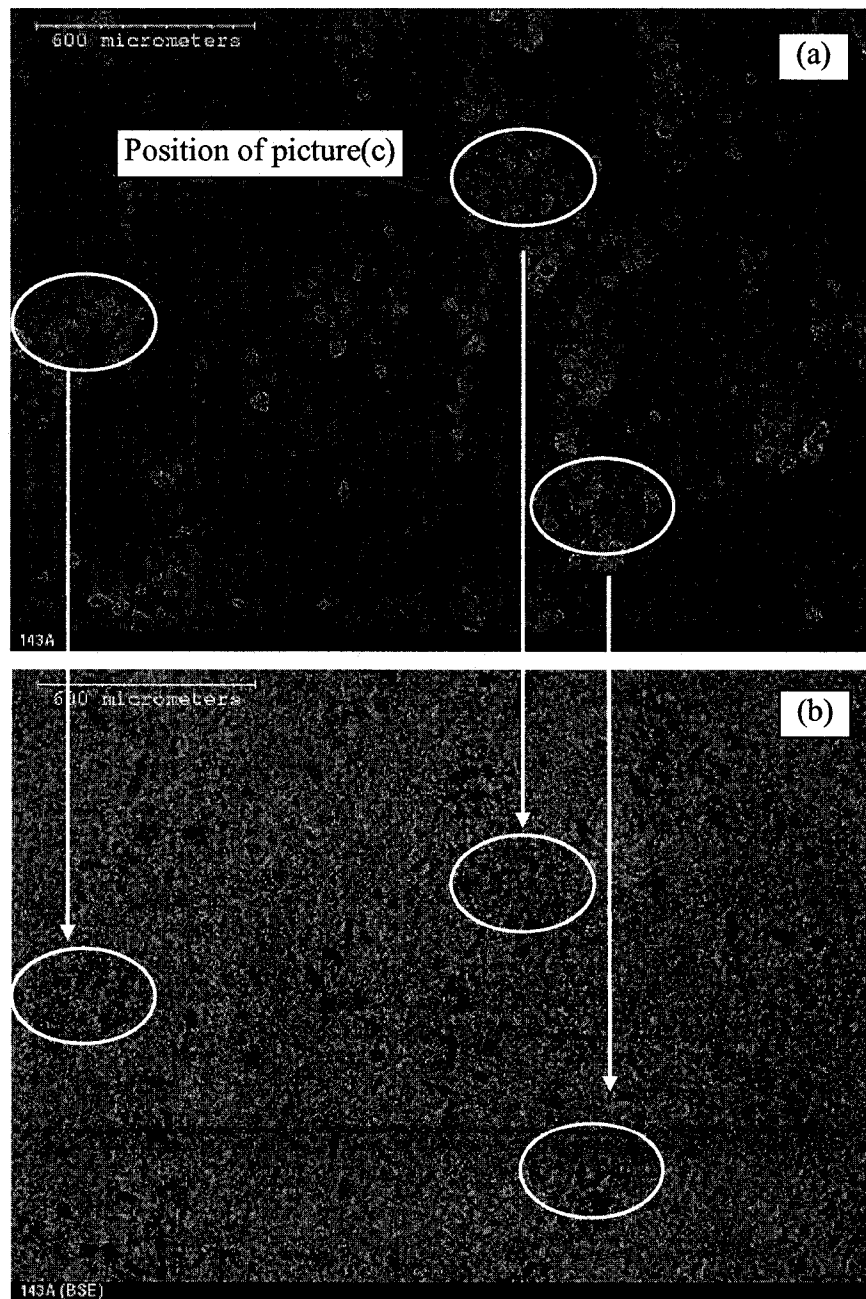
The morphology of each alloy after erosion-corrosion tests was examined with the SEM to clarify the main mechanism for corrosion-enhanced erosion. The morphology pictures were taken with Secondary Electron Image Technique (SE), and the corresponding Backscattered Electron images (BSE) were also obtained to determine the phase distribution. In a BSE picture, the phase with higher average atomic number is brighter than that with lower average atomic number. **Figure 9** shows the morphology with low and high magnification and the corresponding phase distribution for 143A after the erosion-corrosion test in the slurry. In the low magnification picture, the position for the high magnification picture was marked. It can be noticed from the pictures that the surface damage was not uniform. The area concentrated with dark phase was damaged more severely, and the correlation was

marked in some areas in the picture. To determine the composition of these phases, elemental analysis was carried out with the EDX technique. The detection positions were marked in **Figures 9 (a) and (b)** and the results are shown in **Figure 10**. Firstly, the result for the overall element analysis is shown in **Figure 10 (a)**, and it can be found that except for elements Al, Si and Cu, which could be impurity elements of the alloy, the composition was consistent with **Table 1**. Points 1, 2 and 3, with the same composition, were found to be TiC; points 4 and 5 were the matrix. Consequently, the dark phase in the BSE picture was TiC and the bright phase was the matrix. Similar analysis was also applied to 143H and 128H, and the results are shown in **Figure 11** though **Figure 13** (the result for 128A was similar to that for 128H and thus was not shown). The EDX analysis results are marked on the pictures directly. Similar results were found, i.e., more severe damage was found on areas with high concentration of TiC particles. Moreover, grooves were found around the TiC particles so that the particles looked separated from the matrix rather than embedded in the matrix.

From the SEM analysis result for all the alloys, more severe damage was found on areas with high concentration of TiC particles. Specifically, the average compositions of the area that was severely damaged and that was slightly damaged for 143 H are compared in **Figure 12**. It indicated that the peak height of element Fe in the former area was lower than in the latter area, suggesting higher TiC concentration in the damaged area.

The above observation suggests the preferential dissolution of the metal matrix around the particles. This was attributed to the different roles of the two phases during the corrosion process. The carbide particles, with high corrosion resistance, acted as the cathodic phase and provided sites for the cathodic reduction reaction of oxygen, while the metal matrix, as the anode, dissolved electrochemically. For the interface between the particles and matrix, the metallic atoms had higher energy due to the disordered structure and high internal strain. Also, the electric resistance increased with the distance between the cathode and anode. All these factors could rationalize the higher corrosion rate of the matrix around TiC particles. In addition, as

the concentration of the hard particles increased, the ratio of the cathodic area to anodic area increased correspondingly, that led to a higher dissolution rate of the matrix. Other researchers also reported that the interface of the metallic matrix and dispersoid was the most active region for corrosion [1, 2, 6]. As the matrix dissolved to a certain extent, the hard particles can be removed by attack of the slurry, which sequentially results in acceleration of material loss.



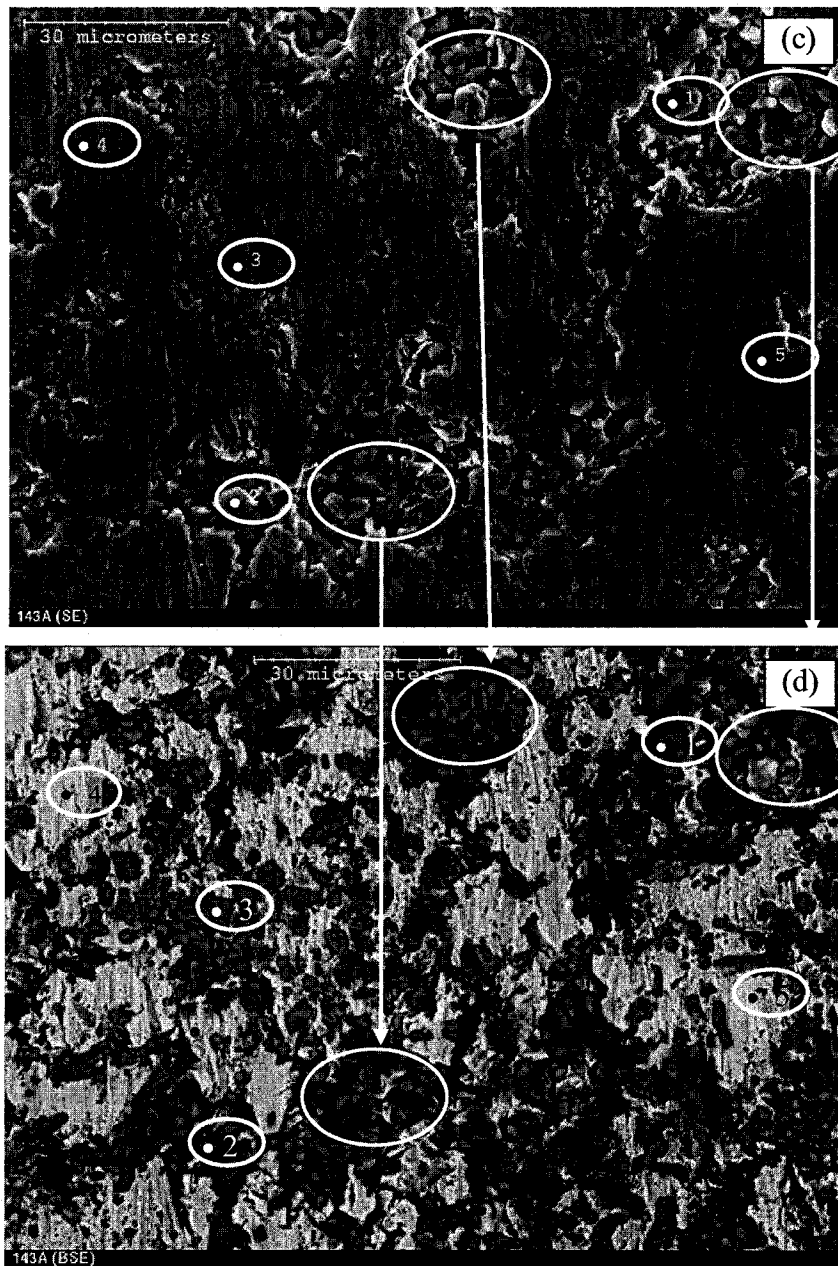


**Figure 9. SEM images for 143A after erosion corrosion in 35% slurry:  
(a) SE with lower magnification; (b) BSE with lower magnification  
(c) SE with higher magnification; (d) BSE with lower magnification.**

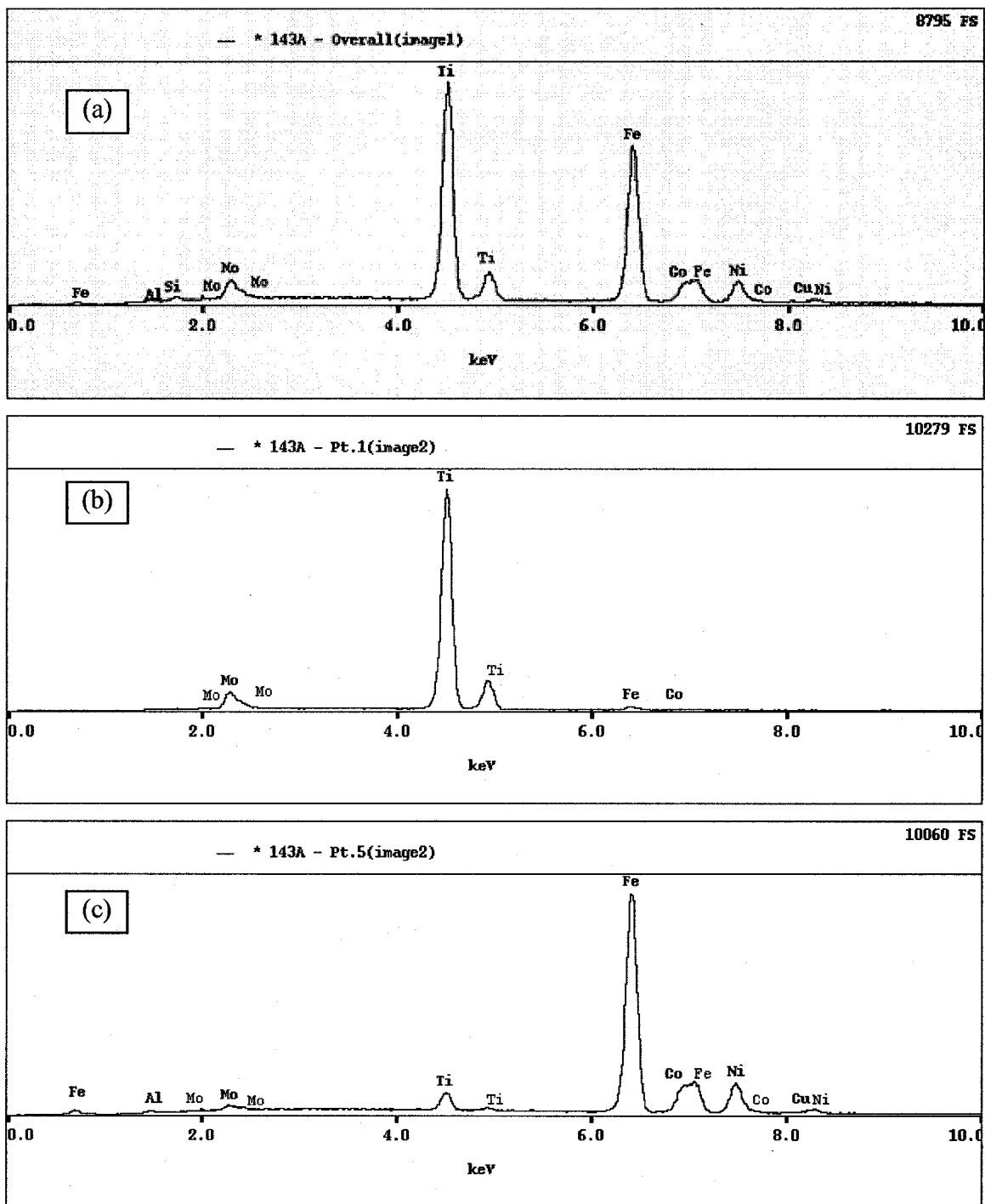
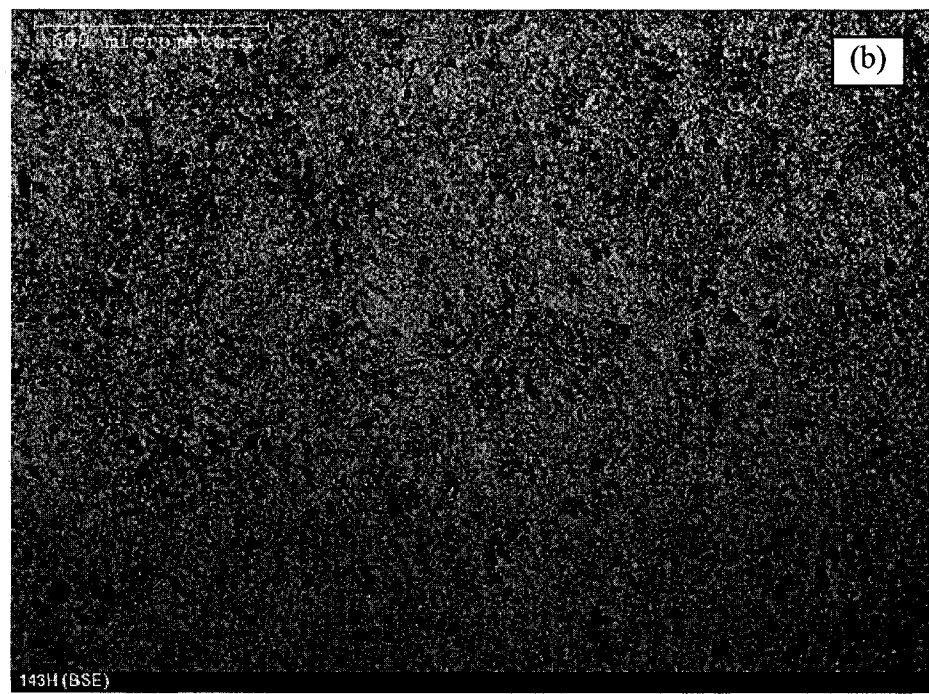
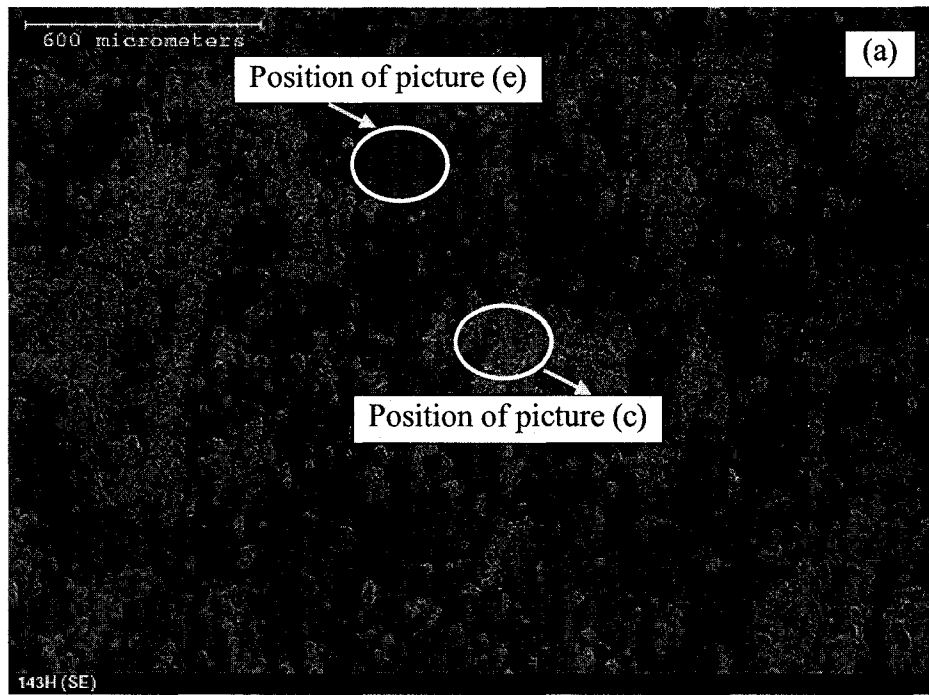
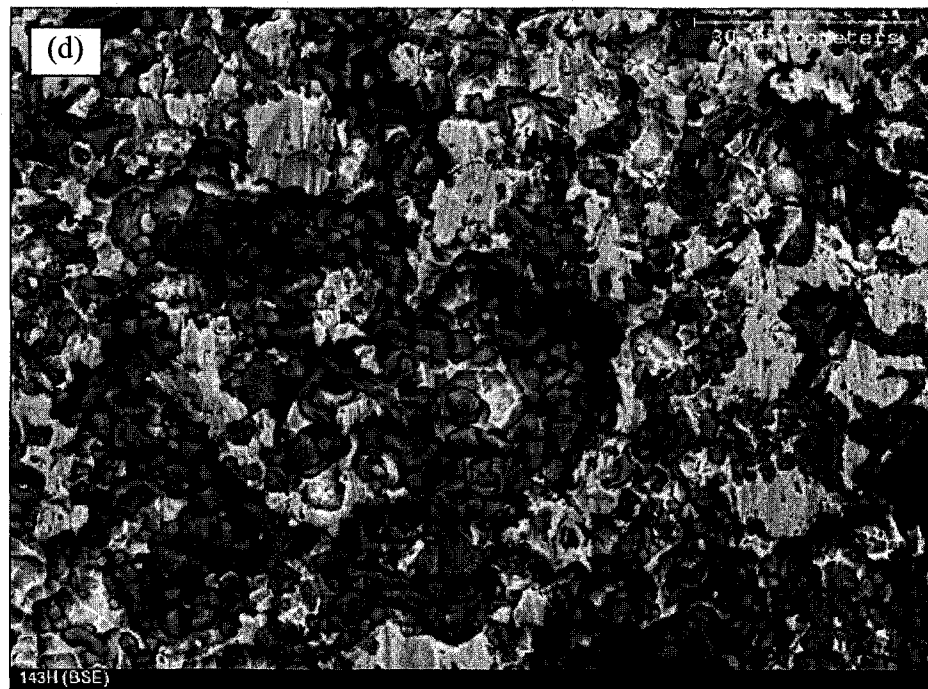
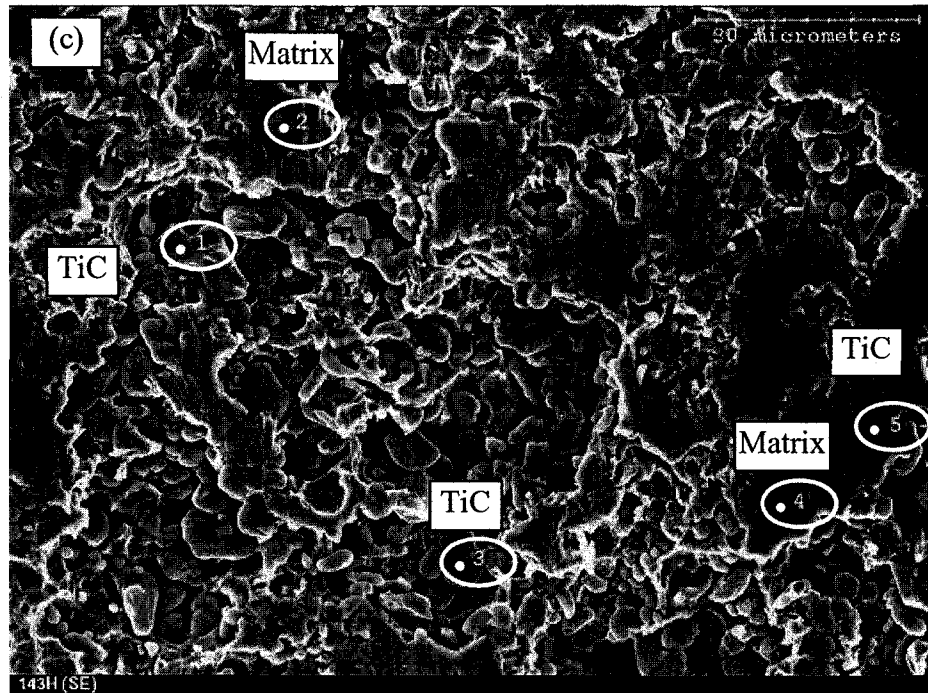
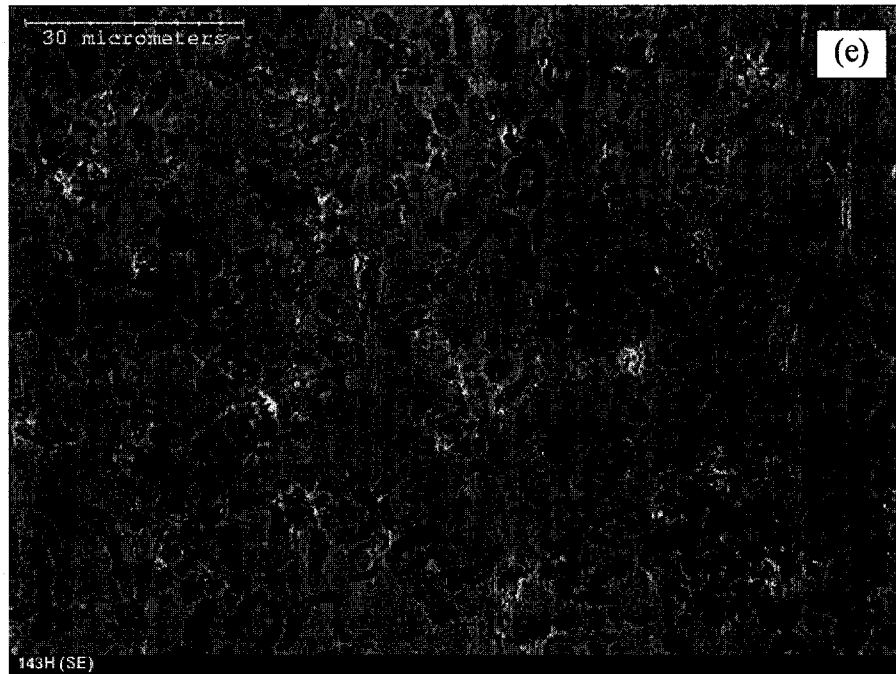


Figure 10. EDX profile for 143A after erosion corrosion on the points marked in Figure 9(c): (a)Overall analysis; (b) Point 1; (c) Point 5.







**Figure 11. SEM images for 143H after erosion corrosion in slurry: (a) SE with lower magnification; (b) BSE with lower magnification; (c) SE with higher magnification on severely damaged area; (d) BSE with lower magnification on severely damaged area; (e) SE with higher magnification on slightly damaged area.**

Hence, without the presence of a corrosion reaction on the metal surface, more impact energy was required for the sand particles to remove the carbide due to its high hardness. Since the size of the carbide was much smaller than the sand particles and the concentration of carbide was rather high, there was no zone free of carbide on the metal surface. With the TiC reinforcing effect, the overall material removal rate was consequently very low, as shown in **Figure 1**. As corrosion occurs at the metal surface, due to the preferential dissolution of the metal matrix, the carbide particles can be removed more easily, and thus the erosion rate is accelerated. Based on this analysis, the corrosion-enhanced erosion was lower for alloys with better corrosion resistance, as long as their other properties were comparable. **Figure 14** shows the comparison for alloys 128 and alloys 143. The corrosion-enhanced erosion,  $W_{c-e}$ , was calculated by subtracting  $W_{e-c}$  from  $W_s$ .  $W_{e-c}$  was determined by the difference of the

corrosion rate in slurry and in solution. It can be observed that alloys 128, with improved corrosion resistance, exhibited lower  $W_{c-e}$  than alloys 143.

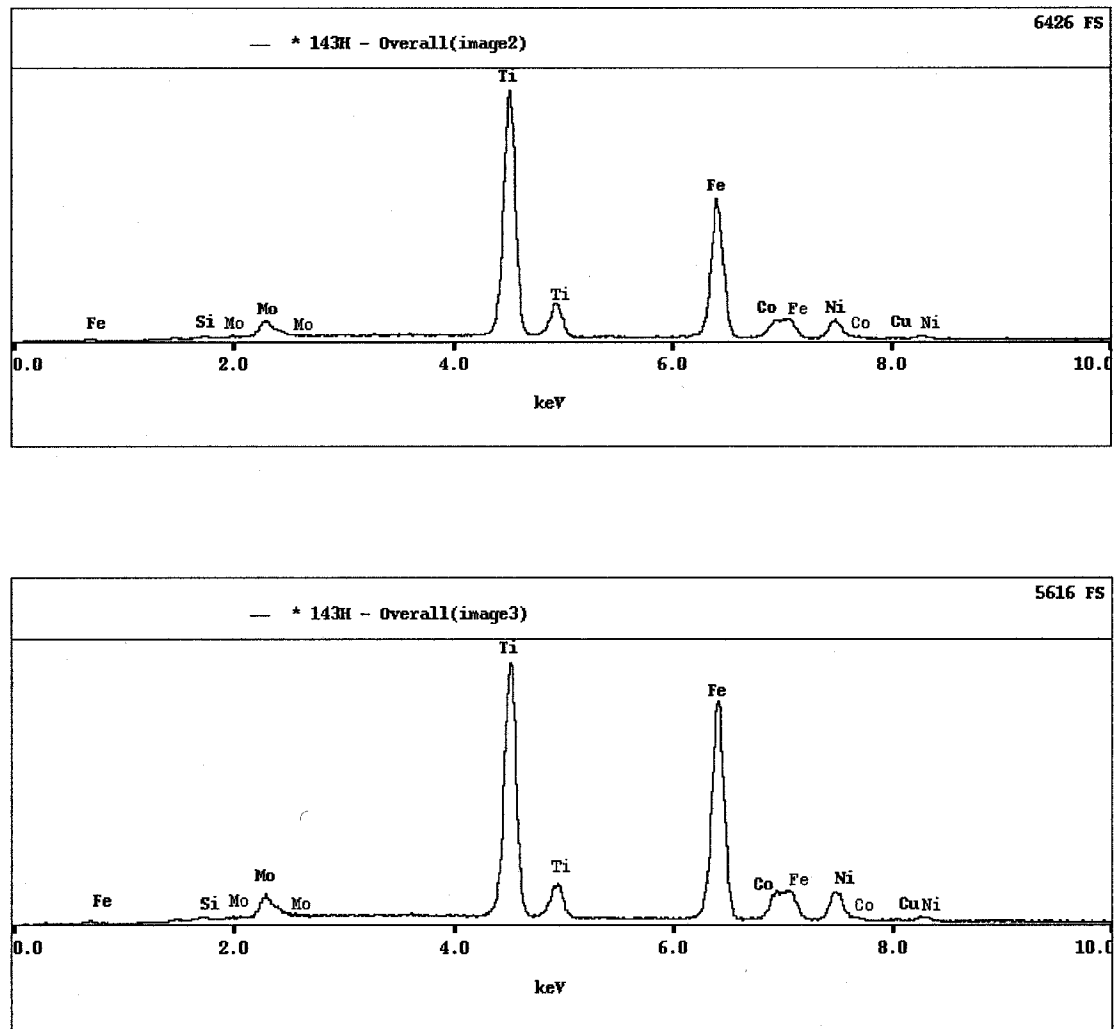


**Figure 12. EDX profile of 143H after erosion corrosion:**  
**(a)Overall element analysis for Figure 11(c); (b) Overall element analysis for Figure 11 (e).**



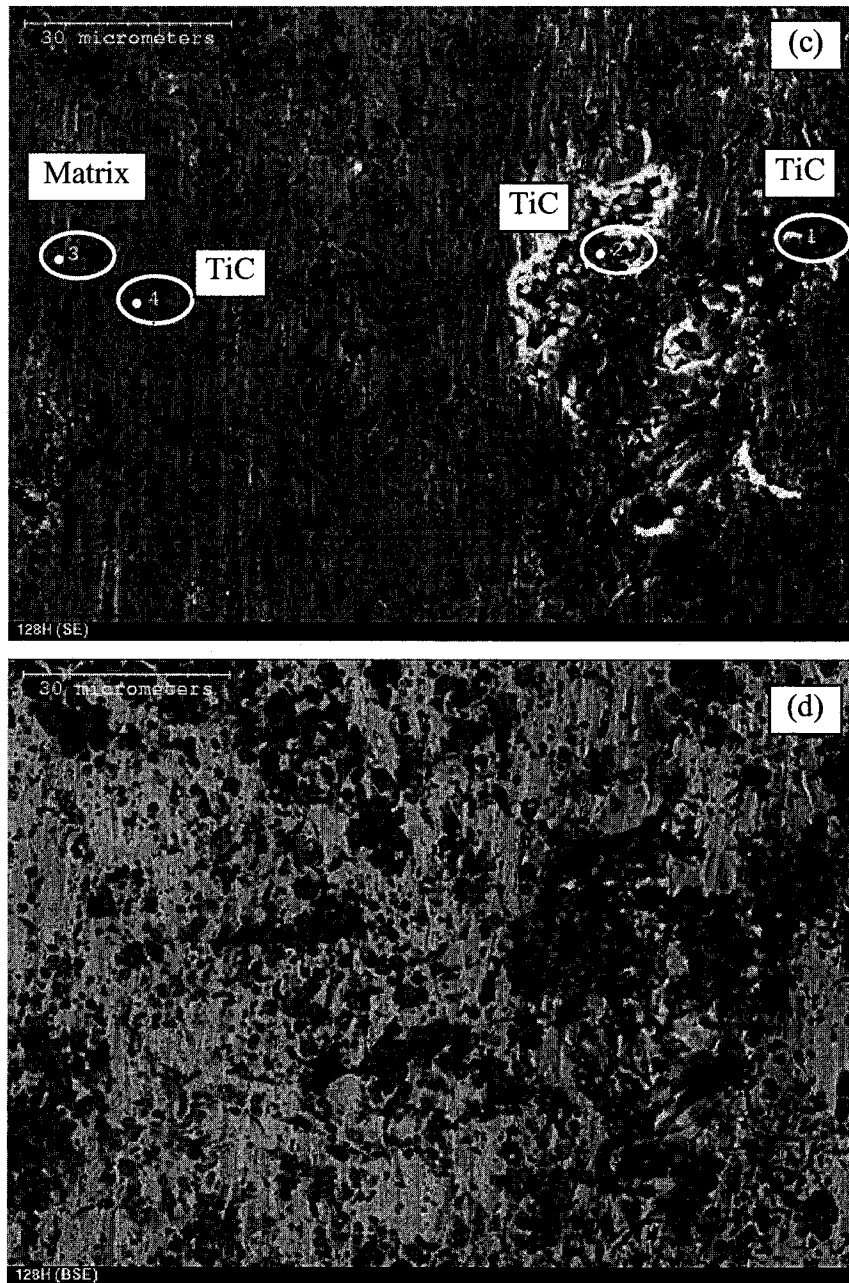


**Figure 13. Images of 128H after erosion corrosion in slurry:  
(a) SE with lower magnification; (b) BSE with lower magnification  
(c) SE with higher magnification; (d) BSE with lower magnification.**

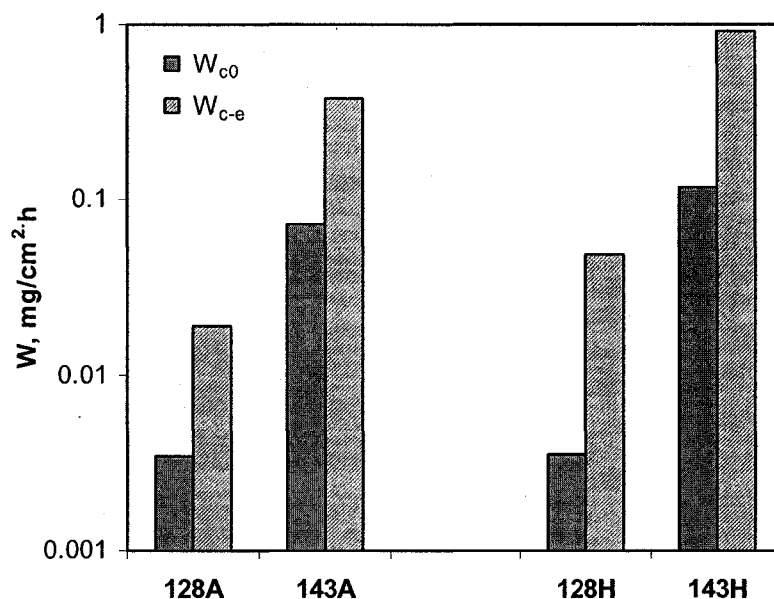
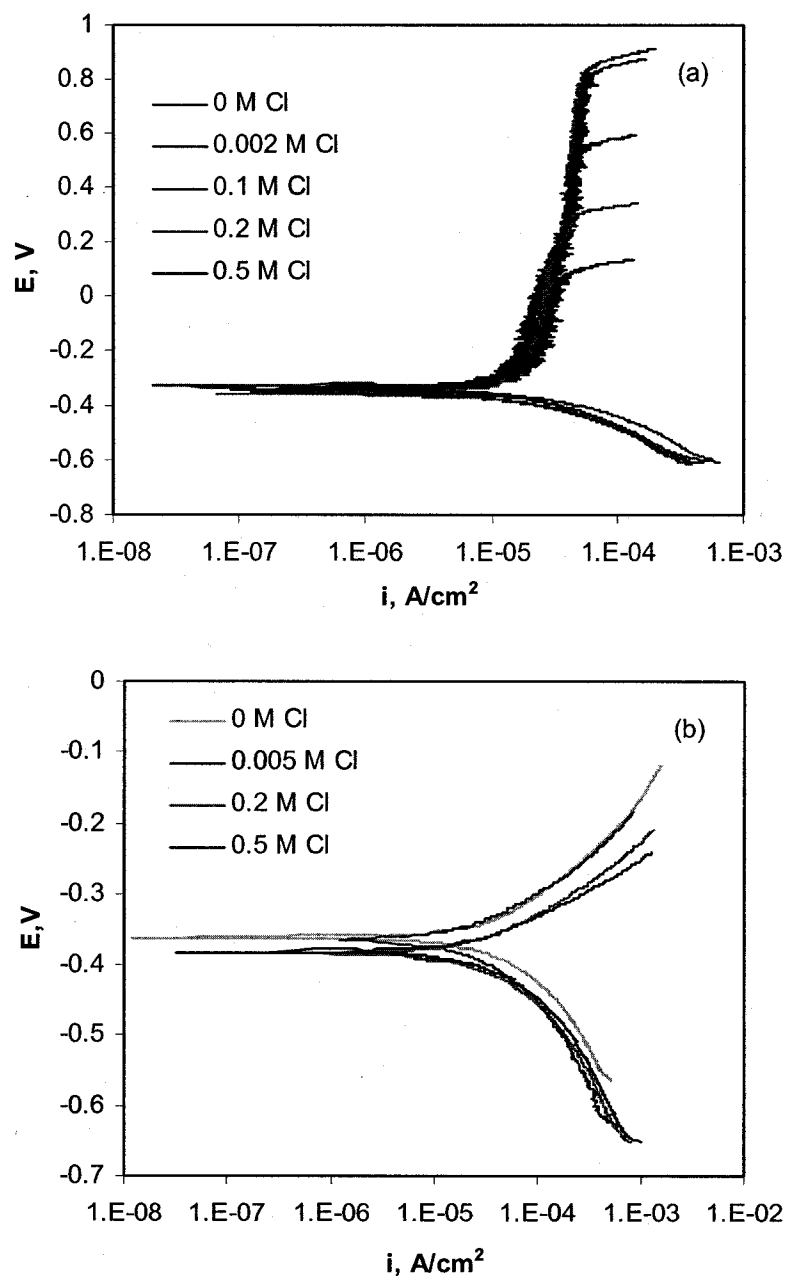


Figure 14. The corrosion-enhanced erosion rate of the alloys.

### A.2.3 Effect of $Cl^-$ on synergy

Usually, chloride in aqueous environments is detrimental for the corrosion resistance of an alloy, especially for passivated alloys, because the adsorption of chloride on the metal surface could deteriorate the protective film. Based on this concern, the effect of chloride ions on the erosion-corrosion behaviour of 128H and 143H was investigated. **Figure 15** illuminates the effect of chloride ions on the polarization curves in 35% slurry with  $pH = 9$  and velocity = 9000 rpm. For 128H alloy, the passive region shrunk with increasing concentration of chloride ions. The pitting potential decreased with chloride concentration. This was in agreement with the results measured for carbon steel A1045 in borate solution (**Figure 4-33**). Similar analysis could apply for the MMC samples. The competitive adsorption of chloride ions on a metal surface can initiate pitting corrosion at a lower potential [7, 8]. Also, chloride ions retard the repassivation of the metastable pit, thereby facilitating pitting corrosion. For 143H, it did not show apparent passive behavior, and the pitting

corrosion was not a typical corrosion form for it. Thus the effect of chloride ions was not profound.



**Figure 15. Potentiodynamic curves for the alloys in slurry with different chloride concentration: (a) 128H ; (b) 143H (35% slurry, 9000 rpm, and pH=9 ).**

Furthermore, the erosion-corrosion rate was measured in 35% slurry with different concentrations of chloride ions, and the results are shown in **Figure 16**. It was very interesting to find that the erosion-corrosion rates of both 143H and 128H were reduced by the addition of chloride ions.

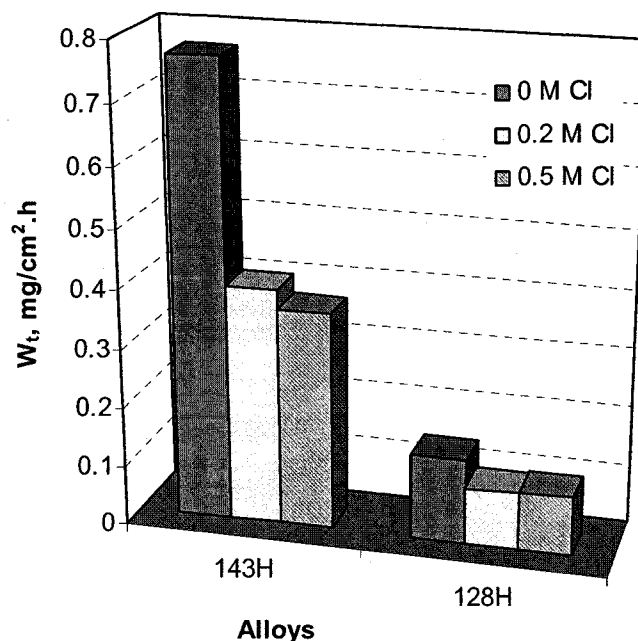


**Figure 16. Erosion corrosion rates of alloys in slurry with different chloride concentration: 35% sand / 0.1 M Na<sub>2</sub>SO<sub>4</sub>, 9000 rpm, under E<sub>c</sub>, and pH=9.**

The effect of chloride should be considered based on the electrochemical dissolution and mechanical wear. From the polarization curves shown in **Figure 15**, however, the corrosion behaviour of the alloys was not inhibited by the presence of chloride ions at EC. Hence, although some researchers reported an inhibition effect of Cl<sup>-</sup> on corrosion of metals [9, 10], such an effect was not found for the present corrosion system. Zhang et al [11] studied the effect of Cl<sup>-</sup> on the corrosive wear of stainless steel in H<sub>3</sub>PO<sub>4</sub> and H<sub>2</sub>SO<sub>4</sub> solutions at comparatively high loads and found that Cl<sup>-</sup> accelerated the corrosive wear rate by assisting surface film cracking. This phenomenon was reasonable as the passive film cannot get repaired under the interaction of Cl<sup>-</sup> and wear, as reported by Hong et al [12]. For the present alloys,

however, no typical passivation occurred on 143H, and the passive film is still protective on 128H at  $E_c$ . No film cracking occurred even in solution containing 0.5 M  $\text{Cl}^-$ . Therefore, the erosion-corrosion process at  $E_c$  did not involve permanent film cracking for the present system.

On the other hand, the presence of  $\text{Cl}^-$  might influence the erosion process. Huang et al. [11] found the friction coefficient of stainless steel decreased slightly with increasing  $\text{Cl}^-$  concentration at  $E_c$ , and they used it to rationalize the slight decrease (12% in 0.2M  $\text{Cl}^-$  solution) of corrosive wear rate at low load. Additionally, mechanical properties of the metal surface may change due to  $\text{Cl}^-$ . Jiang et al. [13] proposed a concept of  $\text{Cl}^-$  induced brittleness based on the observation that the fritters formed in the solution with  $\text{Cl}^-$  were the same as that of brittle materials. They also pointed out this phenomenon only occurs under severe wear conditions and used it to explain the acceleration of corrosive wear rate with  $\text{Cl}^-$  concentration. For the test results presented in **Figure 16**, however, the weight loss was decreased markedly (48% for 143H and 35% for 128H in 0.2 M  $\text{Cl}^-$  solution). Whether the friction coefficient changes, the  $\text{Cl}^-$  brittleness, and/or other mechanisms dominated this process is still not clear at this stage; more experiments are needed to clarify this interesting phenomenon.

### **A.3 Summary**

- (1) A significant synergistic effect was found between erosion and corrosion process for the Nikro alloys, which causes important additional weight loss.
- (2) The effect of erosion on corrosion depends on the corrosion system. In an active dissolution system, no apparent influence on corrosion rate was found, while in a passive system the passive current was accelerated markedly by the impingement of sand particles.
- (3) The chemo-mechanical effect was not the dominant mechanism for the corrosion enhanced-erosion of MMCs. Rather, the acceleration effect of

corrosion on erosion can be attributed to the preferential dissolution of the interface between the particles and metal matrix. It facilitated the removal of TiC particles and thus increased the erosion rate.

- (4) An interesting experimental phenomenon was found that the presence of Cl<sup>-</sup> in solution can substantially reduce the overall erosion-corrosion rate of MMC alloys.

## References

- [1] S. Das, D.P. Mondal, R. Dasgupta, and B.K. Prasad, *Wear* 236 (1-2) (1999) 295.
- [2] J.A. Bester and A. Ball, *Wear* 162-164 (1993) 57.
- [3] H.X. Guo, B.T. Lu, and J.L. Luo, *Electrochimica Acta* 51 (2005) 315.
- [4] E.M. Gutman, *Mechanochemistry of Materials*, Great Abington, Cambridge, UK, Cambridge International Science Publishing, 1998.
- [5] B.T. Lu and J.L. Luo, *Journal of Physical Chemistry B* 110 (9) (2006) 4217.
- [6] M. Reyes and A. Neville, *Journal of Materials Engineering and Performance* 10 (6) (2001) 723.
- [7] Y.M. Zeng, J.L. Luo, and P.R. Norton, *Electrochimica Acta* 49 (2004) 703.
- [8] E. Mccafferty, *Journal of the Electrochemical Society* 137 (12) (1990) 3731.
- [9] Z.A. Iofa, V.V. Batrakov, and Cho-Ngok-Ba, *Electrochimica Acta* 9 (1964) 1645.
- [10] M.T. Makhlouf, S.A. ElShatory, and A. ElSaid, *Materials Chemistry and Physics* 43 (1) (1996) 76.
- [11] Y.L. Huang, X.X. Jiang, and S.Z. Li, *Bullet of Materials Science* 26 (4) (2003) 431.
- [12] M.H. Hong and S.I. Pyun, *Wear* 147 (1) (1991) 69.
- [13] X.X. Jiang, L. Shun, S.Z. Li, and Y.T. Xiao, *Metallurgy Sinica* 28 (1992) B57.